

All-electron G_0W_0 code based on FP-(L)APW+lo and
applications

Master-Physics
Xinzheng Li

Physics Department of Free University
Ph.D thesis

July 28, 2008

The work presented in this thesis was accomplished during the time from December 2003 to April 2008 in Prof. Dr. M. Scheffler's group in the Fritz-Haber-Institut der Max-Planck-Gesellschaft.

Thesis adviser: Prof. Dr. M. Scheffler
Second referee: Prof. Dr. E. K. U. Gross
Date of disputation: July 16th, 2008

Abstract

Single particle excitations in electronic systems are measured by photoemission spectroscopy (PES) and its inverse counterpart (IPES) in experiments. Their theoretical description is a prerequisite for understanding them. State-of-the-art theory addresses these problems by linking the density-functional theory (DFT) with the many-body perturbation theory (MBPT). In recent years, the GW approach, typically applied as a first order correction (G_0W_0 approximation) to the Kohn-Sham (KS) eigenvalues, mostly within the local-density approximation (LDA), has achieved great success in describing single-particle excitations in weakly correlated semiconductors and insulators.

Favored by its implementation simplicity and computational efficiency, the pseudopotential method has almost monopolized the development in this area. The approximations implicit in this method and their limitations are well-known and under control in ground state calculations based on DFT. This has been achieved by taking the all-electron methods, and in particular the full-potential (linearized)-augmented-plane-wave plus local orbitals (FP-(L)APW+lo) method, as benchmark. However, the influence of these approximations on the calculation of the many-body corrections to the LDA eigenvalues is still unclear.

The reported G_0W_0 calculations based on the pseudopotential method usually show a better agreement with experiment than the all-electron calculations available so far. On the other hand, in E. Shirley and R. Martin words “*any calculation following core-valence partitioning can never be better than the accuracy with which the interactions between core and valence electrons have been treated*” [Phys. Rev. B **47**, 15413 (1993)]. That is, the reasons for this disturbing discrepancy are to be traced back to two approximations underlying PP- G_0W_0 , namely, the exclusion of the core electrons (core-valence partitioning) and the use of pseudo-valence wave functions (*pseudoization*) in the calculation of the self-energy.

In this thesis, we present the development of an all-electron G_0W_0 code based on the FP-(L)APW+lo method. With this code, we 1) analyze the discrepancy between all-electron and pseudopotential based G_0W_0 results, mainly focusing on the band gaps, and 2) study the electronic structure of IIb-VI semiconductors and group III nitrides. Our results show that core-valence partitioning and *pseudoization*

are equivalently important factors in explaining the difference between all-electron and PP- G_0W_0 band gaps. In IIb-VI semiconductors and group III nitrides, the LDA based G_0W_0 method systematically underestimates the fundamental band gaps, as well as the binding energy of the semicore d -states. Thus, either going beyond the first order correction to the Kohn-Sham eigenvalues (self-consistency), or starting from an effective one-electron problem that approximates the many-body results better than LDA, is required for an accurate description of these properties.

Contents

Abstract	3
I Introduction	1
1 Introduction	3
II Theoretical Background	7
2 First-Principles Electronic Structure Theory	9
2.1 Wave Function Based Methods	10
2.1.1 The Hartree and Hartree-Fock Approximations	11
2.1.2 Beyond the Hartree-Fock Approximation	13
2.2 Density Functional Theory	14
2.2.1 Thomas-Fermi Theory	14
2.2.2 Density Functional Theory	15
2.2.3 Exchange-Correlation Energy	17
2.2.4 Interpretation of the Kohn-Sham Energies	18
3 Pseudopotential Method and the FP-(L)APW+lo Method	21
3.1 Pseudopotential Method	22
3.1.1 Generation of the Pseudopotential	23
3.1.2 Implicit Approximations	27
3.1.2.1 Frozen Core	27
3.1.2.2 Core-Valence Linearization.	27
3.1.2.3 Pseudoization	28
3.2 FP-(L)APW+lo Method	28
3.2.1 LAPW Basis Functions	31
3.2.2 APW+lo Basis Functions	32
3.2.3 Core States	32

3.2.4	Potential and Density	33
4	Many-Body Green Function Theory and the GW Approximation	35
4.1	Green Function Method	36
4.1.1	The Green Function	36
4.1.2	The Dyson Equation	37
4.1.3	Self-energy: Hedin Equations	40
4.1.4	The Quasiparticle Concept	42
4.2	GW Approximation	44
4.3	G_0W_0 Approximation	46
4.4	Summary	48
III	Implementation and Tests	49
5	Numerical Implementation of the G_0W_0 Code	51
5.1	Summary of the G_0W_0 Equations	52
5.2	The Mixed Basis	53
5.2.1	Definition	54
5.2.2	Completeness Tests	55
5.3	Matrix Form of the G_0W_0 Equations	60
5.4	Brillouin-Zone Integration of the Polarization	61
5.5	Γ Point Treatment for the Brillouin-Zone Integration of the Self-energy	65
5.6	The Frequency Integration	67
5.7	Flowchart	68
6	Convergence Tests	71
6.1	The Basis Set	72
6.2	Frequency Integration	74
6.3	Number of \mathbf{k} -points	76
6.4	Number of Unoccupied States	79
6.5	Experience Based “Menu”	81
IV	Results and Conclusions	87
7	Analysis of the Difference between All-electron and Pseudopotential based G_0W_0 Band Gaps	89
7.1	Disentanglement of Core-Valence Partitioning and Pseudoization . . .	91
7.2	Materials without Semicore States	94
7.3	Materials with Semicore States	99
7.3.1	NaCl and CaSe	100

7.3.2	GaAs	102
7.3.3	Including the Semicore States into Valence	103
7.4	Conclusion	105
8	Iib-VI Semiconductors and Group III Nitrides Revisited	115
8.1	Numerical Details	117
8.2	All-Electron Results	117
8.3	The Role of Core States	124
8.3.1	Postions of the Semicore d Bands	124
8.3.2	Band Gaps	130
8.4	Conclusion	131
9	Conclusions and Outlook	133
9.1	Implementation	133
9.2	All-electron vs. Pseudopotential Based G_0W_0 Band Gaps	134
9.3	Iib-VI semiconductors and Group III Nitrides	135
9.4	Outlook	136
V	Appendices	137
A	Integration of Plane Waves in the Interstitial region	139
B	The Overlap Matrix between a Plane Wave and a Mixed Basis Function in the Muffin-Tin Region	141
C	The Coulomb Matrix	143
C.1	A: Both MT-sphere	143
C.1.1	\mathbf{r}_1 and \mathbf{r}_2 belong to MT-spheres Surrounding Different Atoms	143
C.1.2	\mathbf{r}_1 and \mathbf{r}_2 belong to MT-spheres Surrounding Same Atoms . .	146
C.2	B: Both in the Interstitial Region	147
C.3	C: One in the MT-sphere and the Other in the Interstitial Region . .	148
C.4	The Singularity at the Γ Point	149
D	The Matrix Element $M_{n,m}^i(\mathbf{k}, \mathbf{q})$	151
D.1	$\tilde{\chi}_i^{\mathbf{q}}(\mathbf{r})$ Belongs to the Muffin-Tin Region	151
D.2	$\tilde{\chi}_i^{\mathbf{q}}(\mathbf{r})$ Belongs to the Interstitial Region	152
E	The Brillouin-Zone Integration	153
E.1	The Linear Tetrahedron Method	153
E.1.1	The Isoparametric Transfromation	155
E.1.2	Integrals in One Tetrahedron	156

E.1.3	The Integration Weights	157
E.2	Tetrahedron Method for \mathbf{q} -dependent Brillouin-zone Integration . . .	158
E.2.1	Isoparametric Transformation	160
E.2.2	The Integration Region	160
E.2.3	Polarizability	162
E.2.3.1	Polarisability on the Real Frequency Axis	162
E.2.3.2	Polarisability on the Imaginary Frequency Axis . . .	164
F	The Dielectric Matrix at the Γ Point	167
F.1	The Symmetrized Dielectric Matrix	167
F.2	Plane Wave Expansion at the Γ Point	168
F.2.1	The Head	169
F.2.2	The Wings	170
F.3	Mixed Basis Expansion at the Γ Point	171
G	The Dynamically Screened Potential	175
G.1	General Expression	175
G.2	The Singularity of W	176
H	The Frequency Integration	179
I	Expansion of a Non-local Function	181
J	Useful Mathematical Relations	185
J.1	Spherical Harmonics	185
J.2	Plane Waves	188
J.3	Fourier Transform	188
J.4	Spherical Coordinates	188
J.5	The Step(Heaviside) Function	189
	Bibliography	191
	Acknowledgements	199
	Lebenslauf	201
	Publication	203

List of Figures

1.1	Direct, inverse photoemission and absorption	4
3.1	Pseudo-valence wave functions compared with the all-electron ones . .	24
3.2	Ionic pseudopotentials	25
3.3	The space partition in the augmented plane wave method	29
4.1	The poles of Green function	38
4.2	The self-consistent scheme for the exact solution of Hedin equations .	42
4.3	Spectral function for a discrete and a continuous spectrum	44
4.4	The self-consistent scheme in the GW approximation	46
5.1	Expanding the product of KS wave functions in the interstitial region	56
5.2	Expanding the product of two KS wave functions in the MT sphere .	57
5.3	Relative completeness error of the basis in the MT region	58
5.4	Relative completeness error of basis in the interstitial region	59
5.5	The Fermi surface in the special point and tetrahedron schemes . . .	62
5.6	The integration region in the \mathbf{q} -dependent Brillouin-zone integration .	63
5.7	Polarizability of the free electron gas	64
5.8	Analytical structure of $\Sigma^c = iGW^c$ on the complex frequency plane .	68
5.9	Flowchart of our G_0W_0 code	70
6.1	$\Gamma - X$ band gap vs. N_ω in Si	75
6.2	The fundamental band gap vs. N_ω in GaAs	76
6.3	The macroscopic dielectric constant vs. $N_{\mathbf{k}}$ in Si	77
6.4	$\Gamma - X$ band gap vs. $N_{\mathbf{k}}^{-1}$ in Si	78
6.5	G_0W_0 correction to the $\Gamma - X$ band gap vs. $N_{\mathbf{k}}^{-1}$ in Si	79
6.6	G_0W_0 correction to the fundamental band gap vs. $N_{\mathbf{k}}^{-1}$ in GaAs . . .	80
6.7	Σ^x, Σ^c and V^{xc} vs. $N_{\mathbf{k}}^{-1}$ for the Γ_v state in Si	81
6.8	Σ^x, Σ^c and V^{xc} vs. $N_{\mathbf{k}}^{-1}$ for the X_c state in Si	82
6.9	Σ^x, Σ^c and V^{xc} vs. $N_{\mathbf{k}}^{-1}$ for the Γ_v state in GaAs	83
6.10	Σ^x, Σ^c and V^{xc} vs. $N_{\mathbf{k}}^{-1}$ for the Γ_c state in GaAs	84
6.11	The G_0W_0 correction to the fundamental band gap vs. N_{unocc} in Si .	84

6.12	The G_0W_0 correction to the fundamental band gap vs. N_{unocc} in GaAs	85
7.1	The <i>Pseudoization</i> and core-valence partitioning errors in the G_0W_0 correction to the fundamental band gap	94
7.2	Band diagram of Si	95
7.3	Σ^c , Σ^x , and V^{xc} for the Γ_v state in Si	96
7.4	Σ^c , Σ^x , and V^{xc} for the X_c state in Si	98
7.5	$\Delta\Sigma^c$, $\Delta\Sigma^x$, and ΔV^{xc} over the X_c and Γ_v states in Si	99
7.6	The G_0W_0 correction to the $\Gamma - X$ band gap in Si	100
7.7	Σ^c , Σ^x , and V^{xc} for the Γ_v state in NaCl	105
7.8	Σ^c , Σ^x , and V^{xc} for the Γ_c state in NaCl	107
7.9	$\Delta\Sigma^c$, $\Delta\Sigma^x$, and ΔV^{xc} over the Γ_c and Γ_v states in NaCl.	108
7.10	The G_0W_0 correction to the fundamental band gap in NaCl obtained from the PP, AE-Valence, and AE- G_0W_0 calculations	108
7.11	Band diagram of GaAs	109
7.12	Σ^c , Σ^x , and V^{xc} for the Γ_v state in GaAs	109
7.13	Σ^c , Σ^x , and V^{xc} for the Γ_c state in GaAs	110
7.14	$\Delta\Sigma^c$, $\Delta\Sigma^x$, and ΔV^{xc} over Γ_c and Γ_v states in GaAs	110
7.15	The G_0W_0 correction to the fundamental band gap in GaAs obtained from the PP, AE-Valence, and AE- G_0W_0 calculations	111
7.16	Σ^c , Σ^x , and V^{xc} for the Γ_v state in GaAs obtained from the AE-Valence, AE-Valence2, and AE- G_0W_0 calculations	112
7.17	Σ^c , Σ^x , and V^{xc} for the Γ_c state in GaAs obtained from the AE-Valence, AE-Valence2, and AE- G_0W_0 calculations	112
7.18	$\Delta\Sigma^c$, $\Delta\Sigma^x$, and ΔV^{xc} over Γ_c and Γ_v states in GaAs obtained from the AE-Valence, AE-Valence2, and AE- G_0W_0 calculations	113
7.19	The G_0W_0 band gap corrections in GaAs	113
8.1	The LDA eigenvalues of GaN at the Γ point	116
8.2	Band Diagram of GaN from all-electron LDA and G_0W_0 calculations .	118
8.3	Band Diagram of ZnS from all-electron LDA and G_0W_0 calculations .	119
8.4	Band Diagram of ZnSe from all-electron LDA and G_0W_0 calculations .	119
8.5	Band Diagram of ZnTe from all-electron LDA and G_0W_0 calculations .	120
8.6	Band Diagram of CdS from all-electron LDA and G_0W_0 calculations .	120
8.7	Band Diagram of CdSe from all-electron LDA and G_0W_0 calculations .	121
8.8	Band Diagram of CdTe from all-electron LDA and G_0W_0 calculations .	121
8.9	Band character plot of GaN in the LDA calculation	122
8.10	Band diagrams of GaN obtained from LDA, AE, AE-VAL1 and AE-VAL2 G_0W_0 calculations	126
8.11	Band diagrams of ZnS obtained from LDA, AE, AE-VAL1 and AE-VAL2 G_0W_0 calculations	126

8.12 Band character plot of ZnS for the d component of Zn 129

E.1 Two-dimension sketch for the BZ in the tetrahedron method 159

E.2 The configurations for the region to be integrated 161

List of Tables

3.1	Relativistic quantum numbers	33
6.1	G_0W_0 results for Si using different basis in the MT sphere	72
6.2	G_0W_0 results for Si using different basis in the interstitial region . . .	73
6.3	G_0W_0 results with a higher energy cutoffs for Si using different basis .	74
6.4	G_0W_0 results for GaAs using different basis sets in the MT sphere . .	74
6.5	G_0W_0 results for GaAs using different basis sets in the interstitial region	75
7.1	Comparison of formerly reported G_0W_0 band gaps	91
7.2	Numerical parameters used for the AE- G_0W_0 calculations	92
7.3	Our band gaps in comparison with others	93
7.4	Σ^x , Σ^c and V^{xc} for Si	97
7.5	Σ^x , Σ^c and V^{xc} for C	101
7.6	Σ^x , Σ^c and V^{xc} for BN	102
7.7	Σ^x , Σ^c and V^{xc} for AlP	103
7.8	Σ^x , Σ^c and V^{xc} for LiF	104
7.9	Σ^x , Σ^c and V^{xc} for NaCl	106
7.10	Σ^x , Σ^c and V^{xc} for CaSe	107
7.11	Σ^x , Σ^c and V^{xc} for GaAs	111
8.1	LDA and G_0W_0 fundamental band gaps for GaN, ZnS, ZnSe, ZnTe, CdS, CdSe, and CdTe	123
8.2	d electron binding energies referenced to the valence band maximum for GaN, ZnS, ZnSe, ZnTe, CdS, CdSe, and CdTe	125
8.3	Contributions from Σ^x , Σ^c and V^{xc} to the d -state binding energy in GaN	127
8.4	Contributions from Σ^x , Σ^c and V^{xc} to the d -state binding energy in ZnS	128
8.5	Contributions from Σ^x , Σ^c and V^{xc} to the fundamental band gap in GaN	130

8.6 Contributions from Σ^x , Σ^c and V^{xc} to the fundamental band gap in
ZnS 132

Part I
Introduction

Chapter 1

Introduction

Since the discovery of electron as a particle in 1896-1897, the theory of electrons in matter has ranked among the great challenges in theoretical physics. The fundamental basis for understanding materials and phenomena ultimately rests upon understanding electronic structure. [1] It is without any hesitation that I assent to Richard M. Martin's point of view and take it as the first sentence when it comes to writing this introduction for my Ph.D thesis.

One point implied in this statement is that the concept of electronic structure is polymorphous, in the sense that it covers all properties related to electrons in matter. For example, it can refer to the total energy of the electrons, their density distribution, the energy needed for extracting one electron out of the system, their response to an external perturbation, etc. These properties are in principle measured by different experiments. As a consequence, when saying "electronic structure", one must specify the corresponding property of the electrons it refers to. Among the various properties which can be obtained from theories and experiments about the electronic system, we will focus on those concerning spectroscopies throughout the thesis. Direct and inverse photoemission and absorption are the prototype spectroscopies in this context. The processes of these experiments are described in Fig. 1. For these three processes, a knowledge of the single particle excitations, which corresponds to the information obtained from direct and inverse photoemission, is of fundamental importance. The work to be introduced in this thesis concerns their all-electron theoretical description.

Direct photoemission experiments are an application of the Einstein's photoelectric effect for probing the electronic states in matter. The sample is perturbed by an incoming photon with energy $h\nu$. One electron absorbs this energy and escapes out of the system with a kinetic energy $E_{\mathbf{k}}$ measured at a large distance. The difference between $h\nu$ and $E_{\mathbf{k}}$ corresponds to the energy of the state originally occupied by this photoelectron. In the inverse photoemission experiment, a beam of electrons with kinetic energy $E_{\mathbf{k}}$ is incident upon the sample. After entering the system, these

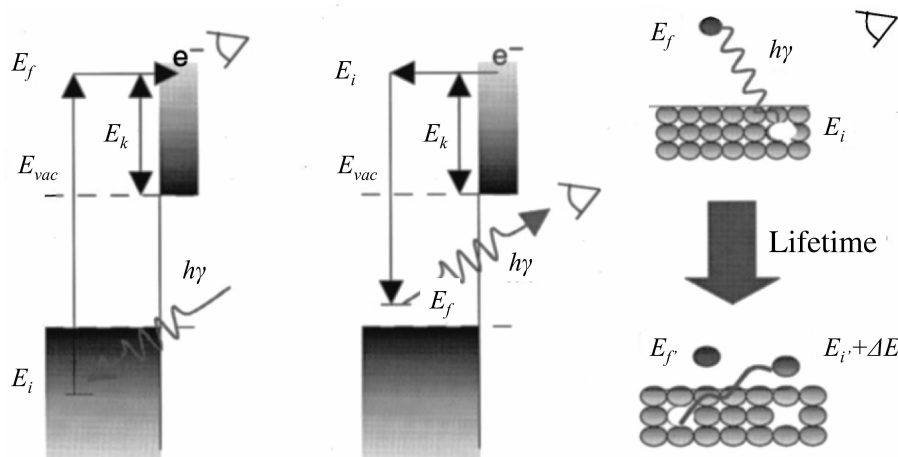


Figure 1.1: Schematic representation of direct, inverse photoemission and absorption. Taken from Ref. [2].

electrons decay radiatively to unoccupied states of lower energy. The energy of the outgoing photons is measured and its difference to $E_{\mathbf{k}}$ corresponds to the energy of the unoccupied states in the system.

In the last years, the computational study of the electronic structure has benefited considerably from the development of feasible simplified treatments in extended systems. Among them, the density-functional theory [3, 4], a method overwhelmingly dominated by the local-density approximation (LDA) and extensions thereof, has achieved tremendous success for the theoretical description of ground state properties. Driven by this tremendous success, the corresponding Kohn-Sham eigenvalues have been conventionally used to interpret the single particle excitation energies measured in direct and inverse photoemission experiments. Reasonably satisfactory results were found in simple metals [5]. However, when the excited state properties of semiconductors and insulators are concerned, universal discrepancies with experiments appear. A well-known example is the systematic 50-100% underestimation of the fundamental band gaps of semiconductors in LDA when compared with experiments.

A formally justified framework for calculating the single particle excitations is the many-body perturbation theory (MBPT) [6]. Within this framework, the quasiparticle concept is introduced to describe an electron surrounded by a positive charge cloud which is generated by its interaction with the system. This interaction, in turn, acts on the quasiparticle, changing its energy. The resulting effective interaction of the quasiparticle with itself is called the self-energy. So defined, the quasiparticles obey a Schrödinger-like equation, where the self-energy plays the role of a non-local, non-hermitian and time (or frequency) dependent potential. It can be formally

demonstrated that the eigenvalues of the quasiparticle equation corresponds to the total energy difference between the ground state and the state with the corresponding quasiparticle removed (added), namely, the quantity that is measured in direct (inverse) photoemission experiments.

The diagrammatic expansion introduced by R. Feynman [7] provides an intuitive method for evaluating the self-energy to all orders in the Coulomb potential. However, this procedure is impractical, due to the long-range nature of the Coulomb interaction, and one must resort to approximations. The simplest of them including dynamical screening effects is the GW approximation proposed by Hedin in 1965, in which the self-energy is written as a product of the Green's function and the screened Coulomb interaction [8]. In their seminal work, Hybertsen and Louie showed that applying Hedin's GW approximation as a first order perturbation to the fictitious, non-interacting Kohn-Sham (KS) particles of density-functional theory (DFT) provides an accurate description of the photoemission spectra in weakly correlated semiconductors and insulators [9, 10]. Since both the Green's function and the screened Coulomb interaction are obtained from the Kohn-Sham orbitals and eigenvalues, this treatment is usually called one-shot GW or G_0W_0 , we will adopt the latter throughout this thesis. Nowadays, this approach has become the standard method for the theoretical description of single particle excitations in real extended systems.

Since its birth, the G_0W_0 approach has been dominated by implementations within the pseudopotential framework, due to their simplified algebra and their computational efficiency. An excellent agreement with experiments has been obtained for a wide range of materials [2, 9, 10, 11, 12]. In 2002 the first all-electron full-potential (FP) implementations of the G_0W_0 method appeared, based on the LMTO [13] and the LAPW [14] methods. In both cases, the results obtained showed a noticeable and systematic underestimation of the band gaps compared with both pseudopotential results and experiments. This triggered a debate in which the validity of the approximations implicit in the pseudopotential method and the numerical precision of the all-electron calculations were questioned [15, 16].

In this work, we present the implementation of a new all-electron G_0W_0 code based on the full-potential (linearized) augmented plane wave plus local orbitals (FP-(L)APW+lo). As its first applications, we carry out a detailed comparison between the all-electron and pseudopotential- G_0W_0 results to uncover the origin of the mentioned discrepancies. We also investigate the role of the electrons in the semicore shell and deeper core states in G_0W_0 calculations.

The thesis is organized as follows. In Chapter 2 we introduce the most common theoretical approaches to the electronic structure of materials. The basic principles behind the pseudopotential method and the FP-(L)APW+lo method are presented in Chapter 3. The many-body perturbation theory, with particular emphasis on the GW approximation is summarized in Chapter 4. The implementation of our

G_0W_0 code is then introduced in Chapter 5. Chapter 6 illustrates the precision and stability of the code through an abridged set of tests. The origin of the differences between all-electron and PP- G_0W_0 results is analyzed in Chapter 7. In Chapter 8 we carry out a systematic study of the role of semicore and deep core-states on the G_0W_0 quasiparticle spectra of some selected II-VI semiconductors and group III nitrides. Finally, we summarize our conclusions in Chapter 9.

Part II

Theoretical Background

Chapter 2

First-Principles Electronic Structure Theory

Any poly-atomic system can be viewed as the intermixture of two coupled subsystems, constituted by M nuclei and N electrons respectively. In principle, the only prerequisite for the description of all the quantum mechanical properties of such a system, in the non-relativistic regime, is the solution of the the many-body Schrödinger equation:

$$\hat{H}\Psi(\mathbf{r}_1, \mathbf{r}_2, \dots, \mathbf{r}_N, \mathbf{R}_1, \mathbf{R}_2, \dots, \mathbf{R}_M) = E\Psi(\mathbf{r}_1, \mathbf{r}_2, \dots, \mathbf{r}_N, \mathbf{R}_1, \mathbf{R}_2, \dots, \mathbf{R}_M), \quad (2.1)$$

where \mathbf{r}_i stands for the coordinate of the i th. electron and \mathbf{R}_i stands for that of the i th. nucleus. The Hamiltonian operator is given by:

$$\hat{H} = -\sum_{i=1}^N \frac{1}{2} \nabla_i^2 + \frac{1}{2} \sum_{i \neq i'} V(\mathbf{r}_i - \mathbf{r}_{i'}) - \sum_{j=1}^M \frac{1}{2M_j} \nabla_j^2 + \frac{1}{2} \sum_{j \neq j'} V(\mathbf{R}_j - \mathbf{R}_{j'}) + \frac{1}{2} \sum_{i,j} V(\mathbf{r}_i - \mathbf{R}_j), \quad (2.2)$$

in atomic units (a. u.) with Hartree as the unit of energy, which will be used in all equations throughout this thesis. The first two terms correspond to the electronic kinetic energy and Coulomb interaction respectively. The third and fourth terms represent the same physical quantities for the nuclei. The fifth term is the Coulomb interaction between the electrons and the nuclei which couples the dynamics of both subsystems.

Since the mass of the nuclei is several orders of magnitude larger than that of the electrons, their velocities will be correspondingly smaller. Taking advantage of these extremely different dynamical regimes, the adiabatic, better known as Born-Oppenheimer, approximation allows to address the dynamics of the electronic subsystem separately from that of the nuclei by considering the later as static. The poly-atomic quantum system including both electrons and nuclei is thus simpli-

fied into a system that only includes the electrons as quantum particles¹ [17]. The Schrödinger equation for the electrons then reads:

$$\hat{H}_e \Phi(\mathbf{r}_1, \mathbf{r}_2, \dots, \mathbf{r}_N) = E_e \Phi(\mathbf{r}_1, \mathbf{r}_2, \dots, \mathbf{r}_N), \quad (2.3)$$

where the Hamiltonian

$$\hat{H}_e = - \sum_{i=1}^N \frac{1}{2} \nabla_i^2 + \frac{1}{2} \sum_{i \neq i'} V(\mathbf{r}_i - \mathbf{r}_{i'}) + \frac{1}{2} \sum_{i,j} V(\mathbf{r}_i - \mathbf{R}_j), \quad (2.4)$$

depends only parametrically on the nuclear coordinates.

The purpose of this chapter is to illustrate the basic principles underlying the current standard methods to accurately solve Eq. 2.3, which represents the main task for the *ab initio* calculations of the electronic structure of materials. The different schemes to achieve this goal can be separated in two big categories. The wave function methods, traditionally known as quantum chemistry methods, and methods based on the density-functional theory (DFT). Both of them have achieved great success within the last half century as evidenced by the Nobel Prize of Chemistry awarded to W. Kohn and J. Pople in 1998. Hereinafter, I will address both of these schemes, with a special emphasis on DFT. Knowledge of their successes and limitations comprises the required point of departure for the discussions about the Green's function method afterwards.

2.1 Wave Function Based Methods

The variational principle, which can be viewed as another form of the many-body Schrödinger equation, states that any state vector of the electrons for which the average energy, defined as,

$$E_e[\Phi] \equiv \frac{\langle \Phi | \hat{H}_e | \Phi \rangle}{\langle \Phi | \Phi \rangle}, \quad (2.5)$$

is stationary corresponds to an eigenvector of \hat{H}_e , with eigenvalue E_e . Furthermore, for any state of the system, the corresponding average energy satisfies

$$E_e[\Phi] \geq E_0, \quad (2.6)$$

where E_0 is the ground state energy of the electronic system.

The essence of the wave function based methods consists in obtaining the stationary solutions of Eq. 2.5 within a trial-function space. The accuracy of the

¹The description of the nuclear subsystem, usually treated classically, with the total energy of the electronic system, which is a function of the nuclear coordinates, playing the role of an external potential, is beyond the scope of this work.

method is naturally determined by the choice of this trial-function space. By taking more sophisticated approximations for the trial many-body wave function of these electrons, the accuracy can be systematically improved, as well as, unfortunately, its computational cost. In this section, we will introduce some of these approximations in order of increasing complexity.

2.1.1 The Hartree and Hartree-Fock Approximations

Since the many body wave function can always be written as a linear combination of products of one particle wave functions, the simplest possible ansatz, first proposed by Hartree [18], for the many-body electronic wave function is to assume it as the product of the single particle wave functions:

$$\Phi(\mathbf{r}_1, \mathbf{r}_2, \dots, \mathbf{r}_N) = \varphi_1(\mathbf{r}_1)\varphi_2(\mathbf{r}_2)\dots\varphi_N(\mathbf{r}_N). \quad (2.7)$$

Substituting this trial wave function into Eq. 2.5, making use of the variational principle, the many-body problem of this electronic system is mapped onto a set of single particle, Schrödinger like, equations:

$$\hat{h}_i\varphi_i(\mathbf{r}_i) = \epsilon_i\varphi_i(\mathbf{r}_i) \quad (2.8)$$

with the Hamiltonian given by:

$$\hat{h}_i = \left[-\frac{\nabla^2}{2} + V_{\text{ext}}(\mathbf{r}) + V^{\text{H}}(\mathbf{r}) + V_i^{\text{SIC}}(\mathbf{r})\right] \quad (2.9)$$

The solutions of Eq. 2.8 are coupled through the Hartree potential

$$V^{\text{H}}(\mathbf{r}) = \int \frac{n(\mathbf{r}')}{|\mathbf{r} - \mathbf{r}'|} d\mathbf{r}' \quad (2.10)$$

which depends on the electron density, defined as:

$$n(\mathbf{r}) = \sum_{j=1}^N |\varphi_j(\mathbf{r})|^2. \quad (2.11)$$

Thus, the set of Eqs. 2.8 to 2.11 has to be solved selfconsistently. Summarizing, the Hartree approximation maps the many-particle problem into a set of independent particles moving in the mean Coulomb field of the other particles.

The last term in Eq. 2.9 corrects for the interaction of the electron with itself included in the Hartree potential.

$$V_i^{\text{SIC}}(\mathbf{r}) = - \int \frac{|\varphi_i(\mathbf{r}')|^2}{|\mathbf{r} - \mathbf{r}'|} d\mathbf{r}' \quad (2.12)$$

Solving these equations, the ground state energy of the electronic system can be calculated as

$$E_e = \sum_{i=1}^N \epsilon_i - \frac{1}{2} \sum_{i=1}^N \sum_{j \neq i}^N \iint \frac{|\varphi_i(\mathbf{r})|^2 |\varphi_j(\mathbf{r}')|^2}{|\mathbf{r} - \mathbf{r}'|} d\mathbf{r} d\mathbf{r}' \quad (2.13)$$

The Hartree approximation has a major drawback, namely, the many-particle wave function of the electrons does not obey the Pauli principle, which forbids two Fermi particles to occupy the same quantum mechanical state, and therefore, prevents electrons with the same spin from getting close to each other. Lacking this feature, the Hartree approximation generally underestimates the average distances between electrons. Correspondingly, the average Coulomb repulsion between them is overestimated as well as the total energy.

In order to fulfill the Pauli principle, the many-particle wave-function has to be antisymmetric among the exchange of two particles with same spin. The simplest ansatz for a many-particle wave function, obeying Pauli's principle, is obtained by the anti-symmetrized product, known as the Slater Determinant. This improved ansatz, proposed by V. Fock [19], is known as the Hartree-Fock approximation. For non spin-polarized systems in which every electronic orbital is doubly occupied by two electrons with opposite spins (closed shell), this method can be introduced in a very simple form. For a N-electron system, the Slater Determinant representing the many-particle wave function is written as:

$$\Phi(\mathbf{r}_1, \sigma_1, \dots, \mathbf{r}_N, \sigma_N) = \frac{1}{\sqrt{(N)!}} \begin{vmatrix} \varphi_1(\mathbf{r}_1, \sigma_1) & \varphi_1(\mathbf{r}_2, \sigma_2) & \cdots & \varphi_1(\mathbf{r}_N, \sigma_N) \\ \varphi_2(\mathbf{r}_1, \sigma_1) & \varphi_2(\mathbf{r}_2, \sigma_2) & \cdots & \varphi_2(\mathbf{r}_N, \sigma_N) \\ \vdots & \vdots & & \vdots \\ \varphi_N(\mathbf{r}_1, \sigma_1) & \varphi_N(\mathbf{r}_2, \sigma_2) & \cdots & \varphi_N(\mathbf{r}_N, \sigma_N) \end{vmatrix} \quad (2.14)$$

where σ_i represents the spin coordinate of the i -th electron.

Substituting this equation into Eq. 2.5 and making use of the orthogonality of the space orbitals and spin states, one arrives at a set of equations for the single particle orbitals:

$$\begin{aligned} & \left[-\frac{\nabla^2}{2} + V_{\text{ext}}(\mathbf{r}) + V^{\text{H}}(\mathbf{r}) \right] \varphi_i(\mathbf{r}, \sigma) - \int d\mathbf{r}' \sum_j \frac{\varphi_j^*(\mathbf{r}', \sigma') \varphi_j(\mathbf{r}, \sigma)}{|\mathbf{r} - \mathbf{r}'|} \delta_{\sigma, \sigma'} \varphi_i(\mathbf{r}', \sigma') \\ & = \epsilon_i \varphi_i(\mathbf{r}, \sigma), \end{aligned} \quad (2.15)$$

The only difference with Eq. 2.9 is the last term, representing the exchange interaction between electrons and known as the Fock operator. It is non-local, and affects only the dynamics of electrons with the same spin. Notice that when $j = i$, the

exchange term equals the corresponding term in the Hartree potential, *i. e.* the Hartree-Fock approximation is self-interaction free.

In terms of the single particle orbitals, the total energy of the system can be represented as:

$$E_e = \langle \Phi | \hat{H}_e | \Phi \rangle = \sum_i^N H_{i,i} + \sum_i^N \sum_j^N \left(\frac{J_{i,j}}{2} - \frac{K_{i,j}}{4} \right) \quad (2.16)$$

where:

$$H_{i,i} = \int \varphi_i^*(\mathbf{r}, \sigma) \left[-\frac{1}{2} \nabla^2 + V_{\text{ext}}(\mathbf{r}) \right] \varphi_i(\mathbf{r}, \sigma) d\mathbf{r} d\sigma \quad (2.17)$$

$$J_{i,j} = \iint \varphi_i^*(\mathbf{r}, \sigma) \varphi_i(\mathbf{r}, \sigma) \frac{1}{|\mathbf{r} - \mathbf{r}'|} \varphi_j^*(\mathbf{r}', \sigma') \varphi_j(\mathbf{r}', \sigma') d\mathbf{r} d\sigma d\mathbf{r}' d\sigma' \quad (2.18)$$

$$K_{i,j} = \iint \varphi_i^*(\mathbf{r}, \sigma) \varphi_j(\mathbf{r}, \sigma) \frac{1}{|\mathbf{r} - \mathbf{r}'|} \varphi_j^*(\mathbf{r}', \sigma') \varphi_i(\mathbf{r}', \sigma') d\mathbf{r} d\sigma d\mathbf{r}' d\sigma'. \quad (2.19)$$

Here, H_{ii} is the non-interacting single particle energy in the external field. J_{ij} is the “classical” Coulomb interaction between electrons in the states i and j and K_{ij} is the exchange interaction between them. The first two terms appear also in the Hartree method, the last term is introduced by imposing the Pauli principle on the many-body wave function and tends to reduce the total energy.

For spin-polarized systems the method becomes more cumbersome. Since the number of electrons with each spin is not balanced anymore, the contribution from the Fock operator will be different for different spins. Consequently, also the single particle eigenvalues and eigenfunctions will be different [20].

2.1.2 Beyond the Hartree-Fock Approximation

In the Hartree-Fock approximation the electron-electron interaction is treated by means of a time-independent average potential. The fulfillment of Pauli’s principle imposes a “static” correlation of the position of electrons with the same spin (exchange hole). However, it completely neglects dynamical effects due to the Coulomb interaction, in other words, the fact that the movement of a given electron affects and is affected by, *i. e.* “is correlated with”, the movement of the other particles. This is the main limitation of the Hartree-Fock approximation. For atoms, and small molecules, where this approximation works at best, this limitation leads to errors of around 0.5 % in the total energy. For example, in a carbon atom, where the total energy is around 1000 eV, this corresponds to 5 eV, which already reaches the order of magnitude of a chemical single-bond energy. Thus, to obtain a reliable description of chemical reactions, more sophisticated approximations are required.

Within the framework of the wave-function based methods, this can be achieved by making more elaborate approximations for the many-body wave function. Among the, so called, post Hartree-Fock methods, the Configuration Interaction (CI) method [21], the Møller-Plesset (MP) perturbation theory [22], and the Coupled-Cluster (CC) method [23, 24] have achieved the greater success in the last years. As a general shortcoming of all these methods, their application is limited to atoms and small molecules due to the scaling of the computational cost with the system size.

2.2 Density Functional Theory

The formalism of the density-functional theory (DFT) was introduced by Hohenberg and Kohn (HK) in 1964 [3]. In 1965, Kohn and Sham (KS) [4] presented a scheme to treat approximately the interacting electron system within this formalism. It is currently the most popular and successful method for studying the ground state electronic structures. Although far from a panacea for all physical problems in this domain, very accurate calculations can be performed with a computational cost comparable to the Hartree method. In this chapter, we will present some major components of this theory. The discussion begins with its precursor: the Thomas-Fermi Theory.

2.2.1 Thomas-Fermi Theory

The Thomas-Fermi theory was proposed independently by Thomas and Fermi in 1927 [25, 26, 27]. In its original version, the Hartree method is reformulated in a density-based expression for an electron gas with slowly varying density. The kinetic energy is locally approximated by that of a non-interacting homogeneous electron gas with the same density.

Later, Dirac introduced the exchange term into the model using the same local approximation [28]. The total energy of the electronic system, including the exchange term, is written as:

$$\begin{aligned}
 E_e[n] &= T + U^{\text{ext}} + U^{\text{H}} + U^{\text{X}} \\
 &= \frac{3}{10} (3\pi^2)^{2/3} \int d\mathbf{r} n(\mathbf{r})^{5/3} + \int d\mathbf{r} V_{\text{ext}}(\mathbf{r}) n(\mathbf{r}) \\
 &\quad + \frac{1}{2} \int \int d\mathbf{r} d\mathbf{r}' \frac{n(\mathbf{r}) n(\mathbf{r}')}{|\mathbf{r} - \mathbf{r}'|} - \frac{3}{4} \left(\frac{3}{\pi}\right)^{1/3} \int d\mathbf{r} n(\mathbf{r})^{4/3}. \quad (2.20)
 \end{aligned}$$

This expression gives the exact energy for the homogeneous electron gas in the Hartree-Fock approximation. It is also a good approximation for slowly varying densities.

The density is obtained by minimizing the total energy under the constraint of particle number conservation

$$\delta\{E_e - \mu[\int n(\mathbf{r})d\mathbf{r} - N]\} = 0. \quad (2.21)$$

Substituting Eq. 2.20 into Eq. 2.21, one obtains the Thomas-Fermi equation:

$$\frac{1}{2} (3\pi^2)^{2/3} n(\mathbf{r})^{2/3} + V_{\text{ext}}(\mathbf{r}) + V^{\text{H}}(\mathbf{r}) + V^{\text{x}}(\mathbf{r}) - \mu = 0, \quad (2.22)$$

where the Hartree potential, $V^{\text{H}}(\mathbf{r})$ is the same as defined in Eq. 2.10, and the exchange potential is given by

$$V^{\text{x}}(\mathbf{r}) = - \left[\frac{3}{\pi} n(\mathbf{r}) \right]^{1/3}. \quad (2.23)$$

Being based on too crude approximations, lacking the shell character of atoms, and binding behavior, Thomas-Fermi theory fails by destiny in a proper description of real systems.

2.2.2 Density Functional Theory

In 1964, Hohenberg and Kohn formulated two theorems, which formally justified the use of the density as the basic variable in determining the total energy of an interacting many-body system [3]. The first theorem proved the existence of a one-to-one correspondence between the external potential $V_{\text{ext}}(\mathbf{r})$, the ground state many-body wave function Φ , and the ground state density $n(\mathbf{r})$. Thus, the total energy of a system, which is a functional of the many-body wave function Φ , can also be reformulated as a functional of the density:

$$E_e[n(\mathbf{r})] = \int V_{\text{ext}}(\mathbf{r}) n(\mathbf{r}) d\mathbf{r} + F[n(\mathbf{r})]. \quad (2.24)$$

$F[n(\mathbf{r})]$ contains the potential energy of the electronic interactions and the kinetic energy of the electrons. It is a universal functional independent of the external potential. Unfortunately, its exact form is unknown.

Since the expression for the Hartree energy as a functional of the density is known, the functional $F[n(\mathbf{r})]$ in Eq. 2.24 can be further decomposed into:

$$F[n(\mathbf{r})] = U^{\text{H}}[n(\mathbf{r})] + G[n(\mathbf{r})] \quad (2.25)$$

where the expression of the Hartree energy $U^{\text{H}}[n(\mathbf{r})]$ is already given by the third term on the right hand side of Eq. 2.20. Like $F[n(\mathbf{r})]$, $G[n(\mathbf{r})]$ is an unknown

universal functional of the density independent of the external potential. The total energy can then be written:

$$E_e = \int V_{\text{ext}}(\mathbf{r}) n(\mathbf{r}) d\mathbf{r} + \frac{1}{2} \int \int \frac{n(\mathbf{r}) n(\mathbf{r}')}{|\mathbf{r} - \mathbf{r}'|} d\mathbf{r} d\mathbf{r}' + G[n(\mathbf{r})]. \quad (2.26)$$

The second theorem proves that the exact ground state energy of the electronic system corresponds to the global minimum of $E_e[n(\mathbf{r})]$, and the density $n(\mathbf{r})$ that minimizes this functional is the exact ground state density $n_0(\mathbf{r})$.

In 1965, Kohn and Sham proposed a scheme to calculate $G[n(\mathbf{r})]$ [4]. One can decompose it into two parts:

$$G[n] = T^s[n] + E^{\text{xc}}[n]. \quad (2.27)$$

The first term is the kinetic energy of a non-interacting system with the same density. The second term is the exchange-correlation energy.

Minimizing the total energy in Eq. 2.24 under the constraint of particle number conservation (Eq. 2.21) one gets:

$$\int \delta n(\mathbf{r}) \left\{ V_{\text{eff}}(\mathbf{r}) + \frac{\delta T^s[n]}{\delta n(\mathbf{r})} - \mu \right\} d\mathbf{r} = 0, \quad (2.28)$$

where μ is the chemical potential and

$$V_{\text{eff}}(\mathbf{r}) = V_{\text{ext}}(\mathbf{r}) + \int \frac{n(\mathbf{r}')}{|\mathbf{r} - \mathbf{r}'|} d\mathbf{r}' + V^{\text{xc}}(\mathbf{r}). \quad (2.29)$$

$V^{\text{xc}}(\mathbf{r})$ is called the exchange-correlation potential, given by:

$$V^{\text{xc}}(\mathbf{r}) = \frac{\delta E^{\text{xc}}[n]}{\delta n(\mathbf{r})}. \quad (2.30)$$

Assuming a set of non-interacting particles with the same density:

$$n(\mathbf{r}) = \sum_{i=1}^N |\varphi_i(\mathbf{r})|^2, \quad (2.31)$$

Eq. 2.28 is equivalent to:

$$\left\{ -\frac{1}{2} \nabla^2 + V_{\text{eff}}(\mathbf{r}) \right\} \varphi_i(\mathbf{r}) = \epsilon_i \varphi_i(\mathbf{r}). \quad (2.32)$$

Thus, the Kohn-Sham scheme maps the complex, interacting electronic systems into a set of fictitious independent particles moving in an effective, local potential. Since

this effective potential depends on the density, Eq. 2.29, 2.31, and 2.32 have to be solved selfconsistently.

The total energy in the KS scheme is given by:

$$E_e[n(\mathbf{r})] = \sum_{\text{occ}} \epsilon_i - \frac{1}{2} \int \int \frac{n(\mathbf{r}) n(\mathbf{r}')}{|\mathbf{r} - \mathbf{r}'|} d\mathbf{r} d\mathbf{r}' + E^{\text{xc}}[n(\mathbf{r})] - \int n(\mathbf{r}) V^{\text{xc}}(\mathbf{r}) d\mathbf{r}. \quad (2.33)$$

Our discussion in this section is based on the original papers (Ref. [3, 4]), and therefore restricted to the non-degenerate, non-spin-polarized, and non-relativistic cases. Extensions to the *spin-polarized system* can be found in Ref. [29, 30, 31], to the *degenerate system* in Ref. [32, 33, 34, 35, 36]. Overall discussion of these extensions can be found in Chapter 3 of Ref. [37]. The inclusion of relativistic effect are addressed in Ref. [38]. Further extension of the theory to superconductors may be found in Ref. [39, 40]. Detailed discussion about the *v-representability* and related questions can be found in Ref. [32, 35]. An excellent review on the formal justification of the theory can be found in Chapter 2 of Ref. [37].

2.2.3 Exchange-Correlation Energy

In the Kohn-Sham scheme, all the complexity of the many-body interaction is put into the exchange-correlation energy $E^{\text{xc}}[n(\mathbf{r})]$. Unfortunately, not only the exact expression of this functional is unknown, but also a systematic series of approximations converging to the exact result is missing. While semiempirical approaches allow to obtain very precise results within the fitting sample space, their physical origin can be sometimes obscure and their precision outside that space unpredictable. In order to remain within the first-principles framework, the most universal and, to some extent, systematic scheme is the “constrain satisfaction” approach [41]. These “constraints” consist of exact properties that the exchange-correlation functional can be proven to fulfill. In this approach, the approximations to the exchange-correlation functional are assigned to various rungs of the “so-called” *Jacob’s ladder* [41] according to the number of ingredients they contain. The best nonempirical functional for a given rung is constructed to satisfy as many exact theoretical constraints as possible while providing satisfactory numerical predictions for real systems. Increasing the number of ingredients allows the satisfaction of more constraints, thus increasing, in principle, the accuracy.

The simplest approximation for $E^{\text{xc}}[n(\mathbf{r})]$ is the local-density approximation (LDA), proposed in the original paper of Kohn and Sham. It reads:

$$E^{\text{xc}}[n(\mathbf{r})] = \int n(\mathbf{r}) \epsilon_{\text{xc}}(n(\mathbf{r})) d\mathbf{r}, \quad (2.34)$$

where $\epsilon_{\text{xc}}(n(\mathbf{r}))$ is the exchange-correlation (XC) energy per particle of a homogeneous electron gas with the same density n [4].

The exchange contribution to ϵ_{xc} can be obtained analytically (Ref. [6]), giving

$$\epsilon_x(n) = -\frac{3}{4} \left(\frac{3n}{\pi} \right)^{1/3}. \quad (2.35)$$

The correlation contribution has to be calculated numerically. In 1980, Ceperley and Alder performed a set of Quantum Monte Carlo calculations for the homogeneous electron gas with different densities [42]. The correlation term of the LDA functionals used nowadays rely on different parametrizations of these results. One of the most used parametrization is that proposed by Perdew and Zunger in 1981 [43].

The LDA is exact for the homogeneous electron gas, and expected to be valid for inhomogeneous systems with slowly varying density. A large number of calculations have shown that it works remarkably well for several real systems with strongly inhomogeneous electron densities [31].

The natural ingredient to improve over the local-density approximation is the inclusion of the dependence on the gradient of the density. This approach gave rise to the generalized gradient approximations (GGA) introduced in the late 1980's [44, 45]. The exchange-correlation energy is written as:

$$E^{xc}[n(\mathbf{r})] = \int n(\mathbf{r}) \epsilon_{xc}(n(\mathbf{r}), \nabla n(\mathbf{r})) d\mathbf{r}. \quad (2.36)$$

The so called PBE functional [46] is the most commonly used non-empirical GGA functional nowadays. it improves over the LDA for many properties, for example, the geometries and ground state energy of molecules [46, 47, 48, 49].

Further climbing Jacob's ladder meta-GGA's functionals are found in the third rung, its description as well as prescriptions for the fourth and fifth rungs can be found in Ref. [50].

2.2.4 Interpretation of the Kohn-Sham Energies

The Kohn-Sham eigenvalues appear as formal Lagrange multipliers in Eq. 2.21 and correspond to the eigenstates of the fictitious, non-interacting Kohn-Sham particles. A crucial question is therefore whether they have any physical meaning.

Janak's theorem, together with Slater's transition state theory, provide a justification for the interpretation of the highest occupied state's eigenvalue as the ionization energy in extended systems [51, 52]. Later this justification was extended to the finite systems [53]. For the other states, the Kohn-Sham eigenvalue, when calculated at a half occupation, gives a good estimation of the corresponding total energy difference [54]. When the Kohn-Sham potential is continuous with respect to the electron density, these energy differences can even be approximated by the Kohn-Sham eigenvalues calculated with full occupation. However, since the exact

form of $E^{\text{xc}}[n]$ is unknown, the comparison between the Kohn-Sham eigenvalues and experiments always relies on approximations of the exchange-correlation potential.

For the local-density approximation and generalized gradient approximations, the result of such a comparison can be easily summarized: the work function and bandstructures in metals are found to be reasonably well described [5, 55], for semiconductors and insulators, universal underestimations of 50-100% for the fundamental band gaps are found. A well-known problem of the local-density approximation is the self-interaction. By using the exact exchange optimized effective potential (OEPx), which is self-interaction free, these band gaps are improved [56, 57, 58, 59, 60].

On the other hand, the fundamental band gap is determined from the ground state energy of the $N-1$, N , and $N+1$ -electron systems. The Kohn-Sham band gap is calculated as the difference between the lowest unoccupied and highest occupied Kohn-Sham eigenvalues in a N -electron system. It was proven that they differ by a term given by the discontinuity of the exchange-correlation potential [61, 62, 63], that is:

$$E_g = E_g^{\text{KS}} + \Delta_{xc}, \quad (2.37)$$

where

$$\Delta_{xc} = \lim_{\delta \rightarrow 0^+} [V^{\text{xc}}|_{N+\delta} - V^{\text{xc}}|_{N-\delta}]. \quad (2.38)$$

In both LDA and GGA, this discontinuity is zero. In OEPx, it is not zero. Adding this term to the Kohn-Sham band gaps through the above equations, Grüning, Marini, and Rubio have shown that similar fundamental band gaps as the Hartree-Fock method can be obtained [64]. The exact exchange-correlation functional would allow the calculation of the band gap through Eq. 2.37. Nevertheless, for the description of the excited state properties in general a different theoretical approach is required. The standard treatment nowadays is the Green function method we are going to address in this thesis.

Chapter 3

Pseudopotential Method and the FP-(L)APW+lo Method

As has been shown in the previous chapter, in the Kohn-Sham scheme to the Density-Functional Theory the many-body electronic problem is reduced to an independent particle problem (Eq. 2.32) under the action of an effective, density dependent potential (Eqs. 2.29 and 2.30). Any numerical implementation of this scheme to polyatomic systems has to deal with two extremely different regimes: The core states tightly bound to the nucleus, and the delocalized valence states. The former are represented by localized wave functions of atomic character, and their role in the bonding of the system is mainly the screening of the nuclear potential. The valence states play a determinant role in the bonding, which reciprocally determines the characteristics of the wave functions of these states, going from localized states in ionic systems, to fully itinerant ones in simple metals. However itinerant the valence wave function may be, it also presents a fast oscillating behavior in the region close to the nuclei, while it oscillates gently in the interstitial region. In particular for periodic systems, where the reciprocal space representation is more efficient, planewaves are a natural basis set. However, they are inefficient for representing both the strongly localized core states and the rapid oscillations of the valence wave functions in the nuclear region.

During the years, different strategies have been developed to address these co-existent regimes. They can be arranged in two big groups, namely: all-electron and pseudopotential methods. The all-electron methods rely on the use of more sophisticated basis functions for the expansion of the wave functions. These basis functions can address the oscillation of the wave functions in the nuclear region, as well as the core states, at a reasonable computational cost. The pseudopotential methods, on the other hand, replace the strong nuclear potential and the core contribution to the Hartree and exchange-correlation potentials by an effective ionic potential (*i. e.* the pseudopotential), which is designed to be much softer than the full-potential

in the atomic region. In this way, the valence wave functions behave smoothly in the nuclear region and can be efficiently expanded in planewaves. Only the valence electrons are treated explicitly.

In this chapter, we will give a brief introduction of one class of pseudopotential method, the norm-conserving pseudopotentials, focusing on its basic principles. We will also introduce one all-electron method: the Full-potential (Linearized-) Augmented Plane Waves plus local orbitals method (FP-(L)APW+lo), which is currently the most accurate method in DFT calculations in periodic systems.

3.1 Pseudopotential Method

The main idea behind the pseudopotential method is that, as long as the core electrons are tightly bound, they do not participate actively in the bonding process. Thus, the strong ion potential, including contributions from the nucleus and the core electrons, can be replaced by an angular dependent pseudopotential constructed from the free atom of the corresponding element [65]. In this way, only the valence states are included explicitly in the polyatomic system, which significantly reduces the computational cost. Inside the core region, the pseudopotential is designed to be much softer than the ionic one. Outside the core region, it is required that the corresponding pseudo wave function equals its all electron counterpart in order to obtain the correct behavior over a wide range of chemical environments (transferability).

A pseudopotential fulfilling the above mentioned prerequisites can be generated in arbitrarily many ways. The most used one is the “norm-conserving” scheme originally proposed by Hamann, Schlüter, and Chiang [66], and later applied to elements from H to Pu by Bachelet, Hamann, and Schlüter [67]. In this scheme the integral of the pseudo charge density inside the core region is required to agree with the all-electron one. This condition guarantees that the electrostatic potential produced outside the core radius is equal in both cases. Furthermore, the energy dependence of the scattering properties of the pseudopotential is of the second order and can be ignored without affecting the transferability. Nevertheless, for some cases, *e. g.* O $2p$ or Ni $3d$ orbitals, it has been found impossible to construct a pseudo wave function much softer than its all-electron counterpart [68]. Such drawbacks can be overcome by the ultra-soft pseudopotentials proposed in Ref. [68] and [69], where the norm-conserving constraint is lifted. In this work, we restrict ourselves to the norm-conserving scheme for a clear illustration of the principles underlying the method.

3.1.1 Generation of the Pseudopotential

The initial step for generating a norm-conserving pseudopotential is to perform an all-electron DFT calculation for the free atom. This corresponds to obtain a self-consistent solution of the radial, Schrödinger like equation:

$$\left[-\frac{1}{2} \frac{d^2}{dr^2} + \frac{l(l+1)}{2r^2} + V(r) - \epsilon_l \right] u_l(\epsilon_l, r) = 0 \quad (3.1)$$

where $V(r)$ is obtained from the set of equations 2.31, 2.30 and 2.29 with $\varphi_{l,m}(\mathbf{r}) = \frac{u_l(\epsilon_l, r)}{r} Y_{l,m}(\hat{r})$.

For each angular momentum number “ l ” (from now on channel), a cutoff radius (r_l^c) is chosen and the pseudo-valence radial wave function $u_l^{\text{ps}}(\epsilon_l^{\text{ps}}, r)$ is derived from its all-electron counterpart $u_l(\epsilon_l, r)$ with the following minimal constraints:

- i. The pseudo-valence state has the same eigenvalue as the all-electron one ($\epsilon_l^{\text{ps}} = \epsilon_l$).
- ii. $u_l^{\text{ps}}(\epsilon_l, r)$ equals $u_l(\epsilon_l, r)$ beyond the cutoff radius (designated by r^{match} in Fig. 3.1).
- iii. $u_l^{\text{ps}}(r)$ is nodeless. In order to obtain a continuous pseudopotential regular at the origin, it is also required to be twice differentiable and satisfy $\lim_{r \rightarrow 0} u_l^{\text{ps}} \propto r^{l+1}$.
- iv. The pseudo-valence radial wave function is normalized (the norm-conserving constraint), which, together with (ii) implies:

$$\int_0^{r'} |u_l^{\text{ps}}(\epsilon_l^{\text{ps}}; r)|^2 dr \equiv \int_0^{r'} |u_{n,l}(\epsilon_{n,l}; r)|^2 dr \text{ for } r' \geq r_l^c. \quad (3.2)$$

Once the pseudo wave function has been obtained, one can construct the screened¹ pseudopotential $V_l^{\text{ps,scr}}(r)$, which acts as the effective potential on the pseudo-valence state, by inverting the radial Schrödinger equation, leading to:

$$V_l^{\text{ps,scr}}(r) = \epsilon_l^{\text{ps}} - \frac{l(l+1)}{2r^2} + \frac{1}{2u_l^{\text{ps}}(r)} \frac{d^2}{dr^2} u_l^{\text{ps}}(\epsilon_l, r). \quad (3.3)$$

In a last step the pseudocharge density \tilde{n}_v^0 is obtained by:

$$\tilde{n}_v^0(r) = \sum_l^{\text{occ}} \left| \frac{u_l^{\text{ps}}(r)}{r} \right|^2, \quad (3.4)$$

¹In this context, the term *screened* is used in the sense that $V_l^{\text{ps,scr}}(r)$ also contains the interaction between valence states.

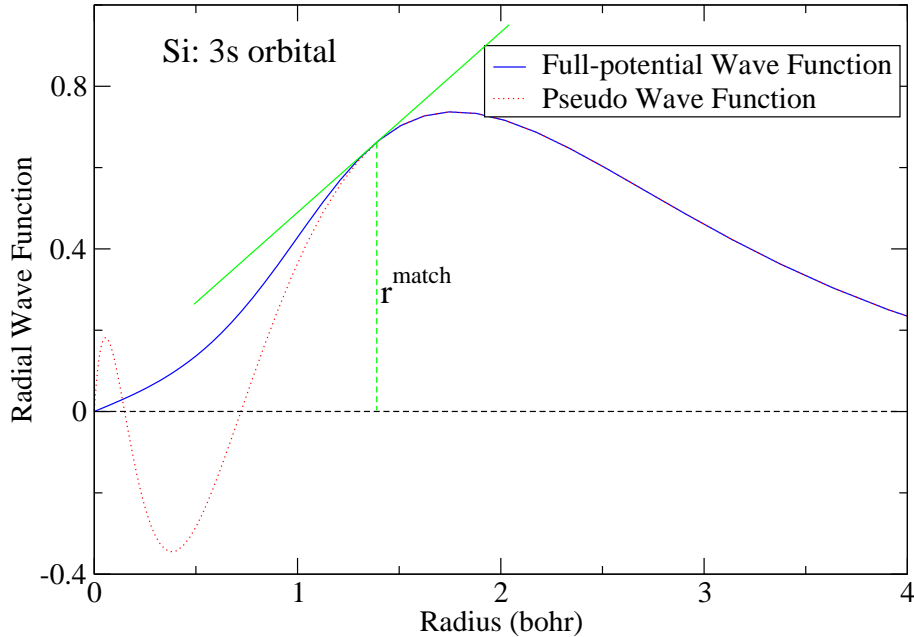


Figure 3.1: Pseudo-valence wave functions in comparison with the all-electron ones. The two wave functions agree with each other outside the matching radius, while the pseudo one is much softer inside this radius. Their norms equal.

and the pseudopotential is *unscreened* by subtracting the Hartree and exchange-correlation potential corresponding to this pseudocharge;

$$V_l^{\text{ps}}(r) = V_l^{\text{ps,scr}}(r) - V^{\text{H}}[\tilde{n}_v^0; r] - V^{\text{xc}}[\tilde{n}_v^0; r] \quad (3.5)$$

So defined, the ionic pseudopotential generated from Eq. 3.5 includes all the interactions of the valence electrons with the ion on the DFT level, and is much softer in the core region than its all-electron counterpart (Fig. 3.2). The distinct procedures for generating a norm-conserving pseudopotential differ only in the way the pseudo-valence radial wave functions (Fig. 3.1) are designed and the constraints they are required to fulfill.

In the Hamann scheme [66], an intermediate pseudopotential $V_l^{\text{ps,i}}$ is constructed by cutting off the singularity of the full-potential at the nucleus:

$$V_l^{\text{ps,i}}(r) = V(r) \left[1 - f\left(\frac{r}{r_{cl}}\right) \right] + c_l f\left(\frac{r}{r_{cl}}\right) \quad (3.6)$$

where $f(x)$ is a cutoff function which is unity at the origin, cuts off at $x \sim 1$ and decreases rapidly as $x \rightarrow \infty$. The free parameter c_l is adjusted so that the nodeless

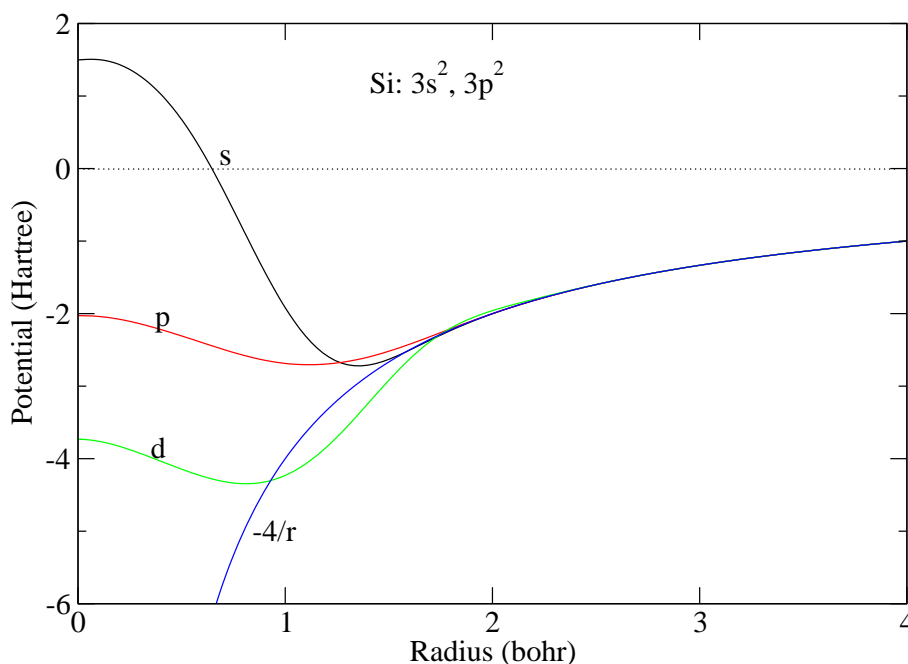


Figure 3.2: Ionic pseudopotentials for $l = 0, 1, 2$ in Si atom. The pseudopotential is much softer in the region close to the nuclear compared with the behavior of $-Z/r$, where Z is the ionic charge.

solution w_l of the radial equation:

$$\left[-\frac{1}{2} \frac{d^2}{dr^2} + \frac{l(l+1)}{2r^2} + V_l^{\text{ps},i}(r) - \epsilon_l^{(i)} \right] w_l(\epsilon_l, r) = 0 \quad (3.7)$$

has the same eigenvalue as its all-electron counterpart ($\epsilon_l^{(i)} = \epsilon_l$). Since both w_l and u_l are solutions of the same potential outside the core region, one can write:

$$\gamma_l w_l(r) \rightarrow u_l(r), r > r_{cl}. \quad (3.8)$$

The pseudo wave function is now modified by adding a correction in the core region:

$$u_l^{\text{ps}}(r) = \gamma_l [w_l(r) + \delta_l g_l(r)] \quad (3.9)$$

where $g_l(r)$ must vanish as r^{l+1} for small r to give a regular pseudopotential at the origin, and it must vanish rapidly for $r > r_{cl}$ since $\gamma_l w_l(r)$ is already the desired solution in that region. At this point the normalization condition is used to set the value of δ_l ;

$$\gamma_l^2 \int |w_l(r) + \delta_l g_l(r)|^2 dr = 1. \quad (3.10)$$

The pseudo wave functions generated by this procedure fulfill conditions i), iii) and iv). Condition ii) is reached exponentially beyond the cutoff radius. Even within this procedure, the pseudopotential is not unique. It depends on the choice of states included in the core, the selection of the cutoff functions and the core radii (See Ref. [67] for details). Later on, Hamann [70] also extended this procedure to generate pseudopotentials for the atomic unbound states.

In the Troullier-Martins scheme [71] the pseudo-valence radial wave function equals exactly the all-electron one outside the cutoff radius. Inside the cutoff radius it is assumed to have the following analytic form:

$$u_l^{\text{ps}}(r) = r^{(l+1)} e^{p(r)} \quad (3.11)$$

where $p(r)$ is a polynomial of sixth order in r^2 . The coefficients are determined from conditions (ii)-(iv), plus the additional constraints of continuity of the first four derivatives at r_l^c and zero curvature of the screened pseudopotential at the origin ($\frac{d^2}{dr^2} V_l^{\text{ps,scr}}(r)|_{r=0} = 0$). Condition (i) is accomplished directly by solving Eq. 3.3. As a consequence of the additional requirements, the Troullier-Martins pseudopotentials are softer than the Hamann ones.

The different radial dependence of the above defined pseudopotentials for each channel results in the total pseudopotential being semilocal (*i. e.* non-local in the angular coordinates, but local in the radial one);

$$V^{\text{ps}}(\mathbf{r}, \mathbf{r}') = V^{\text{loc}}(r) \delta(\mathbf{r} - \mathbf{r}') + \sum_{l=0}^{l_{\text{max}}} \sum_{m=-l}^{m=l} Y_{l,m}^*(\hat{r}) \delta V_l^{\text{ps}}(r) \frac{\delta(r-r')}{r^2} Y_{l,m}(\hat{r}'), \quad (3.12)$$

where $\delta V_l^{\text{ps}}(r) = V_l^{\text{ps}}(r) - V^{\text{loc}}(r)$. The l -independent term ($V^{\text{loc}}(r)$) is chosen such that the semilocal terms (δV_l^{ps}) are confined to the core region and eventually vanish beyond some l_{max} .

Kleinman and Bylander (KB) [72] proposed a transformation of the semilocal terms into a fully non-local form defining:

$$\delta V^{\text{KB}}(\mathbf{r}, \mathbf{r}') = \sum_{l,m} \frac{\delta V_l^{\text{ps}}(r) \tilde{\varphi}_{l,m}(\mathbf{r}) \tilde{\varphi}_{l,m}^*(\mathbf{r}') \delta V_l^{\text{ps}}(r')}{\langle \tilde{\varphi}_{l,m} | \delta V_l^{\text{ps}} | \tilde{\varphi}_{l,m} \rangle} \quad (3.13)$$

where $\tilde{\varphi}_{lm}(\mathbf{r}) = \frac{u_l^{\text{ps}}(\epsilon_l, r)}{r} Y_{lm}(\hat{r})$. It can be easily verified that

$$\int \delta V^{\text{KB}}(\mathbf{r}, \mathbf{r}') \tilde{\varphi}_{l,m}^*(\mathbf{r}') d^3 \mathbf{r}' = \delta V_l^{\text{ps}}(r) \tilde{\varphi}_{l,m}(\mathbf{r}) \quad (3.14)$$

namely, the Kleinman-Bylander form is equivalent to the semilocal one in the sense that it produces the same atomic pseudoorbitals. At the expense of a more complicated expression in real space, the Kleinman-Bylander form is fully separable,

strongly reducing the number of integrations necessary, *e. g.* in a plane waves basis set, to calculate the Hamiltonian matrix elements. It is used in most of the electronic structure codes nowadays.

3.1.2 Implicit Approximations

3.1.2.1 Frozen Core

The main assumption in the pseudopotential method is that the core states, strongly bound to the nucleus and localized, are insensitive to the environment surrounding the atom. Therefore, they can be excluded from the self-consistent calculation in the polyatomic system. This is the “frozen core” approximation.

The pseudopotential is defined by the requirements that the wave functions and eigenvalues are accurately reproduced, however, no conditions on total energies are imposed. In 1980, von Barth and Gelatt [73] demonstrated that the error in the total energy is of second order in the difference between frozen and true core densities. Their calculations for Mo further confirmed this conclusion, thus validating the application of the pseudopotential method in total energy calculations.

3.1.2.2 Core-Valence Linearization.

The definition of the pseudopotential in Eq. 3.5 implies that the self-consistent total exchange-correlation potential in a condensed matter system is written as:

$$V^{\text{xc}} [n(\mathbf{r})] = \{ V^{\text{xc}} [n^0(\mathbf{r})] - V^{\text{xc}} [\tilde{n}_v^0(\mathbf{r})] \} + V^{\text{xc}} [\tilde{n}_v(\mathbf{r})] \quad (3.15)$$

where the terms in curly brackets are included in the pseudopotential. Equation 3.15 would be exact, within the frozen core approximation, if the exchange-correlation potential were a linear functional of the density². As it is clearly not the case, the assumption of validity of Eq. 3.15 is known as *core-valence linearization*.

However, the errors due to this approximation are small in most cases, as long as the overlap between the core and valence densities are not significant. Louie, Froyen and Cohen [74] developed a method for the generation and usage of pseudopotentials that explicitly treats the nonlinear core-valence exchange-correlation interaction. The method consists in modifying Eq. 3.5 to:

$$V_l^{\text{ps}}(r) = V_l^{\text{ps,scr}}(r) - V^{\text{H}}[\tilde{n}_v^0; r] - V^{\text{xc}}[\tilde{n}_v^0 + \tilde{n}_c; r] \quad (3.16)$$

where \tilde{n}_c is a partial core density. It reproduces the full core density in the region where it overlaps with the valence density, outside a chosen cutoff radius r^{nlc} . Inside

²Notice that Eq. 3.15 is also exact in a non-selfconsistent calculation, since in that case $n(\mathbf{r}) = n^0(\mathbf{r})$ and $\tilde{n}_v(\mathbf{r}) = \tilde{n}_v^0(\mathbf{r})$.

this radius, it is chosen to match the true density at r^{nlc} , minimize the integrated density and be easily Fourier transformed in order to optimize its use within the plane wave basis set. This density has to be added to the pseudo-valence density in the selfconsistent calculation whenever V^{xc} or E^{xc} are computed.

3.1.2.3 Pseudoization

By *pseudoization* we refer to the fact that the wave functions of the valence states in the pseudopotential method are, by construction, nodeless and much smoother than their all-electron analogue. It is only observable in the core region, which constitutes a small portion of space. As long as the full potential is local, the errors in the energies, within this region, are taken care for in the pseudopotential by construction. Furthermore, the norm-conserving constraint ensures that the Hartree potential generated by the pseudo-charge outside the core region is the same as in the all-electron treatment. Nevertheless, whether it is also negligible in the calculation of non-local operators is unclear, as was mentioned in Ref. [14]. The fact that *pseudoization* can lead to qualitative differences between PP and AE calculations has been pointed out in Ref. [75], where significant discrepancies in the electron-hole distribution function of LiF were observed.

3.2 FP-(L)APW+lo Method

The FP-(L)APW+lo method is a development of the augmented planewave method (APW) originally proposed by Slater [76]. Thus, we introduce our discussion with an short overview of the APW method. The essential idea motivating the method is that in the region close to nuclei, the potential and wave functions are similar to those in the free atoms, strongly varying but nearly spherical. In the space between the atoms, both of them are smooth. In his seminal work, Slater proposed a division of the space in the unit cell into a set of non-overlapping spheres centered at each atom and the interstitial region between them (Fig. 3.3). The potential was taken as spherically symmetric inside the spheres and constant outside (later on known as the muffin-tin approximation, for obvious reasons). Accordingly, the eigenfunctions of the Hamiltonian corresponding to each of the regions are taken as basis functions, namely, plane waves in the interstitial and atomic orbitals in the “muffin-tin” spheres. Adding the continuity condition at the sphere boundary the augmented planewaves were born:

$$\phi_{\mathbf{G}}^{\mathbf{k}}(\mathbf{r}) = \begin{cases} \frac{1}{\Omega} e^{i(\mathbf{G}+\mathbf{k})\cdot\mathbf{r}} & r \in \text{Interstitial} \\ \sum_{l,m} A_{l,m}(\mathbf{k} + \mathbf{G}) u_l(r^\alpha, \epsilon) Y_{l,m}(\mathbf{r}^\alpha) & r \in \text{MT}. \end{cases} \quad (3.17)$$

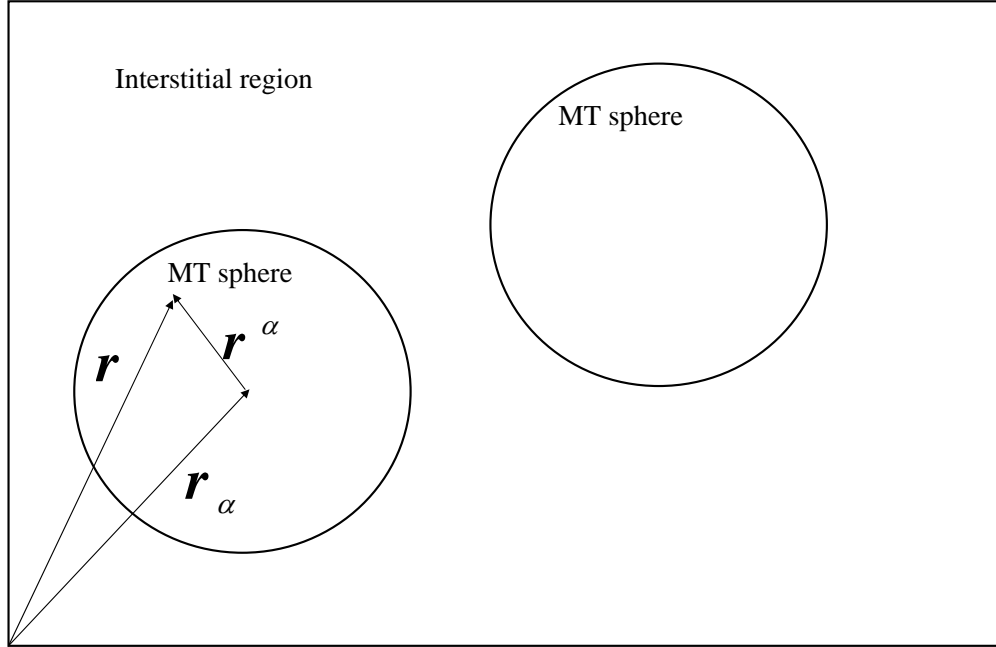


Figure 3.3: Schematic view of the space partition in the augmented plane wave method. The space is divided into the interstitial region and a series of non-overlapping muffin-tin regions. The potential in the muffin-tin region is atomic like, while that in the interstitial region is much softer.

Inside each muffin-tin sphere, the radial wave function $u_l(r^\alpha, \epsilon)$ at the reference energy ϵ_l , is obtained from:

$$\left\{ -\frac{d^2}{dr^2} + \frac{l(l+1)}{r^2} + V(r) - \epsilon_l \right\} r u_l(r, \epsilon_l) = 0. \quad (3.18)$$

The augmentation coefficients ensuring the continuity of the wave function at the sphere boundary are given by:

$$A_{l,m}(\mathbf{k} + \mathbf{G}) = \frac{4\pi i^l}{\Omega^{1/2} u_l(R_{\text{MT}}^\alpha, \epsilon_l)} j_l(|\mathbf{k} + \mathbf{G}| R_{\text{MT}}^\alpha) Y_{l,m}^*(\mathbf{k} + \mathbf{G}). \quad (3.19)$$

This optimized choice of basis functions in different regions is the essence of the augmented methods and all its descendants. The wave function is expanded in terms

of these augmented plane waves as:

$$\varphi_{n,\mathbf{k}}(\mathbf{r}) = \sum_{\mathbf{G}} C_{\mathbf{G}}^m \phi_{\mathbf{G}}^{\mathbf{k}}(\mathbf{r}), \quad (3.20)$$

The coefficients $C_{\mathbf{G}}^m$ are obtained solving the eigenvalue equation:

$$\sum_{\mathbf{G}'} (H_{\mathbf{G},\mathbf{G}'} - \epsilon_n S_{\mathbf{G},\mathbf{G}'}) C_{\mathbf{G}}^m = 0 \quad (3.21)$$

for each \mathbf{k} . Where $H_{\mathbf{G},\mathbf{G}'}(S_{\mathbf{G},\mathbf{G}'})$ are the Hamiltonian (overlap) matrix elements in the APW basis.

The major drawback of this method is that, inside the muffin-tin sphere, the APWs are solutions of the Schrödinger equation only at the reference energy (*i.e.* $\epsilon_l = \epsilon_n$). Thus, the eigenvalue equation (3.21) becomes non-linear and its solution much more computationally demanding for each \mathbf{k} -point. Furthermore, it is hard, though not impossible (Ref. [77, 78]) to extend the method to the full potential case. When the potential inside a muffin-tin sphere is not spherical, the exact solution of the particle's wave function inside this muffin-tin sphere does not correspond to the solution of the radial Schrödinger equation with the same eigenvalue.

Another shortcoming of the APW method, known as the asymptote problem, is related to the indetermination of the augmentation coefficients when the radial function has a node at the muffin-tin radius ($u_l(R_{\text{MT}})$ in the denominator of Eq. 3.19). In the vicinity of this region, the relation between $A_{l,m}$ and $C_{\mathbf{G}}$ becomes numerically unstable.

With the aim of overcoming these limitations, Andersen [79] proposed a modification of the APW method in which the wave functions and their derivatives are made continuous at the muffin-tin radius by matching the interstitial plane waves to linear combination of a radial function, and its energy derivative, calculated at a fixed reference energy. The method, known as Linearized Augmented Plane Waves (LAPW) method, rapidly demonstrated its power and accuracy, becoming, during decades, the benchmark for electronic structure calculations within the Kohn-Sham scheme. Recently, Sjösted, Nordström, and Singh [80] proposed an alternative method in which the APW wave functions are recovered, but with the radial functions calculated at a fixed energy. The flexibility of the basis is achieved by adding a set of local orbitals constructed as linear combinations of the same radial functions and their energy derivatives, with the condition that the function cancels at the sphere radius. This method, called APW plus local orbitals (APW+lo), requires less plane waves for an accurate description of the electronic structure properties, thus increasing the computational efficiency. However, this improvement is limited by the large number of required local orbitals for large l 's. Nowadays, the state-of-the-art method is a combination of both, using APW+lo's for small l and LAPW's for the large

ones [81], known as (L)APW+lo method. The rest of the chapter is devoted to an overview of this method.

3.2.1 LAPW Basis Functions

The LAPW basis set is defined by:

$$\phi_{\mathbf{k}+\mathbf{G}}(\mathbf{r}) = \begin{cases} \frac{1}{\Omega} e^{i(\mathbf{G}+\mathbf{k})\cdot\mathbf{r}} & r \in \text{Interstitial} \\ \sum_{l,m} [A_{l,m}(\mathbf{k}+\mathbf{G}) u_l(r^\alpha, \epsilon_l) + B_{l,m}(\mathbf{k}+\mathbf{G}) \dot{u}_l(r^\alpha, \epsilon_l)] Y_{l,m}(\mathbf{r}^\alpha) & r \in \text{MT}, \end{cases} \quad (3.22)$$

where $(\dot{u}_l(r, \epsilon_l) = \partial u_l(r, \epsilon) / \partial \epsilon|_{\epsilon=\epsilon_l})$. The augmentation coefficients $A_{l,m}$ and $B_{l,m}$ are obtained by requiring both the value and the slope of the basis function to be continuous on the MT sphere boundary.

Making a Taylor expansion of the radial wave function around the reference energy ϵ_l , one has:

$$u_l(r, \epsilon) = u_l(r, \epsilon_l) + (\epsilon - \epsilon_l) \dot{u}_l(r, \epsilon_l) + O((\epsilon - \epsilon_l)^2), \quad (3.23)$$

which shows that in the linearized treatment, the error in the wave function is of second order in $(\epsilon - \epsilon_l)$. Taking into account the variational principle, this leads to an error of fourth order, $(\epsilon - \epsilon_l)^4$, in the band energy. In other words, the LAPWs form a good basis over a relatively large energy region, typically allowing the calculation of all the valence bands with a single set of reference energies, *i. e.* by a single diagonalization of Eq. 3.21.

However, there are situations in which the use of a single set of reference energies is inadequate for all the bands of interest. Such a situation arises, for example, when two (or more, but rarely) states with the same l participate in the chemical bonding (semi-core states), or when bands over an unusually large energy region are required, like for high lying excited states. To address such cases, the local orbitals were introduced by D. J. Singh in 1991 [82]:

$$\phi_{\text{LAPW}}^{\text{LO}}(\mathbf{r}) = \begin{cases} 0 & r \in \text{Interstitial} \\ \left[A_{l,m}^\alpha u_l(r^\alpha, \epsilon_l) + B_{l,m}^\alpha \dot{u}_l(r^\alpha, \epsilon_l) + C_{l,m}^\alpha u_l(r^\alpha, \epsilon_l^{(2)}) \right] Y_{l,m}(\mathbf{r}^\alpha) & r \in \text{MT}. \end{cases} \quad (3.24)$$

In this way, a second set of energy parameters $\epsilon_l^{(2)}$ is introduced to provide the additional variational freedom required for an accurate representation of the different states with the same l . The coefficients $A_{l,m}^\alpha$, $B_{l,m}^\alpha$ and $C_{l,m}^\alpha$ are determined by requiring the local orbital and its radial derivative to be zero at the MT sphere boundary and normalized.

3.2.2 APW+lo Basis Functions

The LAPW basis set is designed to be flexible in describing the wave functions in the vicinity of the reference energy. However, the requirement of continuous derivatives at the muffin-tin radius increase the number of plane waves needed to achieve a given level of convergence with respect to the APW method.

Recently, Sjösted, Nordström, and Singh [80] proposed an alternative way to linearize the APW method in which the continuous derivative condition is released. In this method, the eigenvalue problem of the original APW method is linearized by choosing fixed linearization energies (ϵ_l) for the APW basis functions in Eq. 3.17. Then, the flexibility of the basis set with respect to the reference energy is obtained by adding a set of local orbitals (lo):

$$\phi_{\text{APW}}^{\text{lo}}(\mathbf{r}) = \begin{cases} 0 & r \in \text{Interstitial} \\ [A_{l,m}u_l(r^\alpha, \epsilon_l) + B_{l,m}\dot{u}_l(r^\alpha, \epsilon_l)] Y_{l,m}(\mathbf{r}^\alpha) & r \in \text{MT}, \end{cases} \quad (3.25)$$

using the same linearization energies. The coefficients are obtained by requiring the function to be zero at the sphere boundary and normalized.

The APW basis functions keep the convergence behavior of the original APW method while the local orbitals (lo) make it flexible with respect to choice of the reference energy. The complete APW+lo basis set therefore consists of two different types of basis functions, the APWs (Eq. 3.17 at fixed linearization energies) and the lo's (Eq. 3.25). As in the LAPW method, when different states with the same l (semicore states) have to be treated, a second set of local orbitals of the form:

$$\phi_{\text{APW}}^{\text{LO}}(\mathbf{r}) = \begin{cases} 0 & r \in \text{Interstitial} \\ [A_{l,m}u_l(r^\alpha, \epsilon_l) + C_{l,m}u_l^{(2)}(r^\alpha, \epsilon_l^{(2)})] Y_{l,m}(\mathbf{r}^\alpha) & r \in \text{MT} \end{cases} \quad (3.26)$$

can be added. The coefficients are determined by matching the function to zero at the muffin-tin radius, with no condition on the slope.

3.2.3 Core States

As already mentioned, the (L)APW+lo is an all-electron method. However, it does not mean that core and valence states are treated in the same way. While the latter are expanded in the previously described basis set using the crystal potential, the former are calculated numerically solving the relativistic radial Schrödinger equation for the atom. The influence of the core states on the valence is carried out by the inclusion of the core density in the Hartree and exchange-correlation potentials. Reciprocally, the core states are calculated using the spherical average of the crystal potential in the muffin-tin sphere. Thus, both core and valence states are calculated selfconsistently.

Table 3.1: Relativistic quantum numbers

		$j = l + \frac{s}{2}$		κ		max. occupation	
	l	$s = -1$	$s = +1$	$s = -1$	$s = +1$	$s = -1$	$s = +1$
s	0		1/2		-1		2
p	1	1/2	3/2	1	-2	2	4
d	2	3/2	5/2	2	-3	4	6
f	3	5/2	7/2	3	-4	6	8

In the Wien2k code, the wave function of each core state is represented as:

$$\tilde{\varphi}_{an,j,m_j}^{core}(\vec{r}) = u_{an,\kappa}(r^a) |jm_j\rangle_l \quad (3.27)$$

where

$$|jm_j\rangle_l \equiv \sum_{\sigma=-\frac{1}{2}}^{\frac{1}{2}} (l \frac{1}{2} m_l \sigma |j m_j) Y_{lm_l}(\hat{r}^a) |\sigma\rangle \delta_{m+\sigma,m_j} \quad (3.28)$$

and $(l \frac{1}{2} m_l \sigma |j m_j)$ is the corresponding Clebsch-Gordon coefficient (Ref. [83]).

The radial wave function is defined by the relativistic quantum number $\kappa = -s(j + \frac{1}{2})$ as shown in Table 3.2.3.

3.2.4 Potential and Density

The representation of the density and the potential has to confront the same difficulties as the representation of the wave functions, namely, rapid variations in the muffin-tin spheres and soft oscillations in the interstitial. The use of a dual representation as for the wave functions, which is the basis of the (L)APW+lo efficiency, seems the natural choice. However, an expansion in spherical harmonics inside the spheres and plane waves in the interstitial is clearly inefficient. The complete representation of the density requires a basis set at least eight times larger than the basis required for the wave functions. Since also the number of augmentation functions in the MT sphere increases four times, the number of augmentation coefficients is 2^5 times larger.

This can be reduced by exploiting the symmetries of the density(potential), namely:

- i. Inside the muffin-tin sphere they respect the symmetry of the corresponding nuclear site.
- ii. In the interstitial region they have the symmetry of the corresponding space group.

iii. Both are real quantities.

Inside the muffin-tin spheres, properties i and iii allow the representation of the density in a lattice harmonic expansion [84]. For the interstitial region, the use of stars ensures both properties ii and iii to be fulfilled with a minimum number of coefficients. More details can be found in Ref. [65].

Chapter 4

Many-Body Green Function Theory and the GW Approximation

In Sec. 2.2.4, we pointed out that although the Kohn-Sham eigenvalues provide a good zeroth order approximation for the single particle excitation energies, LDA fails for a good description of the fundamental band gaps in semiconductors and insulations. On the other hand, many-body Green function theory provides the formal basis for evaluating the experimentally observed quasiparticle band structure. This chapter presents a short overview of the Green function method in the many-body electronic system, with a special emphasis on the GW approximation. This will set up the theoretical framework for our numerical implementation and the analysis of the results presented in this thesis.

In the first part of the chapter (Sec. 4.1) we describe the main ingredients of the theory. Starting from the definition of the single-particle Green function, the central physical quantity in this method, in Sec. 4.1.1 we show the correspondence between its poles and the single-particle excitation energies of the many-body system. In Sec. 4.1.2 we present a short deduction of the Dyson equation, that relates the Green function in the interacting system to the non-interacting one through the self-energy. Section 4.1.3 is devoted to the concept of self-energy and its expansion in terms of the dynamically screened Coulomb potential (Hedin equations). We end the section by introducing the quasiparticle concept (Sec. 4.1.4).

The simplest approximation to the self-energy, including dynamical screening effects, is the GW approximation, which we address in the second part of this chapter (Sec. 4.2). The current standard treatment for condensed matter systems, the G_0W_0 approach, is described in Sec. 4.3. In the end, a brief summary of the chapter is given in Sec. 4.4.

4.1 Green Function Method

4.1.1 The Green Function

The single-particle Green function is defined as:

$$G(\mathbf{r}, t; \mathbf{r}', t') = -i \langle N | \hat{T} \{ \hat{\psi}(\mathbf{r}, t) \hat{\psi}^\dagger(\mathbf{r}', t') \} | N \rangle, \quad (4.1)$$

where $\hat{\psi}(\mathbf{r}, t)$ and $\hat{\psi}^\dagger(\mathbf{r}, t)$ are the quantum field operators describing the annihilation and creation of one electron at position \mathbf{r} and time t . The operator \hat{T} is the time-ordering operator, which reorders the field operators in ascending time order from right to left. $|N\rangle$ is the groundstate eigenfunction of the N electrons system. Making use of the Heaviside function (Appendix J), and the commutation relations for Fermionic operators, Eq. 4.1 can be rewritten as:

$$\begin{aligned} G(\mathbf{r}, t; \mathbf{r}', t') &= -i \langle N | \hat{\psi}(\mathbf{r}, t) \hat{\psi}^\dagger(\mathbf{r}', t') | N \rangle \Theta(t - t') \\ &\quad + i \langle N | \hat{\psi}^\dagger(\mathbf{r}', t') \hat{\psi}(\mathbf{r}, t) | N \rangle \Theta(t' - t). \end{aligned} \quad (4.2)$$

making evident that for $t > t'$ ($t < t'$) the Green function describes the propagation of an added electron (hole) in the system.

In the Heisenberg representation, the field operator is written as:

$$\hat{\psi}(\mathbf{r}, t) = e^{i\hat{H}t} \hat{\psi}(\mathbf{r}) e^{-i\hat{H}t}, \quad (4.3)$$

where \hat{H} is the Hamiltonian operator and $\hat{\psi}(\mathbf{r})$ is the field operator in the Schrödinger representation.

Inserting Eq. 4.3 into Eq. 4.2 and making use of the completeness relation in the Fock-space:

$$1 = \sum_{n=0}^{\infty} \sum_s |n, s\rangle \langle n, s|, \quad (4.4)$$

where $|n, s\rangle$ corresponds to the s -th eigenstate of the the n -electron system, we can transform Eq. 4.2 into:

$$\begin{aligned} G(\mathbf{r}, t; \mathbf{r}', t') &= -i \sum_s \langle N | \hat{\psi}(\mathbf{r}) | N + 1, s \rangle e^{-i(E_{N+1}^s - E_N)(t-t')} \\ &\quad \cdot \langle N + 1, s | \hat{\psi}^\dagger(\mathbf{r}') | N \rangle \Theta(t - t') + i \sum_s \langle N | \hat{\psi}^\dagger(\mathbf{r}') | N - 1, s \rangle \\ &\quad \cdot e^{-i(E_{N-1}^s - E_N)(t'-t)} \langle N - 1, s | \hat{\psi}(\mathbf{r}) | N \rangle \Theta(t' - t). \end{aligned} \quad (4.5)$$

Here, E_N stands for the ground state energy of the N -electron system, and $E_{N\pm 1}^s$ for the s -th excited state energy of the $N \pm 1$ electronic system.

Using the excitation energy ϵ_s and amplitude $\psi_s(\mathbf{r})$ defined by:

$$\begin{aligned}\epsilon_s &= E_{N+1}^s - E_N \quad , \quad \psi_s(\mathbf{r}) = \langle N | \hat{\psi}(\mathbf{r}) | N+1, s \rangle, \text{ for } \epsilon_s \geq \mu \\ \epsilon_s &= E_N - E_{N-1}^s \quad , \quad \psi_s(\mathbf{r}) = \langle N-1, s | \hat{\psi}(\mathbf{r}) | N \rangle, \text{ for } \epsilon_s < \mu,\end{aligned}\quad (4.6)$$

where μ is the chemical potential of the N -electron system ($\mu = E_{N+1} - E_N$)¹, we can further simplify Eq. 4.5 into the form:

$$\begin{aligned}G(\mathbf{r}, \mathbf{r}'; t - t') &= -i \sum_s \psi_s(\mathbf{r}) \psi_s^*(\mathbf{r}') e^{-i\epsilon_s(t-t')} \\ &\quad [\Theta(t-t') \Theta(\epsilon_s - \mu) - \Theta(t'-t) \Theta(\mu - \epsilon_s)].\end{aligned}\quad (4.7)$$

Performing a Fourier transform to the frequency axis, we obtain the spectral, or Lehmann [86], representation:

$$G(\mathbf{r}, \mathbf{r}', \omega) = \lim_{\eta \rightarrow 0^+} \sum_s \psi_s(\mathbf{r}) \psi_s^*(\mathbf{r}') \left[\frac{\Theta(\epsilon_s - \mu)}{\omega - (\epsilon_s - i\eta)} + \frac{\Theta(\mu - \epsilon_s)}{\omega - (\epsilon_s + i\eta)} \right]. \quad (4.8)$$

The key feature of Eq. 4.8 is that the Green function has single poles corresponding to the exact excitation energies of the many-body system. For excitation energies larger (smaller) than the chemical potential, these singularities lie slightly below (above) the real axis in the complex frequency plane (Fig. 4.1).

It can be easily shown that in the non-interacting case, Eq. 4.8, reduces to:

$$G_0(\mathbf{r}, \mathbf{r}', \omega) = \lim_{\eta \rightarrow 0^+} \sum_n \varphi_n(\mathbf{r}) \varphi_n^*(\mathbf{r}') \left[\frac{\Theta(\epsilon_n - \epsilon_F)}{\omega - (\epsilon_n - i\eta)} + \frac{\Theta(\epsilon_F - \epsilon_n)}{\omega - (\epsilon_n + i\eta)} \right]. \quad (4.9)$$

where $\epsilon_n(\varphi_n)$ is the eigenvalue (eigenfunction) of the single particle Hamiltonian and ϵ_F is the Fermi energy.

4.1.2 The Dyson Equation

The time evolution of the field operator, in the Heisenberg representation is given by the equation of motion:

$$i \frac{\partial}{\partial t} \hat{\psi}(\mathbf{r}, t) = [\hat{\psi}(\mathbf{r}, t), \hat{H}], \quad (4.10)$$

¹In Fig. 4.1, this corresponds to the energy of the lowest unoccupied state when $T \rightarrow 0\text{K}$, deduction refer to Ref. [85].

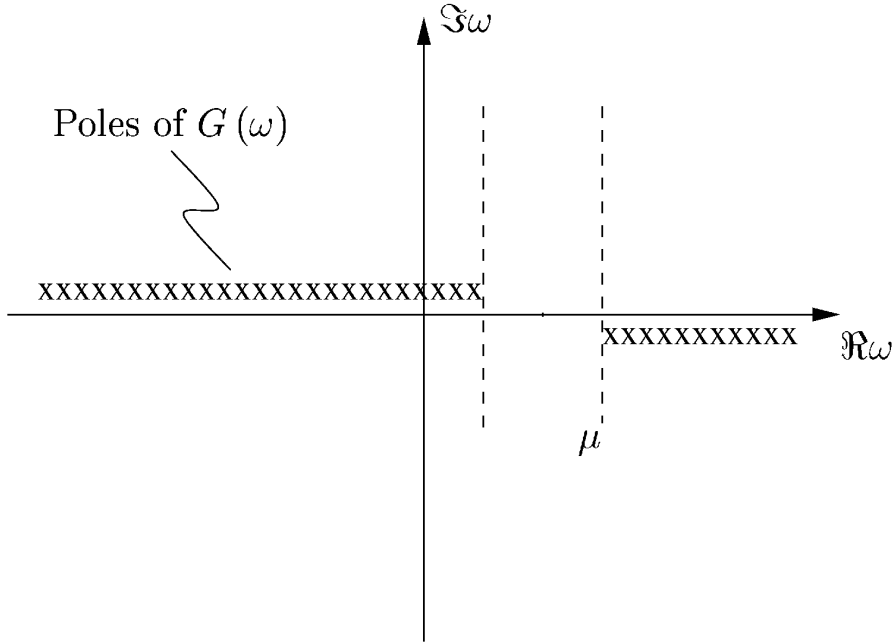


Figure 4.1: Position of the poles of the Green function (Eq. 4.8) in the complex frequency plane. Those corresponding to the unoccupied states are slightly below the real frequency axis while those corresponding to the occupied states are slightly above it.

with the Hamiltonian operator given by:

$$\begin{aligned} \hat{H} = & \int d\mathbf{r} dt \hat{\psi}^\dagger(\mathbf{r}, t) \left[-\frac{1}{2} \nabla^2 + V_{\text{ext}}(\mathbf{r}) \right] \hat{\psi}(\mathbf{r}, t) \\ & + \frac{1}{2} \int \int d\mathbf{r} dt d\mathbf{r}' dt' \hat{\psi}^\dagger(\mathbf{r}, t) \hat{\psi}^\dagger(\mathbf{r}', t') v(\mathbf{r}, t; \mathbf{r}', t') \hat{\psi}(\mathbf{r}', t') \hat{\psi}(\mathbf{r}, t), \end{aligned} \quad (4.11)$$

where $v(\mathbf{r}, t; \mathbf{r}', t') = \delta(t - t') / |\mathbf{r} - \mathbf{r}'|$ is the Coulomb interaction. By evaluating the commutator in Eq. 4.10, the equation of motion for the single particle Green function can be obtained:

$$\begin{aligned} \left[i \frac{\partial}{\partial t} + \frac{1}{2} \nabla^2 - V_{\text{ext}}(\mathbf{r}) \right] G(\mathbf{r}, t; \mathbf{r}', t') \\ + i \int d\mathbf{r}_1 \frac{1}{|\mathbf{r} - \mathbf{r}_1|} \langle N | T \left[\hat{\psi}^\dagger(\mathbf{r}_1, t) \hat{\psi}(\mathbf{r}_1, t) \hat{\psi}(\mathbf{r}, t) \hat{\psi}^\dagger(\mathbf{r}', t') \right] | N \rangle \\ = \delta(\mathbf{r} - \mathbf{r}') \delta(t - t'), \end{aligned} \quad (4.12)$$

the quantity in the integrand of the second term is the two-particle Green function. Following the same procedure to obtain the equation of motion for the two-particle

Green function will give a term depending on the three-particle Green function, and so on. To break this hierarchy, the mass-operator is introduced, defined by:

$$\int d\mathbf{r}_1 dt_1 M(\mathbf{r}, t; \mathbf{r}_1, t_1) G(\mathbf{r}_1, t_1; \mathbf{r}', t') = -i \int d\mathbf{r}_1 v(\mathbf{r} - \mathbf{r}_1) \langle N|T [\hat{\psi}^\dagger(\mathbf{r}_1, t) \hat{\psi}(\mathbf{r}_1, t) \hat{\psi}(\mathbf{r}, t) \hat{\psi}^\dagger(\mathbf{r}', t')] |N\rangle. \quad (4.13)$$

Eq. 4.12 can then be rewritten:

$$\left[i \frac{\partial}{\partial t} + \frac{1}{2} \nabla^2 - V_{\text{ext}}(\mathbf{r}) \right] G(\mathbf{r}, t; \mathbf{r}', t') - \int d\mathbf{r}_1 dt_1 M(\mathbf{r}, t; \mathbf{r}_1, t_1) G(\mathbf{r}_1, t_1; \mathbf{r}', t') = \delta(\mathbf{r} - \mathbf{r}') \delta(t - t'). \quad (4.14)$$

Since the Hartree interaction is a one-particle operator, it is usually separated from the mass operator M to define the self-energy, $\Sigma = M - V_{\text{H}}$. Replacing the mass-operator in Eq. 4.14 we arrive at:

$$\left[i \frac{\partial}{\partial t} - H_0(\mathbf{r}) \right] G(\mathbf{r}, t; \mathbf{r}', t') - \int d\mathbf{r}_1 dt_1 \Sigma(\mathbf{r}, t; \mathbf{r}_1, t_1) G(\mathbf{r}_1, t_1; \mathbf{r}', t') = \delta(\mathbf{r} - \mathbf{r}') \delta(t - t'), \quad (4.15)$$

where:

$$H_0(\mathbf{r}) = -\frac{1}{2} \nabla^2 + V_{\text{ext}}(\mathbf{r}) + V_{\text{H}}(\mathbf{r}). \quad (4.16)$$

In the Hartree approximation Eq. 4.15 becomes:

$$\left[i \frac{\partial}{\partial t} - H_0(\mathbf{r}) \right] G_0(\mathbf{r}, t; \mathbf{r}', t') = \delta(\mathbf{r} - \mathbf{r}') \delta(t - t'). \quad (4.17)$$

Multiplying Eq. 4.15 by G_0 on the left and using the hermiticity of the single particle operator together with Eq. 4.17, and integrating, yields the well-known Dyson equation:

$$G(\mathbf{r}, t; \mathbf{r}', t') = G_0(\mathbf{r}, t; \mathbf{r}', t') + \iint d\mathbf{r}_1 dt_1 d\mathbf{r}_2 dt_2 G_0(\mathbf{r}, t; \mathbf{r}_2, t_2) \Sigma(\mathbf{r}_2, t_2; \mathbf{r}_1, t_1) G(\mathbf{r}_1, t_1; \mathbf{r}', t'). \quad (4.18)$$

Recurrently replacing G on the right-hand side by $G_0 + G_0 \Sigma G^2$ leads to the series expansion:

$$G = G_0 + G_0 \Sigma G_0 + G_0 \Sigma G_0 \Sigma G_0 + \dots \quad (4.19)$$

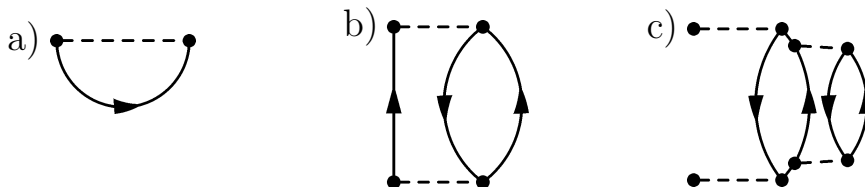
²In this symbolic notation, products imply an integration, as a product of matrices with continuous indices, *i. e.* $AB = \int A(1, 3)B(3, 2)d3$

which shows that the single-particle propagator $G(\mathbf{r}, t; \mathbf{r}', t')$ is equal to the “free” particle propagator $G_0(\mathbf{r}, t; \mathbf{r}', t')$ plus the sum of the probability amplitudes of propagating from (\mathbf{r}, t) to \mathbf{r}', t' after single, double, etc.. scattering processes, with Σ playing the role of the scattering potential. Diagrammatically, this relation is shown as:

where the double plain arrow represents the interacting Green function, the plain arrow represents the non-interacting one.

4.1.3 Self-energy: Hedin Equations

For an electron propagating in a solid or molecule, the origin of the scattering processes lies in the Coulomb interaction with the Fermi sea. Thus, it is natural to expand the self-energy in terms of the bare Coulomb interaction. In the diagrams below, we show examples of some simple (low order) scattering processes. Diagram (a) is a first order scattering process that describes the propagating electron exchanging instantaneously, via the Coulomb interaction, its position with one electron from the Fermi sea. It corresponds to the exchange interaction. Solving the Dyson equation (4.15) including only this term in the self-energy and updating the Green function self-consistently yields the Hartree-Fock approximation. In diagram (b) the interaction of the probe electron with the Fermi sea excites an electron out of it, generating an electron-hole pair, which annihilate each other at a later time, interacting again with the probe electron. This second order scattering process, called “bubble” diagram, represents an electron repelling another from its neighborhood, thus generating a positive charge cloud around it. It is the simplest dynamical screening processes. In diagram (c), the excited electron in the electron-hole pair of diagram (b) further excites another electron-hole pair from the Fermi sea, changing the positive charge cloud around the probe electron again. Nevertheless, the long-range of the bare Coulomb interaction results in a poor convergence of this expansion for the self-energy, in fact, it diverges for metals.



In 1965, L. Hedin [8] proposed a different approach for obtaining the self-energy, by expanding it in terms of a dynamically screened Coulomb potential instead of

the bare one. The derivation using the functional derivative technique can be found in Ref. [8, 87, 88]. Here, we just present the resulting set of equations:

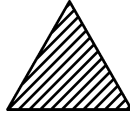
$$\Gamma(1, 2, 3) = \delta(1, 2) \delta(2, 3) + \int d(4, 5, 6, 7) \frac{\delta \Sigma(1, 2)}{\delta G(4, 5)} G(4, 6) G(7, 5) \Gamma(6, 7, 3) \quad (4.20a)$$

$$P(1, 2) = -i \int G(2, 3) G(4, 2) \Gamma(3, 4, 1) d(3, 4) \quad (4.20b)$$

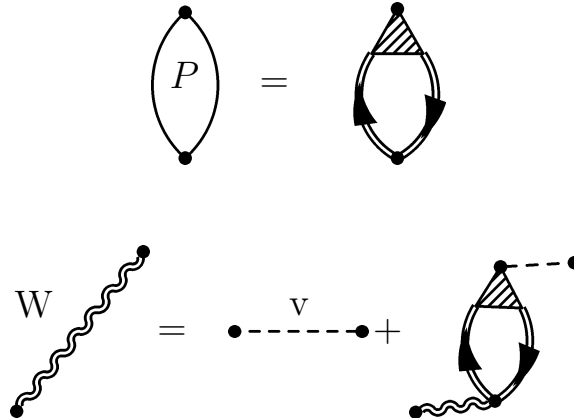
$$W(1, 2) = v(1, 2) + \int W(1, 3) P(3, 4) v(4, 2) d(3, 4) \quad (4.20c)$$

$$\Sigma(1, 2) = i \int d(3, 4) G(1, 3^+) W(1, 4) \Gamma(3, 2, 4). \quad (4.20d)$$

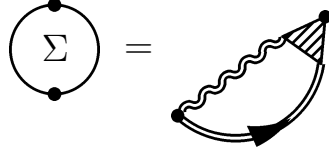
where we used $1 = (\mathbf{r}_1, t_1)$ to simplify the notation. Γ is a vertex function, P the polarizability and W the dynamically screened Coulomb potential. In Eq. 4.20a the vertex function is written in terms of a four point kernel (given by the functional derivative of the self-energy). Replacing the self-energy by the expression in Eq. 4.20d would allow to expand the vertex function in terms of the screened Coulomb potential. For the aim of this thesis, it will nevertheless be sufficient to represent it by a filled triangle:



Eq. 4.20b, 4.20c, and 4.20d can then be represented diagrammatically as:



and



where the double wiggly line represents the screened Coulomb potential.

The set of equations 4.20, together with the Dyson equation (4.18), constitute the definitive solution of the quantum mechanical many-body problem. One just needs to solve them self-consistently to obtain the single-particle Green function of the interacting system (see Fig. 4.2). However, a direct numerical solution is prevented by the functional derivative in Eq. 4.20a, and, as usual, one has to rely on approximations. This will be the subject of the second part of this chapter.

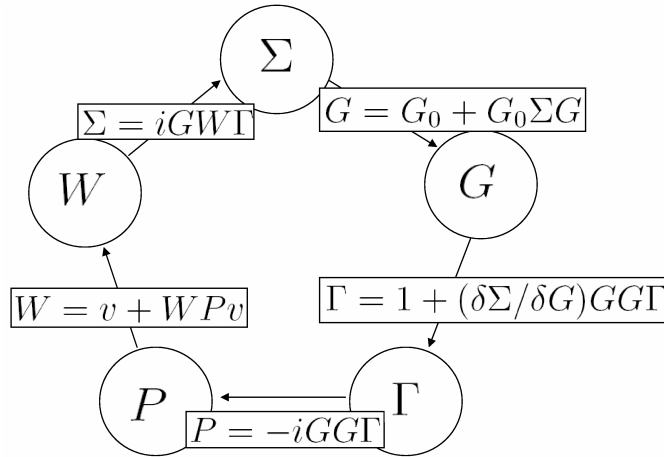


Figure 4.2: Schematic representation of the self-consistent solution of the Hedin equations in conjunction with the Dyson equation for the determination of the Green function (G) and the self-energy (Σ). Entries in boxes symbolize the mathematical relations that link Σ , G , Γ , P and W .

4.1.4 The Quasiparticle Concept

Defining the excitation energies ϵ_s and amplitudes $\psi_s(\mathbf{r})$ (Eq. 4.6) allowed us to write the Green function of the interacting system in the spectral representation (Eq. 4.8). The expression obtained has the same form as the Green function of the non-interacting system (Eq. 4.9), with the excitation energies (amplitudes) playing the role of the single particle eigenvalues (eigenfunctions). We may ask, under which condition can the object defined by $\psi_s(\mathbf{r})$ and ϵ_s be interpreted as a “particle” that can be measured experimentally.

The experimentally obtained quantity in photoemission experiments is the spectral function³, *i. e.*, the density of the excited states that contribute to the spectrum. For a finite system it is defined by (Fig. 4.3, left panel):

$$A(\mathbf{r}, \mathbf{r}'; \omega) = \sum_s \psi_s(\mathbf{r}) \psi_s^*(\mathbf{r}') \delta(\omega - \epsilon_s) \quad (4.21)$$

And the Green function can be rewritten as:

$$G(\mathbf{r}, \mathbf{r}', \omega) = \lim_{\eta \rightarrow 0^+} \int d\omega' \frac{A(\mathbf{r}, \mathbf{r}'; \omega')}{\omega - \omega' + i \operatorname{sgn}(\omega' - \mu)\eta}. \quad (4.22)$$

Therefore, the interpretation of the excitation as a “particle” presents no difficulty in a finite system. Furthermore, inserting the expression for the Green function in terms of ϵ_s and $\psi_s(\mathbf{r})$ (Eq. 4.7) in Eq. 4.15 it can be shown that they are solutions of the quasiparticle equation⁴:

$$\left[-\frac{1}{2} \nabla^2 + V_{\text{ext}}(\mathbf{r}) + V_{\text{H}}(\mathbf{r}) \right] \psi_s(\mathbf{r}) + \int d\mathbf{r}' \Sigma(\mathbf{r}, \mathbf{r}'; \epsilon_s) \psi_s(\mathbf{r}') = \epsilon_s \psi_s(\mathbf{r}). \quad (4.23)$$

In an extended system, the delta functions in Eq. 4.21 form a continuous spectrum (Fig. 4.3, right panel). However, if in a given energy window the spectrum can be described by a series of Lorentzian peaks with finite widths, so that the spectral *density* function can be written as:

$$A(\mathbf{r}, \mathbf{r}'; \omega) = \sum_s \psi_s(\mathbf{r}) \psi_s^*(\mathbf{r}') \frac{\Gamma_s}{(\omega - \bar{\epsilon}_s)^2 + \Gamma_s^2} \quad (4.24)$$

where $\bar{\epsilon}_s$ is the center of the peak and Γ_s the width. Then Eq. 4.22 can be integrated analytically, and the results of Eq. 4.7 and 4.8 are recovered, provided one redefines $\epsilon_s = \bar{\epsilon}_s + i\Gamma_s$. In this case, the object defined by $\psi_s(\mathbf{r})$ and the complex ϵ_s is called a “quasiparticle”. It describes the group behavior of a set of excitations with continuous excitation energies. The real part of ϵ_s corresponds to the average energy of these related excitations. The imaginary part leads to a decaying factor $e^{-\Gamma_s t}$, *i. e.* the excitation has a finite lifetime given by $\tau = \Gamma_s^{-1}$. That the quasiparticle “disappears” can be physically understood taking into account that one is dealing with an infinite system. In other words, the quasiparticle can decay to the “infinite” reservoir. The quasiparticle equation 4.23 remains valid provided one performs an analytic continuation of the self-energy to the complex frequency plane. A more detailed discussion on the subject can be found in Ref. [93].

³Assuming the cross section of the perturbation to be independent of the energy and neglecting experimental errors.

⁴This equation was first derived by J. Schwinger in Ref. [89]. It was applied to the many-body electronic system by G. Pratt in Ref. [90, 91], and later systematically by L. Hedin in Ref. [92] and Ref [8]

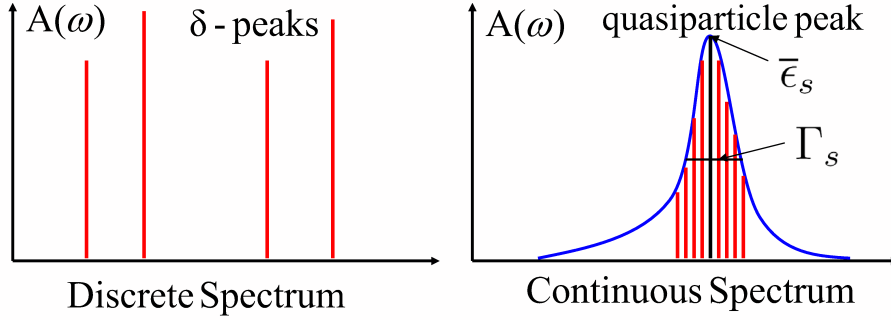


Figure 4.3: Spectral function for a discrete (left) and a continuous (right) spectrum.

4.2 *GW* Approximation

The *GW* approximation was also first proposed by L. Hedin in 1965 (Ref. [8]). Mathematically it amounts to take the zeroth order expansion of the vertex function in terms of W . Thus we are left with:

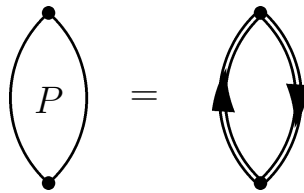
$$\Gamma(1, 2, 3) = \delta(1, 2) \delta(2, 3) \quad (4.25a)$$

$$P(1, 2) = -iG(1, 2)G(2, 1), \quad (4.25b)$$

$$W(1, 2) = v(1, 2) + \int d(3, 4) W(1, 3) P(3, 4) v(4, 2), \quad (4.25c)$$

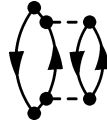
$$\Sigma(1, 2) = iG(1, 2)W(1^+, 2). \quad (4.25d)$$

Diagrammatically, the three-point Γ function is collapsed into a point. The elementary unit in this set of equations is the bubble diagram of the polarizability operator:



This approximation for the polarizability is known as the random-phase approximation (RPA). Physically, it represents the polarization generated by the creation and annihilation of a dressed electron-hole pair, while the interaction between the (dressed) electron and hole is neglected. In other words, scattering processes where the electron or the hole in the electron-hole pair interact with the medium are taken

into account. For example, the process represented by the following diagram:



can be included. However, processes like:



where the electron and the hole interact with each other are neglected.

The screened Coulomb interaction resulting from Eq. 4.25c is the same as in Eq. 4.20c:

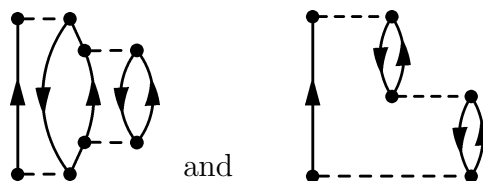
$$W = v + \text{diagram}$$

Except that now the polarizability is represented in the RPA.

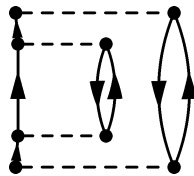
In Eq. 4.25d, the self-energy is written as a product of the Green function and the screened Coulomb interaction, diagrammatically:

$$\Sigma = \text{diagram}$$

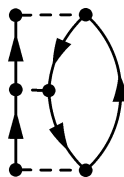
The shape of this diagram is similar to the Hartree-Fock approximation, with the instantaneous bare Coulomb potential replaced by the dynamically screened Coulomb one. This approximation to the self-energy includes processes represented, for example, by the diagrams:



etc. through the screened Coulomb potential. Also processes like:



are included through the interacting Green function. However, diagrams like:



where the added electron interacts with that of the electron hole pair, are neglected.

In Fig. 4.4 we show a sketch of the selfconsistent procedure required to solve the GW equations (4.25) together with the Dyson equation. However, this procedure is still extremely computationally demanding and rarely carried out.

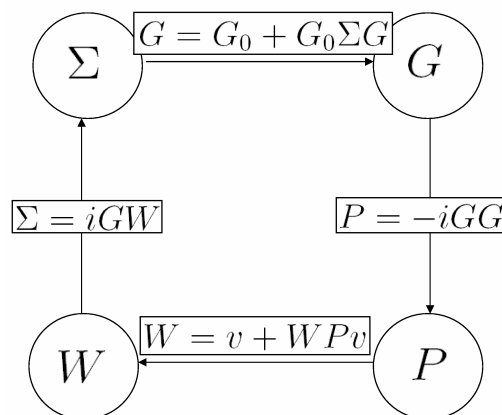


Figure 4.4: Schematic representation of the self-consistent solution of Hedin equations in GW approximation. Entries in boxes symbolize the mathematical relations that link Σ , G , P and W .

4.3 G_0W_0 Approximation

Assuming one counts on an effective single-particle potential $V^{\text{xc}}(\mathbf{r})$, which contains some of the exchange-correlation effects in a many-body system and approximates

reasonably well the self-energy, *i. e.*, the solutions of the single particle equation,

$$\hat{H}_{\text{eff}}(\mathbf{r})\varphi_i(\mathbf{r}) = \epsilon_i\varphi_i(\mathbf{r}) \quad (4.26)$$

with

$$\hat{H}_{\text{eff}}(\mathbf{r}) = -\frac{1}{2}\nabla^2 + V_{\text{ext}}(\mathbf{r}) + V^{\text{H}}(\mathbf{r}) + V^{\text{xc}}(\mathbf{r}) \quad (4.27)$$

are such that $\varphi_i(\mathbf{r}) \approx \psi_s(\mathbf{r})$ and $\epsilon_i \approx \Re(\epsilon_s)$ ($\psi_s(\mathbf{r})$ and ϵ_s are the solutions of Eq. 4.23). The quasiparticle equation (4.23) can be rewritten,

$$\left[-\frac{1}{2}\nabla^2 + V_{\text{ext}}(\mathbf{r}) + V^{\text{H}}(\mathbf{r}) + V^{\text{xc}}(\mathbf{r}) \right] \psi_s(\mathbf{r}) + \int d\mathbf{r}' \Delta\Sigma(\mathbf{r}, \mathbf{r}'; \epsilon_s) \psi_s(\mathbf{r}') = \epsilon_s \psi_s(\mathbf{r}) \quad (4.28)$$

where

$$\Delta\Sigma(\mathbf{r}, \mathbf{r}'; \epsilon_s) = \Sigma(\mathbf{r}, \mathbf{r}'; \epsilon_s) - V^{\text{xc}}(\mathbf{r}') \delta(\mathbf{r} - \mathbf{r}'). \quad (4.29)$$

Since, according to our assumptions, the correction due to $\Delta\Sigma$ are small, one can obtain the quasiparticle energies applying first order perturbation theory;

$$\begin{aligned} \psi_i(\mathbf{r}) &= \varphi_i(\mathbf{r}) \\ \epsilon_i^{\text{qp}} &= \epsilon_i + \langle \varphi_i(\mathbf{r}_1) | \Re[\Delta\Sigma(\mathbf{r}_1, \mathbf{r}_2; \epsilon_i^{\text{qp}})] | \varphi_i(\mathbf{r}_2) \rangle. \end{aligned} \quad (4.30)$$

Taking the self-energy in the GW approximation, and further assuming that the non-interacting Green function G_0 corresponding to \hat{H}_{eff} is a good approximation to the interacting one, the self-energy can be calculated through:

$$P_0(1, 2) = -iG_0(1, 2)G_0(2, 1), \quad (4.31a)$$

$$W_0(1, 2) = v(1, 2) + \int d(3, 4) W_0(1, 3)P(3, 4)v(4, 2), \quad (4.31b)$$

$$\Sigma(1, 2) = iG_0(1, 2)W_0(1^+, 2). \quad (4.31c)$$

usually known as the G_0W_0 approximation.

The Kohn-Sham scheme to the density-functional theory naturally provides a single particle effective potential that includes exchange-correlation effects. Thus, one usually starts from the Kohn-Sham Green function:

$$\begin{aligned} G_0(1, 2) &= -i \sum_j \varphi_j^{\text{KS}}(\mathbf{r}_1) \varphi_j^{\text{KS}*}(\mathbf{r}_2) e^{-i\epsilon_j^{\text{KS}}(t_1 - t_2)} \\ &\quad [\Theta(t_1 - t_2) \Theta(\epsilon_j^{\text{KS}} - \mu) - \Theta(t_2 - t_1) \Theta(\mu - \epsilon_j^{\text{KS}})]. \end{aligned} \quad (4.32)$$

The first application of this method to real materials was carried out by Hybertsen and Louie in 1985 [9]. Since then, it has achieved an impressive success in reproducing the experimental single particle excitation spectra for a wide range of

systems; among others: simple metals [94, 95], and weakly correlated semiconductors and insulators [11, 12, 96], becoming nowadays the standard method to calculate the single-electron excitations of condensed matter systems. The numerical implementation of the G_0W_0 approximation on the Full-Potential, Linear Augmented Plane Wave (LAPW) method and some of its application is the main subject of this thesis.

4.4 Summary

In summary, the Green function method within many-body perturbation theory offers a theoretically justified method for the interpretation of the bandstructure as the experimentally measured single particle excitations. The key issue is the approximation chosen for the self-energy. Hedin equations offer an efficient scheme to get reasonably good approximations for the self-energy. The simplest one, taking the zeroth order expansion of the vertex function in terms of the screened Coulomb potential, yields the GW approximation. However, its expensive computational cost inhibits the application to real system. The standard approach nowadays is the “so called” one-shot treatment (G_0W_0), where the self-energy is calculated from the Green function and the screened Coulomb potential generated from the Kohn-Sham states and used as a perturbation to the exchange-correlation potential. In the last years, this approach has achieved a great success in reproducing the single particle excitation energies measured experimentally.

Part III

Implementation and Tests

Chapter 5

Numerical Implementation of the G_0W_0 Code

This chapter describes the implementation of our all-electron G_0W_0 code based on the Full-Potential (Linearized) Augmented Plane Wave plus local orbitals (FP-(L)APW+lo) method [79, 80]. Due to its combined abilities to provide the most reliable results for periodic systems within DFT, and to address the widest range of materials, this method is currently considered to set the benchmark in DFT calculations. Consequently, the development of a G_0W_0 code has constituted a demanding task. The whole process has been imbued by the compromise between computational efficiency and the numerical precision necessary to achieve the ambitious goals of reliability and wide applicability complying with the FP-(L)APW+lo standards.

Among the different existing implementations of the method, we have taken Wien2k code [97] as the base on top of which we have built ours.

In the first section (5.1) we present a summary of the G_0W_0 equations, the system we want to solve numerically. The representation of the non-local operators (polarization, dielectric function, bare and screened Coulomb potentials) requires an efficient basis set, able to address extended as well as localized valence states and core states. We use an optimized set of functions consisting of plane waves in the interstitial region and a spherical harmonics expansion within the muffin-tin (MT) spheres, the latter based on the product basis originally proposed by Aryasetiawan and Gunnarsson [88]. This mixed basis functions are introduced in Sec. 5.2. In Sec. 5.3 we summarize the matrix form of the G_0W_0 equations after expansion in the mixed basis.

Calculating the polarization for a given wavevector \mathbf{q} requires the integration over all possible transitions from occupied to unoccupied states and back which conserve the total wavenumber. In other words, a precise \mathbf{q} -dependent Brillouin-zone integration is required. The efficiency of the linear tetrahedron method is comparable to the special points methods for semiconductors and insulators, while it

is clearly superior for metallic systems. To be able to treat the widest possible range of materials, we have extended the linear tetrahedron method to the \mathbf{q} -dependent case. A description of this development, together with the special requirements for the polarization, are described in section 5.4.

The frequency dependence of the polarization is calculated numerically, without relying on further approximations such as plasmon pole models. A well known difficulty in reciprocal space implementations of MBPT is the divergence of the Coulomb potential at the Γ -point ($\mathbf{q} = 0$). By taking the symmetrized dielectric function, and calculating analytically the limit for $\mathbf{q} \rightarrow 0$ using the $\mathbf{k} \cdot \mathbf{p}$ perturbation theory we obtain a regular expression at Γ within our basis set. The calculation of the self-energy still has to deal with the divergence of both, bare and screened Coulomb potentials. However, this singularity is integrable in 3 dimensions, provided that the necessary care is taken to avoid the numerical instabilities, as we will show in Sec. 5.5. The frequency convolution of the correlation self-energy is presented in Sec. 5.6.

We are confident that all these features make the code the most accurate implementation of the G_0W_0 approximation to date. We end the chapter with an outline of the flowchart of the code.

Important to mention, the code was basically written by Dr. Ricardo Gomez-Abal. The main contribution from the author of the thesis is the development of the \mathbf{q} -dependent linear tetrahedron method in section 5.4.

5.1 Summary of the G_0W_0 Equations

In the G_0W_0 approach, the quasiparticle energy $\epsilon_{n,\mathbf{k}}^{\text{qp}}$ is obtained as a first order correction to the Kohn-Sham energy eigenvalue $\epsilon_{n,\mathbf{k}}$:

$$\epsilon_{n,\mathbf{k}}^{\text{qp}} = \epsilon_{n,\mathbf{k}} + \langle \varphi_{n,\mathbf{k}}(\mathbf{r}_1) | \Re [\Sigma(\mathbf{r}_1, \mathbf{r}_2; \epsilon_{n,\mathbf{k}}^{\text{qp}})] - V^{\text{xc}}(\mathbf{r}_1) \delta(\mathbf{r}_1 - \mathbf{r}_2) | \varphi_{n,\mathbf{k}}(\mathbf{r}_2) \rangle, \quad (5.1)$$

where $\varphi_{n,\mathbf{k}}(\mathbf{r})$ and V^{xc} are the Kohn-Sham eigenfunctions and exchange-correlation potential respectively. The self-energy $\Sigma(\mathbf{r}_1, \mathbf{r}_2; \omega)$ is obtained from the Fourier transform of Eq. 4.31c:

$$\Sigma(\mathbf{r}_1, \mathbf{r}_2; \omega) = \frac{i}{2\pi} \int G_0(\mathbf{r}_1, \mathbf{r}_2; \omega + \omega') W_0(\mathbf{r}_2, \mathbf{r}_1; \omega') d\omega', \quad (5.2)$$

where G_0 is the Green's function in the Kohn-Sham scheme, defined by:

$$G_0(\mathbf{r}_1, \mathbf{r}_2; \omega) = \sum_{n,\mathbf{k}} \frac{\varphi_{n,\mathbf{k}}(\mathbf{r}_1) \varphi_{n,\mathbf{k}}^*(\mathbf{r}_2)}{\omega - \epsilon_{n,\mathbf{k}} \pm i\eta} \quad (5.3)$$

and the dynamically screened Coulomb potential $W_0(\mathbf{r}_2, \mathbf{r}_1; \omega)$ is given by:

$$W_0(\mathbf{r}_1, \mathbf{r}_2; \omega) = \int \varepsilon^{-1}(\mathbf{r}_1, \mathbf{r}_3; \omega) v(\mathbf{r}_3, \mathbf{r}_2) d\mathbf{r}_3. \quad (5.4)$$

$\varepsilon(\mathbf{r}_1, \mathbf{r}_2; \omega)$ is the dielectric function, it can be calculated from:

$$\varepsilon(\mathbf{r}_1, \mathbf{r}_2; \omega) = 1 - \int v(\mathbf{r}_1, \mathbf{r}_3) P(\mathbf{r}_3, \mathbf{r}_2; \omega) d\mathbf{r}_3, \quad (5.5)$$

where the polarizability $P(\mathbf{r}_1, \mathbf{r}_2; \omega)$, in the random phase approximation (RPA), is written as:

$$P(\mathbf{r}_1, \mathbf{r}_2; \omega) = -\frac{i}{2\pi} \int G_0(\mathbf{r}_1, \mathbf{r}_2; \omega + \omega') G_0(\mathbf{r}_2, \mathbf{r}_1; \omega') d\omega' \quad (5.6)$$

The self-energy can be separated into the exchange and correlation terms. If we define:

$$W_0^c(\mathbf{r}_1, \mathbf{r}_2; \omega) = W_0(\mathbf{r}_1, \mathbf{r}_2; \omega) - v(\mathbf{r}_1, \mathbf{r}_2), \quad (5.7)$$

where $v(\mathbf{r}_1, \mathbf{r}_2) = \frac{1}{|\mathbf{r}_1 - \mathbf{r}_2|}$ is the bare Coulomb potential, the exchange and correlation term of the self-energy can be calculated from:

$$\begin{aligned} \Sigma^x(\mathbf{r}_1, \mathbf{r}_2) &= \frac{i}{2\pi} \int G_0(\mathbf{r}_1, \mathbf{r}_2; \omega') v(\mathbf{r}_2, \mathbf{r}_1) d\omega' \\ &= \sum_{n, \mathbf{k}}^{\text{occ}} \varphi_{n, \mathbf{k}}(\mathbf{r}_1) v(\mathbf{r}_2, \mathbf{r}_1) \varphi_{n, \mathbf{k}}^*(\mathbf{r}_2) \end{aligned} \quad (5.8)$$

and

$$\Sigma^c(\mathbf{r}_1, \mathbf{r}_2; \omega) = \frac{i}{2\pi} \int G_0(\mathbf{r}_1, \mathbf{r}_2; \omega + \omega') W_0^c(\mathbf{r}_2, \mathbf{r}_1; \omega') d\omega' \quad (5.9)$$

separately.

The required input for solving this set of equations are the eigenfunctions, $(\varphi_{n, \mathbf{k}}(\mathbf{r}))$, eigenvalues $(\epsilon_{n, \mathbf{k}})$ and the exchange correlation potential $(V_{xc}(\mathbf{r}))$ from a Kohn-Sham calculation. These data are obtained from a self-consistent DFT calculation using the Wien2k [97] implementation of the FP-(L)APW+lo method.

5.2 The Mixed Basis

For periodic systems, the reciprocal space representation improves the efficiency by exploiting explicitly the translational symmetry of the Bravais lattice. However, a direct Fourier transform of the operators, which implies taking plane-waves as a basis set, is computationally inefficient for their representation in a full-potential,

all-electron implementation (see Chapter 3). Analogous to the proposal of Kotani and van Schilfgaarde [13] we expand the different operators in an optimized set of functions satisfying Bloch's theorem. This "mixed" basis set uses the space partition in muffin-tin spheres and interstitial region following the APW philosophy. In this section, we introduce the mixed basis set and show its efficiency and numerical stability through different sets of tests.

5.2.1 Definition

Replacing the expression of Eq. 5.3 for the Green's function into Eq. 5.6, one obtains an expression for the polarizability where its spatial dependence on each coordinate is written as a series of products of two Kohn-Sham wave functions. Thus, the basis set chosen to expand it should be efficient in representing those products.

The Kohn-Sham wave functions are linear combinations of (L)APW+lo basis functions (Appendix 3.2). In other words, they are expanded in terms of spherical harmonics in the muffin-tin spheres and plane waves in the interstitial region. Obviously, the product of two plane waves is also plane wave and the product of two spherical harmonics can be expanded in spherical harmonics using the Clebsch-Gordan coefficients.

The same kind of space partition is taken to define our basis set. Inside the MT sphere of atom α , we define our basis functions as:

$$\gamma_{\alpha,N,L,M}(\mathbf{r}^\alpha) = v_{\alpha,N,L}(r^\alpha) Y_{L,M}(\mathbf{r}^\alpha). \quad (5.10)$$

To obtain an optimal set of radial functions $v_{\alpha,N,L}(r^\alpha)$, we proceed as follows:

- $\dot{u}_l(r)$'s are not taken into account because $\int |\dot{u}_l(r)|^2 r^2 dr$ is typically less than 10% of $\int |u_l(r)|^2 r^2 dr$. Possible errors will be taken care by the other basis functions.
- To truncate the expansion, we take a maximum l_{\max} for the choice of $u_l(r^\alpha)$'s.
- For each L in $v_{\alpha,N,L}(r^\alpha)$, we take all the products of two radial functions $u_l(r^\alpha)u_{l'}(r^\alpha)$ which fulfill the triangular condition $|l - l'| \leq L \leq l + l'$.
- We calculate the overlap matrix between this set of product radial functions:

$$\mathbb{O}_{(l,l');(l_1,l'_1)} = \int_0^{R_{\text{MT}}^\alpha} u_{\alpha,l}(r^\alpha)u_{\alpha,l'}(r^\alpha)u_{\alpha,l_1}(r^\alpha)u_{\alpha,l'_1}(r^\alpha)(r^\alpha)^2 dr^\alpha \quad (5.11)$$

- The matrix $\mathbb{O}_{(l,l');(l_1,l'_1)}$ is diagonalized, obtaining the corresponding set of eigenvalues λ^N and eigenvectors $\{c_{l,l'}^N\}$.

- Eigenvectors corresponding to eigenvalues (λ^N) smaller than a certain tolerance λ_{\min} are assumed to be linear dependent and discarded.
- The remaining eigenvectors, after normalization, constitute the radial basis set: $v_{\alpha,N,L}(r^\alpha) = \sum_{l,l'} c_{l,l'}^N u_l(r^\alpha) u_{l'}(r^\alpha)$

So defined, the functions $\{\gamma_{\alpha,N,L,M}\}$ constitute an orthonormal basis set. The translational symmetry of the lattice is imposed by taking the Bloch summation:

$$\gamma_{\alpha,N,L,M}^{\mathbf{q}}(\mathbf{r}) = \frac{1}{\sqrt{N_c}} \sum_{\mathbf{R}} e^{i\mathbf{q}\cdot(\mathbf{R}+\mathbf{r}_\alpha)} \gamma_{\alpha,N,L,M}(\mathbf{r}^\alpha), \quad (5.12)$$

where \mathbf{r}_α is the position of atom α in the unit cell, and \mathbf{R} is a Bravais lattice vector.

Since the interstitial plane waves are not orthogonal, we diagonalize the overlap matrix by solving the eigenvalue equation (details in Appendix A):

$$\sum_{\mathbf{G}'} \mathbb{O}_{\mathbf{G},\mathbf{G}'} S_{\mathbf{G}',i} = \varepsilon_i S_{\mathbf{G},i}, \quad (5.13)$$

where $\mathbb{O}_{\mathbf{G},\mathbf{G}'}^{\mathbf{q}} \equiv \langle P_{\mathbf{G}}^{\mathbf{q}} | P_{\mathbf{G}'}^{\mathbf{q}} \rangle$ and $\langle \mathbf{r} | P_{\mathbf{G}}^{\mathbf{q}} \rangle = \frac{1}{\sqrt{V}} e^{i(\mathbf{G}+\mathbf{q})\cdot\mathbf{r}}$.

The orthogonal basis set in the interstitial region is defined by:

$$\tilde{P}_i^{\mathbf{q}}(\mathbf{r}) \equiv \sum_{\mathbf{G}} \tilde{S}_{\mathbf{G},i} P_{\mathbf{G}}^{\mathbf{q}}(\mathbf{r}). \quad (5.14)$$

where $\tilde{S}_{\mathbf{G},i} = \frac{1}{\sqrt{\varepsilon_i}} S_{\mathbf{G},i}$ so that the orthogonal IPW's are normalized. The plane wave expansion is truncated at a certain G_{\max} . In fact, we introduce a parameter Q that defines G_{\max} in units of G_{\max}^{LAPW} (the plane wave cut off of the LAPW basis functions). Finally, our orthonormal mixed basis set is:

$$\{\chi_j^{\mathbf{q}}(\mathbf{r})\} \equiv \left\{ \gamma_{\alpha,N,L,M}^{\mathbf{q}}(\mathbf{r}), \tilde{P}_{\mathbf{G}}^{\mathbf{q}}(\mathbf{r}) \right\}, \quad (5.15)$$

5.2.2 Completeness Tests

The basis set was derived from the requirement of efficiency to expand products of Kohn-Sham eigenfunctions. The principal quantity for such expansion, and also a central quantity for the whole implementation are the matrix elements (see Appendix D):

$$M_{n,m}^i(\mathbf{k}, \mathbf{q}) \equiv \int_{\Omega} [\chi_i^{\mathbf{q}}(\mathbf{r}) \varphi_{m,\mathbf{k}-\mathbf{q}}(\mathbf{r})]^* \varphi_{n,\mathbf{k}}(\mathbf{r}) d^3r. \quad (5.16)$$

Assuming that the basis is complete, *i. e.*

$$\sum_i |\chi_i^{\mathbf{q}}(\mathbf{r})\rangle \langle \chi_i^{\mathbf{q}}(\mathbf{r}')| = \delta(\mathbf{r} - \mathbf{r}'), \quad (5.17)$$

any product of two Kohn-Sham wave functions can be expanded as:

$$\varphi_{n,\mathbf{k}}(\mathbf{r}) \varphi_{n',\mathbf{k}-\mathbf{q}}^*(\mathbf{r}) = \sum_i M_{n,n'}^i(\mathbf{k}, \mathbf{q}) \chi_i^{\mathbf{q}}(\mathbf{r}). \quad (5.18)$$

Eq. 5.18 can be directly applied to analyze pictorially the quality of the basis set. To be more clear, we analyze the interstitial and muffin-tin regions separately.

In Fig. 5.1, we show the real part of the product of two Kohn-Sham wave functions in the line joining two Si atoms in bulk Si and compare it with the expansion defined in Eq. 5.18 for different values of Q . The pair of wave functions selected is arbitrary, but the trend observed is similar in all the cases. As expected, increasing Q improves the quality of the expansion. The product of two Kohn-Sham wave functions is well represented in the interstitial region with $Q \geq 1.0$.

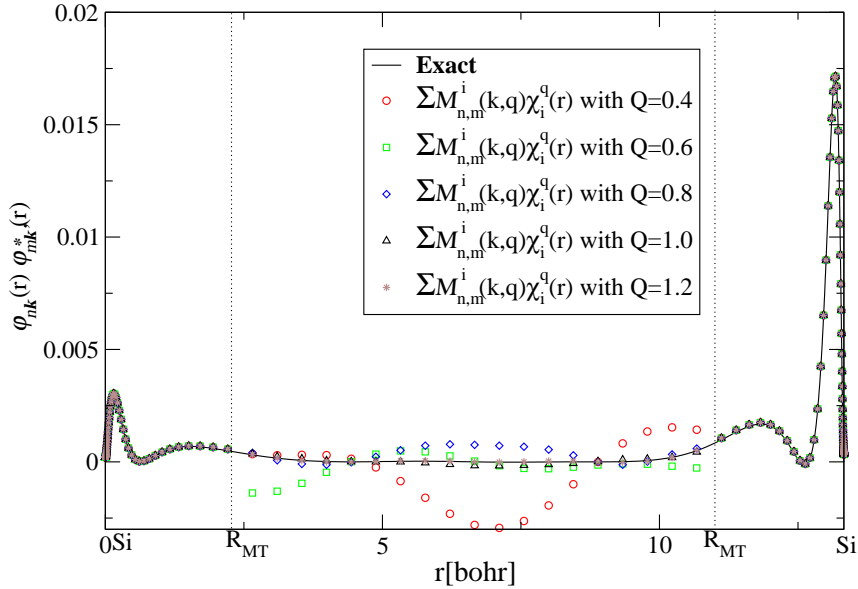


Figure 5.1: Expansion of the real part of the product of two Kohn-Sham wave functions of Si for $\mathbf{k} = \Gamma$, $\mathbf{k}' = \frac{\pi}{2a}(1, 1, 1)$, and $n = 5$, $m = 4$ using different values of Q with $l_{\max} = 2$ and $\lambda_{\min} = 10^{-4}$. a is the lattice constant of the crystal.

The same expansion is shown in Fig. 5.2 for fixed Q and different values of l_{\max} and λ_{\min} . It is clear that with $l_{\max} = 0$ the basis set is inappropriate for representing the product of these two Kohn-Sham wave functions. Taking $l_{\max} = 1$ gives very poor results. The results improve by increasing l_{\max} . Already with $l_{\max} = 2$, the product is represented rather well. Fixing $l_{\max} = 2$, the basis set is improved decreasing λ_{\min} from 10^{-2} to 10^{-3} . The improvement obtained by further reducing it to 10^{-4} cannot be distinguished by bare eyes.

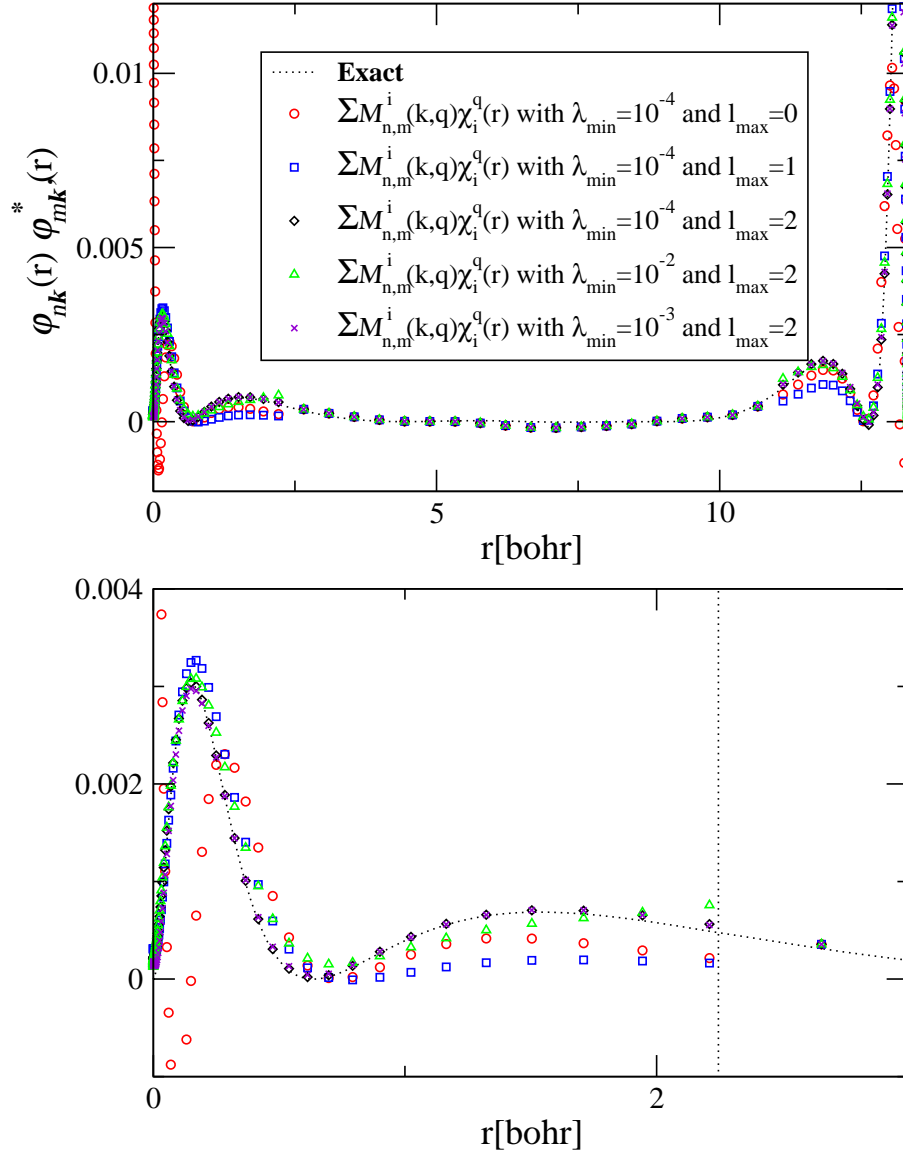


Figure 5.2: Expansion of the real part of the product of two Kohn-Sham wave functions of Si for $\mathbf{k} = \Gamma$, $n = 5$, $\mathbf{k}' = \frac{\pi}{2a}(1, 1, 1)$, and $m = 4$ using $Q = 1.0$ and different l_{\max} and λ_{\min} . a is the lattice constant of the crystal. The lower panel zooms the muffin-tin region.

To be able to observe further improvements we take the mean square error of the expansion, defined as:

$$\begin{aligned} \int_{\Omega} \left| \varphi_{n,\mathbf{k}}(\mathbf{r}) \varphi_{n',\mathbf{k}-\mathbf{q}}^*(\mathbf{r}) - \sum_i M_{n,n'}^i(\mathbf{k}, \mathbf{q}) \chi_i^{\mathbf{q}}(\mathbf{r}) \right|^2 d\mathbf{r} \\ = \int_{\Omega} |\varphi_{n,\mathbf{k}}(\mathbf{r}) \varphi_{m,\mathbf{k}-\mathbf{q}}(\mathbf{r})|^2 d\mathbf{r} - \sum_i |M_{n,m}^i(\mathbf{k}, \mathbf{q})|^2. \end{aligned} \quad (5.19)$$

The relative error is then given by:

$$\Delta = 1 - \frac{|M_{n,m}^i(\mathbf{k}, \mathbf{q})|^2}{\int_{\Omega} |\varphi_{n,\mathbf{k}}(\mathbf{r}) \varphi_{m,\mathbf{k}-\mathbf{q}}(\mathbf{r})|^2 d\mathbf{r}}. \quad (5.20)$$

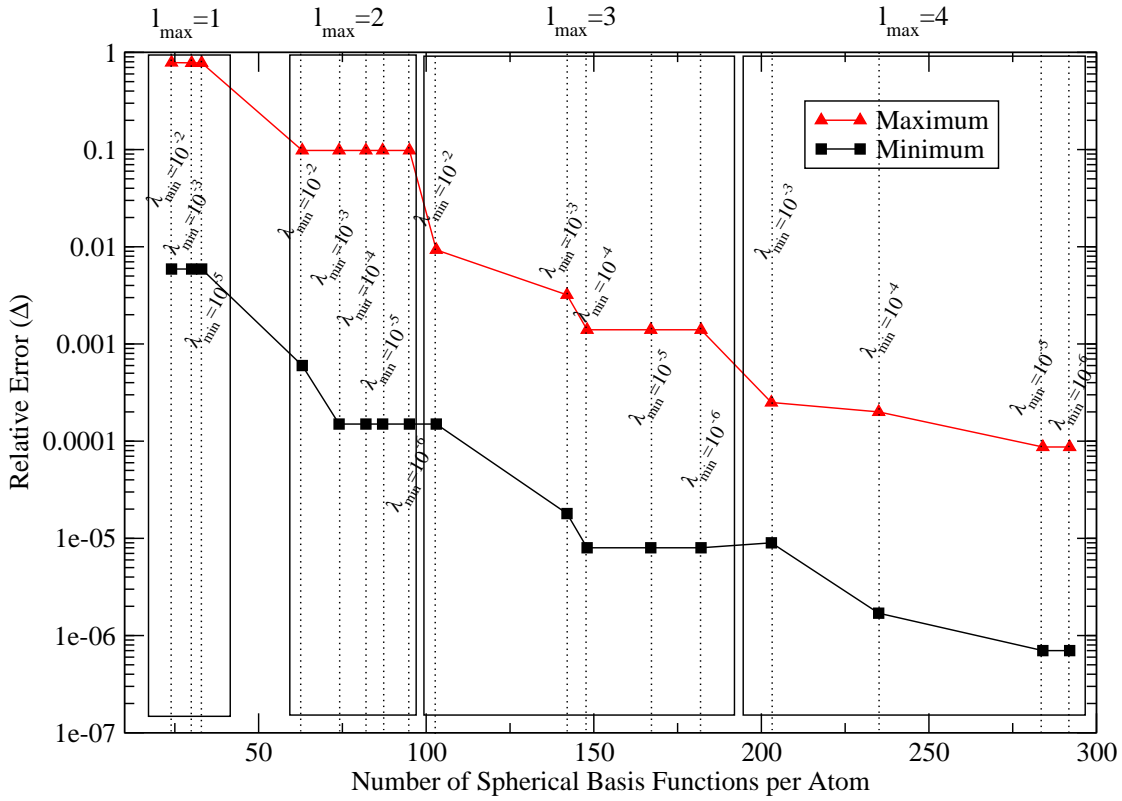


Figure 5.3: Dependence of the relative completeness error with the number of basis functions in the MT region. It decreases with the increase of the number of basis functions. For each l_{\max} , there exists a saturation value for λ_{\min} , after which when decreasing this tolerance the relative error doesn't change, indicating a larger l_{\max} is required for higher accuracy.

We have calculated the relative error for a large set of product functions. In Fig. 5.3, we show the maximum and minimum values as a function of the number of basis functions in the muffin-tin region. The error in the interstitial region is shown in Fig. 5.4. In both cases the error decreases by increasing the size of the basis set, evidencing the capability of the mixed basis for the expansion of products as well as the numerical stability of the algorithm to generate it. We want to call the attention to the plateaus for fixed l_{\max} appearing in Fig. 5.3. Further reduction of λ_{\min} beyond its maximum value at the plateau increases the size of the basis set without improving its quality. The beginning of each plateau clearly determines the optimum λ_{\min} for each given l_{\max} . In the interstitial region (Fig. 5.4), increasing Q decreases the relative error monotonically. The optimum Q is chosen to give a relative error comparable to the muffin-tin region.

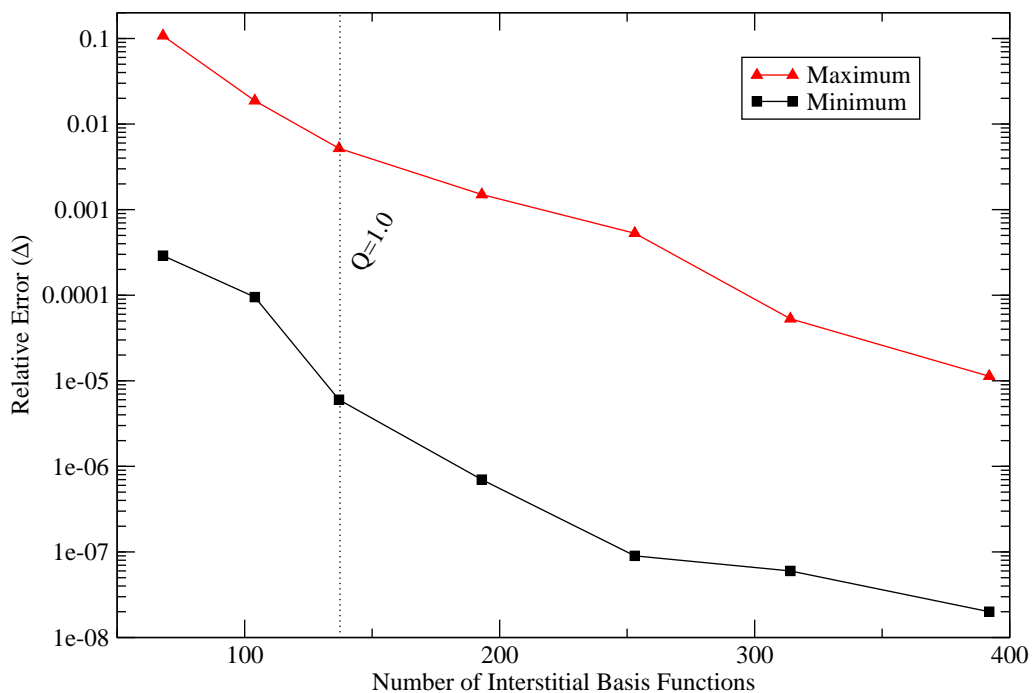


Figure 5.4: Relative completeness error as a function of the number of basis functions in the interstitial region.

5.3 Matrix Form of the G_0W_0 Equations

Following the expansion of non-local operators in periodic systems (Appendix I, Eq. I.6), we can write the Coulomb potential matrix elements in the mixed basis as:

$$v_{i,j}(\mathbf{q}) = \int_{\Omega} \int_{\Omega} (\chi_i^{\mathbf{q}}(\mathbf{r}_1))^* \sum_{\mathbf{R}} v(\mathbf{r}_1, \mathbf{r}_2 - \mathbf{R}) e^{-i\mathbf{q}\cdot\mathbf{R}} \chi_j^{\mathbf{q}}(\mathbf{r}_2) d\mathbf{r}_2 d\mathbf{r}_1. \quad (5.21)$$

Detailed expressions are given in Appendix C.

Using the matrix element defined in Eq. 5.16, the polarizability can be calculated by:

$$P_{i,j}(\mathbf{q}, \omega) = \sum_{\mathbf{k}} \sum_n^{BZ} \sum_{n'}^{\text{occ unocc}} M_{n,n'}^i(\mathbf{k}, \mathbf{q}) [M_{n,n'}^j(\mathbf{k}, \mathbf{q})]^* \left\{ \frac{1}{\omega - \epsilon_{n',\mathbf{k}-\mathbf{q}} + \epsilon_{n,\mathbf{k}} + i\eta} - \frac{1}{\omega - \epsilon_{n,\mathbf{k}} + \epsilon_{n',\mathbf{k}-\mathbf{q}} - i\eta} \right\} \quad (5.22)$$

To avoid the divergence at $\mathbf{q} = 0$ of the dielectric function as defined in Eq. 5.5, we resort to the symmetrized dielectric function (see Appendix F), defined as:

$$\tilde{\epsilon}_{i,j}(\mathbf{q}, \omega) = \delta_{i,j} - \sum_{l,m} v_{i,l}^{\frac{1}{2}}(\mathbf{q}) P_{l,m}(\mathbf{q}, \omega) v_{m,j}^{\frac{1}{2}}(\mathbf{q}). \quad (5.23)$$

Using Eq. G.3, the correlation term of the screened Coulomb interaction can be calculated through:

$$W_{i,j}^c(\mathbf{q}, \omega) = \sum_{l,m} v_{i,l}^{\frac{1}{2}}(\mathbf{q}) [\tilde{\epsilon}_{l,m}^{-1} - \delta_{l,m}] (\mathbf{q}, \omega) v_{m,j}^{\frac{1}{2}}(\mathbf{q}) \quad (5.24)$$

The diagonal matrix element of the self-energy in the basis of the Kohn-Sham states is:

$$\begin{aligned} \Sigma_{n,\mathbf{k}}^c(\omega) &= \langle \varphi_{n,\mathbf{k}} | \Sigma^c(\mathbf{r}_1, \mathbf{r}_2; \omega) | \varphi_{n,\mathbf{k}} \rangle \\ &= \frac{i}{2\pi} \sum_{\mathbf{q}} \sum_{i,j}^{BZ} \sum_{n'} [M_{n,n'}^i(\mathbf{k}, \mathbf{q})]^* M_{n,n'}^j(\mathbf{k}, \mathbf{q}) \int_{-\infty}^{\infty} \frac{W_{i,j}^c(\mathbf{q}, \omega')}{\omega + \omega' - \epsilon_{n',\mathbf{k}-\mathbf{q}} \pm i\eta} d\omega'. \end{aligned} \quad (5.25)$$

for the correlation term, and

$$\begin{aligned} \Sigma_{n,\mathbf{k}}^x &= \langle \varphi_{n,\mathbf{k}} | \Sigma^x(\mathbf{r}_1, \mathbf{r}_2) | \varphi_{n,\mathbf{k}} \rangle \\ &= - \sum_{\mathbf{q}} \sum_{i,j}^{BZ} v_{i,j}(\mathbf{q}) \sum_{n'}^{\text{occ}} [M_{n,n'}^i(\mathbf{k}, \mathbf{q})]^* M_{n,n'}^j(\mathbf{k}, \mathbf{q}) \end{aligned} \quad (5.26)$$

for the exchange term.

The quasiparticle energies should be obtained solving Eq. 5.1 self-consistently, since the self-energy depends on the quasiparticle energy $\epsilon_{n,\mathbf{k}}^{\text{QP}}$. Usually, a first order Taylor expansion of the self-energy around $\epsilon_{n,\mathbf{k}}^{\text{KS}}$ is used instead. The quasiparticle energies are then given by:

$$\epsilon_{n,\mathbf{k}}^{\text{QP}} = \epsilon_{n,\mathbf{k}}^{\text{KS}} + Z_{n,\mathbf{k}} \left[\Sigma_{n,\mathbf{k}}^{\text{c}}(\epsilon_{n,\mathbf{k}}^{\text{KS}}) + \Sigma_{n,\mathbf{k}}^{\text{x}} - \langle \varphi_{n,\mathbf{k}}^{\text{KS}} | V_{\text{XC}}^{\text{KS}}(\mathbf{r}) | \varphi_{n,\mathbf{k}}^{\text{KS}} \rangle \right] \quad (5.27)$$

where:

$$Z_{n,\mathbf{k}} = \left[1 - \left(\frac{\partial}{\partial \omega} \Sigma_{n,\mathbf{k}}^{\text{c}}(\omega) \right)_{\epsilon_{n,\mathbf{k}}^{\text{KS}}} \right]^{-1}. \quad (5.28)$$

In our implementation, these two equations are used to get a first set of quasiparticle energies, which are then taken as the starting point to solve Eq. 5.1 iteratively with respect to $\epsilon_{n,\mathbf{k}}^{\text{QP}}$. To ensure the conservation of the quasiparticle number, the quasiparticle Fermi level is aligned to the Kohn-Sham one after each iteration for Eq. 5.1. We stop the iteration when this shift is smaller than a chosen tolerance.

5.4 Brillouin-Zone Integration of the Polarization

Brillouin-zone integration is an important ingredient of any reciprocal space method and has been a subject of interest since the earliest implementation of electronic structure codes. Fundamental quantities like the total energy or the density of states require an integration over the Brillouin-zone of a certain operator, *e. g.* the eigenvalues weighted by the Fermi distribution function for the former, the energy derivative of the Fermi distribution for the latter.

In the 1970's, a large number of studies were carried out for solving these problems, among which the special point [98, 99, 100, 101] and the linear tetrahedron method [102, 103, 104] are the most used ones nowadays. These two methods perform identically well for insulators and semiconductors. For metals, the Brillouin-zone integration becomes more cumbersome due to the presence of the Fermi surface, which defines the integration region in the Brillouin-zone. The linear tetrahedron method becomes advantageous in these systems thanks to its better description of the Fermi surface (Fig. 5.5) and, therefore, of the integration region [105].

In the linear tetrahedron method, first proposed by Jepsen and Andersen in Ref. [102] and Lehmann *et al.* in Ref. [103], the Brillouin-zone is divided into a set of tetrahedra. The energy eigenvalues ($\epsilon_{n,\mathbf{k}}$) and the integrand are calculated on the vertices of these tetrahedra and, through the procedure known as isoparametrization, linearly interpolated inside each of them. The values of the integrand can be factorized out of the integral. The remaining integrals, independent of the values at the vertices, can be integrated analytically and added to obtain integration weights

dependent only on the \mathbf{k} -point and the band index (Appendix E). In metallic systems the Fermi surface is approximated, through the isoparametrization, by a plane that limits the integration region inside the tetrahedra it intersects. The occupied region of the Brillouin-zone can thus be described much better than in any of the special points methods (Fig. 5.5).

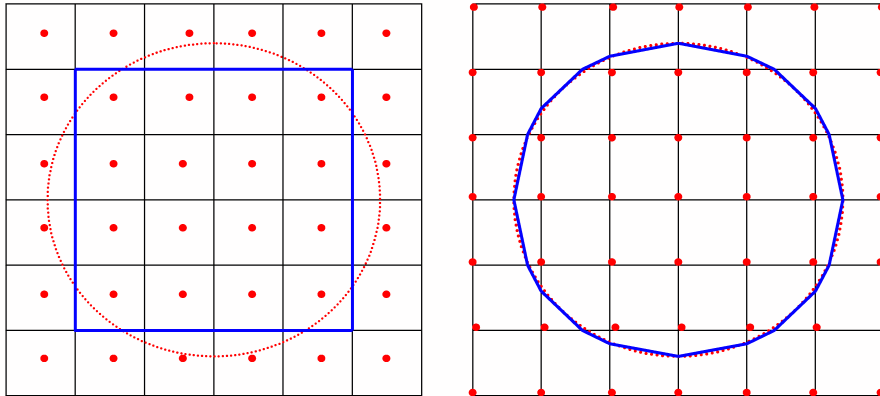


Figure 5.5: Two dimensional sketches of the description of the Fermi surface in the special points (left panel) and the linear tetrahedron method (right panel). In dotted red line the exact Fermi surface, in full blue line the approximated one. The \mathbf{k} -points grid is represented by red dots. Tetrahedron method gives better description of the Fermi surface.

The calculation of quantities like the polarizability (Eq. 5.22) or magnetic susceptibility, presents particular characteristics that require a different treatment. The integral depends on a second vector \mathbf{q} , it is weighted by two Fermi functions, so that the states at \mathbf{k} are occupied while those at $\mathbf{k} - \mathbf{q}$ are unoccupied, and finally, the eigenvalues appear in the denominator of the integrand. The grid of \mathbf{k} -points for this integration is chosen as usual in the tetrahedron method. On the other hand, the calculation of the self-energy (Eq. 5.25 and 5.26), requires a grid of \mathbf{q} -points also be suitable for integration. To avoid the repeated generation of eigenvalues and eigenvectors at several different grids, the set of \mathbf{q} -points should be such that $\{\mathbf{k}\} = \{\mathbf{k} - \mathbf{q}\}$. For this equality to hold, the set of \mathbf{q} -points must include the Γ point. In our implementation, we take the same mesh for \mathbf{k} and \mathbf{q} .

Due to the presence of the eigenvalues in the denominator of the integrand, a simultaneous isoparametrization of both, the integrand and the eigenvalues, becomes inappropriate. In 1975, Rath and Freeman proposed a solution to this problem for the calculation of the static magnetic susceptibilities in metals [104]. They approximated the numerator of the integrand by its mean value in each tetrahedron, while the denominator was included in the analytic integration to obtain the weights. In this work, we go two steps further. We apply the isoparametrization not only to

the eigenvalues but also to the numerator of the integrand, improving the accuracy, and also extended the method to include the frequency dependence. The integration inside each tetrahedron can still be performed analytically (See Appendix E).

Since the integration runs simultaneously on two tetrahedra (at \mathbf{k} and $\mathbf{k} - \mathbf{q}$), there will be situations, in metallic systems, where both tetrahedra are intersected by the Fermi surface. In this case the integration region inside the tetrahedron is delimited by the two Fermi “planes” under the condition $\epsilon_{n\mathbf{k}} < \epsilon_F < \epsilon_{m\mathbf{k}-\mathbf{q}}$, as shown in Fig. 5.6. The complexity of the integration region is such that the integration can not be performed analytically on the whole tetrahedron as in the standard tetrahedron method. However, as pointed out in Ref. [104], the integration region can always be subdivided into, at most six, tetrahedra. The integration can be performed analytically inside each of these tetrahedra and then projected onto the vertices of the original tetrahedron to obtain the weights for each \mathbf{k} -point. We have analyzed and classified the different configurations of the distinct integration regions determined by two Fermi “planes” (See Fig. E.2 in Appendix E).

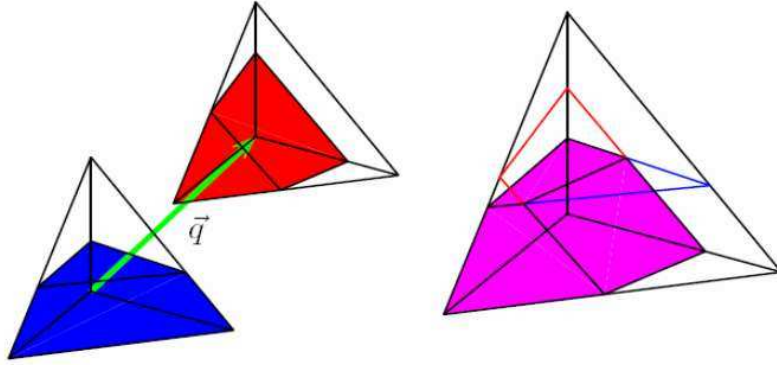


Figure 5.6: The integration region in the tetrahedron method for \mathbf{q} -dependent Brillouin-zone integration. The two tetrahedra on the left side are connected by the vector \mathbf{q} (green arrow). The blue zone corresponds to the occupied region for the state (n, \mathbf{k}) , the red one to the unoccupied region for the state $(n', \mathbf{k} - \mathbf{q})$. The resulting integration region, determined by superimposing the two tetrahedra on the left and taking the intersection of the blue and red zones, is the lilac region in the tetrahedron on the right hand side.

To test the accuracy and stability of our implementation, we have calculated the static polarizability of the free electron gas and compared it to its well-known analytical solution (the Lindhard function). The results are shown in Fig. 5.7. Our method performs really well for the free electron gas, which is one of the most demanding examples for the Brillouin-zone integration. Comparison of Fig. 5.7(a) with Fig. 4 in Ref. [104], shows that our implementation achieves a comparable accuracy with a coarser mesh (13x13x13 compared to 24x24x24 in Ref. [104]).

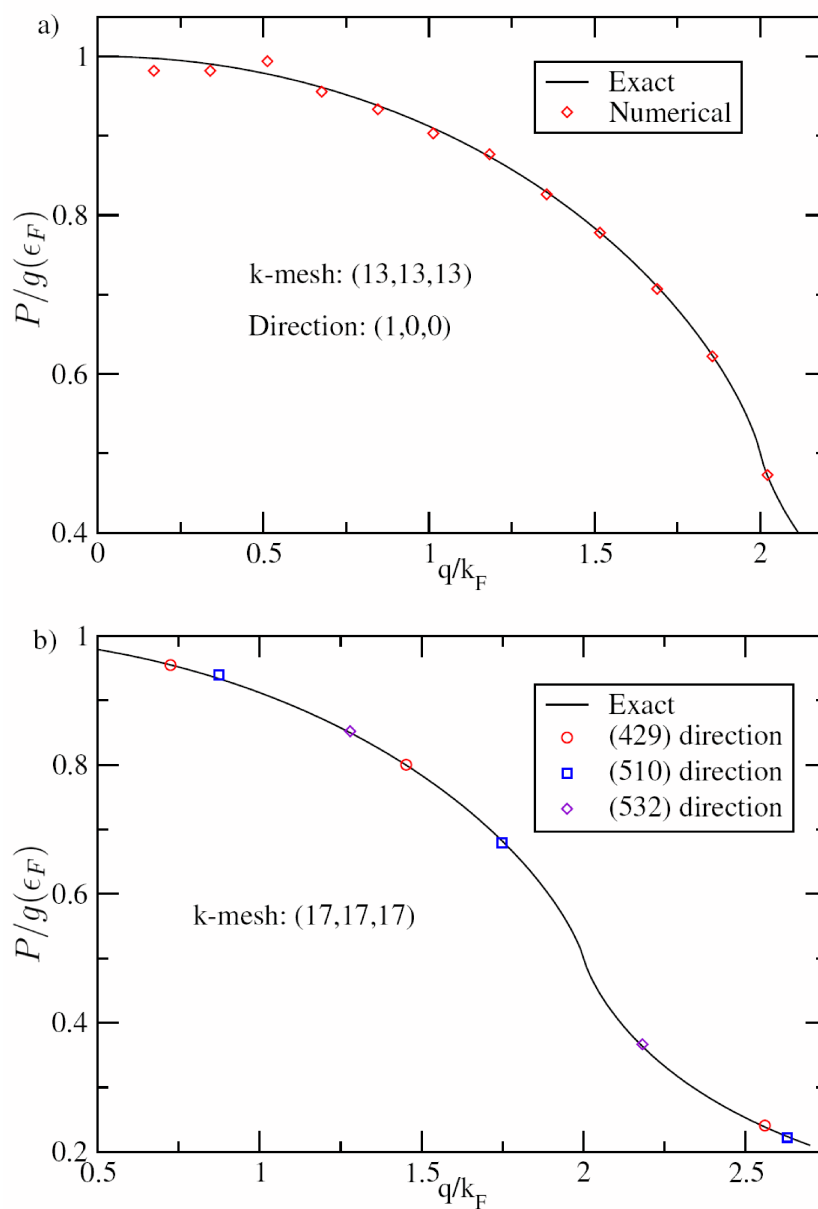


Figure 5.7: Comparison of the numerical (points) and analytical (line) results for the polarizability of the free electron gas (Lindhard function) as function of \mathbf{q} (a) on the (100) direction and (b) on other directions.

5.5 Γ Point Treatment for the Brillouin-Zone Integration of the Self-energy

Calculating the matrix elements of the self-energy (Eq. 5.25 and Eq. 5.26) requires an integration in \mathbf{q} over the Brillouin-zone. For the exchange term, Eq. 5.25, the integral runs over the occupied states at $\mathbf{k} - \mathbf{q}$, while for the correlation term, Eq. 5.26, it runs over all, occupied and unoccupied states. The integration itself presents, therefore, no new requirements; the former can be integrated by the standard linear tetrahedron method, while a direct sum is enough for the latter.

In the previous section, we pointed out that the \mathbf{q} mesh has to be commensurated with the \mathbf{k} mesh, that is,

$$\forall \mathbf{k}_1 \wedge \mathbf{k}_2 \in \{\mathbf{k}\} \exists \mathbf{q} \in \{\mathbf{q}\} / \mathbf{k}_1 - \mathbf{k}_2 = \mathbf{q}. \quad (5.29)$$

Taking $\mathbf{k}_1 = \mathbf{k}_2$ it is obvious that the Γ -point belongs to the \mathbf{q} -mesh. This entails the treatment of the divergency of the Coulomb potential at $\mathbf{q} = 0$, which affects the calculation of the dielectric function and both terms of the self-energy. We have already mentioned (Section 5.3) that the divergence of the dielectric function can be avoided by resorting to the symmetrized one (Appendix F). In this section we discuss how to handle the divergence in the \mathbf{q} -point integration.

To simplify the notation, we write the matrix elements of the self-energy as:

$$\Sigma_{n,\mathbf{k}}^\alpha = \sum_{\mathbf{q}}^{BZ} \Upsilon_{n,\mathbf{k}}^\alpha(\mathbf{q}). \quad (5.30)$$

where $\alpha = x$ (exchange) or c (correlation), and from Eq 5.26 and 5.25:

$$\begin{aligned} \Upsilon_{n,\mathbf{k}}^x(\mathbf{q}) &= - \sum_{i,j} v_{i,j}(\mathbf{q}) \sum_{n'}^{\text{occ}} [M_{n,n'}^i(\mathbf{k}, \mathbf{q})]^* M_{n,n'}^j(\mathbf{k}, \mathbf{q}) \\ \Upsilon_{n,\mathbf{k}}^c(\mathbf{q}, \omega) &= \frac{i}{2\pi} \sum_{i,j} \sum_{n'} [M_{n,n'}^i(\mathbf{k}, \mathbf{q})]^* M_{n,n'}^j(\mathbf{k}, \mathbf{q}) \int_{-\infty}^{\infty} \frac{W_{i,j}^c(\mathbf{q}, \omega')}{\omega + \omega' - \epsilon_{n',\mathbf{k}-\mathbf{q}} \pm i\eta} d\omega' \end{aligned} \quad (5.31)$$

In the following, we disregard in the equations the explicit dependence of the correlation term on the frequency to simplify the notation. Since $\Upsilon^{x(c)}$ is proportional to the bare (screened) Coulomb potential, its divergent terms can be separated as in Eq. C.33 and Eq. G.8. Thus, we can rewrite Eq. 5.30 as:

$$\Sigma_{n,\mathbf{k}}^\alpha = \sum_{\mathbf{q}}^{BZ} \left\{ \frac{\Upsilon_{n,\mathbf{k}}^{\alpha s2}(\mathbf{q})}{|\mathbf{q}|^2} + \frac{\Upsilon_{n,\mathbf{k}}^{\alpha s1}(\mathbf{q})}{|\mathbf{q}|} + \tilde{\Upsilon}_{n,\mathbf{k}}^\alpha(\mathbf{q}) \right\} \quad (5.32)$$

The singularity at the Γ point appearing in Eq. 5.32 is integrable, but a direct numerical integration will converge very slowly. Following Ref. [106], we add and subtract to the right hand side of Eq. 5.32 an auxiliary function G^α having the same singularities as Υ^α :

$$G^\alpha(\mathbf{q}) = \Upsilon_{n,\mathbf{k}}^{\alpha s2}(0)F_2(\mathbf{q}) + \Upsilon_{n,\mathbf{k}}^{\alpha s1}(0)F_1(\mathbf{q}) \quad (5.33)$$

with $F_n(\mathbf{q}) \rightarrow |\mathbf{q}|^{-n}$ for $\mathbf{q} \rightarrow 0$. Thus we have:

$$\begin{aligned} \Sigma_{n,\mathbf{k}}^\alpha = & \sum_{\mathbf{q}}^{\text{BZ}} \left\{ \frac{\Upsilon_{n,\mathbf{k}}^{\alpha s2}(\mathbf{q})}{|\mathbf{q}|^2} - \Upsilon_{n,\mathbf{k}}^{\alpha s2}(0)F_2(\mathbf{q}) + \frac{\Upsilon_{n,\mathbf{k}}^{\alpha s1}(\mathbf{q})}{|\mathbf{q}|} - \Upsilon_{n,\mathbf{k}}^{\alpha s1}(0)F_1(\mathbf{q}) + \tilde{\Upsilon}_{n,\mathbf{k}}^\alpha(\mathbf{q}) \right\} + \\ & \Upsilon_{n,\mathbf{k}}^{\alpha s2}(0) \sum_{\mathbf{q}}^{\text{BZ}} F_2(\mathbf{q}) + \Upsilon_{n,\mathbf{k}}^{\alpha s1}(0) \sum_{\mathbf{q}}^{\text{BZ}} F_1(\mathbf{q}) \end{aligned} \quad (5.34)$$

For the auxiliary functions we choose:

$$F_1(\mathbf{q}) = \frac{1}{\Omega} \sum_i \frac{e^{-\beta|\mathbf{q}+\mathbf{G}_i|^2}}{|\mathbf{q} + \mathbf{G}_i|} \quad (5.35a)$$

$$F_2(\mathbf{q}) = \frac{1}{\Omega} \sum_i \frac{e^{-\beta|\mathbf{q}+\mathbf{G}_i|^2}}{|\mathbf{q} + \mathbf{G}_i|^2} \quad (5.35b)$$

The periodicity ensures that its gradient is continuous at the zone boundary. β is a parameter chosen so that the width of the Gaussian is comparable to the Brillouin-zone diameter. The mean value of the functions is:

$$\frac{\Omega}{(2\pi)^3} \int_{\text{BZ}} F_1(\mathbf{q}) d\mathbf{q} = \frac{1}{4\pi^2\beta} \quad (5.36a)$$

$$\frac{\Omega}{(2\pi)^3} \int_{\text{BZ}} F_2(\mathbf{q}) d\mathbf{q} = \frac{1}{4\pi^2} \sqrt{\frac{\pi}{\beta}} \quad (5.36b)$$

To obtain the parameter β we require $\beta R_{\text{BZ}} = 1$, using $\frac{4\pi}{3} R_{\text{BZ}}^3 = \frac{(2\pi)^3}{\Omega}$ we get:

$$\beta = \left(\frac{\Omega}{6\pi^2} \right)^{\frac{1}{3}} \quad (5.37)$$

Finally, we can write the self-energy as:

$$\Sigma_{n,\mathbf{k}}^\alpha = \sum_{\mathbf{q} \neq 0}^{\text{BZ}} \left\{ \Upsilon_{n,\mathbf{k}}^\alpha(\mathbf{q}) - \Upsilon_{n,\mathbf{k}}^{\alpha s2}(0)F_2(\mathbf{q}) - \Upsilon_{n,\mathbf{k}}^{\alpha s1}(0)F_1(\mathbf{q}) \right\} + \frac{\Upsilon_{n,\mathbf{k}}^{\alpha s2}(0)}{4\sqrt{\pi^3\beta}} + \frac{\Upsilon_{n,\mathbf{k}}^{\alpha s1}(0)}{4\pi^2\beta} \quad (5.38)$$

The function in curly brackets has no singularities and can be integrated numerically.

5.6 The Frequency Integration

In this section, we discuss the methodology to calculate the frequency convolution for the correlation term of the self-energy (Eq. 5.25). Due to the poles of both the Green's function and W^c , infinitesimally close to the real axis (Fig. 5.8), this integral is difficult to converge numerically, requiring a large number of frequencies.

Several schemes have been proposed to improve the computational efficiency in the evaluation of this convolution. One of the first methods was proposed by Godby, Schlüter, and Sham [107]. Using the idea of the well-known Matsubara summation [6, 108], which analytically continues the integrand into the complex frequency plane and calculates the integral over the real frequency axis from the integral over the imaginary axis plus the sum of the residues corresponding to the poles of the Green's function between the given frequency and the Fermi energy, they have shown that the simple form of the integrand in the imaginary axis allows a precise calculation of the integral with few frequencies only. In a different approach, proposed by Rieger *et al.*[109], the screened Coulomb potential is Fourier transformed to the imaginary time axis. The self energy is then obtained by direct product, according to Eq. 4.31c and transformed back to the imaginary frequency axis. Afterwards it is fitted by an analytic function and continued to the complex plane to obtain its dependence on the real frequency axis.

In our implementation, we calculate the screened Coulomb potential, the Green's function and the self-energy directly on the imaginary frequency axis. Eq. 5.25 in this case becomes:

$$\Sigma_{n,\mathbf{k}}^c(i\omega) = \frac{1}{\pi} \sum_{\mathbf{q}}^{BZ} \sum_{i,j} \sum_{n'} [M_{n,n'}^i(\mathbf{k}, \mathbf{q})]^* \int_0^\infty \frac{(\epsilon_{n',\mathbf{k}-\mathbf{q}} - i\omega) W_{i,j}^c(\mathbf{q}, i\omega')}{(i\omega - \epsilon_{n',\mathbf{k}-\mathbf{q}})^2 + \omega'^2} d\omega' M_{n,n'}^j(\mathbf{k}, \mathbf{q}) \quad (5.39)$$

where we have made use of the inversion symmetry of W^c on the imaginary frequency axis:

$$W_{i,j}^c(\mathbf{q}, i\omega) = W_{i,j}^c(\mathbf{q}, -i\omega), \quad (5.40)$$

The integrand in Eq. 5.39 is singular when $\omega = \omega'$ and $\epsilon_{n',\mathbf{k}-\mathbf{q}} = 0$. Therefore, a direct numerical integration becomes unstable for small eigenvalues. The numerical details, as well as the method to avoid this instability are shown in Appendix H. The extreme efficiency of these scheme can be seen in the numerical tests in the next chapter, Section 6.2.

Each matrix element of the self-energy is fitted with a function of the form:

$$\Sigma_{n,\mathbf{k}}^c(i\omega) = \frac{\sum_{j=0}^m a_{n,\mathbf{k},j}(i\omega)^j}{\sum_{j=0}^{m+1} b_{n,\mathbf{k},j}(i\omega)^j} \quad (5.41)$$

which is then analytically continued onto the real frequency axis.

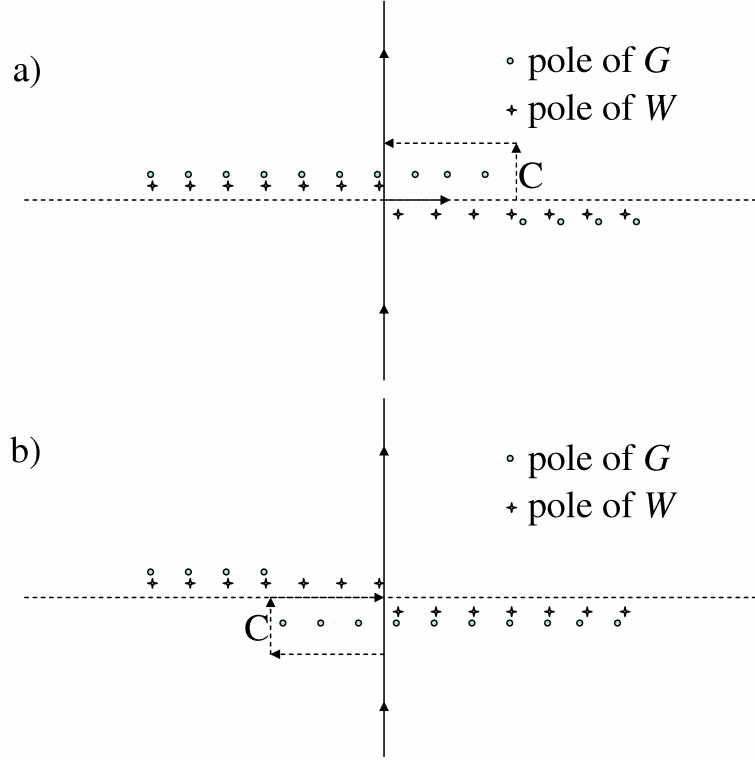
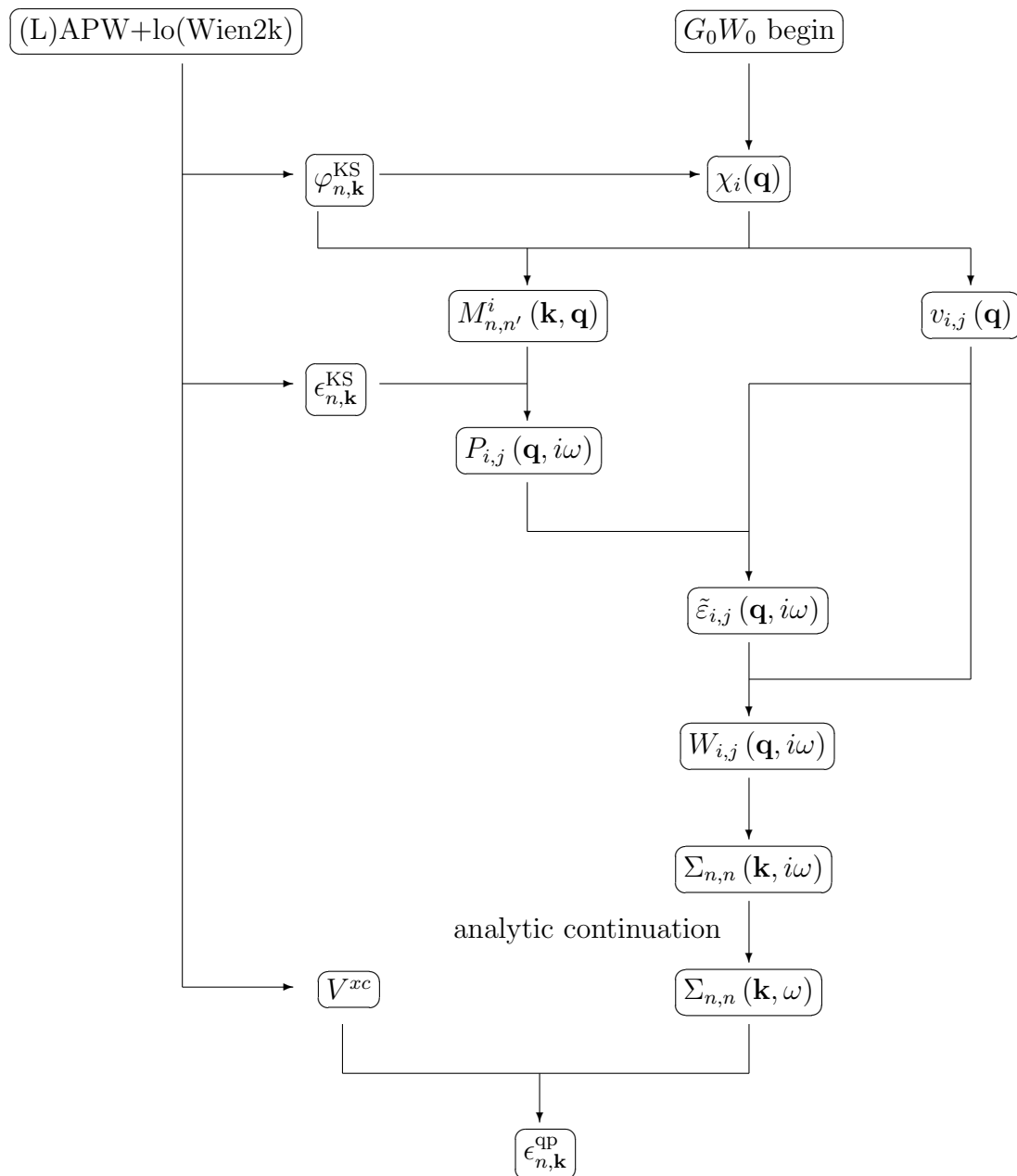


Figure 5.8: The analytic structure of $\Sigma^c = iGW^c$ from $\omega > \mu$ (a) and $\omega < \mu$ (b). Frequency integration of the self-energy along the real axis is equivalent to the integration along the imaginary axis including the path C.

5.7 Flowchart

We conclude this chapter with a short summary of the procedure carried out by our implementation of the G_0W_0 method. The flowchart of code is shown in Fig. 5.9. The Kohn-Sham eigenvalues and eigenfunctions, as well as the exchange-correlation potential are taken from Wien2k. The eigenfunctions are used to obtain the mixed basis as was described in Sec. 5.2. Having defined the basis functions, we can calculate the bare Coulomb matrix according to Appendix C and the matrix elements $M_{n,n'}^i(\mathbf{k}, \mathbf{q})$ following Appendix D. Afterwards, the Kohn-Sham eigenvalues are required for calculating the Brillouin-zone integration weights as described in Sec. 5.4 and Appendix E. Together with the matrix elements, $M_{n,n'}^i(\mathbf{k}, \mathbf{q})$, these weights are used to obtain the polarization matrix (Eq. 5.22). The latter, together with the bare Coulomb matrix, is the input required to obtain the dielectric matrix (numerical details in Appendix F). The screened Coulomb potential is calculated following Appendix G. The matrix elements of the exchange and correlation terms of the self-energy are calculated separately. The coefficients of the expansion described in

Sec. 3.2.4 of the exchange-correlation potential are obtained from the Wien2k code, and used to obtain its diagonal matrix elements for each eigenstate. Finally, a first set of G_0W_0 quasiparticle energies are obtained solving Eq. 5.27, which are used as the starting point for solving Eq. 5.1 selfconsistently.

Figure 5.9: Flowchart of our G_0W_0 code

Chapter 6

Convergence Tests

The advantage of all-electron methods in general, and the FP-(L)APW+lo in particular, is that they rely on no other approximation but the theory which they implement. In other words, they are exact, except for the numerical accuracy. For the evaluation of the self-energy, the latter include:

- i. The completeness of basis functions (Sec. 5.2),
- ii. the density of the \mathbf{k} - and \mathbf{q} -point meshes for the Brillouin-zone integration (Sec. 5.4 and 5.5),
- iii. the number of frequencies (Sec. 5.6 and Appendix H) used to calculate the self-energy, and
- iv. the cutoff for the number of unoccupied states included in the calculation of the correlation term (Ref. [110]) and the linearization error for these states.

The convergence of the results with respect to the choice of these parameters is essential for the reliability of values obtained. In addition, the convergence of the Kohn-Sham results used as input also requires attention, since they could affect the G_0W_0 output.

In this chapter we study systematically the convergence of the G_0W_0 results with respect to the various parameters mentioned. Si is taken as the trunk example, but tests for other materials are also included. In Sec. 6.1 we study the convergence of the results with respect to the parameters defining the basis set. The convergence with respect to the grid for the frequency integration is tested in Sec. 6.2. In Sec. 6.3, we analyze the convergence with respect to the number of \mathbf{k} - and \mathbf{q} -points used for the Brillouin-zone integration. The effect of the number of unoccupied states included in the G_0W_0 calculations is discussed in Sec. 6.4. In the end, an experience based menu on how well-converged G_0W_0 results can be obtained in a new material is given in Sec. 6.5.

6.1 The Basis Set

In Sec. 5.2, we verified the completeness of the mixed basis set in expanding the products of two Kohn-Sham wave functions. In this section, we analyze how the convergence of the G_0W_0 results, in particular the fundamental band-gap and the matrix elements of the exchange and correlation terms of self-energy, are affected by the parameters defining the basis set. The rest of the parameters are fixed at $\omega_0 = 10.88$ eV and $N_\omega = 16$ for the frequency integration, $N_{\mathbf{k}} = N_{\mathbf{q}} = 64$ for the Brillouin-zone integration, the number of excited states is limited by an energy cutoff of 34.0 eV, which corresponds to around 19 excited states. For the (L)APW+lo basis set we take $RK_{\max} = 7.00$. With these parameters, the fundamental band gaps shown in this section can not be converged. However, they still provide insight into the convergence behavior of the G_0W_0 results with respect to these parameters related to the definition of the basis set. As in Sec. 5.2, the tests with respect to the parameters defining the basis set in the muffin-tin and interstitial regions are carried out separately.

In the muffin-tin sphere, the linear dependence tolerance λ_{\min} for each l_{\max} is chosen at its optimum value, *i. e.* at the beginning of the corresponding plateau in Figure 5.3. In Table 6.1 we present the result for the fundamental bandgap and the matrix elements of the self-energy for the valence band maximum at the Γ point (VBM) and the conduction band minimum at the X point (CBM) for different values of l_{\max} . The results clearly show that $l_{\max} = 3$ ($\lambda_{\min} = 10^{-4}$) ensures convergence of both the fundamental band gap and the matrix elements within 1 meV.

Table 6.1: Fundamental G_0W_0 band gap and matrix elements of the self-energy of Si for different basis sets in the muffin-tin spheres. N_{wf}^{MT} represent the total number of basis functions in the muffin-tin region. Since the energy cutoff for the excited states is low, these results are not converged. In all cases $Q = 1.0$ and eV units are used.

l_{\max}	2	3	4
λ_{\min}	10^{-3}	10^{-4}	10^{-5}
N_{wf}^{MT}	148	296	568
E_g	0.8155	0.8113	0.8114
Σ_{VBM}^x	-14.9280	-14.9309	-14.9309
Σ_{CBM}^x	-5.9791	-5.9813	-5.9814
Σ_{VBM}^c	1.7922	1.7920	1.7917
Σ_{CBM}^c	-3.4031	-3.4135	-3.4126

With the value of l_{\max} fixed, we test the convergence of same quantities as a function of the number of interstitial plane waves. The results in Table 6.2 show that taking $Q = 1.0$ already attains a precision of 1 meV. Summarizing, a mixed

basis set defined by the parameters $l_{\max} = 3$, $\lambda_{\min} = 10^{-4}$ and $Q = 1.0$ (433 wave functions, 296 in the muffin-tin spheres and 137 in the interstitial region) ensures that the errors due to basis set incompleteness remain below 2 meV in the G_0W_0 results for Si.

Table 6.2: Fundamental G_0W_0 band gap and matrix elements of the self-energy in Si using different number of interstitial plane waves. Same as Table 6.1, since the energy cutoff for the excited states is low, these results are not converged. In all cases $l_{\max} = 3$ and eV units are used.

Q	0.8	1.0	1.2	1.4
N_{wf}^{Int}	65	137	242	388
E_g	0.8077	0.8113	0.8122	0.8122
Σ_{VBM}^x	-14.9283	-14.9309	-14.9310	-14.9291
Σ_{CBM}^x	-5.9789	-5.9813	-5.9813	-5.9808
Σ_{VBM}^c	1.7954	1.7920	1.7912	1.7909
Σ_{CBM}^c	-3.4134	-3.4135	-3.4130	-3.4128

It is known ([110]) that accurate G_0W_0 calculations require a large number of excited states to be included in the calculation of the correlation term of the self-energy (see Sec. 6.4). This raises a further question of whether a basis set ensuring converged results for a small number of excited states is also reliable when more unoccupied states are included in the G_0W_0 calculations. To this end, in Table 6.3, we compare the matrix elements of the correlation term of the self-energy on the valence band maximum state at the Γ point and conduction band minimum state at the X point together with the fundamental band gaps in Si obtained with different l_{\max} for $\epsilon_{\max} = 142.8$ eV (~ 134 unoccupied bands). The rest of the parameters are kept constant, except for $RK_{\max} = 8.00$ in the Wien2k calculations, since the LAPW-basis has to be able to address a larger number of states. We keep $Q = 1.0$, since it increases the basis proportionally with RK_{\max} . The exchange term of the self-energy is not shown because it is independent of the excited states. Clearly, in the muffin-tin region the same basis set as in Table 6.1 ($l_{\max} = 3$) ensures the convergence for the fundamental band gap and the matrix elements of the correlation term of the self-energy in the same order of magnitude (2 meV for the band gap and 4 meV for the matrix elements respectively).

In Table 6.4 and 6.5, we display the convergence of the bandgap and the matrix elements of the self-energy for the valence band maximum (VBM) and the conduction band minimum (CBM), both at the Γ point with respect to the size of mixed basis set within the muffin-tin sphere and the interstitial regions in GaAs respectively. The behavior is similar to that observed for Si. Using $l_{\max} = 3$, $\lambda_{\min} = 10^{-4}$, and $Q = 1.0$ ensures convergence within 3 meV.

Table 6.3: Fundamental G_0W_0 band gap of Si for different basis sets in the muffin-tin spheres for $\epsilon_{\max} = 142.8$ eV. In all cases $Q = 1.0$ and eV units are used. The corresponding values of λ_{\min} are the same as in Table 6.1. Since the energy cutoff is much bigger than what we have taken in Table 6.1 and 6.2, the fundamental band gaps are bigger than the ones shown there.

l_{\max}	2	3	4
$E_g(\text{eV})$	0.936	0.963	0.965
Σ_{VBM}^c	1.093	1.035	1.031
Σ_{CBM}^c	-4.002	-4.034	-4.036

Table 6.4: Fundamental band gap and the matrix elements of the self-energy and exchange-correlation potential in GaAs using different basis sets in the muffin-tin Region. In all cases $Q = 1.0$ and eV units are used.

l_{\max}	2	3	4
λ_{\min}	10^{-3}	10^{-4}	10^{-5}
N_{wf}	317	489	787
E_g	1.3771	1.3884	1.3888
Σ_{VBM}^x	-17.1233	-17.1313	-17.1313
Σ_{CBM}^x	-11.7849	-11.7884	-11.7884
Σ_{VBM}^c	2.2103	2.2080	2.2078
Σ_{CBM}^c	-3.0233	-3.0187	-3.0185

In both materials the bonding valence bands are of sp character. In Si one would expect that the inclusion of s and p wave functions would suffice for a good description. For GaAs, where $3d$ semicore states are present, inclusion of d orbitals would be necessary. However, in both cases the wave functions of f character have to be included in the generation of the mixed basis to obtain accurate G_0W_0 results. This is a clear indication that, for high precision calculations, physical intuition is insufficient and one has to rely on systematic numerical tests.

6.2 Frequency Integration

The numerical precision of frequency integration, required to obtain the correlation term of the self-energy (Sec. 5.6) is determined by two parameters, ω_0 and N_ω (See Appendix H). Clearly, N_ω is the value that ultimately determines the precision of the procedure. However, the N_ω -dependence of the convergence will be affected by the choice of ω_0 . In this section we test the convergence of the results with respect to both parameters. The basis set is defined according to the values obtained in

Table 6.5: Fundamental band gap and the matrix elements of the self-energy and exchange-correlation potential in GaAs using different number of interstitial plane waves. In all cases $l_{\max} = 3$ and eV units are used.

Q	0.8	1.0	1.2	1.4
N_{wf}^{Int}	65	137	242	388
E_g	1.3883	1.3884	1.3921	1.3903
Σ_{VBM}^x	-17.1232	-17.1313	-17.1329	-17.1303
Σ_{CBM}^x	-11.7787	-11.7884	-11.7860	-11.7869
Σ_{VBM}^c	2.2101	2.2080	2.2076	2.2072
Σ_{CBM}^c	-3.0191	-3.0187	-3.0196	-3.0182

the previous section, *i.e.* $l_{\max} = 3$, $\lambda_{\min} = 10^{-4}$ and $Q = 1.0$. The rest of the parameters, not related to the frequency integration are kept at the same values as before, namely, $N_{\mathbf{k}} = 64$, $\epsilon_{\max} = 34.0$ eV and $RK_{\max} = 7$.

In Fig. 6.1, we show four convergence curves of the $\Gamma - X$ band gap with respect to N_{ω} with different ω_0 . From this figure, we see that convergence is reached very quickly when $\omega_0 = 10.9$ or 13.6 eV, where $N_{\omega} = 16$ already ensures accuracy within 2 meV. In the rest of our calculation, we take always $\omega_0 = 10.9$ eV and $N_{\omega} = 16$ for the frequency integration in Si.

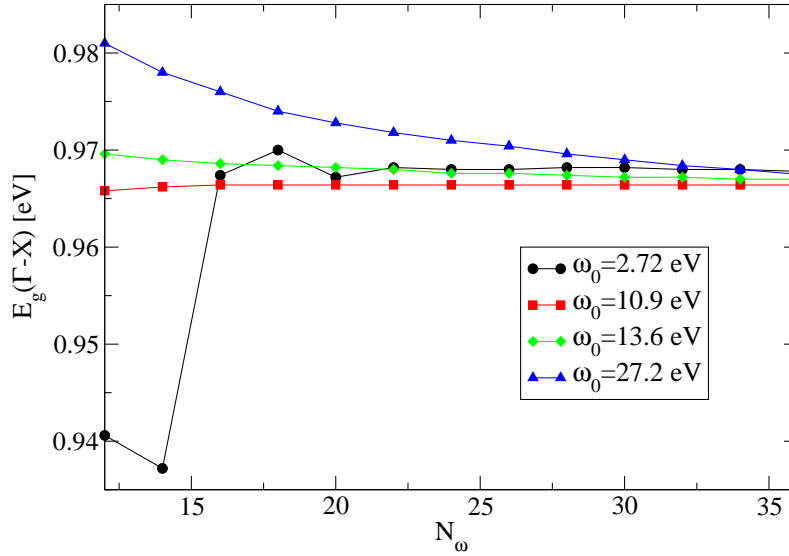


Figure 6.1: Convergence of the $\Gamma - X$ band gap of Si with respect to the number of sample frequency points N_{ω} for different values of ω_0 . It converges by increasing N_{ω} . For $\omega_0 = 10.9, 13.6$ eV, the convergence can be obtained quickly.

In Fig. 6.2, we show the results of a similar test for GaAs (other parameters the

same as what we used in Si). Again, choosing $\omega_0 = 10.9$ or 16.3 eV ensures quicker convergence compared other options. However, choosing $N_\omega = 16$ only ensures the convergence of the band gap within 4 meV. To get it converged within 1 meV, one needs $N_\omega = 30$.

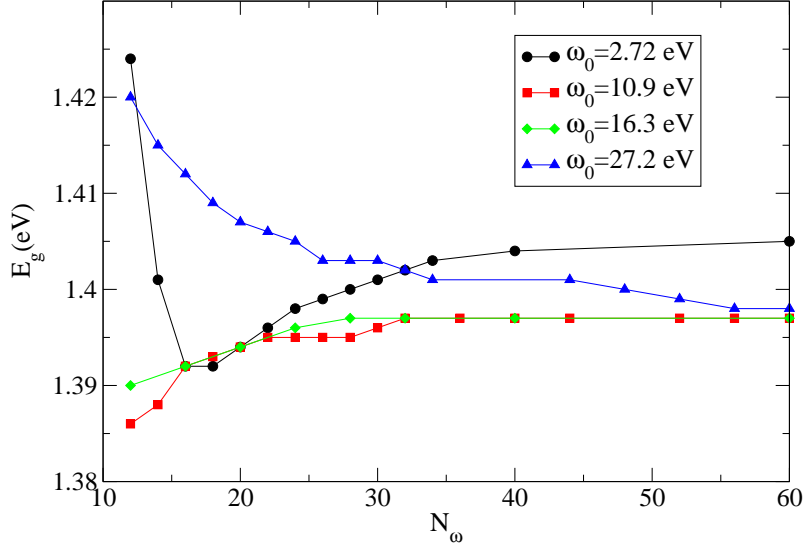


Figure 6.2: Convergence of the fundamental band gap with respect to N_ω using different ω_0 in GaAs. Same as what we found in Si, the convergence is also obtained faster if we choose $\omega_0 = 10.9$.

6.3 Number of \mathbf{k} -points

In this section we test the convergence of the results with respect to the number of \mathbf{k} and \mathbf{q} -points used for the Brillouin-zone integration. Since in our implementation the number of \mathbf{k} and \mathbf{q} -points are always the same, only one parameter, namely $N_{\mathbf{k}}$ has to be tested. The parameters for the mixed basis set and frequency integration are taken from the previous sections. The number of unoccupied states 19 ($\epsilon_{\max} = 34.0$ eV) and $RK_{\max} = 7.00$.

The macroscopic dielectric constant neglecting local field effects (also known as the “head” of the dielectric matrix - Appendix F) converges very slowly with respect to $N_{\mathbf{k}}$. As can be seen in Fig. 6.3, at least a $(12 \times 12 \times 12)$ mesh is required for a convergence within 0.01. Such a dense mesh would make G_0W_0 calculations, which scale quadratically with $N_{\mathbf{k}}$, unacceptably expensive. Thus, the question raises about to what extent the convergence of the head affects the final G_0W_0 results. In addition, the same question raises about the number of \mathbf{k} -points used to

generate the LDA density, and correspondingly, the exchange correlation potential. These considerations lead to four different schemes for the convergence of the G_0W_0 results with respect to the number of \mathbf{k} -points, namely:

- scheme 1: The LDA-density and the “head” of the dielectric matrix are converged with a large number of \mathbf{k} -points. These quantities are used in the G_0W_0 calculation with a coarser mesh, defined by $N_{\mathbf{k}}$.
- scheme 2: The density generated from the LDA calculation is converged with a dense mesh. The “head” is calculated using the same coarse mesh as the G_0W_0 calculation.
- scheme 3: The “head” is converged separately with a dense mesh. The LDA-density is generated with the same mesh as the G_0W_0 calculation.
- scheme 4: The LDA density, the “head” and the G_0W_0 calculation are performed using the same mesh.

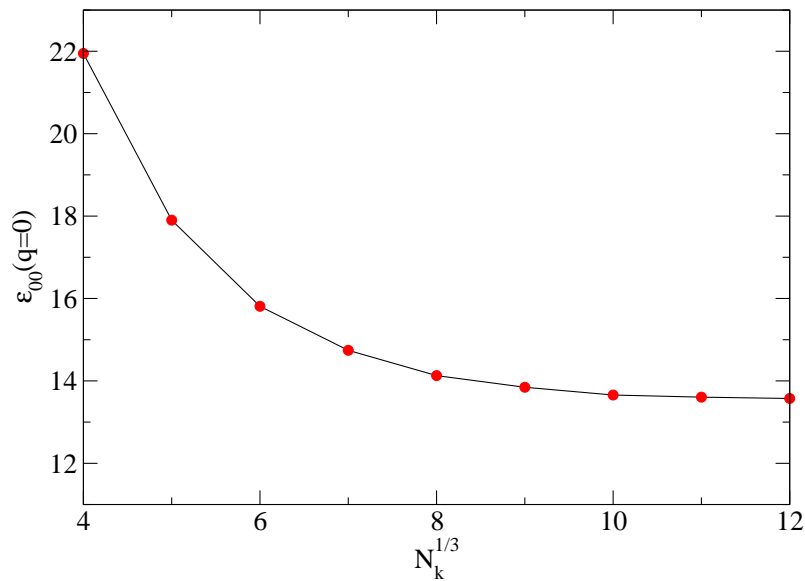


Figure 6.3: Convergence of the macroscopic dielectric constant without local field effects with respect to $N_{\mathbf{k}}$ in Si. To get a convergence within 0.01, one needs a $(12 \times 12 \times 12)$ mesh.

The convergence of the $\Gamma - X$ band gap in Si with respect to the density of \mathbf{k} -points ($N_{\mathbf{k}}^{-1}$) using these four schemes is shown in Fig. 6.4. For a convergence within 0.01 eV, a $(6 \times 6 \times 6)$ mesh is required in all cases. However, comparing scheme 4 with the convergence of the LDA band-gap one observes they behave similarly. In

Fig. 6.5 we show the convergence of G_0W_0 band gap correction with $N_{\mathbf{k}}$, we found that scheme 4 converges already with a $(4 \times 4 \times 4)$ mesh, within 0.01 eV, much faster than any other scheme. This indicates that the slow convergence of the G_0W_0 band gap using this scheme in Fig. 6.4 is due to a low convergence of the LDA band gaps. In Fig. 6.6, we shown similar tests for GaAs. A $(6 \times 6 \times 6)$ mesh is required for a convergence of this band gap correction within 0.01 eV. Again, scheme 4 works best among these four schemes. We deduce that some favorable error cancellations exist when the band gap correction is calculated in this way. Either a special treatment of the Γ -point (separate convergence of the “head”) or of the exchange-correlation potential with respect to the self-energy remove this cancellation, worsening the \mathbf{k} -point convergence.

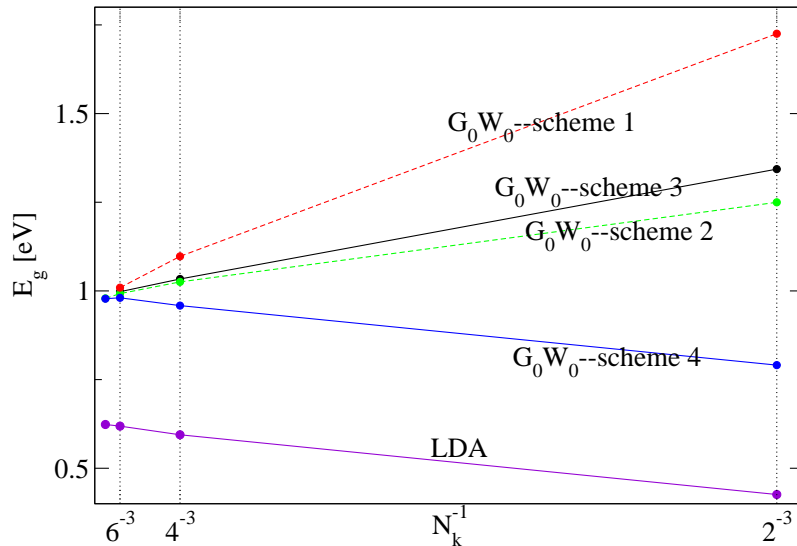


Figure 6.4: Convergence of the $\Gamma - X$ band gap with respect to $N_{\mathbf{k}}^{-1}$ in Si using different schemes. The band gap does not converge with a $(4 \times 4 \times 4)$ mesh. Among these four schemes, using the same mesh for everything gives the best convergence behavior.

Based on this analysis, in the rest of this work, we will use scheme 4 to converge the G_0W_0 band gap corrections with respect to $N_{\mathbf{k}}$. The G_0W_0 band gaps are obtained by adding these corrections to the LDA eigenvalues converged separately.

In the next chapter, we will analyze the reasons for the difference between all-electron and pseudopotential G_0W_0 band gaps by introducing a set of all-electron valence-only calculations (AE-valence), where the self-energy and exchange-correlation potential in Eq. 5.1 are calculated from the all-electron valence wave functions and valence density. The matrix elements obtained from these AE-valence calculations will be compared with those from the all-electron and pseudopotential based G_0W_0

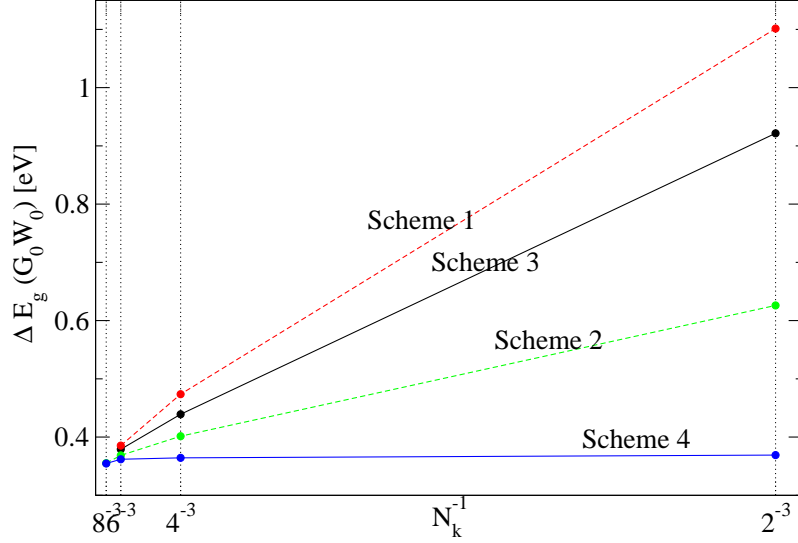


Figure 6.5: Convergence of the G_0W_0 correction to the $\Gamma - X$ band gap with respect to $N_{\mathbf{k}}^{-1}$ in Si using different schemes. The band gap correction obtained using scheme 4 converges within 0.01 eV with a $(4 \times 4 \times 4)$ mesh.

calculations. Thus, we have to analyze the convergence of the matrix elements of the self-energy and xc potential with respect to the number of \mathbf{k} -points. For Si, the convergence of all these quantities for the valence band maximum at Γ point and conduction band minimum at X point are shown in Fig. 6.7 and Fig. 6.8 respectively. It can be observed that the matrix elements of the xc potential are well-converged using a $(4 \times 4 \times 4)$ mesh. However, those of the exchange and correlation terms of the self-energy (Σ^x and Σ^c) are not. The fast convergence of the band gap correction is due to an error cancellation between these two terms. Fortunately, the same behavior can be observed in the pseudopotential based (red lines) and AE-valence G_0W_0 calculations (blue lines). Although the values of the matrix elements are not converged, the relations among them are. The validity of our conclusions are therefore unaffected, as long as they are drawn on the comparison between the matrix elements and not their absolute values. The same behavior is found in GaAs (Figs. 6.9 and 6.10) and the rest of the materials we have calculated.

6.4 Number of Unoccupied States

Finally, we study the convergence of the fundamental band gap with respect to the number of unoccupied states involved in the G_0W_0 calculation, which is also the main criticism against the fundamental band gap of Si obtained by Ku and Eguluz in Ref. [14].

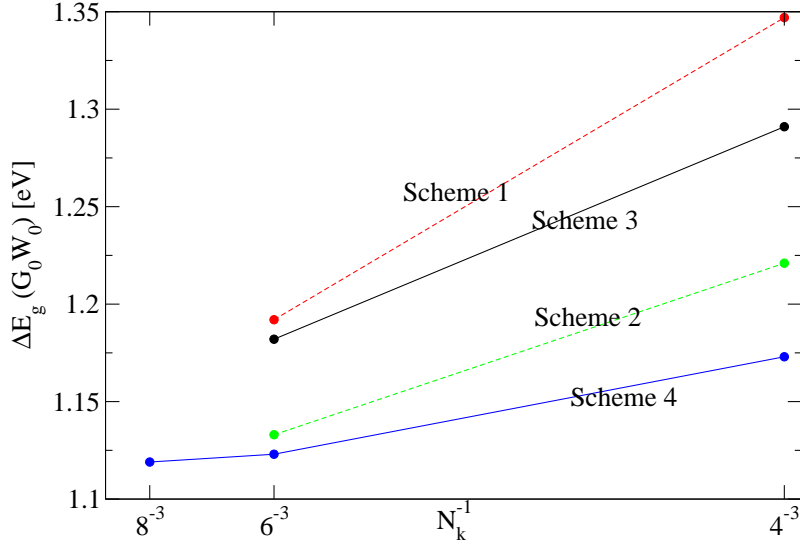


Figure 6.6: Convergence of the G_0W_0 correction to the fundamental band gap with respect to N_k^{-1} in GaAs using different schemes. Same as what we found in Si, using the same mesh for everything gives the best convergence behavior.

In order to enable the LAPW-basis to describe a large number of excited states, we take $RK_{\max} = 9.00$ in the Wien2k calculations. In Fig. 6.11, we show the convergence of the G_0W_0 correction to the fundamental band gap in Si. It converges within 5 meV when ~ 150 bands are used. The result increases monotonically with the number of unoccupied states, the saturated fundamental band gap for Si is 1.00 eV. Summing all the possible sources of errors related to our numerical implementation analyzed above, we estimate a precision of 0.02 eV for this result.

Since our calculation is based on the (L)APW+lo method, the linearization error of the basis set for the highly excited states forms another possible source of error for the final result. There are two schemes to eliminate it, i. e. adding local orbitals for the highly occupied states, and including the non-linear energy dependency of the basis. In Ref. [111], it was shown that including this non-linear energy dependency of the basis functions only increases the fundamental band gap of Si by 0.03 eV, in the same order of magnitude as the precision of our implementation. Since the discrepancy between all-electron and PP- G_0W_0 results is always of the order of 0.1 eV, this error is negligible when it comes to the applications of our code.

In Fig. 6.12, we also show the convergence of the fundamental band gap correction in GaAs. Using ~ 150 bands ensures the convergence of the band gap correction within 0.001 eV. The convergence is faster than in Si.

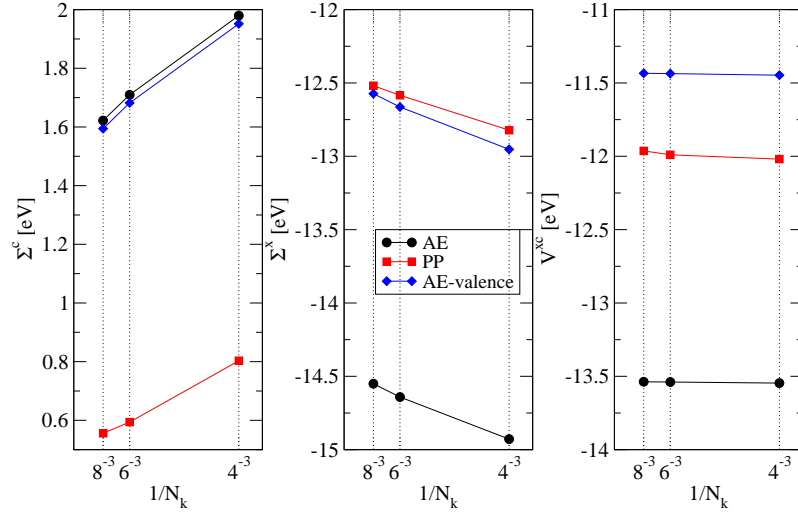


Figure 6.7: Convergence of the self-energy (exchange and correlation terms) and exchange-correlation potential matrix elements of the valence band maximum of Si at the Γ -point with respect to N_k^{-1} . These correlation self-energies, Σ^c , are not converged with respect to the number of unoccupied states included in the G_0W_0 calculations. Thus, absolute values of them are meaningless.

6.5 Experience Based “Menu”

In above sections, we have analyzed the convergence of the fundamental band gaps and matrix elements of the self-energy and exchange-correlation potential with respect to the parameters used in the numerical treatments. These tests are not independent, *e.g.* the convergence with respect to the mixed basis set is influenced by the number of unoccupied states included (Sec. 6.1). Therefore, obtaining well-converged G_0W_0 results requires an overall test on all these aspects. For a new material, one needs to go through the above four sections step by step. To reduce the amount of work required in this process, we provide an experience based menu in this section. The aim is to provide a reasonable range of choice for each parameter, so that the number of tests required for the well-converged G_0W_0 results to be obtained can be reduced.

The first parameters to be fixed are normally those related to the definition of the basis set. Our experience has shown that only including the physically important components in the LDA wave functions, *e.g.* s , p orbitals in Si, is not enough for well-converged G_0W_0 band gaps. One normally needs to include the d , f orbitals when the basis functions in the Muffin-Tin region are constructed. For other semiconductors including the s , p , and d orbitals, *e.g.* NaCl, LiF, and GaAs (d states are semicore states) etc., the situation is similar. For systems with f electrons, further

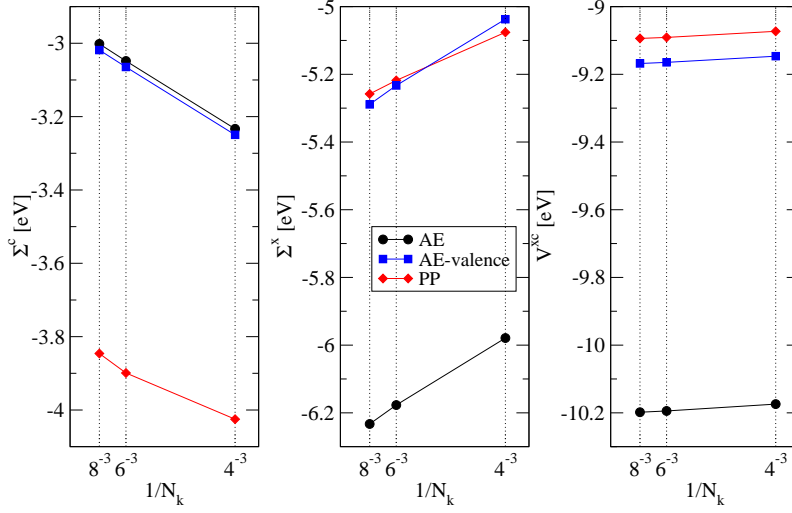


Figure 6.8: Convergence of the self-energy (exchange and correlation terms) and exchange-correlation potential matrix elements of the conduction band minimum of Si at the X -point with respect to $N_{\mathbf{k}}^{-1}$.

tests are still required. For the mixed basis in the interstitial region, taking $Q = 1.0$ is usually enough. To make sure that the basis set is complete for the converged G_0W_0 calculations to be performed, one also needs to test this convergence with a high energy cut-off in the end.

The convergence of the G_0W_0 results with respect to the grid for the frequency integration has to be tested. According to our experience, taking $\omega_0 \sim 10\text{eV} \pm 4\text{eV}$ normally gives fast convergence, 14 is the minimum value for the number of sample points. For all the materials we have calculated, we never need more than 36 points.

The convergence with respect to the number of \mathbf{k} - and \mathbf{q} -points is dependent on the shape of the band diagram. As mentioned in Sec. 6.3, taking the same mesh for the LDA and G_0W_0 (scheme 4 in Sec. 6.3, the “head” is also calculated using this mesh) calculations ensures faster convergence. For most of the semiconductors we have studied, taking a $(4 \times 4 \times 4)$ mesh ensures convergence within 0.01 eV for the fundamental band gaps except in diamond and GaAs. In diamond, the conduction band minimum is not on the sample points if the $(4 \times 4 \times 4)$ mesh is used. And the energy difference between the lowest unoccupied states on the sample points and the true conduction band minimum state (which lies at 66.7% of the distance between Γ and X) is as large as 0.4 eV. When the $(6 \times 6 \times 6)$ mesh is taken, the conduction band minimum state is just on the sample point. In GaAs, the conduction band minimum state is at the bottom of a sharp valley, therefore a denser mesh is required for this convergence to be reached.

The last parameter to be fixed is normally the number of occupied states in-

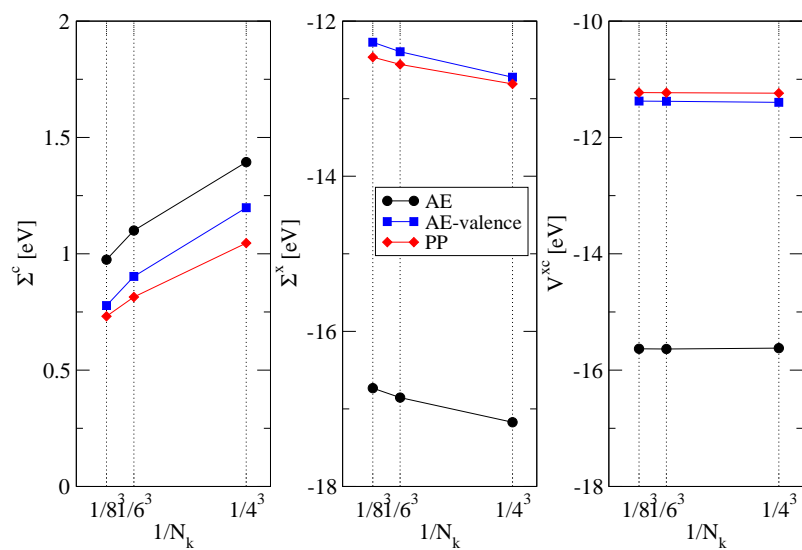


Figure 6.9: Convergence of the self-energy (exchange and correlation terms) and exchange-correlation potential matrix elements of the valence band maximum of GaAs at the Γ -point with respect to $N_{\mathbf{k}}^{-1}$.

cluded. For all the materials we have studied, we need 90 to 250 unoccupied states for this convergence to be reached.

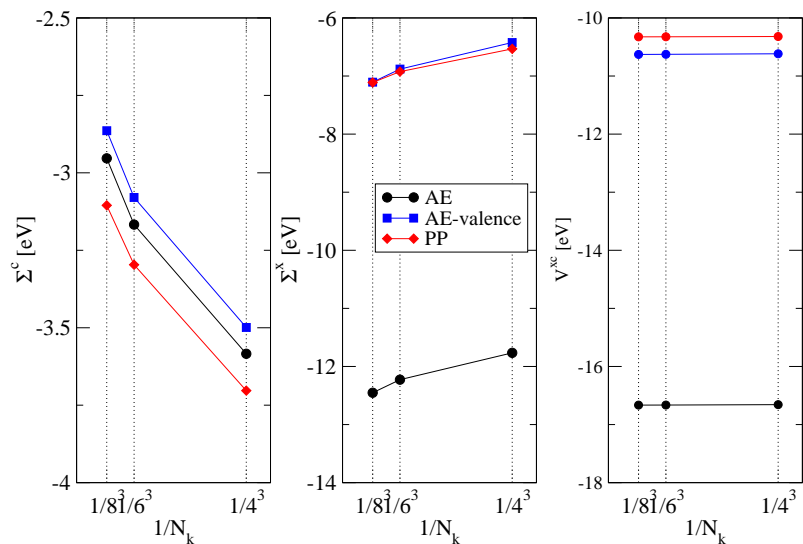


Figure 6.10: Convergence of the self-energy (exchange and correlation terms) and exchange-correlation potential matrix elements of the conduction band minimum of GaAs at the Γ -point with respect to $N_{\mathbf{k}}^{-1}$.

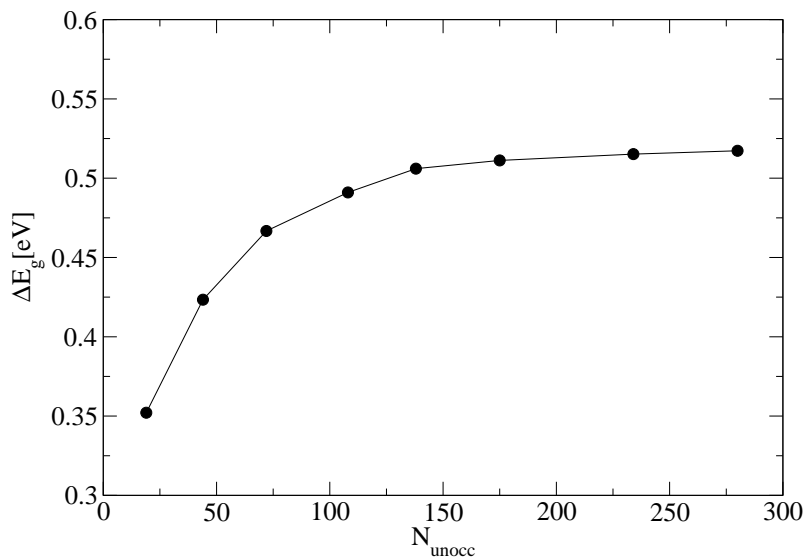


Figure 6.11: Convergence of the G_0W_0 correction to the fundamental band gap of Si with respect to N_{unocc} .

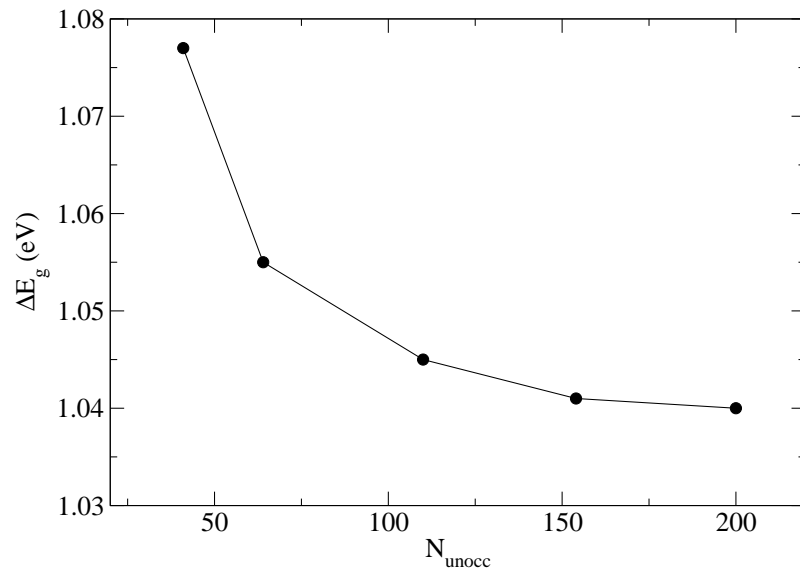


Figure 6.12: Convergence of the G_0W_0 correction to the fundamental band gap of GaAs with respect to N_{unocc} .

Part IV

Results and Conclusions

Chapter 7

Analysis of the Difference between All-electron and Pseudopotential based G_0W_0 Band Gaps

In chapter 5, we introduced a new all-electron G_0W_0 code based on the FP-(L)APW+lo method. Its reliability and precision were demonstrated through an extensive set of tests in chapter 6. In this chapter we will apply it to analyze the difference between all-electron (AE) and pseudopotential (PP) based G_0W_0 band gaps.

As mentioned in Chapter 1, for already more than two decades, the G_0W_0 approach implemented within the pseudopotential method has achieved an impressive success in reproducing the fundamental band gaps and bandstructures of weakly correlated semiconductors and insulators [2, 88]. A few years ago the first all-electron G_0W_0 implementations appeared. The results obtained showed noticeable discrepancies with the PP- G_0W_0 ones (Table 7.1). Usually, the all-electron band-gaps were smaller, and in worse agreement with experiments.

Taking Si as the guiding example, PP- G_0W_0 calculations obtain values between 1.18eV and 1.29 eV for its fundamental band gap [12, 112, 113, 114]. This is within 0.12 eV accuracy compared with the experimental value of 1.17 eV. On the other hand, first all-electron G_0W_0 calculations obtained 0.85 eV [14] and 0.90 eV [13]. These results triggered a debate about the reliability of both pseudopotential and all-electron based G_0W_0 results [15, 16]. In Ref. [14], this discrepancy was assigned mainly to the exclusion of the core electrons in the calculation of the self-energy, the possible role of pseudoization was only tangentially mentioned. On the other hand, the main criticism to the value of 0.85 eV in Ref. [14], put forward in Ref. [15], was the lack of convergence with respect to the number of unoccupied states included in the calculation¹. The validity of this criticism has been confirmed by the all-electron

¹Related to other arguments put forward in this discussion, namely the cancellation of errors

G_0W_0 result from Friedrich *et al.* [111], who obtained, after careful convergence with respect to the number of unoccupied states, a fundamental band-gap in Si of 1.05 eV. Our own results, shown below, also confirm this trend. The value of 0.90 eV in Ref. [13], based on the LMTO method, has been further increased to 0.95 eV in Ref. [115] after including local orbitals. However, a discrepancy of around 0.2 eV with the PP- G_0W_0 results still remains. In 2004, Tiago, Ismail-Beigi, and Louie [110] performed a set of pseudopotential calculations for Si in which only the $1s$ orbitals are treated as core, obtaining a fundamental band gap of 1.04 eV for Si. Although the precision of these results can be questioned due to the application of the plasmon-pole approximation, they were interpreted by the authors as a corroboration of the validity of the pseudopotential based G_0W_0 calculation. In the light of the recent all-electron results, it confirms, in fact, the important role of the core states for a correct calculation of the self-energy.

Once the convergence issue has been settled, these discrepancies can be traced back to the approximations underlying the PP- G_0W_0 method. We have discussed them within the Kohn-Sham scheme in section 3.1.2. When G_0W_0 approximation is applied, the correction to the Kohn-Sham energy eigenvalues is calculated from the pseudo-valence wave functions only, thus one has

$$\Delta\epsilon_{n,\mathbf{k}}^{pp} = \Re \left(\langle \tilde{\varphi}_{n,\mathbf{k}} | \Sigma \left(\{ \tilde{\varphi}_{n,\mathbf{k}} \}, \epsilon_{n,\mathbf{k}}^{\text{qp}} \right) | \tilde{\varphi}_{n,\mathbf{k}} \rangle \right) - \langle \tilde{\varphi}_{n,\mathbf{k}} | V^{\text{xc}}[\tilde{n}_{\text{val}}] | \tilde{\varphi}_{n,\mathbf{k}} \rangle, \quad (7.1)$$

where the tilded symbols indicate pseudo wave functions and density. This implies not only a core-valence linearization of the self-energy but also replacing the core contributions to the self-energy by the core-valence xc potential included in the pseudopotential, which is kept at the Kohn-Sham level. To correct for this “core-valence partitioning”, Shirley and Martin extended the PP- GW formalism to include core contributions to the self-energy through the incorporation of core polarization potentials (CPP) [117] into the GW method [12]. A deviation from the traditional PP- G_0W_0 results towards the recent all-electron values can be observed for Si, Ge, and GaAs.

On the other hand, in an all-electron G_0W_0 calculation, the correction to the Kohn-Sham energy eigenvalue is calculated from:

$$\Delta\epsilon_{n,\mathbf{k}} = \Re \left(\langle \varphi_{n,\mathbf{k}} | \Sigma \left(\{ \varphi_{n,\mathbf{k}}, \varphi_{\text{core}} \}, \epsilon_{n,\mathbf{k}}^{\text{qp}} \right) | \varphi_{n,\mathbf{k}} \rangle \right) - \langle \varphi_{n,\mathbf{k}} | V^{\text{xc}}[n] | \varphi_{n,\mathbf{k}} \rangle. \quad (7.2)$$

The difference between Eq. 7.1 and Eq. 7.2 can be separated into two contributions: Core-valence partitioning, namely, the omission of the core wave functions (density) in the calculation of the self-energy (xc potential), and *pseudoization*, meaning the use of the pseudo wave functions and pseudo density in the calculation. While the

between lack of self-consistency and absence of vertex correction, we consider them pertinent to support the G_0W_0 approach itself, but irrelevant to an explanation of the differences between all-electron and pseudopotential based calculations

Table 7.1: Comparison of band gaps from formerly reported all-electron and pseudopotential based G_0W_0 calculations.

	Expt	all-electron- $G_0W_0^a$	traditional PP- G_0W_0
C	5.50	5.49	5.54 ^c
Si	1.17	0.90, 0.85 ^b	1.18 ^c , 1.19 ^d , 1.24 ^e , 1.42 ^f ,
AlAs($\Gamma - X$)	2.23	1.68	2.08 ^f
AlAs($\Gamma - \Gamma$)	3.13	2.69	2.75 ^f
AlP	2.50	2.15	2.59 ^g
AlSb	1.69	1.32	1.64 ^g
Ge($\Gamma - L$)	0.74	0.47, 0.51 ^a	0.75 ^f
Ge($\Gamma - \Gamma$)	0.89	0.79, 1.11 ^a	0.71 ^f
GaAs	1.63	1.42	1.29 ^f
GaP($\Gamma - X$)	2.35	1.90	2.55 ^h
GaP($\Gamma - \Gamma$)	2.86	2.53	2.93 ^h
GaSb	0.82	0.49	0.62 ^g
InP	1.42	1.25	1.44 ^g
InAs	0.42	0.32	0.40 ^g
InSb	0.24	0.32	0.18 ^g
ZnS	3.80	3.22	3.98 ⁱ
ZnSe	2.80	2.21	2.84 ⁱ
CdTe	1.61	1.07	1.76 ⁱ

^a Ref. [13], ^b Ref. [14], ^c Ref. [113], ^d Ref. [112], ^e Ref. [114], ^f Ref. [12],
^g Ref. [11], ^h Ref. [116], ⁱ Ref. [96].

former effect on GaAs and Si has been reported in Ref. [13, 115], which explains part of the discrepancy between the all-electron and PP- G_0W_0 results, the latter has never been studied. In this chapter, we analyze in detail the discrepancy between AE and PP- G_0W_0 band gaps by separating the effects of *pseudoization* from those of core-valence partitioning.

7.1 Disentanglement of Core-Valence Partitioning and Pseudoization

In order to separate the two effects, one should compare both methods with a third calculation in which only one of the approximations is done. To this end we have carried out a series of calculations in which the G_0W_0 correction, *i. e.* self-energy and the xc potential matrix elements, is obtained only from the all-electron valence

wave functions and valence density (in the following referred to as “AE-Valence” calculations). That is:

$$\Delta\epsilon_{n,\mathbf{k}}^{val} = \Re(\langle\varphi_{n,\mathbf{k}}|\Sigma(\{\varphi_{n,\mathbf{k}}\}, \epsilon_{n,\mathbf{k}}^{\text{qp}})|\varphi_{n,\mathbf{k}}\rangle) - \langle\varphi_{n,\mathbf{k}}|V^{\text{xc}}[n_{\text{val}}]|\varphi_{n,\mathbf{k}}\rangle, \quad (7.3)$$

In this way, the interaction between the valence electrons is corrected to the G_0W_0 level, while the core electrons’ contribution to the self-energy still stays at the Kohn-Sham level, which is implicitly included in the Kohn-Sham eigenvalues. The differences between the corrections defined by Eq. 7.3 and Eq. 7.2 can therefore be assigned exclusively to core-valence partitioning errors, while the discrepancies between Eq. 7.1 and Eq. 7.3 are caused by the *pseudoization*.

We take diamond, Si, BN, AlP, GaAs, LiF, NaCl, and CaSe as example materials for our analysis. Experimental lattice constants (Table 7.2) and the local-density approximation are used throughout this chapter in order to compare with other G_0W_0 results.

Table 7.2: Numerical parameters used for the AE- G_0W_0 calculations. In all cases the parameters defining the mixed basis are $l_{\text{max}} = 3$, $\lambda_{\text{min}} = 10^{-4}$, and $Q = 1.0$; and $\omega_0 = 0.40$ Hartree.

	C	Si	BN	AlP	LiF	NaCl	GaAs	CaSe
a [Å]	3.57	5.43	3.62	5.45	4.02	5.63	5.66	5.91
$N_{\mathbf{k}}$	216	64	64	64	64	64	216	64
$\sim N_{\text{unocc}}$	90	200	120	150	150	250	150	200
N_{ω}	16	16	16	16	16	16	30	16

For the PP- G_0W_0 calculations, we use the SFHingX package for the PP-KS calculations [118] and the GWST [109, 119] code for the G_0W_0 correction. The norm-conserving pseudopotentials (Chapter 3) are generated using fhi98PP [120]. Only the outermost shell of each atom is included explicitly in the calculation. Except in GaAs and NaCl, the Troullier-Martin scheme is used to generate the pseudopotentials. In GaAs we use the Hamann scheme to avoid the ghost states of the p channel that appear when using Troullier-Martin pseudopotentials. In NaCl, in order to get an optimum tuning of scattering and transferability behavior, we use a mixed scheme, where different pseudopotentials are used for different l -channels.

The numerical parameters used for the AE (and AE-Valence) G_0W_0 calculations, were summarized in Table 7.2 (how they were chosen refer to Sec. 6.5). Based on our tests, as shown in Chapter 6, we estimate these parameters to ensure a precision of 0.02 eV in all cases. For the AE-Valence calculation we take the same valence configuration as in the corresponding pseudopotential calculation.

In Table 7.3, we compare our all-electron and PP- G_0W_0 band gaps with theoretical and experimental results from the literature. Our all-electron band gaps agree with those of Kotani and van Schilfgaarde [13] and Friedrich *et al.* [111] within 0.05 eV. In all cases the value is underestimated compared to experiments. Comparing our PP- G_0W_0 results with those from the literature, we obtain an agreement within 0.1 eV for diamond, Si, BN, and AlP. For GaAs, the results in the literature scatter between 1.02 eV and 1.58 eV. The lower limit compares well to our result. For NaCl, our band gap is ~ 0.7 eV smaller than the one reported in Ref. [121]. This is because they use the LDA lattice constant, which significantly increases the band gap. For LiF, the core-polarization potential and a partial self-consistency by updating the energy eigenvalues are used in Ref. [122], explaining the discrepancy of ~ 0.7 eV.

Table 7.3: The band gaps [in eV] in comparison with other calculations and experiments

	C	Si	BN	AlP	LiF	NaCl	GaAs	CaSe
This work								
AE-LDA	4.10	0.49	4.35	1.44	8.97	4.74	0.25	1.86
AE- G_0W_0	5.42	1.00	6.03	2.18	13.19	7.60	1.29	3.36
PP-LDA	4.15	0.50	4.39	1.47	8.79	4.70	0.35	1.84
PP- G_0W_0	5.68	1.25	6.35	2.50	13.56	7.89	0.97	3.30
Literature								
AE- G_0W_0	5.48 ^a	1.05 ^b		2.15 ^c			1.31 ^c	
PP- G_0W_0	5.60 ^d	1.18 ^e	6.30 ^f	2.59 ^g	14.3 ^h	8.64 ⁱ	1.02 ^j , 1.58 ^k	
Expt.	5.48 ^l	1.17 ^l	6.10 ^m	2.50 ^l	14.2 ⁿ	8.50 ^o	1.63 ^p	
^a Ref. [123]		^b Ref. [111]		^c Ref. [13]			^d Ref. [10]	
^e Ref. [113]		^f Ref. [124]		^g Ref. [11]			^h Ref. [125]	
ⁱ Ref. [121]		^j Ref. [12]		^k Ref. [107]			^l Ref. [126]	
^m Ref. [127]		ⁿ Ref. [122]		^o Ref. [128]			^p Ref. [129]	

In Fig. 7.1 we show the core-valence partitioning error ($\Delta\epsilon_{n,\mathbf{k}}^{val} - \Delta\epsilon_{n,\mathbf{k}}$) and the *pseudoization* error ($\Delta\epsilon_{n,\mathbf{k}}^{pp} - \Delta\epsilon_{n,\mathbf{k}}^{val}$) for the band gap correction of the mentioned set of materials. It can be observed that the *pseudoization* effect is an important source of error. In addition, in NaCl, GaAs, and CaSe, core-valence partitioning reduces the G_0W_0 correction. The common characteristic of these materials, that differentiates them from the rest, is the presence of semicore states. Accordingly, we will analyze the materials with and without semicore states separately.

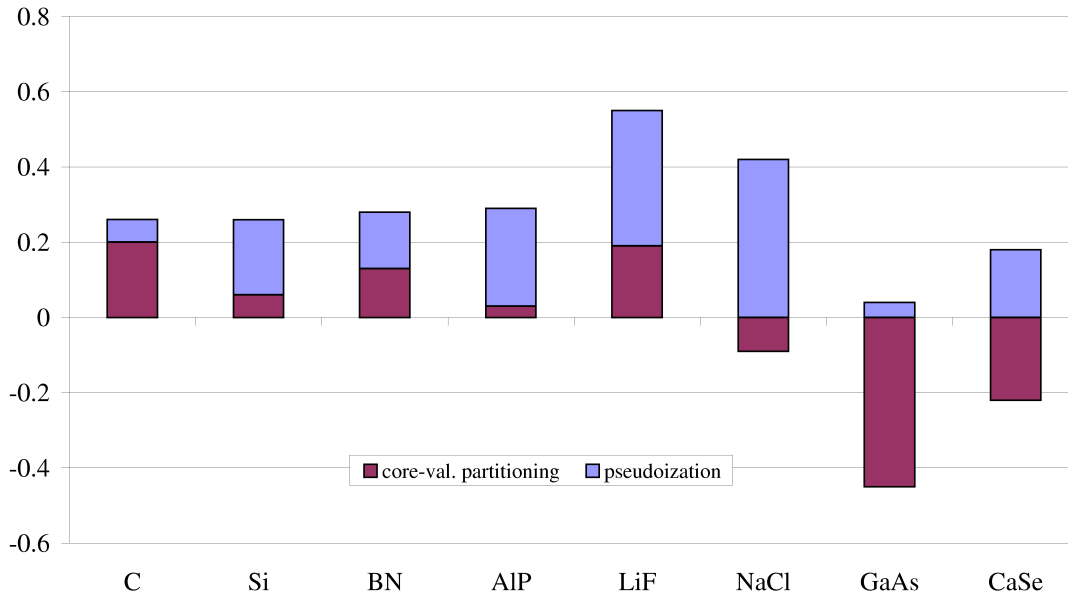


Figure 7.1: *Pseudoization* (blue) and core-valence partitioning (magenta) errors in the G_0W_0 correction to the fundamental band gap (in eV).

7.2 Materials without Semicore States

This category includes diamond, Si, BN, AlP, and LiF. Their common feature is a clear splitting of the core and valence states. The former lie low in energy and the corresponding wave functions are confined within the atomic region. Accordingly, the pseudopotential method gives reliable results within density-functional theory. We start our discussion with Si, which has been historically taken as the test case in the debate about the discrepancies between all-electron and pseudopotential G_0W_0 calculations [14, 15, 16].

The fundamental band gap of Si is indirect, with the bottom of the conduction band lying at 85% of the distance between Γ and X . In Fig. 7.2, we show its band diagram obtained by the AE- G_0W_0 method and compare it with the corresponding LDA values. The blue circles are taken from the k -resolved inverse photoemission spectra (KRIPES) measured by Straub, Ley, and Himpsel in Ref. [130]. The G_0W_0 correction clearly improves the agreement with the experimental results. However, the all-electron G_0W_0 method still underestimates systematically the conduction band positions, which is consistent with the results for the fundamental band gaps.

Taking into account the separation of the self-energy in its exchange and correlation terms according to Eq. 5.25 and 5.26, the G_0W_0 correction to the Kohn-Sham

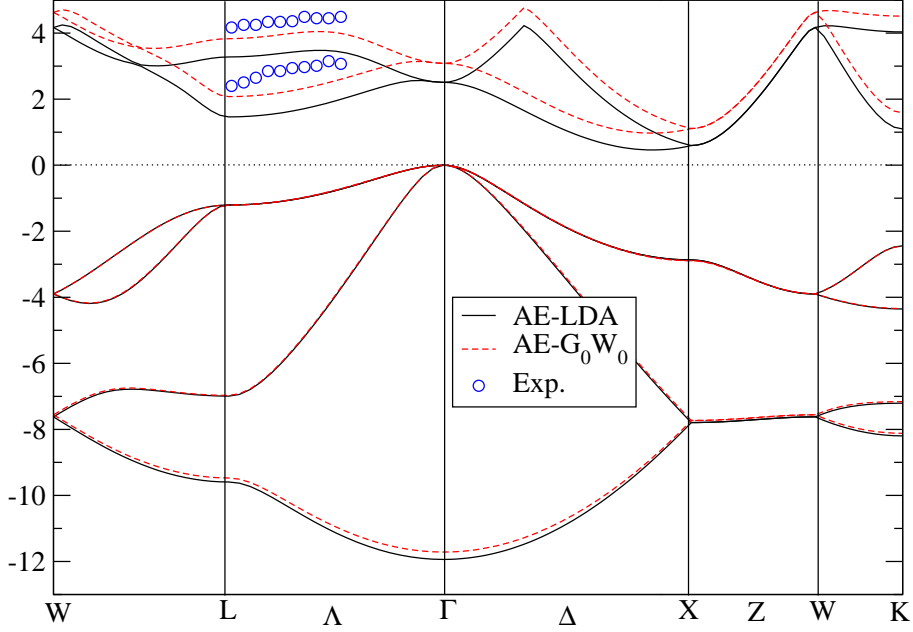


Figure 7.2: Band diagram of Si (in eV, referenced to the Fermi level) obtained from the all-electron LDA (black solid) and G_0W_0 (red dash) calculations. The experimental results (blue circles) are taken from Ref. [130].

eigenvalues (Eq. 7.1, 7.2, and 7.3) can be written as:

$$\Delta\epsilon_{n,\mathbf{k}} = \Sigma_{n,\mathbf{k}}^c + \Sigma_{n,\mathbf{k}}^x - V_{n\mathbf{k}}^{\text{xc}} \quad (7.4)$$

where we have defined $V_{n,\mathbf{k}}^{\text{xc}} = \langle \varphi_{n,\mathbf{k}} | V^{\text{xc}}[n] | \varphi_{n,\mathbf{k}} \rangle$. This matrix element of the exchange-correlation potential can be further separated into the pure exchange term, calculated from $V_{n,\mathbf{k}}^x = \langle \varphi_{n,\mathbf{k}} | V^x[n] | \varphi_{n,\mathbf{k}} \rangle$, and the correlation term, using $V_{n,\mathbf{k}}^c = V_{n,\mathbf{k}}^{\text{xc}} - V_{n,\mathbf{k}}^x$, in the AE-Valence- and AE- G_0W_0 calculations.

In Fig. 7.3 we show these matrix elements for the valence band maximum state at the Γ -point (denoted as Γ_v) obtained by the three different schemes. The corresponding source data, as well as those for the conduction band minimum state at the X -point (denoted as X_c) and the difference between them are taken from Table 7.4. To analyze the effect of core valence partitioning on this valence band maximum state we compare the AE-Valence- and AE- G_0W_0 values. The main features are:

- i. Core-valence partitioning has a negligible influence (~ 0.02 eV) on the correlation term of self-energy (Σ^c). The core electrons of Si, low in energy and tightly bound to the nucleus, don't contribute to the screening of the valence states.

- ii. It has a very strong effect, in the order of eV, in the xc potential (V^{xc}) and the exchange term of the self-energy (Σ^x).
- iii. From table 7.4, we see that this strong effect on V^{xc} is dominated by the contribution from V^x . The core-valence partitioning effect on the matrix elements of the correlation potential V^c is negligible.
- iv. When calculating the G_0W_0 correction, the errors on V^{xc} (1.97 eV) and Σ^x (2.10 eV) tend to cancel each other.

These features lead to an overall error in the G_0W_0 correction generated by core-valence partitioning in the order of 0.1 eV. Comparison between the pseudopotential and AE-valence matrix elements reveal the influence of *pseudoization*. In all cases, *i. e.* Σ^c , Σ^x and V^{xc} , it is in the order of 0.1 eV.

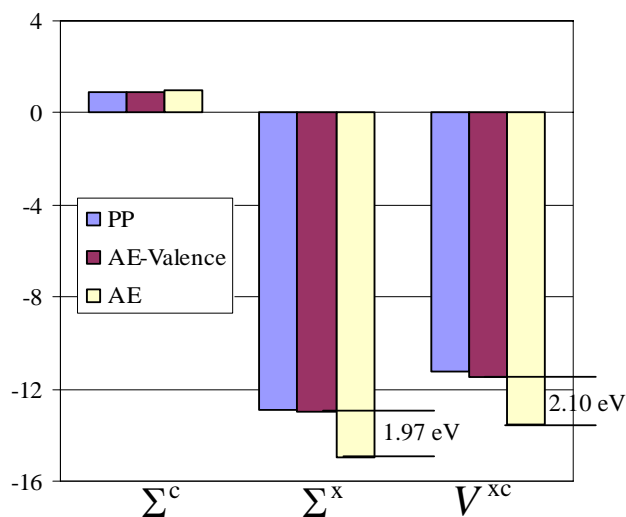


Figure 7.3: Matrix elements of the self-energy [in eV] (correlation term: Σ^c , exchange term: Σ^x) and exchange-correlation potential V^{xc} for the valence band maximum state at Γ point (Γ_v) in Si in our all-electron, AE-Valence, and PP- G_0W_0 calculations.

Summarizing, the main, and large, differences between all-electron and pseudopotential G_0W_0 calculations appear in the Σ^x and V^{xc} matrix elements, and are due to core-valence partitioning. These differences, however, tend to cancel each other. For Σ^c , the main, and in this case small, differences are due to the effect of *pseudoization*. The same conclusions can be drawn for the matrix elements on the conduction band minimum at X point, shown in Fig. 7.4 and Table 7.4.

Table 7.4: Matrix elements of the self-energy [in eV] (correlation term: Σ^c , exchange term: Σ^x) and exchange-correlation potential V^{xc} (correlation potential: V^c , exchange potential: V^x) for Si in our all-electron, AE-Valence, and PP- G_0W_0 calculations.

	ϵ_{LDA}	Σ^c	Σ^x	V^c	V^x	V^{xc}	$\Sigma^x - V^{xc}$	$\epsilon_{G_0W_0}$
All-electron G_0W_0 :								
Γ_v	0.00	0.96	-14.93	-1.57	-11.98	-13.55	-1.38	0.00
X_c	0.62	-4.09	-5.98	-1.36	-8.82	-10.18	4.20	1.15
$X_c - \Gamma_v(\Delta)$	0.62	-5.05	8.95	0.21	3.16	3.37	5.58	1.15
AE-Valence G_0W_0 ($3s, 3p$):								
Γ_v	0.00	0.94	-12.96	-1.52	-9.93	-11.45	-1.51	0.00
X_c	0.62	-4.09	-5.04	-1.33	-7.82	-9.15	4.11	1.21
$X_c - \Gamma_v(\Delta)$	0.62	-5.03	7.92	0.19	2.11	2.30	5.62	1.21
PP- G_0W_0 ($3s, 3p$):								
Γ_v	0.00	0.90	-12.92			-11.26	-1.64	0.00
X_c	0.63	-3.96	-5.14			-9.09	3.96	1.38
$X_c - \Gamma_v(\Delta)$	0.63	-4.86	7.78			2.17	5.60	1.38

The G_0W_0 correction to the band gap can be calculated directly taking the difference between the correction to the energies of the valence band maximum and the conduction band minimum states. Accordingly, the contribution from each term (Σ^c , Σ^x and V^{xc}) can be obtained as the difference between the corresponding matrix elements. In Fig. 7.5 (also in Table 7.4), we show these contributions to the $\Gamma - X$ gap of silicon ($\Delta F = F(X_c) - F(\Gamma_v)$ where $F = \Sigma^c, \Sigma^x, V^{xc}$) for the three types of calculations. The situation is the same as found for the matrix elements themselves: core-valence partitioning effects are very large on the contribution of the exchange term of the self-energy and the exchange-correlation potential to the gap, and negligible on the contribution of the correlation term. The former two effects cancel each other, reducing the error by almost two orders of magnitude (~ 0.04 eV). The influence of *pseudoization* is in the order of 0.1 eV for the three terms. The corresponding changes in $\Delta\Sigma^x$ and ΔV^{xc} almost cancel each other. With the left differences on $\Delta\Sigma^c$ (0.17 eV) accounting for the band gap opening in the PP- G_0W_0 calculations. In Fig. 7.6, the effects of core-valence partitioning and *pseudoization* on the band gap correction are separated. As we have shown in Fig. 7.1 for the fundamental band gap, *pseudoization* gives the main contribution to the discrepancy between all-electron and PP- G_0W_0 results.

All the materials without semicore states studied here present a situation similar to that found for Si. To avoid repeating ourselves, we just summarize the results obtained for the matrix elements and the different contributions to the gaps in Tables

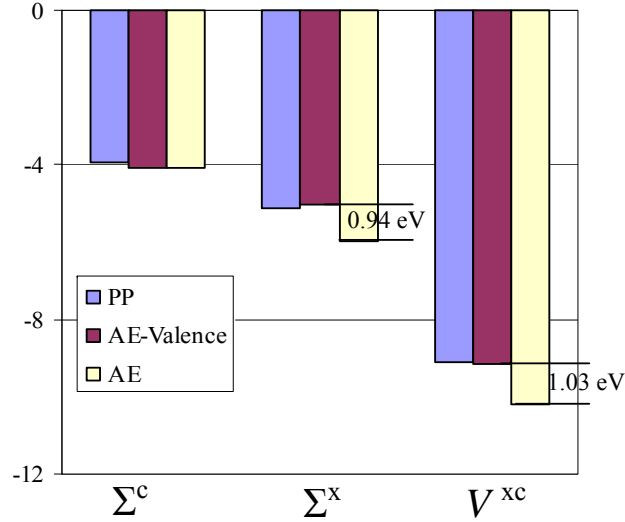


Figure 7.4: Matrix elements of the self-energy [in eV] (correlation term: Σ^c , exchange term: Σ^x) and exchange-correlation potential V^{xc} for the conduction band minimum state at X point (X_c) in Si in our all-electron, AE-Valence, and PP- G_0W_0 calculations.

7.5, 7.6, 7.7, and 7.8. As general trends we can state:

- i. The effect of core-valence partitioning on the correlation term of the self-energy, and its contribution to the gap are in the order of 0.01 eV and therefore negligible.
- ii. The largest errors appear in the exchange term of the self-energy Σ^x , the exchange-correlation potential V^{xc} (dominated by the contribution from V^x) and the corresponding contributions to the band gap. They are in the order of 1 eV and due to core valence partitioning.
- iii. These errors cancel each other. The differences in the contribution to the gap of the difference between the exchange term of the self-energy and the exchange-correlation potential are reduced to values between 0.00 eV in AlP and 0.24 in diamond.
- iv. Core-valence partitioning increases the band gap correction, but not enough to explain solely the discrepancies between all-electron and pseudopotential G_0W_0 results.

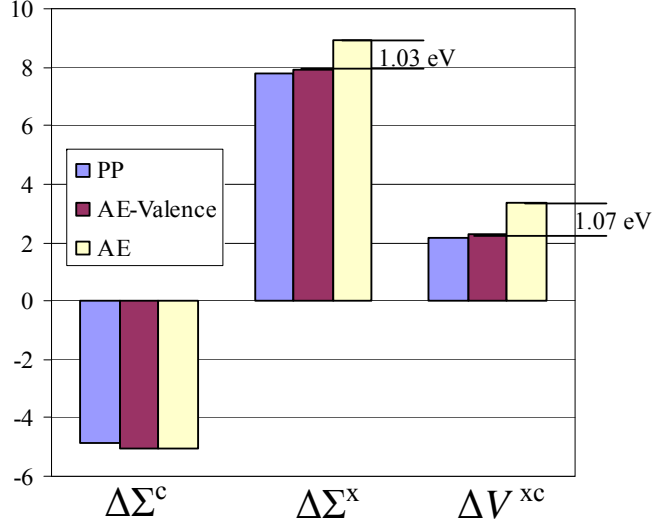


Figure 7.5: Differences between the matrix elements of the self-energy [in eV] (correlation term: $\Delta\Sigma^c$, exchange term: $\Delta\Sigma^x$) and exchange-correlation potential ΔV^{xc} over the conduction band minimum state at X point (X_c) and the valence band maximum state at Γ point (Γ_v) in Si in our all-electron, AE-Valence, and PP- G_0W_0 calculations.

- v. Pseudoization effects, although small in general (~ 0.1 eV) play an important role in the differences observed, ranging from 0.06 eV in diamond, almost within our numerical error, to 0.36 eV in LiF.

7.3 Materials with Semicore States

The common feature of the remaining materials studied in this chapter, namely NaCl, CaSe, and GaAs, is the presence of semicore states. This distinctive characteristic seems to correlate with the effect of core-valence partitioning in the G_0W_0 calculations (Fig. 7.1), which in these cases is negative. In NaCl and CaSe, the semicore states are the p orbitals in the second outermost shell of the cation. In GaAs, the $3d$ states of Ga are even closer to the Fermi level. Thus, we will analyze it separately.

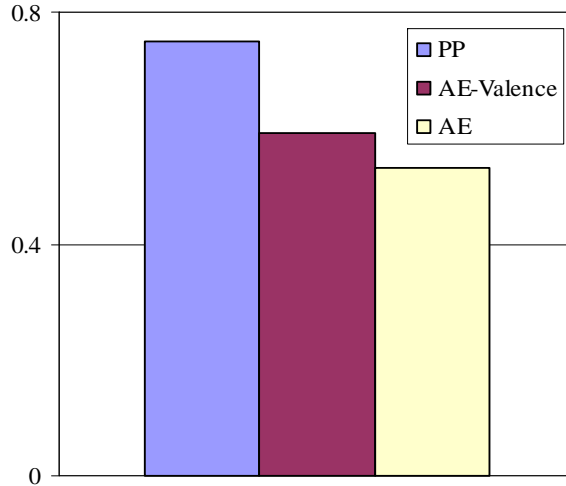


Figure 7.6: The G_0W_0 correction (in eV) to the $\Gamma - X$ band gap in Si obtained from the PP, AE-Valence, and AE- G_0W_0 calculations.

7.3.1 NaCl and CaSe

For the analysis of the different contributions to the G_0W_0 correction we follow the same procedure as for Si. The matrix elements of the self-energy and the xc potential on the valence band maximum (at the Γ -point, denoted as Γ_v throughout the discussion) of NaCl obtained from the three calculations are shown in Fig. 7.7. The source data, as well as those for the conduction band minimum (at the Γ point, denoted as Γ_c) and their differences are shown in Table 7.9. In this case, core-valence partitioning has a noticeable influence, in the order of 0.1 eV, on the correlation term of the self-energy (Σ^c) at the valence band maximum. The semicore states contribute to the screening of the valence electrons and consequently to the correlation term of the self-energy. However, this behavior is not observed from the matrix element of the correlation potential V^c in Table 7.9. This is because the energy dependence of the correlation interaction is absent when it is described using this correlation potential. Consequently, effects like screening, which is sensitive to the energy dependence, may be hard to be observed. For Σ^x and V^{xc} (still, mainly on V^x) the effects of core-valence partitioning are very large and tend to cancel each other, similar to the situation in materials without semicore states. *Pseudoization* produces errors in the order of 0.1 eV for Σ^x and V^{xc} , while its effect is quite larger (~ 0.5 eV) on Σ^c . Similar conclusions can be drawn for matrix elements at the conduction band minimum shown in Fig. 7.8, except that in this case, the effect of

Table 7.5: Matrix elements of the self-energy [in eV] (correlation term: Σ^c , exchange term: Σ^x) and exchange-correlation potential V^{xc} (correlation term: V^c , exchange term: V^x) for C in our all-electron, AE-Valence, and PP- G_0W_0 calculations.

	ϵ_{LDA}	Σ^c	Σ^x	V^c	V^x	V^{xc}	$\Sigma^x - V^{xc}$	$\epsilon_{G_0W_0}$
All-electron G_0W_0 :								
Γ_v	0.00	1.58	-20.14	-1.80	-16.20	-18.00	-2.14	0.00
CBM*	4.10	-5.01	-9.75	-1.67	-13.85	-15.52	5.77	5.42
CBM- $\Gamma_v(\Delta)$	4.10	-6.59	10.39	0.13	2.35	2.48	7.91	5.42
AE-Valence G_0W_0 ($2s, 2p$):								
Γ_v	0.00	1.60	-19.15	-1.76	-15.00	-16.76	-2.39	0.00
CBM	4.10	-5.03	-8.69	-1.65	-12.80	-14.45	5.76	5.62
CBM- $\Gamma_v(\Delta)$	4.10	-6.63	10.46	0.11	2.20	2.31	8.15	5.62
PP- G_0W_0 ($2s, 2p$):								
Γ_v	0.00	1.24	-19.15			-16.81	-2.34	0.00
CBM	4.15	-5.20	-8.67			-14.30	5.63	5.68
CBM- $\Gamma_v(\Delta)$	4.15	-6.44	10.48			2.51	7.97	5.68

* In diamond the bottom of the conduction band, denoted as CBM in this table, lies at 66.7% of the distance between Γ and X , and belongs to the $(6 \times 6 \times 6)$ mesh used in the calculations.

pseudoization and core-valence partitioning on Σ^c tend to cancel each other.

Analyzing the contribution of each term to the band gap correction (Fig. 7.9), we observe a discrepancy of 0.26 eV in $\Delta\Sigma^c$ due to core-valence partitioning. The effect of the removal of the core (and semicore) states on $\Delta\Sigma^x$ and ΔV^{xc} is strongly reduced with respect to the one on the matrix elements. However, in this case, they do not cancel each other, and tend to reduce the gap correction, opposite to the situation observed in the absence of semicore states. Fortunately, these remaining difference is almost cancelled by the change in $\Delta\Sigma^c$, leading to a very small, and negative, effect. The effect of *pseudoization* has an influence in the order of 0.1 eV on all three terms, with the corresponding change in $\Delta\Sigma^c$ accounting for the opening of the band gap in the PP- G_0W_0 calculation.

In Fig. 7.10 we show the G_0W_0 corrections to the band gap according to the different calculations. The discrepancy between all-electron and PP- G_0W_0 band gaps can be decomposed into the errors stemming from core-valence partitioning and *pseudoization* respectively. The error from core-valence partitioning is small and negative in this case. *Pseudoization* is responsible for the increasing of the correction in PP- G_0W_0 and, therefore, the discrepancy with the all-electron results.

The results obtained for CaSe are summarized in Table 7.10. The trends are the same as observed for NaCl, core-valence partitioning effects on $\Delta\Sigma^x$ and ΔV^{xc} do

Table 7.6: Matrix elements of the self-energy [in eV] (correlation term: Σ^c , exchange term: Σ^x) and exchange-correlation potential V^{xc} (correlation term: V^c , exchange term: V^x) for BN in our all-electron, AE-Valence, and PP- G_0W_0 calculations.

	ϵ_{LDA}	Σ^c	Σ^x	V^c	V^x	V^{xc}	$\Sigma^x - V^{xc}$	$\epsilon_{G_0W_0}$
All-electron G_0W_0 :								
Γ_v	0.00	2.72	-23.01	-1.85	-17.62	-19.47	-3.54	0.00
X_c	4.35	-4.91	-7.91	-1.59	-12.09	-13.68	5.77	6.03
$X_c - \Gamma_v(\Delta)$	4.35	-7.63	15.10	0.26	5.53	5.79	9.31	6.03
AE-Valence G_0W_0 ($2s, 2p$):								
Γ_v	0.00	2.73	-22.00	-1.81	-16.47	-18.28	-3.72	0.00
X_c	4.35	-4.93	-7.17	-1.57	-11.35	-12.92	5.75	6.16
$X_c - \Gamma_v(\Delta)$	4.35	-7.66	14.83	0.24	5.12	5.36	9.47	6.16
PP- G_0W_0 ($2s, 2p$):								
Γ_v	0.00	2.30	-21.92			-18.31	-3.61	0.00
X_c	4.39	-4.91	-7.34			-12.90	5.56	6.35
$X_c - \Gamma_v(\Delta)$	4.39	-7.21	14.58			5.41	9.17	6.35

not cancel each other completely and their contribution to the band gap correction is negative. This effect is weakened by the corresponding change in $\Delta\Sigma^c$, yet still leading to a negative core-valence partitioning error for the band gap correction. *Pseudoization* again increases the band gap correction, but, in this case, its total effect is smaller than that due to core-valence partitioning.

7.3.2 GaAs

GaAs is a prototype III-V semiconductor with a direct band gap of 1.52 eV at the Γ point. The lowest conduction band has a narrow tip. This tip gives a small effective mass for electrons at these states and correspondingly high electron velocity in the electronic devices. In Fig. 7.11, we compared our LDA, AE- G_0W_0 band diagrams with experimental results from Ref. [129, 131, 132]. The LDA results already agree well with the experimental values for the valence bands. The G_0W_0 correction shifts up the conduction bands significantly, however, the fundamental band gap and the conduction band positions at X point are still underestimated by ~ 0.3 eV and ~ 0.6 eV respectively.

In Fig. 7.12, Fig. 7.13, and Fig. 7.14 we show the matrix elements for the highest occupied and the lowest unoccupied states as well as their differences at the Γ point respectively. The corresponding source data are shown in Table 7.11. Again, the effect of core-valence partitioning on Σ^x and V^{xc} is very large. Compared with NaCl and CaSe, the error cancellation between them is even worse. The hybridization

Table 7.7: Matrix elements of the self-energy [in eV] (correlation term: Σ^c , exchange term: Σ^x) and exchange-correlation potential V^{xc} (correlation term: V^c , exchange term: V^x) for AlP in our all-electron, AE-Valence, and PP- G_0W_0 calculations.

	ϵ_{LDA}	Σ^c	Σ^x	V^c	V^x	V^{xc}	$\Sigma^x - V^{xc}$	$\epsilon_{G_0W_0}$
All-electron G_0W_0 :								
Γ_v	0.00	1.45	-16.05	-1.58	-12.49	-14.07	-1.98	0.00
X_c	1.44	-3.93	-5.26	-1.31	-8.09	-9.40	4.14	2.18
$X_c - \Gamma_v(\Delta)$	1.44	-5.38	10.79	0.27	4.40	4.67	6.12	2.18
AE-Valence G_0W_0 ($3s, 3p$):								
Γ_v	0.00	1.43	-14.09	-1.53	-10.50	-12.03	-2.06	0.00
X_c	1.44	-3.92	-4.47	-1.29	-7.25	-8.54	4.06	2.21
$X_c - \Gamma_v(\Delta)$	1.44	-5.35	9.61	0.24	3.25	3.49	6.12	2.21
PP- G_0W_0 ($3s, 3p$):								
Γ_v	0.00	1.34	-14.09			-11.82	-2.27	0.00
X_c	1.47	-3.82	-4.57			-8.49	3.92	2.50
$X_c - \Gamma_v(\Delta)$	1.47	-5.16	9.52			3.33	6.19	2.50

of the semicore $3d$ states with the valence electrons is much stronger than that of the semicore p orbitals in the previous two materials. As a result, the effect of core-valence partitioning on $\Delta\Sigma^x - \Delta V^{xc}$ reduces the band gap correction by 0.90 eV. Since the semicore states are also shallower than those in NaCl and CaSe, the core-valence partitioning effect on $\Delta\Sigma^c$ is also larger (0.45 eV). This effect increases the the gap correction, counteracting the core-valence partitioning effect on $\Delta\Sigma^x - \Delta V^{xc}$. Still, a discrepancy of -0.45 eV remains. *Pseudoization* effects on $\Delta\Sigma^c$, $\Delta\Sigma^x$ and ΔV^{xc} are again in the order of 0.1 eV, slightly opening the band gap compared with the AE-Valence result. Nevertheless, this change is much smaller than the corresponding core-valence partitioning effect (Fig. 7.15). The core-valence partitioning has a very large, and negative, effect on the band gap correction which constitutes the main reason for the discrepancy between AE and PP- G_0W_0 results.

7.3.3 Including the Semicore States into Valence

Summarizing our analysis, in materials without semicore states the errors due to core-valence partitioning increase the band gap correction in G_0W_0 calculations in the order of 0.1 eV. Their influence on Σ^c is negligible, while for Σ^x , and V^{xc} , the large errors observed cancel each other (Sec. 7.2). In the presence of semicore states these conclusions fail. The higher in energy the semicore states are, the larger the core-valence partitioning errors become. Going from NaCl, through CaSe, to GaAs, where the center of the semicore band is -22.7 eV, -17.3 eV, and -10.6 eV

Table 7.8: Matrix elements of the self-energy [in eV] (correlation term: Σ^c , exchange term: Σ^x) and exchange-correlation potential V^{xc} (correlation term: V^c , exchange term: V^x) for LiF in our all-electron, AE-Valence, and PP- G_0W_0 calculations.

	ϵ_{LDA}	Σ^c	Σ^x	V^c	V^x	V^{xc}	$\Sigma^x - V^{xc}$	$\epsilon_{G_0W_0}$
All-electron G_0W_0 :								
Γ_v	0.00	5.60	-31.85	-1.97	-22.26	-24.23	-7.62	0.00
Γ_c	8.97	-3.34	-7.61	-1.45	-11.70	-13.15	5.53	13.19
$\Gamma_c - \Gamma_v(\Delta)$	8.97	-8.94	24.24	0.52	10.56	11.08	13.16	13.19
AE-Valence G_0W_0 ($2s, 2p$):								
Γ_v	0.00	5.58	-30.61	-1.94	-21.03	-22.97	-7.64	0.00
Γ_c	8.97	-3.31	-5.47	-1.39	-9.74	-11.13	5.66	13.38
$\Gamma_c - \Gamma_v(\Delta)$	8.97	-8.89	25.14	0.55	11.29	11.84	13.30	13.38
PP- G_0W_0 ($2s, 2p$):								
Γ_v	0.00	4.45	-30.43			-22.81	-7.62	0.00
Γ_c	8.79	-3.68	-5.77			-11.05	5.28	13.56
$\Gamma_c - \Gamma_v(\Delta)$	8.79	-8.13	24.66			11.76	12.90	13.56

respectively, the corresponding core-valence partitioning errors are -0.09 eV, -0.22 eV, and -0.46 eV. In Ref. [133], it was illustrated that the PP- G_0W_0 results in this kind of materials can be improved by including the full shell of the semicore states into the valence region. Based on this consideration, we have studied the effect of core-valence partitioning and *pseudoization* for GaAs when the shell of the semicore states is treated as a valence shell. Since the pseudopotential codes we used in this work are limited to one projector per channel, we have taken the PP- G_0W_0 results from Ref. [110], albeit its limited reliability due to the use of the plasmon-pole approximation.

We performed a second set of all-electron valence-only G_0W_0 calculations including the $3s, 3p, 3d, 4s,$ and $4p$ states of both Ga and As in the valence region, denoted as AE-Valence2 hereafter. The matrix elements for $\Sigma^c, \Sigma^x,$ and V^{xc} obtained from the AE-Valence, AE-Valence2, and AE- G_0W_0 ² calculations for the valence band maximum and conduction band minimum of GaAs are shown in Fig. 7.16 and Fig. 7.17. The effect of core-valence partitioning in Σ^c , of 0.28 eV when the 3rd. shell is treated as core, becomes negligible when these states are included in the valence region. The errors in Σ^x and V^{xc} are reduced from several to less than 1 eV when going from AE-Valence to AE-Valence2 calculations. The same happens for the contributions of the different terms to the band-gap correction (see Fig. 7.18). Summing all these contributions, the effect of core-valence partitioning for the band gap correction, -0.45 eV in the AE-Valence calculations, is strongly reduced in mag-

²The pseudopotential results for the matrix elements are not available in the literature

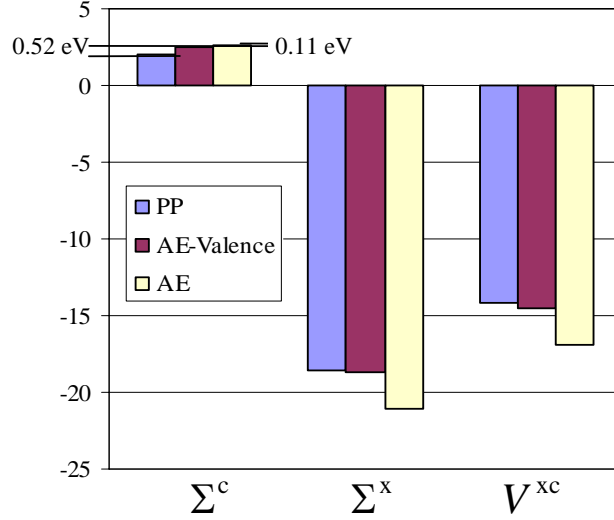


Figure 7.7: Matrix elements of the self-energy [in eV] (correlation term: Σ^c , exchange term: Σ^x) and exchange-correlation potential V^{xc} for the valence band maximum state at Γ point (Γ_v) in NaCl in our all-electron, AE-Valence, and PP- G_0W_0 calculations.

nitude and changes sign when including the semicore shell in the G_0W_0 correction, becoming 0.12 eV.

This clearly demonstrates that the distinct effects of core-valence partitioning in materials with (Sec. 7.3) and without (Sec. 7.2) semicore states is, as expected, due to the treatment of these states as core.

Comparing our AE-Valence2 calculations with the PP- G_0W_0 results with the same valence configuration in Ref. [110], Fig. 7.19, we observe the same trend as in materials without semicore states, *i. e.* the PP- G_0W_0 band gap correction is slightly larger than the AE-Valence2, which is also slightly larger than the AE result. While the latter discrepancy is clearly due to core-valence partitioning, we can not assign the former to the effect of pseudoization, which could be either cancelled or increased by the plasmon-pole approximation used in Ref. [110]. Nevertheless, the similarity with Fig. 7.5 is a clear indication that a *pseudoization* error of the order of 0.1 eV is to be expected.

7.4 Conclusion

From the results shown in this chapter, we can conclude that, although the G_0W_0 method substantially improves the band gap of low correlated materials, it still

Table 7.9: Matrix elements of the self-energy [in eV] (correlation term: Σ^c , exchange term: Σ^x) and exchange-correlation potential V^{xc} (correlation term: V^c , exchange term: V^x) for NaCl in our all-electron, AE-Valence, and PP- G_0W_0 calculations.

	ϵ_{LDA}	Σ^c	Σ^x	V^c	V^x	V^{xc}	$\Sigma^x - V^{xc}$	$\epsilon_{G_0W_0}$
All-electron G_0W_0 :								
Γ_v	0.00	2.62	-21.07	-1.64	-15.22	-16.86	-4.21	0.00
Γ_c	4.74	-3.31	-5.37	-1.15	-8.70	-9.95	4.58	7.60
$\Gamma_c - \Gamma_v(\Delta)$	4.74	-5.93	15.70	0.49	6.52	6.91	8.79	7.60
AE-Valence G_0W_0 (Na: 3s; Cl: 3s, 3p):								
Γ_v	0.00	2.51	-18.66	-1.62	-12.91	-14.53	-4.13	0.00
Γ_c	4.74	-3.16	-3.34	-1.15	-6.50	-7.65	4.31	7.51
$\Gamma_c - \Gamma_v(\Delta)$	4.74	-5.67	15.32	0.47	6.41	6.88	8.44	7.51
PP- G_0W_0 (Na: 3s; Cl: 3s, 3p):								
Γ_v	0.00	1.99	-18.63			-14.22	-4.41	0.00
Γ_c	4.70	-3.33	-3.51			-7.61	4.10	7.89
$\Gamma_c - \Gamma_v(\Delta)$	4.70	-5.32	15.12			6.61	8.51	7.89

underestimates them systematically. The impressive agreement of PP- G_0W_0 calculations with experimental results in the last decades relies in fact on a systematic overestimation of these values, originated in the approximations implicit in the method.

Core-valence partitioning, the usual suspect, leads to large errors, up to several eV's, in the calculation of the many-body self-energy, mainly due to an underestimation of the exchange term. However, when applied as a perturbation to the Kohn-Sham eigenvalues, these errors tend to cancel with those of the exchange-correlation potential. As long as semicore states are absent, or treated as valence states, these cancellation results in a small increase of the band gap correction, which cannot explain solely the discrepancies between pseudopotential and all-electron results.

Pseudoization, presumed innocent, is in fact also responsible for the systematic overestimation of the fundamental band-gaps of these materials. Being it intrinsic to the pseudopotential method, it poses a lower limit to the precision of PP- G_0W_0 results.

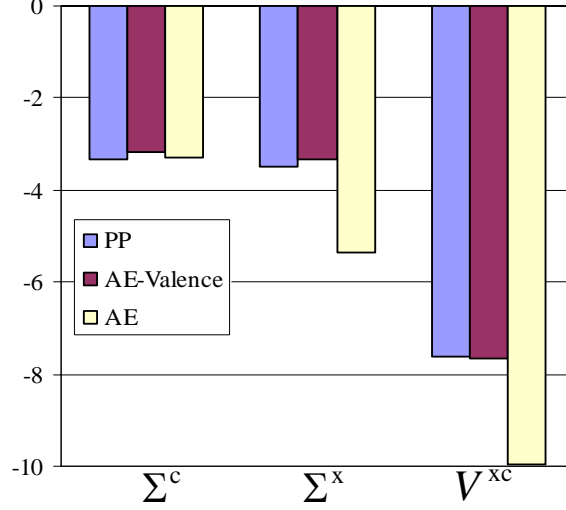


Figure 7.8: Matrix elements of the self-energy [in eV] (correlation term: Σ^c , exchange term: Σ^x) and exchange-correlation potential V^{xc} for the conduction band minimum state at Γ point (Γ_c) in NaCl in our all-electron, AE-Valence, and PP- G_0W_0 calculations.

Table 7.10: Matrix elements of the self-energy [in eV] (correlation term: Σ^c , exchange term: Σ^x) and exchange-correlation potential V^{xc} (correlation term: V^c , exchange term: V^x) for CaSe in our all-electron, AE-Valence, and PP- G_0W_0 calculations.

	ϵ_{LDA}	Σ^c	Σ^x	V^c	V^x	V^{xc}	$\Sigma^x - V^{xc}$	$\epsilon_{G_0W_0}$
All-electron G_0W_0 :								
Γ_v	0.00	1.91	-17.59	-1.61	-13.64	-15.25	-2.34	0.00
X_c	1.86	-4.03	-5.69	-1.39	-9.40	-10.79	5.10	3.36
$X_c - \Gamma_v$	1.86	-5.94	11.90	0.22	4.24	4.46	7.44	3.36
AE-Valence G_0W_0 (Ca: $3s, 3p$); Se: $4s, 4p$:								
Γ_v	0.00	1.79	-14.47	-1.52	-10.54	-12.06	-2.41	0.00
X_c	1.86	-3.79	-2.57	-1.19	-5.83	-7.02	4.45	3.14
$X_c - \Gamma_v$	1.86	-5.58	11.90	0.33	4.71	5.04	6.86	3.14
PP- G_0W_0 (Ca: $3s, 3p$; Se: $4s, 4p$):								
Γ_v	0.00	1.56	-14.50			-11.92	-2.58	0.00
X_c	1.84	-3.68	-2.78			-6.90	4.12	3.30
$X_c - \Gamma_v$	1.84	-5.24	11.72			5.02	6.70	3.30

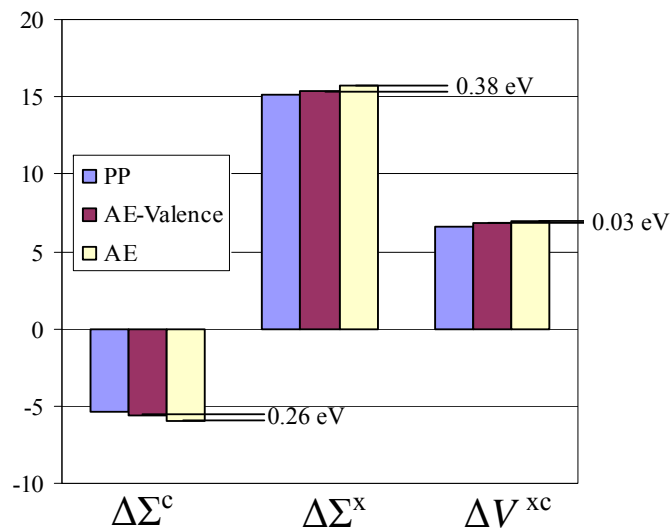


Figure 7.9: Differences between the matrix elements of the self-energy [in eV] (correlation term: $\Delta\Sigma^c$, exchange term: $\Delta\Sigma^x$) and exchange-correlation potential ΔV^{xc} over the conduction band minimum and valence band maximum states at the Γ point (Γ_c and Γ_v) in NaCl in our all-electron, AE-Valence, and PP- G_0W_0 calculations.

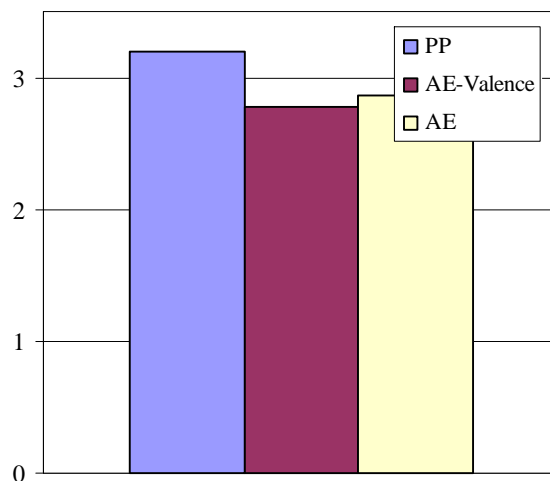


Figure 7.10: The G_0W_0 correction (in eV) to the fundamental band gap in NaCl obtained from the PP, AE-Valence, and AE- G_0W_0 calculations.

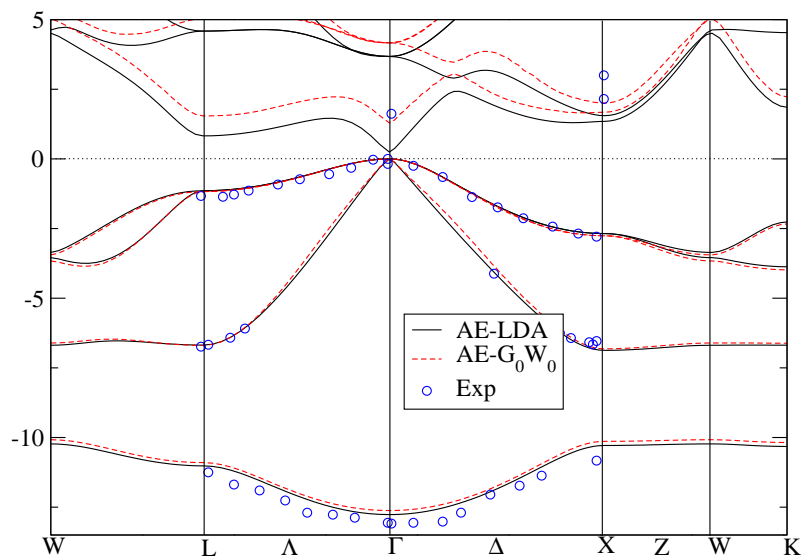


Figure 7.11: Band diagram of GaAs (in eV, referenced to the Fermi level) obtained from all-electron LDA and G_0W_0 calculations. Experimental results (blue circles) taken from Ref. [129, 131, 132]

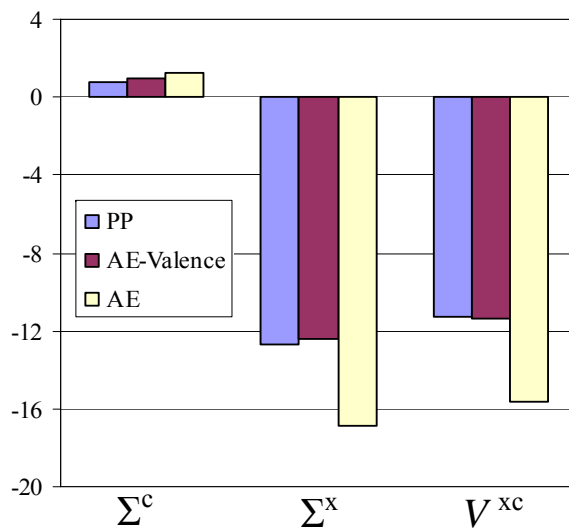


Figure 7.12: Matrix elements of the self-energy [in eV] (correlation term: Σ^c , exchange term: Σ^x) and exchange-correlation potential V^{xc} for the valence band maximum state at Γ point (Γ_v) in GaAs in our all-electron, AE-Valence, and PP- G_0W_0 calculations.

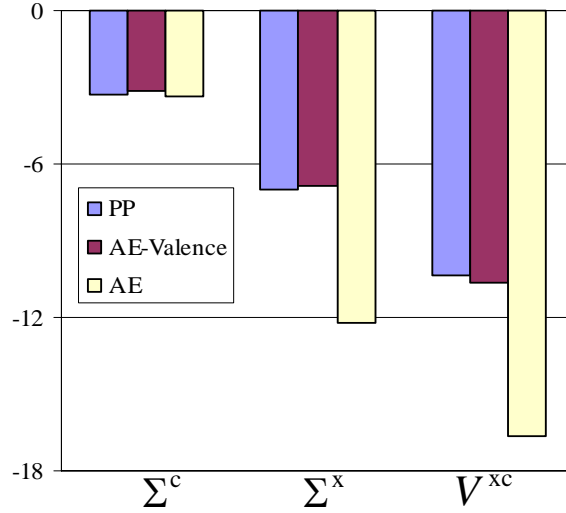


Figure 7.13: Matrix elements of the self-energy [in eV] (correlation term: Σ^c , exchange term: Σ^x) and exchange-correlation potential V^{xc} for the conduction band minimum state at Γ point (Γ_c) in GaAs in our all-electron, AE-Valence, and PP- G_0W_0 calculations.

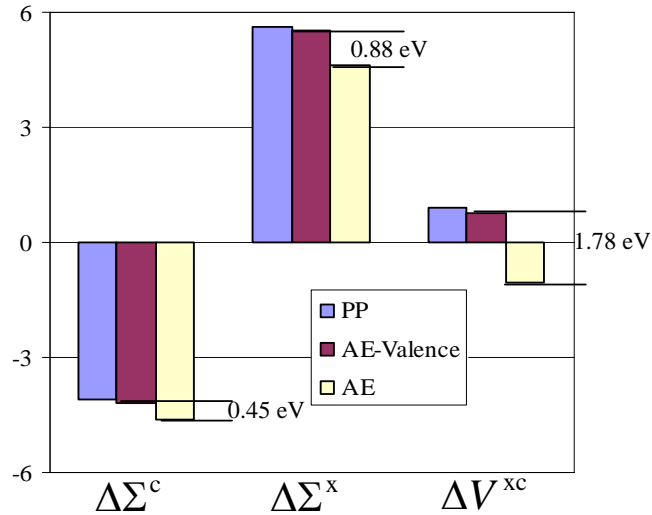


Figure 7.14: Differences between the matrix elements of the self-energy [in eV] (correlation term: $\Delta\Sigma^c$, exchange term: $\Delta\Sigma^x$) and exchange-correlation potential ΔV^{xc} over the conduction band minimum and valence band maximum states at the Γ point (Γ_c and Γ_v) in GaAs in our all-electron, AE-Valence, and PP- G_0W_0 calculations.

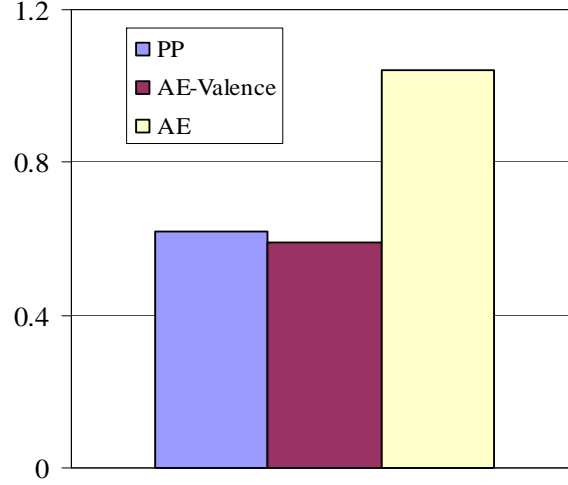


Figure 7.15: The G_0W_0 correction (in eV) to the fundamental band gap in GaAs obtained from the PP, AE-Valence, and AE- G_0W_0 calculations.

Table 7.11: Matrix elements of the self-energy [in eV] (correlation term: Σ^c , exchange term: Σ^x) and exchange-correlation potential V^{xc} (correlation term: V^c , exchange term: V^x) for GaAs in our all-electron, AE-Valence, and PP- G_0W_0 calculations.

	ϵ_{LDA}	Σ^c	Σ^x	V^c	V^x	V^{xc}	$\Sigma^x - V^{xc}$	$\epsilon_{G_0W_0}$
All-electron G_0W_0 :								
Γ_v	0.00	1.28	-16.85	-1.62	-14.02	-15.64	-1.21	0.00
Γ_c	0.25	-3.34	-12.22	-1.63	-15.04	-16.67	4.45	1.29
$\Gamma_c - \Gamma_v$	0.25	-4.62	4.63	-0.01	-1.02	-1.03	5.66	1.29
AE-Valence G_0W_0 ($3s, 3p$):								
Γ_v	0.00	1.00	-12.39	-1.50	-9.88	-11.38	-1.01	0.00
Γ_c	0.25	-3.17	-6.88	-1.44	-9.19	-10.63	3.75	0.84
$\Gamma_c - \Gamma_v$	0.25	-4.17	5.51	0.06	0.69	0.75	4.76	0.84
PP- G_0W_0 ($3s, 3p$):								
Γ_v	0.00	0.82	-12.65			-11.24	-1.41	0.00
Γ_c	0.35	-3.29	-7.01			-10.33	3.32	0.97
$\Gamma_c - \Gamma_v$	0.35	-4.11	5.64			0.91	4.73	0.97

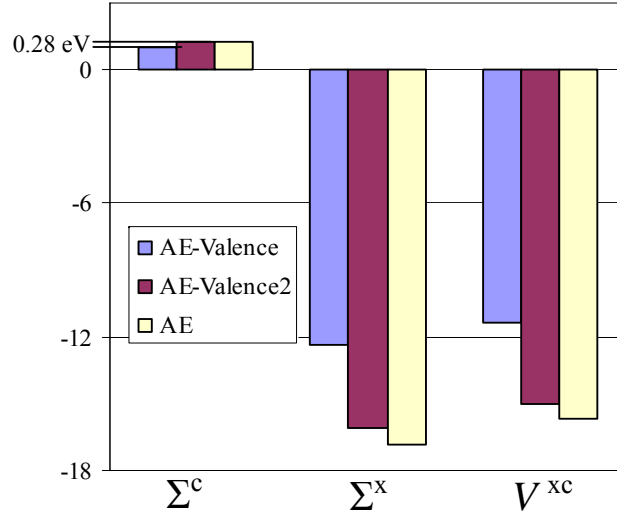


Figure 7.16: Matrix elements of the self-energy [in eV] (correlation term: Σ^c , exchange term: Σ^x) and exchange-correlation potential V^{xc} for the valence band maximum state at Γ point (Γ_v) in GaAs in our AE-Valence, AE-Valence2, and AE- G_0W_0 calculations.

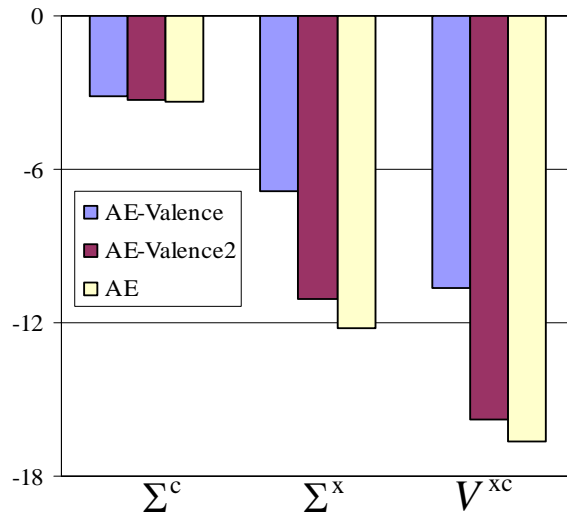


Figure 7.17: Matrix elements of the self-energy [in eV] (correlation term: Σ^c , exchange term: Σ^x) and exchange-correlation potential V^{xc} for the conduction band minimum state at Γ point (Γ_c) in GaAs in our AE-Valence, AE-Valence2, and AE- G_0W_0 calculations.

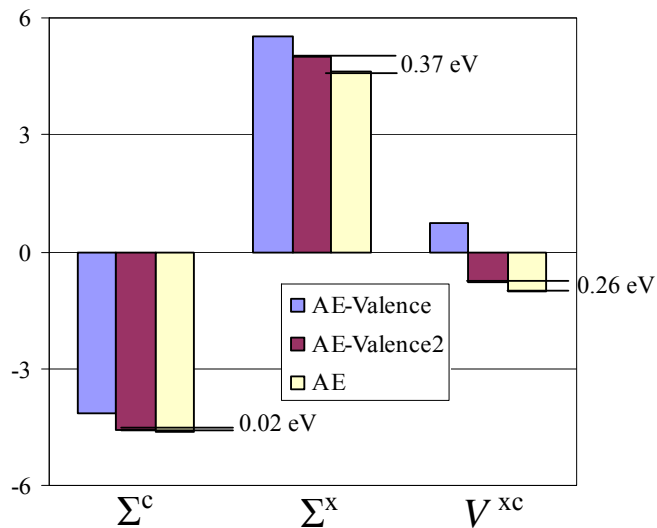


Figure 7.18: Differences between the matrix elements of the self-energy [in eV] (correlation term: $\Delta\Sigma^c$, exchange term: $\Delta\Sigma^x$) and exchange-correlation potential ΔV^{xc} over the conduction band minimum and valence band maximum states at Γ point (Γ_c and Γ_v) in GaAs in our AE-Valence, AE-Valence2, and AE- G_0W_0 calculations.

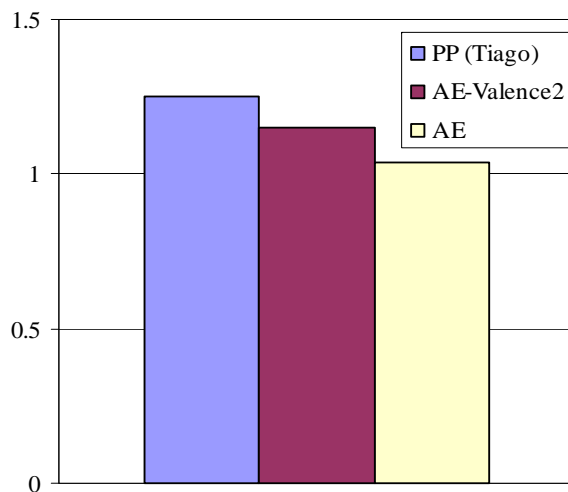


Figure 7.19: The G_0W_0 band gap correction (in eV) in GaAs obtained from the PP (Ref. [110]), AE-Valence2, and AE- G_0W_0 calculations.

Chapter 8

IIB-VI Semiconductors and Group III Nitrides Revisited

Due to their wide band gaps, IIB-VI semiconductors and group III nitrides are technologically important materials in optical applications. Thin films electroluminescent cells for flat displays, interference coatings for optical components, solar cells, and laser diodes constitute an unfairly short list among the already established and potential applications [134, 135].

It has long been known that the semicore d states from the cation play a crucial role in the chemical bonding of these materials. The presence of these semicore states is, in fact, what distinguishes the IIB-VI from the IIA-VI semiconductors. While the latter form ionic rocksalt structures, the former show a covalent bonding in tetrahedrally coordinated crystal structures (wurtzite or zinc-blende). Already in the late 1980's, all-electron calculations by Wei and Zunger [136] showed that the inclusion of the semicore d states in the valence region is necessary to obtain a correct description of the ground state properties of IIB-VI semiconductors, later confirmed by pseudopotential calculations including those states in the valence region [137]. The same conclusions were obtained for GaN [138]. To illustrate the situation, in Fig. 8.1, we show the LDA eigenvalues at the Γ point for the $3s$, $3p$ core states of Ga, and the valence states in bulk GaN. The labels correspond to the main orbital component of each wave-function. The $3s$, $3p$ states of Ga are very low in energy. The the $3d$ states of Ga are higher in energy than the $2s$ state of N. Thus, treating the semicore d states of Ga as core states is obviously inappropriate.

Despite these considerations, Zakharov *et al.* [96] performed the first quasiparticle band structure calculations for these kind of materials based the pseudopotential method treating the d electrons as core states ¹. Later on, Rohlfing, Krüger, and

¹Non-linear core corrections were applied in the LDA calculations. The plasmon-pole approximation was used to obtain the dielectric function and eigenvalue selfconsistency was performed on the Green's function

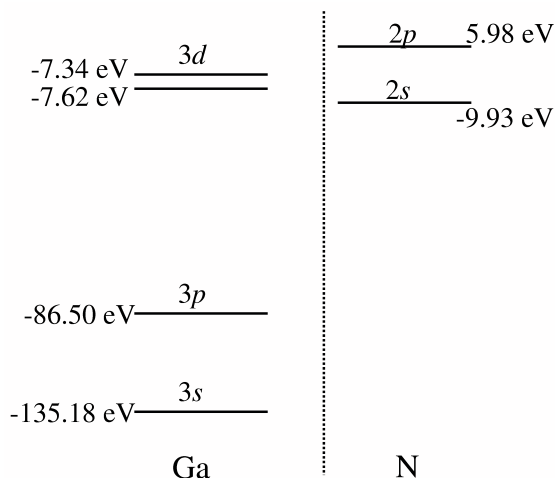


Figure 8.1: The LDA eigenvalues for the $3s$, $3p$ core states of Ga, and the valence states in bulk GaN at the Γ point. The $3s$, $3p$ states of Ga are very low in energy. The $3d$ states of Ga are higher in energy than the $2s$ state of N. Treating the semicore d states of Ga as core states is inappropriate.

Pollmann [133] showed that the reasonable agreement with experiments obtained in Ref. [96] was, in fact, spurious. Furthermore, they pointed out that the inclusion of the d states in the valence region worsened the results, and an explicit treatment of the whole shell of the semicore states² (*e. g.*, the $3d$, $3p$, and $3s$ states of Ga in GaN) is necessary to obtain reliable results both for the band gap and the d band position and width. This trend has been confirmed by further calculations [139, 140, 141]. Recently, Rinke *et al.* [142] obtained an excellent agreement with experiments within the PP- G_0W_0 method including only the d states in the valence region, taking the exact exchange optimized effective potential (OEP_x) as the starting point, which allows some discussion about the description of the core-valence interaction and the starting point dependence in the G_0W_0 method.

On the other hand, although all-electron G_0W_0 calculations have been carried out for a list of materials including some of the IIb-VI semiconductors and group III nitrides [13, 115], to the best of our knowledge, a systematic study of the electronic structure of these materials and the role of the semicore shell and deep core states within the all-electron G_0W_0 method has not been reported yet. Besides, discrepancies up to 0.3 eV for the band gaps and 0.7 eV for the d band positions still remain between the all-electron and PP- G_0W_0 ³ methods.

²In later discussions, we call this shell the semicore shell. Since the s , p states in this shell are clearly core states, as shown in Fig. 8.1 for GaN. To avoid confusions, we call the states belonging to deeper shells deep core states.

³Including the outermost two shells of the cation atoms, and LDA-pseudopotentials

In this chapter, we study the electronic structure of GaN, ZnS, ZnSe, ZnTe, CdS, CdSe, and CdTe within the all-electron G_0W_0 method. The results are compared with the already reported pseudopotential and all-electron G_0W_0 results, as well as with experiments (Sec. 8.2). Afterwards, taking GaN and ZnS as examples, we carry out the same kind of AE-Valence calculations as in the previous chapter, for different valence configurations, to analyze the influence of the semicore shell and the deep core states on the G_0W_0 results (Sec. 8.3).

8.1 Numerical Details

Throughout this chapter we restrict ourselves to the metastable zinc-blende structure, experimental lattice constants (Table 8.1) and the LDA for the exchange-correlation potential. We have tested the convergence of the fundamental bandgaps and d -band positions with respect to the different dimensioning parameters as in Chapter 6 (menu for fixing the parameters refer to Sec. 6.5). For all these materials, we have taken $l_{\max} = 3$, $\lambda_{\min} = 10^{-4}$, $Q = 1.0$ for the mixed basis, $\omega_0 = 10.88$ eV and $N_\omega = 36$ for the frequency integration, and a $(6 \times 6 \times 6)$ mesh for the Brillouin-zone integration, $RK_{\max} = 8$ for the (L)APW+lo basis set and ~ 150 unoccupied bands for the calculation of the self-energy. This ensures the G_0W_0 corrections are converged within 0.02 eV (0.10 eV) for the fundamental band gaps (d band positions).

In the all-electron valence-only calculations of GaN and ZnS, we take two distinct configurations for the valence states. The first one includes the $3d$, $4s$, and $4p$ electrons of the cation and the outermost shell of the anion (denoted as AE-VAL1 in the following). The second one (AE-VAL2) includes the whole semicore shell of the cation. The comparison between these two calculations allows the study of the interaction between the electrons within the semicore shell of the cation. The difference between AE-VAL2 and all-electron calculations reveals the influence of the deep core electrons on the G_0W_0 results.

8.2 All-Electron Results

In Figure 8.2 to 8.8, we show the LDA and G_0W_0 band diagrams of these materials obtained from our all-electron calculations. The effects of G_0W_0 correction can be mainly summarized in: i) the upwards energy shift of the unoccupied bands, and ii) the downwards energy shift of the semicore d states. In other words, an increase of both, the fundamental band gap and the d states binding energy. In both cases the significant discrepancies between the LDA and experimental results is reduced. In GaN, the semicore d states of the cation overlap with the $2s$ states of the anion

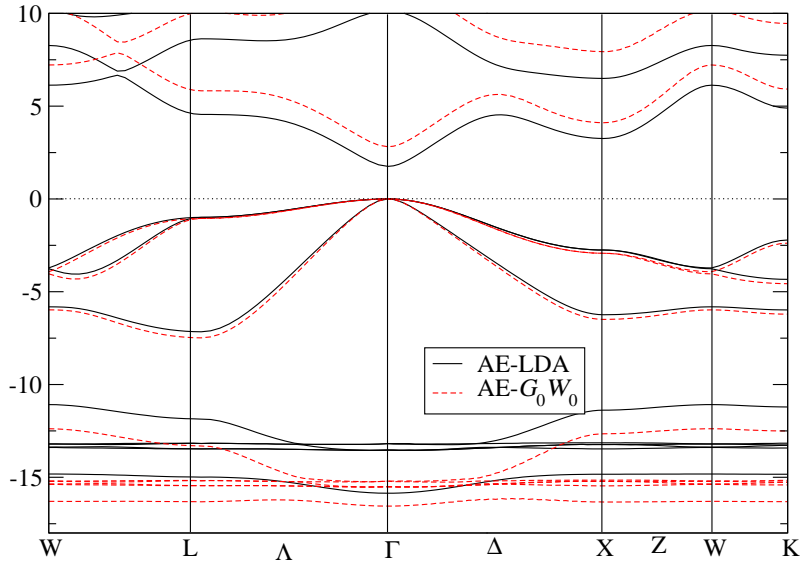


Figure 8.2: Band Diagram of zinc-blende GaN (in eV, taking the Fermi energy as zero) from all-electron LDA and G_0W_0 calculations.

on the energy axis (shown in Fig. 8.9). The highest of these states at the Γ point shows a large Ga- d component, while the lowest one shows a large N- s component. Since the G_0W_0 correction to each state is sensitive to the character of its wave function, the splitting of these bands at the Γ point experiences a noticeable change from LDA to G_0W_0 . In IIb-VI semiconductors, this is not observed because the d bands of cation are separated on the energy axis from the s band of anion. In the following, we will focus on the G_0W_0 corrections to the fundamental band gaps and d band binding energies when discussing the effects of G_0W_0 correction on the electronic structure of these materials.

Our all-electron fundamental band gaps, together with other theoretical and the experimental results are shown in Table 8.1. To compare these results, one should add $\Delta_0/3$ to the experimental values to account for the effect of spin-orbit coupling. The comparison confirms the general trend observed in Chapter 7, the G_0W_0 corrections to LDA systematically underestimate the band gaps. Our results are in excellent agreement with the values reported by Kotani, van Schilfgaarde, and Faleev⁴ [13, 115]. The discrepancies observed for GaN and CdS (~ 0.2 eV smaller) are due to the different crystalline structures, since they have reported on the wurtzite structure of these materials.

The PP- G_0W_0 calculations in Ref. [139] and [143], both treating the outermost two shells as valence states, obtained systematically larger band gaps, consistent

⁴Based on the full-potential (FP) linear muffin-tin orbital(LMTO) method

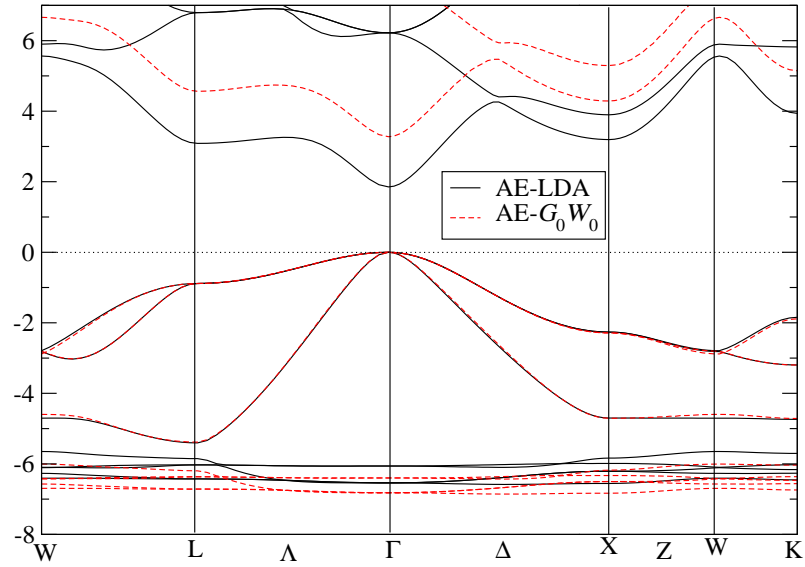


Figure 8.3: Band Diagram of zinc-blende ZnS (in eV, taking the Fermi energy as zero) from all-electron LDA and G_0W_0 calculations.

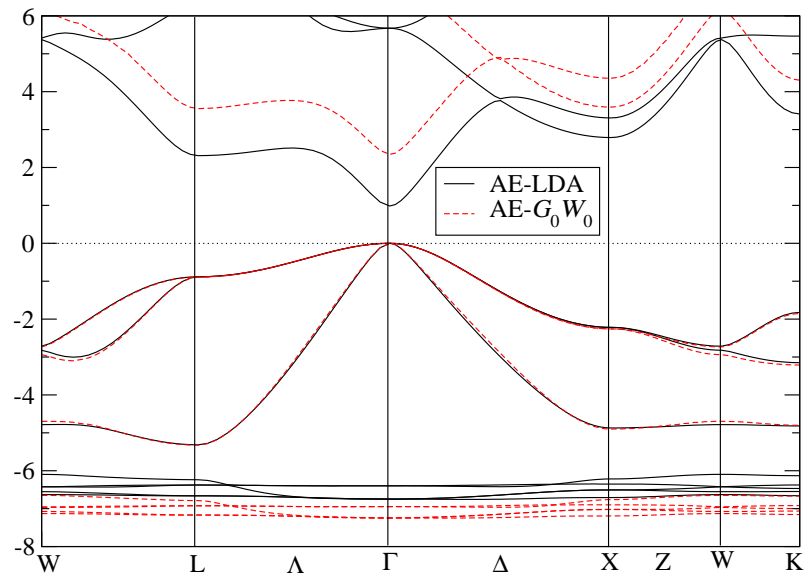


Figure 8.4: Band Diagram of zinc-blende ZnSe (in eV, taking the Fermi energy as zero) from all-electron LDA and G_0W_0 calculations.

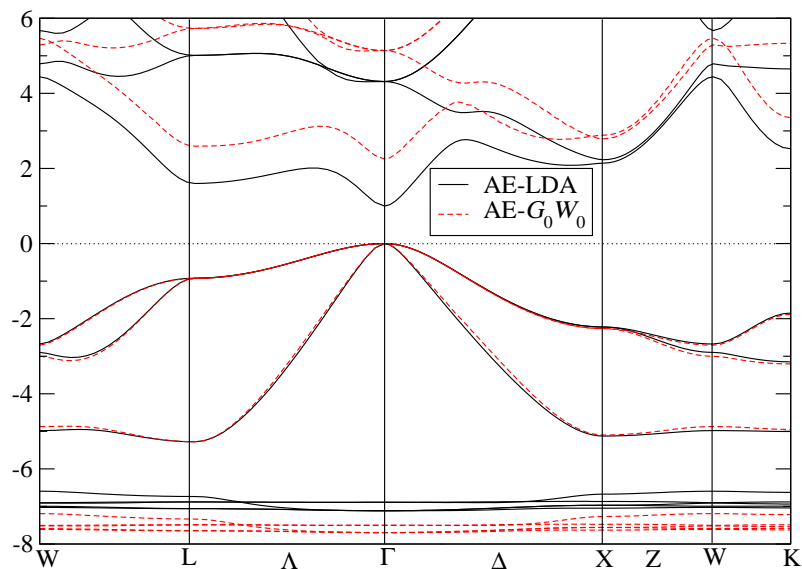


Figure 8.5: Band Diagram of zinc-blende ZnTe (in eV, taking the Fermi energy as zero) from all-electron LDA and G_0W_0 calculations.

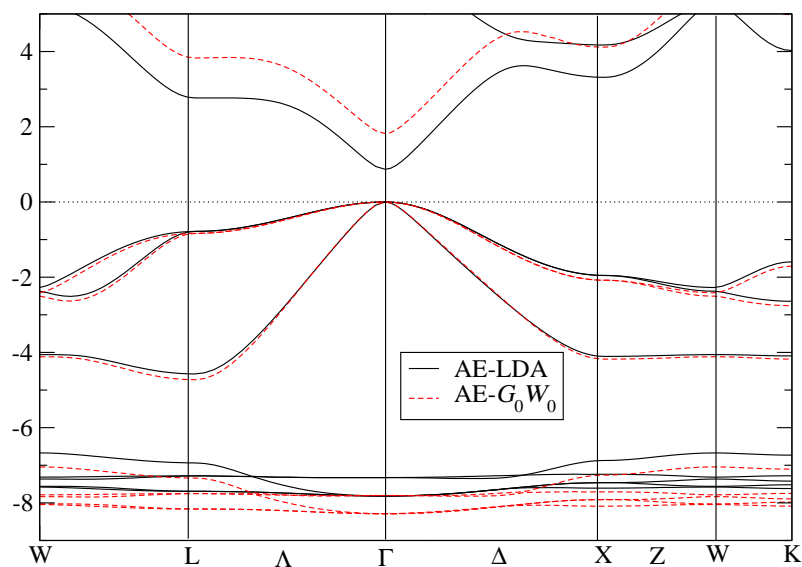


Figure 8.6: Band Diagram of zinc-blende CdS (in eV, taking the Fermi energy as zero) from all-electron LDA and G_0W_0 calculations.

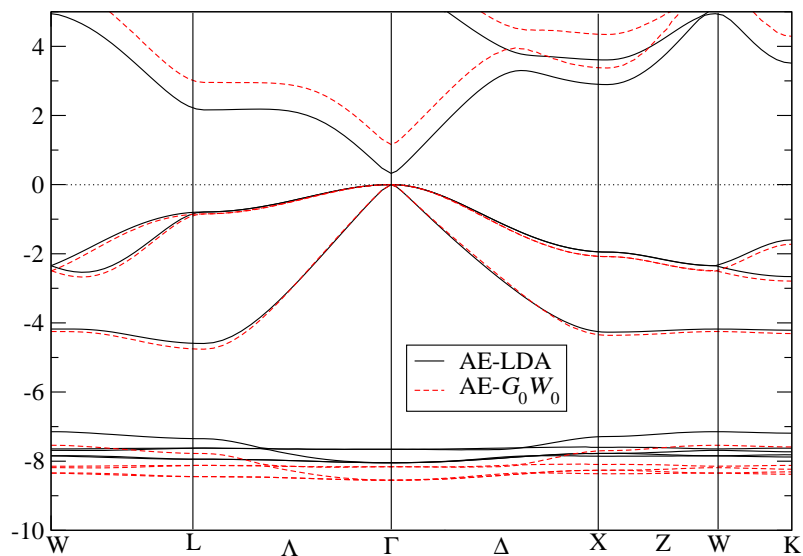


Figure 8.7: Band Diagram of zinc-blende CdSe (in eV, taking the Fermi energy as zero) from all-electron LDA and G_0W_0 calculations.

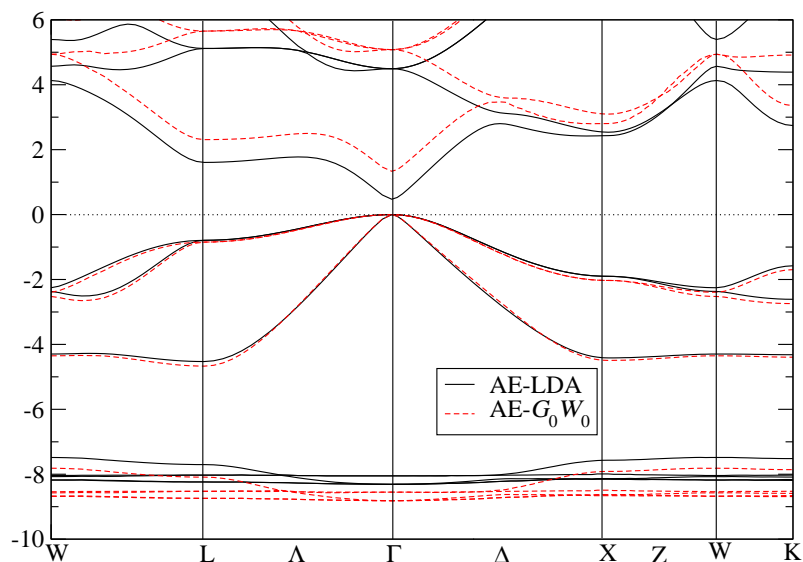


Figure 8.8: Band Diagram of zinc-blende CdTe (in eV, taking the Fermi energy as zero) from all-electron LDA and G_0W_0 calculations.

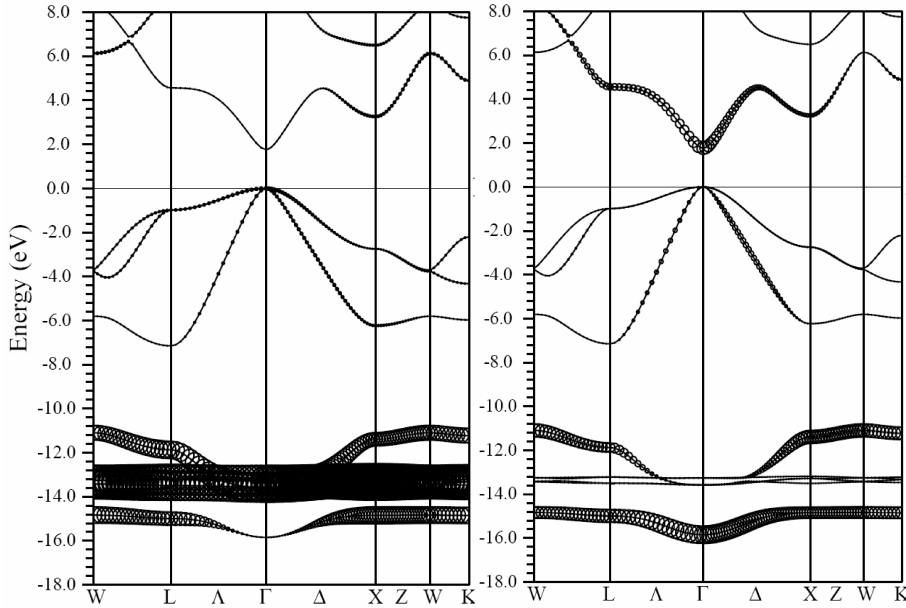


Figure 8.9: Band character plot of GaN (in eV, taking the Fermi energy as zero) in the LDA. Left panel: d component of Ga. Right panel: s component of N. The amount of each character is represented by the radius of the circles.

with the conclusion we have drawn for GaAs in Chapter 7. Since in Ref. [139], the plasmon-pole model⁵ was used to describe the frequency-dependence of dielectric function, to analyze the discrepancies between all-electron and PP- G_0W_0 calculations, we will compare our results to those of Ref. [143], where the explicit ω dependence of the screened Coulomb interaction is calculated.

Even though only the d semicore states are included in the valence region, the PP- G_0W_0 results from Ref. [142], which start from the OEP_x based DFT calculations, give the best agreement with experiments. Since the all-electron G_0W_0 results do not improve over those LDA based PP- G_0W_0 results, the improved agreement with experiments in Ref. [142] is not only due to a better description of the core-valence interactions, but rather, the starting point is the decisive issue.

Concerning the binding energy of the semicore d states, in Table 8.2 we show our results, together with other theoretical and the experimental values. To compare with experiments, one should add $\Delta_0/3$ (in Table 8.1) to these theoretical results to account for the spin-orbital coupling effect. Our results agree within 0.10 eV with the LDA based PP- G_0W_0 results (Ref. [143] and [139]). These consistent results differ considerably from the all-electron results reported in Ref. [13]. Thus, our results reduce the formerly reported discrepancies between the LDA based all-

⁵which is believed to increase fundamental band gaps systematically in these materials [143]

Table 8.1: LDA and G_0W_0 fundamental band gaps (in eV) for GaN, ZnS, ZnSe, ZnTe, CdS, CdSe, and CdTe in the zinc-blende structure. Experimental and theoretical results from the literature are also shown for comparison.

	GaN	ZnS	ZnSe	ZnTe	CdS	CdSe	CdTe
Lattice Constants (\AA)	4.50	5.40	5.67	6.09	5.82	6.05	6.48
$\Delta_0/3$ (eV) [144]	0.00	0.02	0.13	0.32	0.02	0.14	0.32
This work							
LDA	1.76	1.85	1.00	1.02	0.87	0.35	0.50
G_0W_0	2.79	3.19	2.36	2.26	1.85	1.22	1.37
Literature all-electron results							
Kotani <i>et al.</i> LDA	1.81 ^{a*}	1.86 ^b	1.05 ^b	1.03 ^b	0.93 ^{b*}		0.51 ^a
Kotani <i>et al.</i> G_0W_0	3.03	3.21	2.25	2.23	1.98		1.37
Literature PP results using LDA based pseudopotentials ^h							
Rohlfing <i>et al.</i> G_0W_0 ^c	2.88	3.50	2.45				
Fleszar <i>et al.</i> LDA ^d		1.84	1.02	1.04	0.82	0.29	0.49
Fleszar <i>et al.</i> G_0W_0 ^d		3.41	2.37	2.27	2.13	1.38	1.51
Literature PP results using OEP _x based pseudopotentials ⁱ							
Rinke <i>et al.</i> OEP _x ^e	2.76	2.94			1.84		
Rinke <i>et al.</i> G_0W_0 ^e	3.09	3.62			2.36		
Experiments	3.30 ^f	3.87 ^g	2.95 ^g	2.68 ^g	2.50 ^g	1.83 ^g	1.90 ^g

* wurtzite structure, ^a Ref. [13], ^b Ref. [115], ^c Ref. [139], ^d Ref. [143], ^e Ref. [142], ^f Ref. [145], ^g Ref. [144], ^h The outermost two shells are treated as valence, ⁱ The outermost shell and the semicore d states are treated as valence.

electron and PP- G_0W_0 results from up to 0.7 eV to less than 0.3 eV. The G_0W_0 results systematically improve over the LDA values. However, discrepancies with experiments scattering from ~ 1.3 eV (CdSe) to ~ 2.3 eV (ZnTe) still remain.

The OEP_x based PP- G_0W_0 results from Ref. [142] again show better agreement with experiments, except in CdS, where their starting point at the Kohn-Sham level is comparable to our LDA result. Therefore, we conclude that the better agreement with experiments in other materials is due to the better starting point at the Kohn-Sham level, indicating the importance of this issue in the G_0W_0 scheme.

8.3 The Role of Core States

8.3.1 Postions of the Semicore d Bands

To analyze the role of the semicore states in the G_0W_0 calculation, we compare the band diagrams of GaN and ZnS obtained from the AE, AE-VAL1 and AE-VAL2 G_0W_0 calculations in Fig. 8.10 and 8.11.

Including only the outermost shell and the d states in the G_0W_0 correction (AE-VAL1) moves the latter up in energy by several eV's. In GaN, the semicore d states of Ga are taken away from the s states of N (Fig. 8.10). In ZnS, they even go into the regime of the valence p band of the S atom, as can be seen in Fig. 8.11. When the interaction between the $3d$ and $3s$, $3p$ states (the semicore shell) in the cation is included on the G_0W_0 level (AE-VAL2), these bands shift back in the right direction toward the experimental results, showing that the inconsistent treatment of the interactions of the semicore d states with the sp valence states of the anion and the sp states of the cation in the semicore shell is responsible for the unphysical reduction of the binding energy of the $3d$ states. Nevertheless, discrepancies in order of 1 eV with respect to the AE- G_0W_0 results remain. A clear indication that also the many-body interaction with the deep core states is necessary for a correct description of the semicore states.

To analyze the origin of these differences, we follow a procedure analogous to that employed in the previous chapter for the band gaps. In Table 8.3 we show the matrix elements of the self-energy and the exchange-correlation potential at the valence band maximum (VBM) and the highest d state at the Γ point (Γ_d) for GaN, as well as the difference between them ($\Delta F = F(\Gamma_{\text{VBM}}) - F(\Gamma_d)$ where $F = \Sigma^x, \Sigma^c, V^{\text{xc}}$). The correlation term of the self-energy on the valence band maximum state, mainly a $2p$ state of N, shows very small differences between the AE-VAL1, AE-VAL2, and AE- G_0W_0 calculations (< 0.1 eV), indicating that the correlation interaction between this state and the $3s$, $3p$ states of the cation as well as the deep core states is negligible. However, looking at this term on the highest d band, we observe that its correlation interaction with the $3s$, $3p$ states of the cation is

Table 8.2: d states binding energies (in eV) referenced to the valence band maximum for GaN, ZnS, ZnSe, ZnTe, CdS, CdSe, and CdTe in the zinc-blende structure. Experimental and theoretical results from the literature are also shown for comparison.

	GaN	ZnS	ZnSe	ZnTe	CdS	CdSe	CdTe
This work							
LDA	13.46	6.35	6.58	6.99	7.63	7.86	8.18
G_0W_0	15.76	6.84	7.12	7.55	8.16	8.45	8.74
Literature all-electron results							
Kotani <i>et al.</i> LDA [13]	13.60	6.20	6.70		7.50		
Kotani <i>et al.</i> G_0W_0 [13]	16.40	7.10	7.70		8.20		
PP- G_0W_0 results using LDA based pseudopotentials ^a							
Rohlfing <i>et al.</i> G_0W_0 [139]	15.70	6.40			8.10		
Fleszar <i>et al.</i> LDA [143]		6.31	6.55	6.96	7.53	7.72	8.08
Fleszar <i>et al.</i> G_0W_0 [143]		6.84	7.17	7.60	8.13	8.40	8.79
PP- G_0W_0 results using OEP _x based pseudopotentials ^b							
Rinke <i>et al.</i> KS [142]	14.85	6.91			7.57		
Rinke <i>et al.</i> G_0W_0 [142]	16.12	6.97			7.66		
Experiments	17.10[146]	8.7[147]	9.20[144]	9.84[144]	9.50[144]	9.70[148]	10.50[143]

^a The outermost two shells are treated as valence, ^b The outermost shell and the semicore d states are treated as valence.

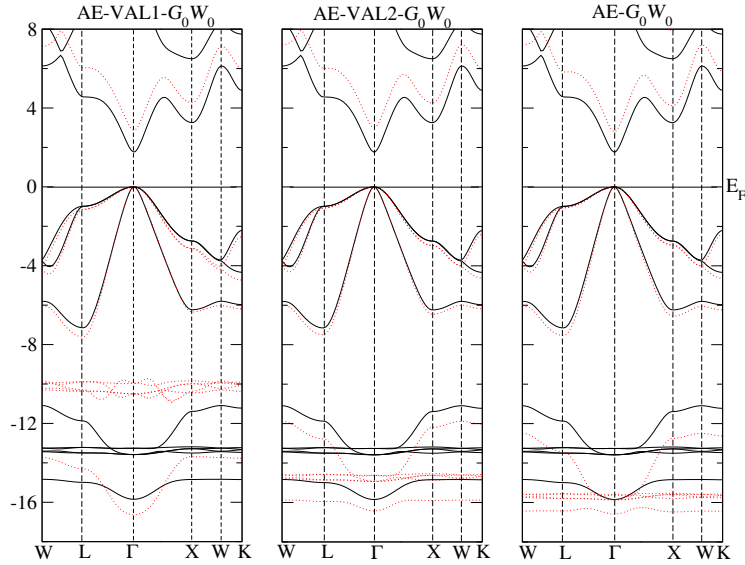


Figure 8.10: Band diagrams of zinc-blende GaN (in eV, taking the Fermi energy as the zero point) obtained from the AE-LDA, AE- G_0W_0 , AE-VAL1- G_0W_0 , and AE-VAL2- G_0W_0 calculations. Solid black lines display LDA results. Dotted red lines display G_0W_0 results.

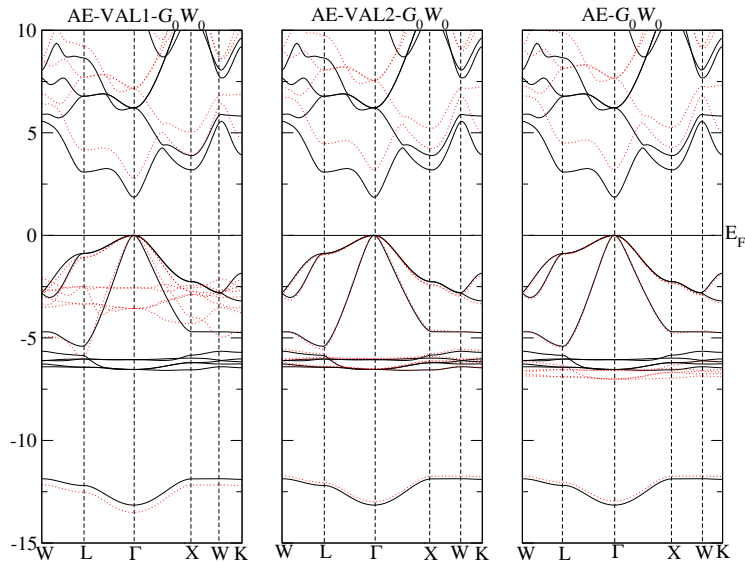


Figure 8.11: Band diagram of zinc-blende ZnS (in eV, taking the Fermi energy as the zero point) obtained from the AE-LDA, AE- G_0W_0 , AE-VAL1- G_0W_0 , and AE-VAL2- G_0W_0 calculations. Solid black lines display LDA results. Dotted red lines display G_0W_0 results.

very strong, producing a decrease of the binding energy of the order of 2 eV when going from the AE-VAL1 to the AE-VAL2 G_0W_0 calculations. This is due to the strong overlap between wave functions in the same shell. Explicitly including their interaction at the G_0W_0 level is obviously necessary. Inclusion of the deep core states further increases the correlation term of self-energy by 0.27 eV, much smaller but still noticeable. According to these considerations, the good agreement of the PP- G_0W_0 results for the d states binding energies obtained by Rinke *et al.* are mainly due to the exclusion of the correlation contribution of the core-states.

Table 8.3: Matrix elements of the self-energy [in eV] (correlation term: Σ^c , exchange term: Σ^x) and exchange-correlation potential V^{xc} for the highest d state (Γ_d), the valence band maximum (Γ_{VBM}), and the differences between them in GaN in our AE-VAL1, AE-VAL2, and AE- G_0W_0 calculations.

	ϵ_{LDA}	Σ^c	Σ^x	$\Sigma^c + \Sigma^x$	V^{xc}	$\Sigma - V^{xc}$	$\epsilon_{G_0W_0}$
AE-VAL1 (Ga: $3d$, $4s$, and $4p$):							
Γ_{VBM}	0.00	3.16	-21.60	-18.44	-18.65	0.21	0.00
Γ_d	-13.26	8.51	-38.28	-29.77	-33.28	3.51	-9.96
$\Gamma_{\text{VBM}} - \Gamma_d (\Delta)$	13.26	-5.35	16.68	11.33	14.63	-3.30	9.96
AE-VAL2 (Ga: $3s$, $3p$, $3d$, $4s$, $4p$):							
Γ_{VBM}	0.00	3.22	-22.62	-19.40	-19.21	-0.19	0.00
Γ_d	-13.26	10.23	-51.90	-41.67	-40.11	-1.56	-14.63
$\Gamma_{\text{VBM}} - \Gamma_d (\Delta)$	13.26	-7.01	29.28	22.27	20.90	1.37	14.63
AE:							
Γ_{VBM}	0.00	3.19	-23.88	-20.69	-20.48	-0.21	0.00
Γ_d	-13.26	10.50	-56.81	-46.31	-43.76	-2.55	-15.60
$\Gamma_{\text{VBM}} - \Gamma_d (\Delta)$	13.26	-7.31	32.93	25.62	23.28	2.34	15.60

The matrix elements for the exchange term of the self-energy (forth column in Table 8.3) on the VBM increase by almost 1 eV by including the $3s$ and $3p$ states (from AE-VAL1 to AE-VAL2) and another 1.3 eV by including the deep core states (from AE-VAL2 to AE). On the other hand, the same matrix elements for the d -state show huge changes (~ 13 eV when including the $3s$ and $3p$ states of Ga and further ~ 5 eV from the deep core electrons of both Ga and N), which are carried along to the binding energy of the $3d$ state. Summing up the many-body contributions to the binding energy ($\Delta\Sigma = \Delta\Sigma^c + \Delta\Sigma^x$ -fifth column in Table 8.3), we obtain a contribution of ~ 10 eV due to the $3s$ and $3p$ states and ~ 3 eV coming from the deep core electrons. The corresponding contributions from the exchange-correlation potential are ~ 6 eV and ~ 2 eV respectively. The correction to the binding energy results from the cancellation of contributions from the self-energy and exchange-correlation potential. Thus, the corresponding G_0W_0 correction to

the d band position from AE-VAL1 to AE-VAL2, and from AE-VAL2 to AE- G_0W_0 , are smaller in absolute values by 4.67 eV and 0.97 eV respectively (last column of Table 8.3).

From this analysis, we conclude that the exchange interaction between the $3s$, $3p$ and the $3d$ states of Ga is the main reason for including all these states in the G_0W_0 calculations in order to obtain reliable values for the binding energy of the semicore d states, in agreement with what was found in Ref. [133]. However the correlation interaction between these states produces large corrections ~ 2 eV and can not be neglected. The deep core states contribute to the d -state binding energies through both exchange and correlation interaction with them. The much larger exchange interaction tends to increase this binding energy, while the correlation interaction tends to reduce it. The overall contribution from the deep core states tends to increase the d -state binding energy. Thus, an all-electron treatment is required for a good description of the semicore d states in these materials.

Table 8.4: Matrix elements of the self-energy [in eV] (correlation term: Σ^c , exchange term: Σ^x) and exchange-correlation potential V^{xc} for the highest d band (Γ_d), the valence band maximum (Γ_{VBM}), and the differences between them in ZnS in our AE-VAL1, AE-VAL2, and AE- G_0W_0 calculations.

	ϵ_{LDA}	Σ^c	Σ^x	$\Sigma^c + \Sigma^x$	V^{xc}	$\Sigma - V^{xc}$	$\epsilon_{G_0W_0}$
AE-VAL1 (Zn: $3d$, $4s$):							
Γ_{VBM}	0.00	2.41	-18.44	-16.03	-16.36	0.33	0.00
Γ_d	-6.06	8.00	-34.21	-26.21	-30.04	3.83	-2.56
$\Gamma_{\text{VBM}} - \Gamma_d (\Delta)$	6.06	-5.59	15.77	10.18	13.68	-3.50	2.56
AE-VAL2 (Zn: $3s$, $3p$, $3d$, $4s$):							
Γ_{VBM}	0.00	2.55	-20.34	-17.79	-17.38	-0.41	0.00
Γ_d	-6.06	9.85	-46.61	-36.76	-36.40	-0.36	-6.01
$\Gamma_{\text{VBM}} - \Gamma_d (\Delta)$	6.06	-7.30	26.27	18.97	19.02	-0.05	6.01
AE:							
Γ_{VBM}	0.00	2.58	-23.08	-20.50	19.93	-0.57	0.00
Γ_d	-6.06	10.13	-50.87	-40.74	-39.65	-1.09	-6.58
$\Gamma_{\text{VBM}} - \Gamma_d (\Delta)$	-6.06	-7.55	27.79	20.24	19.72	0.52	6.58

In Table 8.4 we show the same matrix elements as in Table 8.3 for ZnS. The situation is similar except that the hybridization between the $3d$ states of Zn and the valence band maximum state, which mainly originated from the $3p$ states of S, is stronger compared with GaN. In Fig. 8.12, we show the band character plot of ZnS for the d component of Zn from the LDA calculation. Compared with that for GaN in Fig. 8.9, we see a much stronger d character for the valence band maximum state. Accordingly, the wave function of this valence band maximum state has a

larger overlap with those of the $3s$, $3p$ states in Zn compared with GaN, leading to stronger interactions between the $3s$, $3p$ states of Zn and the valence band maximum. As a result, the changes in the matrix elements of the valence band maximum, when going from the AE-VAL1 to the AE-VAL2 configurations (Table 8.4) are larger than for GaN (Table 8.3). Except for this differences, the conclusions for the interaction between electrons in the semicore shell and the deep core states contribution to the G_0W_0 results are same as in GaN: i) there exist strong exchange and correlation interactions between the $3d$ state and the $3s$, $3p$ states of Zn; ii) the deep core states have a non-negligible contribution to the electronic structure of this material, especially for the semicore d states, again confirming the necessity for an all-electron treatment in the G_0W_0 calculations.

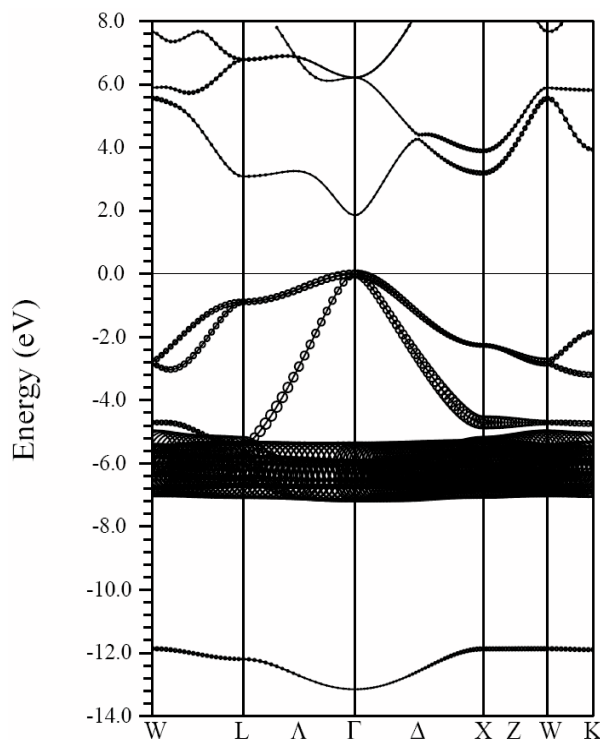


Figure 8.12: Band character plot of ZnS (in eV, taking the Fermi energy as the zero point) for the d component of Zn from the all-electron LDA calculation. The amount of Zn d character is represented by the radius of the circles.

Table 8.5: Matrix elements of the self-energy [in eV] (correlation term: Σ^c , exchange term: Σ^x) and exchange-correlation potential V^{xc} for GaN in our AE-VAL1, AE-VAL2, and AE- G_0W_0 calculations.

	ϵ_{LDA}	Σ^c	Σ^x	$\Sigma^c + \Sigma^x$	V^{xc}	$\Sigma - V^{xc}$	$\epsilon_{G_0W_0}$
AE-VAL1 (Ga: $3d, 4s, 4p$):							
Γ_v	0.00	3.16	-21.60	-18.44	-18.65	0.21	0.00
Γ_c	1.76	-3.75	-9.41	-13.16	-14.47	1.31	2.86
$\Gamma_c - \Gamma_v$	1.76	-6.91	12.19	5.28	4.18	1.10	2.86
AE-VAL2 (Ga: $3s, 3p, 3d, 4s, 4p$):							
Γ_v	0.00	3.22	-22.61	-19.39	-19.21	0.18	0.00
Γ_c	1.76	-3.74	-10.02	-13.76	-14.81	1.05	2.99
$\Gamma_c - \Gamma_v$	1.76	-6.96	12.59	5.63	4.40	1.23	2.99
AE:							
Γ_v	0.00	3.19	-23.88	-20.69	-20.48	-0.21	0.00
Γ_c	1.76	-3.71	-11.59	-15.30	-16.12	0.82	2.79
$\Gamma_c - \Gamma_v$	1.76	-6.90	12.29	5.39	4.36	1.03	2.79

8.3.2 Band Gaps

In the previous chapter we have shown, through GaAs, that including only the outermost shell in the many body correction leads to large core-valence partitioning errors in the G_0W_0 band gaps of materials with semicore states. In GaN and ZnS, the semicore $3d$ states of the cation atom hybridize with the s valence states of N and the p valence states of S respectively (Fig. 8.9 and Fig. 8.12). This hybridization obviously makes the treatment of the d orbital as core states inappropriate. Still, whether the inclusion of the $3s, 3p$ states of the cation explicitly in the many body corrections is required to obtain reliable band gaps, as it is for the d band position, remains an open question. Thus, we use the same calculation schemes of the previous subsection to investigate the influence of the $3s, 3p$ states of the cation as well as deep core electrons on the G_0W_0 band gaps.

In Table 8.5, we show the matrix elements of the self-energy and exchange-correlation potential for the conduction band maximum (denoted as Γ_c in the table) and valence band maximum states (Γ_v) as well as their difference in GaN. The core-valence partitioned treatment using either the AE-VAL1 or the AE-VAL2 schemes has little influence on the correlation term of the self-energy. Its influence on the matrix elements of the exchange term of the self-energy and the exchange-correlation potential is of the order of eV. These errors, as usual, tend to cancel each other so that its influence on both the G_0W_0 correction to the Kohn-Sham energies and the band gaps is reduced to values in the order of 0.1 eV.

The same matrix elements are shown in Table 8.6 for ZnS. Comparing the AE-VAL2 with the AE-VAL1 calculations, we observe that including the $3s$, $3p$ states of Zn in the G_0W_0 correction already has a noticeable effect on the correlation term of the self-energy, in the order of 0.2 eV for its contribution to the band-gap, which was not observed in GaN. This is due to the hybridization between the $3d$ states of Zn and valence band maximum state, which strengthens the interaction between the latter and the $3s$, $3p$ states of Zn. Accordingly, a core-valence partitioning which treats the $3s$, $3p$ states of Zn as core, as in the AE-VAL1 calculation, is inappropriate. When the G_0W_0 band gap correction is calculated, the large changes of the exchange term of the self-energy and the exchange-correlation potential due to the core-valence partitioning do not cancel each other as much as in GaN. This behavior is similar to that observed in the previous chapter for materials with semicore states excluded from the many-body treatment, which also confirms the conclusion in Ref. [133] that splitting the shell in the PP- G_0W_0 calculations can lead to errors due to the different treatment of the interaction of the $3d$ states of the cation with the sp states of the same shell and the sp valence states from the anion. Thus, for the LDA based G_0W_0 method to address these band gaps on relatively safe grounds, an explicit treatment of the whole semicore shell is required. This problem seems to be circumvented using OEP_x based pseudopotentials for the DFT calculations, Ref. [142], due to the better description of the exact exchange interaction implied in the pseudopotential. Already their DFT band gaps show much better agreement with experiments than the LDA results, and their G_0W_0 results obviously benefit from the better starting point.

8.4 Conclusion

In conclusion, the LDA based G_0W_0 method systematically underestimates the semicore d -state binding energies and the fundamental band gaps in the IIb-VI semiconductors and group III nitrides.

The semicore d states interact with the sp states in the same shell through both exchange and correlation, with the former increasing the binding energy and the latter decreasing it. Whilst the contribution from the exchange term of the self-energy is dominant, the correlation term contributes noticeably and can not be neglected. Ignoring these interactions in the G_0W_0 calculations is physically incorrect, resulting a strong underestimation of the d state binding energies. The interaction of the deep core states with the semicore d states is weaker but with similar properties. Including these interactions further increases the d state binding energies, indicating the importance of the all-electron feature in the G_0W_0 calculations.

The effect of the deep core states on the G_0W_0 band-gaps is small (in the order of 0.2 eV). While in GaN, omitting the $3s$ and $3p$ states of Ga still gives a good

Table 8.6: Matrix elements of the self-energy [in eV] (correlation term: Σ^c , exchange term: Σ^x) and exchange-correlation potential V^{xc} for ZnS in our AE-VAL1, AE-VAL2, and AE- G_0W_0 calculations.

	ϵ_{LDA}	Σ^c	Σ^x	$\Sigma^c + \Sigma^x$	V^{xc}	$\Sigma - V^{xc}$	$\epsilon_{G_0W_0}$
AE-VAL1 (Zn: 3d, 4s):							
Γ_v	0.00	2.41	-18.44	-16.03	-16.36	0.33	0.00
Γ_c	1.85	-3.88	-6.64	-10.52	-11.78	1.26	2.78
$\Gamma_c - \Gamma_v$	1.85	-6.29	11.80	5.51	4.58	0.93	2.78
AE-VAL2 (Zn: 3s, 3p, 3d, 4s):							
Γ_v	0.00	2.55	-20.34	-17.79	-17.37	-0.42	0.00
Γ_c	1.85	-3.91	-7.36	-11.27	-12.18	0.91	3.18
$\Gamma_c - \Gamma_v$	1.85	-6.46	12.98	6.52	5.19	1.33	3.18
AE:							
Γ_v	0.00	2.58	-23.08	-20.50	-19.93	-0.57	0.00
Γ_c	1.85	-3.91	-9.37	-13.28	-14.05	0.77	3.19
$\Gamma_c - \Gamma_v$	1.85	-6.49	13.71	7.22	5.88	1.34	3.19

approximation to the fundamental band gap, in ZnS, the interaction between the valence band maximum and the 3s, 3p states of Zn has to be included in the many-body corrections. Otherwise, an error of 0.4 eV due to core-valence partitioning is to be expected. This is due to the hybridization of the 3d semicore state with the p states of the anion, which constitute the highest occupied band. The same behavior can be expected for other IIb-VI semiconductors. Thus, at least the whole semicore shell has to be included in order to obtain reliable G_0W_0 fundamental band gaps. To improve agreement with experiments, efforts beyond the LDA based G_0W_0 framework are still required, e. g. including self-consistency or choosing a better starting point.

Concerning the starting point issue, our results confirm the conclusions of Rinke *et al.* [142] about the improvement of the band gaps by starting from OEP_x based DFT calculations, mainly due to the better KS starting points. Regarding the binding energy of the semicore d states, since their PP- G_0W_0 calculations treat only the outermost shell and the semicore d states of the cation as valence, the correlation contribution from the core states is absent. We have shown that neglecting these interactions leads to an artificial increase of the d state binding energies. This makes their conclusion for the binding energy of semicore d states disputable.

Chapter 9

Conclusions and Outlook

In this thesis, we have presented the implementation of a new all-electron G_0W_0 code based on the FP-(L)APW+lo method. Using this code, we have 1) investigated the origin of the well-known discrepancy between all-electron and pseudopotential based G_0W_0 band gaps; 2) systematically studied the role of semicore and core states in the quasiparticle description of IIb-VI semiconductors and group III nitrides. Hereinafter, we summarize our results.

9.1 Implementation

Part of the difficulties for the implementation of this code is due to the complicated form of the (L)APW+lo basis functions. Expansion of the non-local operators, like P , W , and Σ , requires a set of functions reliable and efficient in reproducing the product of any pair of Kohn-Sham wave functions. For our code, we have chosen the mixed basis set, which follows the same space partition as the APW-based methods. We have shown that, with a careful choice of the parameters defining the basis set in both the muffin-tin and the interstitial regions, an excellent compromise between efficiency and accuracy can be obtained.

The calculation of the polarizability requires a precise \mathbf{q} -dependent integration in the Brillouin-zone, in which all possible transitions from occupied states to unoccupied states and back conserving the wavenumber are included. Based on the early work of Rath and Freeman [104] we have extended the linear tetrahedron method to the \mathbf{q} -dependent case, including also the frequency-dependency of the integrand and the variation of the matrix elements in Eq. 5.22 inside each tetrahedron. The former enables the application of this method beyond the static limit, while the latter improves the efficiency by reducing the number of \mathbf{k} -points required for a given precision. The method is specially efficient for the treatment of metals, as was shown in our tests for the free electron gas.

The inclusion of the Γ -point in the \mathbf{q} mesh poses a major challenge, due to the divergence of the Coulomb matrix (Sec. 5.5). It is well known from the plane-wave expansion, that reformulating the correlation interaction in terms of the symmetrized dielectric matrix, the divergence of the Coulomb matrix is canceled by the zero of the polarization matrix. The analytical expression for this limit within the mixed basis expansion has been obtained, to our knowledge, for the first time (Appendix F). The still remaining singularity in v and W^c can be integrated to obtain the self-energy, but makes it numerically unstable. By adding and subtracting an analytic (and analytically integrable) function with the same singularity at the Γ point (Appendix C and G, and Sec. 5.5). we have achieved an efficient and numerically stable calculation of the self-energy.

The correlation term of the self-energy requires the numerical calculation of the convolution of G and W^c in frequency. This in turn requires a large number of sample points (usually hundreds) due to the rapidly varying shape of both functions. Applying analytical continuation, we can express all the frequency-dependent quantities on the imaginary frequency axis, where both G and W^c are smooth functions. Consequently, an accurate determination of the self-energy for imaginary frequencies requires only a small number of sample points (usually around twenty). These results are then fitted by a function and analytically continued onto the real frequency axis.

We believe that these features make our code the most accurate implementation of the G_0W_0 approximation at present, at the same time applicable to a wide range of materials.

9.2 All-electron vs. Pseudopotential Based G_0W_0 Band Gaps

Comparing all-electron and pseudopotential G_0W_0 calculations with all-electron based calculations where the exchange-correlation potential and self-energy are calculated only from the valence states we have been able to disentangle the role of core-valence partitioning and *pseudoization* in pseudopotential G_0W_0 calculations for a set of distinct materials (C, Si, BN, AlP, LiF, NaCl, GaAs, and CaSe).

Our results show that both approximations contribute noticeably to the discrepancy between all-electron and pseudopotential based G_0W_0 band gaps. While core-valence partitioning produces errors of several eV's in the matrix elements of Σ^x and V^{xc} . These errors tend to cancel each other when calculating the G_0W_0 correction to the Kohn-Sham eigenvalues. In materials without semicore states (C, Si, BN, AlP, and LiF) this cancellation results in a small increase, in the order of 0.1 eV, of the band gaps corrections. On the other hand, in the presence of semicore

states (CaSe, NaCl, and GaAs), the incomplete cancellation between the effects of core-valence partitioning on Σ^x and V^{xc} produces a decrease of the band gap correction, even after adding the contribution from Σ^c . In particular for GaAs, where very shallow $3d$ states appear, this effect can be as large as -0.45 eV. Treating the third shell of Ga explicitly in the many-body correction the same picture as for the materials without semicore states is recovered.

The influence of *pseudoization* on all the matrix elements (Σ^c , Σ^x and V^{xc}) is always in the order of 0.1 eV and produce an increase the G_0W_0 band gap correction of the same order of magnitude.

Based on these results, we conclude that in order to evaluate the G_0W_0 approximation, the full-potential all-electron treatment should be taken as benchmark.

9.3 IIB-VI semiconductors and Group III Nitrides

Taking GaN, ZnS, ZnSe, ZnTe, CdS, CdSe, and CdTe as examples, we have analyzed: 1) the quality of the LDA based all-electron G_0W_0 results, 2) the interaction between electrons in the semicore shell of the cations, and 3) the influence of the deep core states on the G_0W_0 results, in IIB-VI semiconductors and group III nitrides.

We have shown that both exchange and correlation interaction between electrons in the semicore shell of the cation is of crucial importance in the G_0W_0 calculations for a reasonable description of the d -band positions, exchange being the largest. The d -band binding energies are mainly determined by the balance between the interaction of the semicore d states with the sp valence states of the anion and with the sp states of the cation in the same shell. Treating the former at the G_0W_0 level, while keeping the latter in the LDA breaks this balance resulting in an unphysically high position of the semicore d -band. In ZnS, they are even driven into the region of the valence sp bands. Comparing our results to those of Ref. [142], we can confirm that the OEP_x functional sets up a better starting point for the calculation of the G_0W_0 correction to the band gap of these materials. On the other hand, the better agreement obtained for the d band positions is due to the neglect of the correlation interaction between states in the semicore shell.

We have also shown that the deep core states have a significant influence on G_0W_0 results. Their inclusion in the G_0W_0 calculation systematically improves the positions of the d bands (up to 1 eV) due to the strong exchange interaction between them and the semicore d states. This further emphasizes the need of an all-electron treatment in the G_0W_0 calculation of these materials. Nevertheless, our results confirm that LDA based G_0W_0 results systematically underestimate the fundamental band gaps and d -state binding energies of these materials, a clear indication that efforts beyond the LDA+ G_0W_0 treatment are required.

9.4 Outlook

The systematic underestimation of the fundamental band gaps in all the semiconductors studied and the d state binding energies in IIb-VI semiconductors and group III nitrides shows that efforts beyond the LDA+ G_0W_0 treatment are still required. In the near future, we plan to extend our studies by using different starting points, e.g. LDA+U, self-interaction corrected (SIC), or OEPx based DFT calculations. The LDA+U based G_0W_0 method has been implemented and our preliminary results for f systems are promising. In addition, the effect of self-consistency in the GW calculations is also of great importance. As a first step, the GW_0 method, which updates the quasiparticle energies in G self-consistently while keeping W_0 unchanged when calculating the self-energy, has been implemented.

Part V
Appendices

Appendix A

Integration of Plane Waves in the Interstitial region

The overlap matrix is:

$$\mathbb{O}_{\mathbf{G},\mathbf{G}'}^{\mathbf{q}} = \int_V [P_{\mathbf{G}}^{\mathbf{q}}(\mathbf{r})]^* P_{\mathbf{G}'}^{\mathbf{q}}(\mathbf{r}) d\mathbf{r}, \quad (\text{A.1})$$

using the definition of the interstitial plane wave, it can be written as:

$$\begin{aligned} \mathbb{O}_{\mathbf{G},\mathbf{G}'}^{\mathbf{q}} &= \frac{1}{V} \int_I e^{-i(\mathbf{q}+\mathbf{G})\cdot\mathbf{r}} e^{i(\mathbf{q}+\mathbf{G}')\cdot\mathbf{r}} d\mathbf{r} \\ &= \frac{1}{V} \int_I e^{-i(\mathbf{G}-\mathbf{G}')\cdot\mathbf{r}} d\mathbf{r} = \frac{1}{\Omega} \int_{I_\Omega} e^{-i(\mathbf{G}-\mathbf{G}')\cdot\mathbf{r}} d\mathbf{r}. \end{aligned} \quad (\text{A.2})$$

Thus, we can write $\mathbb{O}_{\mathbf{G},\mathbf{G}'}^{\mathbf{q}} \equiv \mathbb{O}_{\mathbf{G},\mathbf{G}'}$ since it has no \mathbf{q} dependence. The advantage is that it only needs to be calculated once. The integral over the interstitial region is carried out by integrating over the whole unit cell and subtracting the contribution from the atomic spheres. That is:

$$\mathcal{I}_{\mathbf{G}} \equiv \int_{I_\Omega} e^{i\mathbf{G}\cdot\mathbf{r}} d\mathbf{r} = \int_{\Omega} e^{i\mathbf{G}\cdot\mathbf{r}} d\mathbf{r} - \sum_{\alpha} \int_{\text{MT}_\alpha} e^{i\mathbf{G}\cdot\mathbf{r}} d\mathbf{r}. \quad (\text{A.3})$$

The integral over the unit cell is:

$$\int_{\Omega} e^{i\mathbf{G}\cdot\mathbf{r}} d\mathbf{r} = \Omega \delta_{\mathbf{G},0}, \quad (\text{A.4})$$

while the integral over the MT sphere is equal to the volume of the muffin-tin sphere (V_{MT}^α) if $\mathbf{G} = 0$. For the case $\mathbf{G} \neq 0$ the integral can be done using the Rayleigh-expansion for a plane wave in terms of spherical harmonics:

$$e^{i\mathbf{G}\cdot\mathbf{r}} = 4\pi e^{i\mathbf{G}\cdot\mathbf{r}_\alpha} \sum_{\lambda\mu} i^\lambda j_\lambda(r^\alpha G) Y_{\lambda,\mu}^*(\hat{G}) Y_{\lambda,\mu}(\hat{r}^\alpha), \quad (\text{A.5})$$

which when substituted in the last term of Eq. A.3 gives:

$$\begin{aligned}
\int_{\text{MT}_\alpha} e^{i\mathbf{G}\cdot\mathbf{r}} d\mathbf{r} &= 4\pi e^{i\mathbf{G}\cdot\mathbf{r}_\alpha} \sum_{\lambda,\mu} Y_{\lambda,\mu}^*(\hat{G}) i^\lambda \int_{\text{MT}_\alpha} j_\lambda(r^\alpha G) Y_{\lambda,\mu}(\hat{r}^\alpha) d\mathbf{r}^\alpha \\
&= 4\pi e^{i\mathbf{G}\cdot\mathbf{r}_\alpha} \sum_{\lambda,\mu} Y_{\lambda,\mu}^*(\hat{G}) i^\lambda \int_0^{R_{\text{MT}}^\alpha} j_\lambda(r^\alpha G) (r^\alpha)^2 dr^\alpha \int Y_{\lambda,\mu}(\hat{r}^\alpha) d\hat{r}^\alpha \\
&= 4\pi e^{i\mathbf{G}\cdot\mathbf{r}_\alpha} \sum_{\lambda,\mu} Y_{\lambda,\mu}^*(\hat{G}) i^\lambda \int_0^{R_{\text{MT}}^\alpha} j_\lambda(r^\alpha G) (r^\alpha)^2 dr^\alpha \sqrt{4\pi} \delta_{\lambda,0} \delta_{\mu,0} \\
&= 4\pi e^{i\mathbf{G}\cdot\mathbf{r}_\alpha} \int_0^{R_{\text{MT}}^\alpha} j_0(r^\alpha G) (r^\alpha)^2 dr^\alpha \\
&= 4\pi e^{i\mathbf{G}\cdot\mathbf{r}_\alpha} \left[\frac{\sin(GR_{\text{MT}}^\alpha) - (GR_{\text{MT}}^\alpha) \cos(GR_{\text{MT}}^\alpha)}{G^3} \right] \\
&= 3V_{\text{MT}}^\alpha e^{i\mathbf{G}\cdot\mathbf{r}_\alpha} \left[\frac{\sin(GR_{\text{MT}}^\alpha) - (GR_{\text{MT}}^\alpha) \cos(GR_{\text{MT}}^\alpha)}{(GR_{\text{MT}}^\alpha)^3} \right].
\end{aligned} \tag{A.6}$$

Thus we have:

$$\mathcal{I}_{\mathbf{G}} = \begin{cases} \Omega - \sum_{\alpha} V_{\text{MT}}^\alpha & \mathbf{G} = 0 \\ -3 \sum_{\alpha} V_{\text{MT}}^\alpha e^{i\mathbf{G}\cdot\mathbf{r}_\alpha} \left[\frac{\sin(GR_{\text{MT}}^\alpha) - (GR_{\text{MT}}^\alpha) \cos(GR_{\text{MT}}^\alpha)}{(GR_{\text{MT}}^\alpha)^3} \right] & \mathbf{G} \neq 0. \end{cases} \tag{A.7}$$

Using this result (Eq. A.7), the overlap matrix can be written as:

$$\boxed{\mathbb{O}_{\mathbf{G},\mathbf{G}'} = \frac{1}{\Omega} \mathcal{I}_{\mathbf{G}'-\mathbf{G}}} \tag{A.8}$$

Appendix B

The Overlap Matrix between a Plane Wave and a Mixed Basis Function in the Muffin-Tin Region

In this section we calculate the overlap matrix elements between the mixed basis function and the plane wave:

$$\mathcal{W}_{\mathbf{G}}^i(\mathbf{q}) = \langle \chi_i^{\mathbf{q}} | \mathbf{q} + \mathbf{G} \rangle = \frac{1}{\sqrt{V}} \int_V [\chi_i^{\mathbf{q}}(\mathbf{r})]^* e^{i(\mathbf{q}+\mathbf{G})\cdot\mathbf{r}} d^3r. \quad (\text{B.1})$$

Inside the MT-sphere, we have:

$$\begin{aligned} \mathcal{W}_{\mathbf{G}}^{\mathcal{L}}(\mathbf{q}) &= \frac{1}{\sqrt{V}} \int_V [\gamma_{\alpha,N,L,M}^{\mathbf{q}}(\mathbf{r})]^* e^{i(\mathbf{q}+\mathbf{G})\cdot\mathbf{r}} d^3r \\ &= \frac{1}{\sqrt{N_c V}} \sum_{\mathbf{R}} e^{-i\mathbf{q}\cdot(\mathbf{R}+\mathbf{r}_\alpha)} e^{i(\mathbf{q}+\mathbf{G})\cdot(\mathbf{R}+\mathbf{r}_\alpha)} \int_{\text{MT}} \gamma_{\alpha,N,L,M}^*(\mathbf{r}^\alpha) e^{i(\mathbf{q}+\mathbf{G})\cdot\mathbf{r}^\alpha} d^3r^\alpha \\ &= \frac{1}{\sqrt{N_c V}} \sum_{\mathbf{R}} e^{i\mathbf{G}\cdot(\mathbf{R}+\mathbf{r}_\alpha)} \int_{\text{MT}} v_{N,L}(r^\alpha) Y_{L,M}^*(T^{-1}\hat{r}^\alpha) e^{i(\mathbf{q}+\mathbf{G})\cdot\mathbf{r}^\alpha} d^3r^\alpha. \end{aligned} \quad (\text{B.2})$$

Using $\mathbf{G} \cdot \mathbf{R} = 2n\pi$ and the Rayleigh expansion (Eq. J.8) we obtain:

$$\begin{aligned}
\mathcal{W}_{\mathbf{G}}^{\mathcal{L}}(\mathbf{q}) &= 4\pi \sqrt{\frac{N_c}{V}} e^{i\mathbf{G} \cdot \mathbf{r}_a} \sum_{\lambda, \mu} i^\lambda Y_{\lambda, \mu}^*(T^{-1}\widehat{\mathbf{q}} + \mathbf{G}) \int_{\text{MT}} v_{N,L}(r^a) Y_{L,M}^*(T^{-1}\hat{r}^a) \times \\
&\quad j_\lambda(|\mathbf{q} + \mathbf{G}|r^a) Y_{\lambda, \mu}(T^{-1}\hat{r}^a) d^3r^a \\
&= \frac{4\pi}{\sqrt{\Omega}} e^{i\mathbf{G} \cdot \mathbf{r}_a} \sum_{\lambda, \mu} i^\lambda Y_{\lambda, \mu}^*(T^{-1}\widehat{\mathbf{q}} + \mathbf{G}) \int_0^{R_{\text{MT}}^a} v_{N,L}(r) j_\lambda(|\mathbf{q} + \mathbf{G}|r) r^2 dr \delta_{\lambda, L} \delta_{\mu, M} \\
&= \frac{4\pi}{\sqrt{\Omega}} e^{i\mathbf{G} \cdot \mathbf{r}_a} i^L Y_{L, M}^*(T^{-1}\widehat{\mathbf{q}} + \mathbf{G}) \int_0^{R_{\text{MT}}^a} v_{N,L}(r) j_L(|\mathbf{q} + \mathbf{G}|r) r^2 dr.
\end{aligned} \tag{B.3}$$

Thus, according to Eq. C.31 we end up with:

$$\boxed{\mathcal{W}_{\mathbf{G}}^{\mathcal{L}}(\mathbf{q}) = \frac{4\pi}{\sqrt{\Omega}} e^{i\mathbf{G} \cdot \mathbf{r}_a} i^L Y_{L, M}^*(T^{-1}\widehat{\mathbf{q}} + \mathbf{G}) \left\langle j_\lambda^{|\mathbf{G} + \mathbf{q}|} \right\rangle_{a, N, L}}. \tag{B.4}$$

In the interstitial region, using Eq. 5.14, we have:

$$\begin{aligned}
\mathcal{W}_{\mathbf{G}}^{\mathcal{L}}(\mathbf{q}) &= \frac{1}{V} \sum_{\mathbf{G}'} \tilde{\mathcal{S}}_{\mathbf{G}', i}^* \int_I e^{-i(\mathbf{q} + \mathbf{G}') \cdot \mathbf{r}} e^{i(\mathbf{q} + \mathbf{G}) \cdot \mathbf{r}} d^3r \\
&= \frac{1}{\Omega} \sum_{\mathbf{G}'} \tilde{\mathcal{S}}_{\mathbf{G}', i}^* \int_I^{WZ} e^{i(\mathbf{G} - \mathbf{G}') \cdot \mathbf{r}} d^3r,
\end{aligned} \tag{B.5}$$

which according to equation A.3 is:

$$\boxed{\mathcal{W}_{\mathbf{G}}^{\mathcal{L}}(\mathbf{q}) = \frac{1}{\Omega} \sum_{\mathbf{G}'} \tilde{\mathcal{S}}_{\mathbf{G}', i}^* \mathcal{I}_{\mathbf{G} - \mathbf{G}'}}. \tag{B.6}$$

Appendix C

The Coulomb Matrix

The coulomb matrix $v_{i,j}(\mathbf{q})$ is given by:

$$v_{i,j}(\mathbf{q}) = \int_V \int_V (\chi_i^{\mathbf{q}}(\mathbf{r}_1))^* v(\mathbf{r}_1, \mathbf{r}_2) \chi_j^{\mathbf{q}}(\mathbf{r}_2) d\mathbf{r}_2 d\mathbf{r}_1, \quad (\text{C.1})$$

which, making use of Eq. I.6, can be written as:

$$v_{i,j}(\mathbf{q}) = N_c \int_{\Omega} \int_{\Omega} (\chi_i^{\mathbf{q}}(\mathbf{r}_1))^* \sum_{\mathbf{R}} v(\mathbf{r}_1, \mathbf{r}_2 - \mathbf{R}) e^{-i\mathbf{q}\cdot\mathbf{R}} \chi_j^{\mathbf{q}}(\mathbf{r}_2) d\mathbf{r}_2 d\mathbf{r}_1. \quad (\text{C.2})$$

According to the region to which \mathbf{r}_1 and \mathbf{r}_2 belong, we can distinguish three different cases. We analyze them separately in the following sections.

C.1 Case A: Both \mathbf{r}_1 and \mathbf{r}_2 belong to a MT-sphere Region

C.1.1 \mathbf{r}_1 and \mathbf{r}_2 belong to MT-spheres Surrounding Different Atoms

In this case Eq. C.2 can be written as:

$$v_{\mathcal{L},\mathcal{L}'}(\mathbf{q}) = N_c \int_{V_{\text{MT}}^{\alpha}} \int_{V_{\text{MT}}^{\alpha'}} (\gamma_{\alpha,N,L,M}^{\mathbf{q}}(\mathbf{r}_1))^* \sum_{\mathbf{R}} v(\mathbf{r}_1, \mathbf{r}_2 - \mathbf{R}) e^{-i\mathbf{q}\cdot\mathbf{R}} \gamma_{\alpha',N',L',M'}^{\mathbf{q}}(\mathbf{r}_2) d\mathbf{r}_2 d\mathbf{r}_1, \quad (\text{C.3})$$

where we have shortened the notation by using a unique index $\mathcal{L} \equiv \{\alpha, N, L, M\}$.

Inserting the specific form of the Coulomb potential and the basis functions (Eq. 5.15), Eq. C.3 can be rewritten as:

$$v_{\mathcal{L},\mathcal{L}'}(\mathbf{q}) = \frac{N_c e^{i\mathbf{q}\cdot(\mathbf{r}_{\alpha'} - \mathbf{r}_\alpha)}}{\sqrt{N_c^2}} \iint_{V_{MT}^\alpha} v_{\alpha,N,L}(r^\alpha) Y_{L,M}^*(\hat{r}^\alpha) \sum_{\mathbf{R}} \frac{e^{-i\mathbf{q}\cdot\mathbf{R}}}{|\mathbf{r}_1^\alpha - \mathbf{r}_2^{\alpha'} + \mathbf{R}_{\alpha,\alpha'}|} v_{\alpha',N',L'}(r_2^{\alpha'}) Y_{L',M'}(\hat{r}_2^{\alpha'}) d\mathbf{r}_2 d\mathbf{r}_1, \quad (\text{C.4})$$

where $\mathbf{R}_{\alpha,\alpha'} = \mathbf{R} + \mathbf{r}_\alpha - \mathbf{r}_{\alpha'}$ and $\mathbf{r}_1^\alpha \equiv \mathbf{r}_1 - \mathbf{r}_\alpha = T_\alpha \mathbf{r}_1^\alpha$.

Making use of the Laplace expansion for the Coulomb potential in terms of spherical harmonics,

$$\begin{aligned} \frac{1}{|\mathbf{r}_1 - \mathbf{r}_2|} &= \sum_{l=0}^{\infty} \sum_{m=-l}^l \frac{4\pi}{2l+1} \frac{r_{<}^l}{r_{>}^{l+1}} Y_{l,m}^*(\hat{r}_{<}) Y_{l,m}(\hat{r}_{>}) \\ &= \sum_{l=0}^{\infty} \sum_{m=-l}^l \frac{4\pi}{2l+1} \frac{r_{<}^l}{r_{>}^{l+1}} Y_{l,m}(\hat{r}_{<}) Y_{l,m}^*(\hat{r}_{>}), \end{aligned} \quad (\text{C.5})$$

where $r_{<} = \min(r_1, r_2)$ and $r_{>} = \max(r_1, r_2)$,¹ and taking into account that muffin-tin spheres do not overlap (if $\alpha \neq \alpha'$ we have $r_{<} = |\mathbf{r}_2^\alpha - \mathbf{r}_1^{\alpha'}|$ and $r_{>} = |\mathbf{R}_{\alpha,\alpha'}|$), the interaction factor in Eq. C.4 becomes:

$$\frac{1}{|\mathbf{r}_1^\alpha - \mathbf{r}_2^{\alpha'} + \mathbf{R}_{\alpha,\alpha'}|} = \sum_{l,m} \frac{4\pi}{2l+1} \frac{|\mathbf{r}_2^\alpha - \mathbf{r}_1^{\alpha'}|^l}{R_{\alpha,\alpha'}^{l+1}} Y_{l,m}^*(\widehat{\mathbf{r}_2^\alpha - \mathbf{r}_1^{\alpha'}}) Y_{l,m}(\hat{R}_{\alpha,\alpha'}). \quad (\text{C.6})$$

Using the Addition Theorem for Solid Harmonics of Ref. [149] we can rewrite Eq. C.6 as:

$$\begin{aligned} \frac{1}{|\mathbf{r}_1^\alpha - \mathbf{r}_2^{\alpha'} + \mathbf{R}_{\alpha,\alpha'}|} &= \\ (4\pi)^{\frac{3}{2}} \sum_{l,m} \sum_{l',m'} \tilde{g}_{l,m;l',m'} \frac{(r_1^\alpha)^l (r_2^{\alpha'})^{l'}}{R_{\alpha,\alpha'}^{l+l'+1}} Y_{l,m}^*(\hat{\mathbf{r}}_1^\alpha) Y_{l',m'}^*(\hat{\mathbf{r}}_2^{\alpha'}) Y_{(l+l'),(m+m')}(\hat{R}_{\alpha,\alpha'}), \end{aligned} \quad (\text{C.7})$$

¹The equivalence of the two expressions can be proved as follows: Under complex conjugation, the spherical harmonics satisfy: $Y_{l,m}^*(\hat{r}) = (-1)^m Y_{l,-m}(\hat{r})$, thus, the sum over m in Eq. C.5 can be written as $\sum_{m=-l}^l (-1)^m Y_{l,-m}(\hat{r}_1) (-1)^m Y_{l,-m}^*(\hat{r}_2) = \sum_{m=-l}^l (-1)^{2m} Y_{l,-m}(\hat{r}_1) Y_{l,-m}^*(\hat{r}_2)$. If we change m by $-m$, and since the sum runs from $-l$ to l it can be written as $\sum_{m=-l}^l Y_{l,m}(\hat{r}_1) Y_{l,m}^*(\hat{r}_2)$.

where, according to Ref. [83],

$$\begin{aligned}\tilde{g}_{l,m;l',m'} &= \frac{(-1)^l \sqrt{[2(l+l')]!} (l, m; l', m' | l+l', m+m')}{\sqrt{(2l'+1)!(2l+1)!(2l+2l'+1)!}} \\ &= (-1)^l \sqrt{\frac{(l+l'+m+m')!(l+l'-m-m')!}{(2l+1)(2l'+1)[2(l+l')+1](l+m)!(l-m)!(l'+m')!(l'-m')!}}\end{aligned}\quad (\text{C.8})$$

and $(l, m; l', m' | l+l', m+m')$ is the corresponding Clebsch-Gordan coefficient. Including Eq. C.7 into Eq. C.4, and using the definition of $\mathbf{R}_{\alpha,\alpha'} = \mathbf{R} + \mathbf{r}_\alpha - \mathbf{r}_{\alpha'}$, we have:

$$\begin{aligned}v_{\mathcal{L},\mathcal{L}'}(\mathbf{q}) &= \sum_{\lambda=0}^{\infty} \sum_{\mu=-\lambda}^{\lambda} \sum_{\lambda_1=0}^{\infty} \sum_{\mu_1=-\lambda_1}^{\lambda_1} (4\pi)^{\frac{3}{2}} \tilde{g}_{\lambda,\mu;\lambda_1,\mu_1} \sum_{\mathbf{R}} \frac{e^{-i\mathbf{q}\cdot\mathbf{R}_{\alpha,\alpha'}}}{R_{\alpha,\alpha'}^{\lambda+\lambda_1+1}} Y_{(\lambda+\lambda_1),(\mu+\mu_1)}(\hat{R}_{\alpha,\alpha'}) \times \\ &\quad \int_{V_{\text{MT}}^\alpha} v_{\alpha,N,L}(r_1^\alpha) Y_{L,M}^*(\hat{\mathbf{r}}_1^\alpha) (r_1^\alpha)^\lambda Y_{\lambda,\mu}^*(\hat{\mathbf{r}}_1^\alpha) d\mathbf{r}_1 \times \\ &\quad \int_{V_{\text{MT}}^{\alpha'}} (r_2^{\alpha'})^{\lambda_1} Y_{\lambda_1,\mu_1}^*(\hat{\mathbf{r}}_2^{\alpha'}) v_{\alpha',N',L'}(r_2^{\alpha'}) Y_{L',M'}(\hat{\mathbf{r}}_2^{\alpha'}) d\mathbf{r}_2.\end{aligned}\quad (\text{C.9})$$

Defining the structure constants

$$\boxed{\mathbb{S}_{l',m';l,m}^{\alpha,\alpha'}(\mathbf{q}) = (4\pi)^{\frac{3}{2}} \tilde{g}_{l',m';l,m} \Sigma_{l'+l,m'+m}^{\alpha,\alpha'}(-\mathbf{q})}, \quad (\text{C.10})$$

with

$$\boxed{\Sigma_{\lambda,\mu}^{\alpha,\alpha'}(\mathbf{q}) = \sum_{\mathbf{R}} \frac{e^{i\mathbf{q}\cdot\mathbf{R}_{\alpha,\alpha'}}}{R_{\alpha,\alpha'}^{(\lambda+1)}} Y_{\lambda,\mu}(\hat{R}_{\alpha,\alpha'})}, \quad (\text{C.11})$$

and separating the integrals over the muffin-tin sphere into the radial and the angular parts, we have:

$$\begin{aligned}v_{\mathcal{L},\mathcal{L}'}(\mathbf{q}) &= \sum_{\lambda,\mu} \sum_{\lambda_1,\mu_1} \mathbb{S}_{\lambda,\mu;\lambda_1,\mu_1}^{\alpha,\alpha'}(\mathbf{q}) \left(\int_0^{R_{\text{MT}}^\alpha} (r_1^\alpha)^\lambda v_{\alpha,N,L}(r_1^\alpha) (r_1^\alpha)^2 dr_1^\alpha \right) \times \\ &\quad \left(\int Y_{L,M}^*(\hat{r}_1^\alpha) Y_{\lambda,\mu}^*(\hat{\mathbf{r}}_1^\alpha) d\hat{r}_1^\alpha \right) \times \\ &\quad \left(\int_0^{R_{\text{MT}}^{\alpha'}} (r_2^{\alpha'})^{\lambda_1} v_{\alpha',N',L'}(r_2^{\alpha'}) (r_2^{\alpha'})^2 dr_2^{\alpha'} \right) \left(\int Y_{\lambda_1,\mu_1}^*(\hat{r}_2^{\alpha'}) Y_{L',M'}(\hat{\mathbf{r}}_2^{\alpha'}) d\hat{r}_2^{\alpha'} \right).\end{aligned}\quad (\text{C.12})$$

For the calculation of $\Sigma_{\lambda,\mu}^{\alpha,\alpha'}(\mathbf{q})$, we follow the method in Ref. [150].

To solve the angular integrals, we make a coordinate transition from the coordinate of the unit cell to the internal coordinate of this atom. The rotation matrix is T_α . We have:

$$Y_{L,M}(\hat{r}^\alpha) = Y_{L,M}(T_\alpha^{-1}\hat{\mathbf{r}}^\alpha) = T_\alpha Y_{L,M}(\hat{\mathbf{r}}^\alpha). \quad (\text{C.13})$$

Now using Eq. 4.8 in Ref. [83], we have:

$$T_\alpha Y_{L,M}(\hat{\mathbf{r}}^\alpha) = \sum_{M_1=-L}^L D_{M_1,M}^{\alpha,L} Y_{L,M_1}(\hat{\mathbf{r}}^\alpha), \quad (\text{C.14})$$

where $D_{M_1,M}^{\alpha,L}$ is the rotation matrix for the spherical harmonics. How to calculate it is illustrated in the same reference.

We define:

$$\langle r^\lambda \rangle_{\alpha,N,L} \equiv \int_0^{R_{\text{MT}}^\alpha} (r^\alpha)^{\lambda+2} v_{\alpha,N,L}(r^\alpha) dr^\alpha. \quad (\text{C.15})$$

Using the orthogonality of $Y_{l,m}$, the relation $Y_{l,m}^* = (-1)^m Y_{l,-m}$ and Eq. C.14, Eq. C.9 becomes:

$$v_{\mathcal{L},\mathcal{L}'}(\mathbf{q}) = \sum_{\mu,\mu_1} \mathbb{S}_{L,\mu;L',\mu_1}^{\alpha,\alpha'}(\mathbf{q}) \langle r^L \rangle_{\alpha,N,L} (-1)^\mu \langle r^{L'} \rangle_{\alpha,N',L'} D_{-\mu,M}^{\alpha,L*} D_{\mu_1,M'}^{\alpha',L'} \quad (\text{C.16})$$

C.1.2 r_1 and r_2 belong to MT-spheres Surrounding Same Atoms

In this case, $\mathbf{R}_{\alpha,\alpha'} = \mathbf{R}$ and the same equations are obtained with the restriction that $\mathbf{R} \neq 0$. When $\mathbf{R} = 0$ and $\alpha = \alpha'$, the application of Eq. C.5 into Eq. C.4 leads to:

$$v_{\mathcal{L},\mathcal{L}'}(\mathbf{q}) = \sum_\lambda \frac{4\pi}{2\lambda+1} \left(\iint_0^{R_{\text{MT}}^\alpha} v_{\alpha,N,L,M}(r_1^\alpha) \frac{r_1^\lambda}{r_2^{(\lambda+1)}} v_{\alpha,N',L',M'}(r_2^\alpha) (r_1^\alpha)^2 dr_1^\alpha (r_2^\alpha)^2 dr_2^\alpha \right) \times \sum_\mu \left(\int Y_{\lambda,\mu}(\hat{\mathbf{r}}_1^\alpha) Y_{L,M}^*(\hat{\mathbf{r}}_1^\alpha) d\hat{\mathbf{r}}_1^\alpha \right) \left(\int Y_{\lambda,\mu}(\hat{\mathbf{r}}_2^\alpha) Y_{L',M'}(\hat{\mathbf{r}}_2^\alpha) d\hat{\mathbf{r}}_2^\alpha \right). \quad (\text{C.17})$$

The double radial integrals in this case can not be separated. If we define:

$$\left\langle \begin{array}{c} r_1^\lambda \\ r_2^{<} \\ r_2^{>} \end{array} \right\rangle_{\alpha,N,L,N',L'} = \iint_0^{R_{\text{MT}}^\alpha} v_{\alpha,N,L}(r_1^\alpha) \frac{r_1^\lambda}{r_2^{(\lambda+1)}} v_{\alpha,N',L'}(r_2^\alpha) (r_1^\alpha)^2 dr_1^\alpha (r_2^\alpha)^2 dr_2^\alpha, \quad (\text{C.18})$$

using again Eqs. C.13 and C.14, C.17 becomes:

$$v_{\mathcal{L},\mathcal{L}'}(\mathbf{q}) = \frac{4\pi}{2L+1} \left\langle \begin{array}{c} r_{<}^L \\ r_{>}^{L+1} \end{array} \right\rangle_{\alpha,N,L,N',L} \sum_{M_1,M_2} D_{M_1,M}^{\alpha,L*} D_{M_2,M'}^{\alpha,L'} \delta_{L,L'} \delta_{M_1,M_2}. \quad (\text{C.19})$$

The sum in the second term of Eq. C.19 can be transformed to

$$\sum_{M_1,M_2} D_{M_1,M}^{\alpha,L*} D_{M_2,M'}^{\alpha,L'} \delta_{L,L'} \delta_{M_1,M_2} = \sum_{M_1} D_{M_1,M}^{\alpha,L} D_{M_1,M'}^{\alpha,L} = \delta_{M,M'}, \quad (\text{C.20})$$

where the last equality holds from the orthogonality of the rotation matrices (see Ref. [83]). Then, for $\alpha = \alpha'$ we have

$$\boxed{v_{\mathcal{L},\mathcal{L}'}(\mathbf{q}) = \sum_{M_1,M_2} \mathbb{S}_{L,M_1;L',M_2}^{\alpha,\alpha}(\mathbf{q}) \langle r^L \rangle_{\alpha,N,L} (-1)^{M_1} \langle r^{L'} \rangle_{\alpha,N',L'} D_{-M_1,M}^{\alpha,L*} D_{M_2,M'}^{\alpha,L'} + \frac{4\pi}{2L+1} \left\langle \begin{array}{c} r_{<}^L \\ r_{>}^{L+1} \end{array} \right\rangle_{\alpha,N,L,N',L} \delta_{L,L'} \delta_{M,M'}}, \quad (\text{C.21})$$

where $\mathbb{S}_{l',m';l,m}^{\alpha,\alpha}(\mathbf{q})$ is the same as Eq. C.10 with:

$$\Sigma_{\lambda,\mu}^{\alpha,\alpha}(\mathbf{q}) = \sum_{\mathbf{R} \neq 0} \frac{e^{i\mathbf{q}\cdot\mathbf{R}}}{R^{(\lambda+1)}} Y_{\lambda,\mu}(\hat{R}). \quad (\text{C.22})$$

C.2 Case B: Both \mathbf{r}_1 and \mathbf{r}_2 belong to the Interstitial Region

In this case, it is better to use expression C.1, which can be written as:

$$v_{i,j}(\mathbf{q}) = \int_V \int_V \left[\tilde{P}_i^{\mathbf{q}}(\mathbf{r}_1) \right]^* \frac{1}{|\mathbf{r}_1 - \mathbf{r}_2|} \tilde{P}_j^{\mathbf{q}}(\mathbf{r}_2) d\mathbf{r}_2 d\mathbf{r}_1. \quad (\text{C.23})$$

Taking the Fourier expansion of the Coulomb interaction:

$$\frac{1}{|\mathbf{r}_1 - \mathbf{r}_2|} = \frac{1}{V} \sum_{\mathbf{q}\mathbf{G}} e^{i(\mathbf{q}+\mathbf{G})\mathbf{r}_1} \frac{4\pi}{|\mathbf{q} + \mathbf{G}|^2} e^{-i(\mathbf{q}+\mathbf{G})\mathbf{r}_2}, \quad (\text{C.24})$$

we can rewrite Eq. C.23 as:

$$v_{i,j}(\mathbf{q}) = \sum_{\mathbf{G}} \left(\frac{1}{\sqrt{V}} \int_V \left[\tilde{P}_i^{\mathbf{q}}(\mathbf{r}_1) \right]^* e^{i(\mathbf{q}+\mathbf{G})\mathbf{r}_1} d\mathbf{r}_1 \right) \frac{4\pi}{|\mathbf{q} + \mathbf{G}|^2} \times \left(\frac{1}{\sqrt{V}} \int_V e^{-i(\mathbf{q}+\mathbf{G})\mathbf{r}_2} \tilde{P}_j^{\mathbf{q}}(\mathbf{r}_2) d\mathbf{r}_2 \right). \quad (\text{C.25})$$

The factors in brackets are the matrix elements $\mathcal{W}_{\mathbf{G}}^i(\mathbf{q})$ defined in Eq. B.6, we end up with:

$$v_{i,j}(\mathbf{q}) = \sum_{\mathbf{G}} \mathcal{W}_{\mathbf{G}}^i(\mathbf{q}) \frac{4\pi}{|\mathbf{q} + \mathbf{G}|^2} \mathcal{W}_{\mathbf{G}}^{*j}(\mathbf{q}). \quad (\text{C.26})$$

C.3 Case C: Either \mathbf{r}_1 or \mathbf{r}_2 belong to the Interstitial Region, the Other to a MT-sphere

Starting again from Eq. C.2, if we suppose that \mathbf{r}_1 is in the interstitial region, and \mathbf{r}_2 belongs to the α -atom MT-sphere we can write:

$$v_{i,\mathcal{L}}(\mathbf{q}) = N_c \int_{\Omega} \int_{\Omega} [\tilde{P}_i^{\mathbf{q}}(\mathbf{r}_1)]^* \sum_{\mathbf{R}} \frac{e^{-i\mathbf{q}\cdot\mathbf{R}}}{|\mathbf{r}_1 - \mathbf{r}_2 + \mathbf{R}|} \gamma_{\alpha,N,L,M}^{\mathbf{q}}(\mathbf{r}_2) d\mathbf{r}_2 d\mathbf{r}_1. \quad (\text{C.27})$$

Making use of Eq. C.24, this equation can be written as:

$$v_{i,\mathcal{L}}(\mathbf{q}) = \frac{N_c}{V} \int_{\Omega} \int_{\Omega} [\tilde{P}_i^{\mathbf{q}}(\mathbf{r}_1)]^* \sum_{\mathbf{q}'} \sum_{\mathbf{G}'} \sum_{\mathbf{R}} \frac{4\pi e^{i(\mathbf{q}'+\mathbf{G}')\cdot(\mathbf{r}_1-\mathbf{r}_2+\mathbf{R})}}{|\mathbf{q}' + \mathbf{G}'|^2} e^{-i\mathbf{q}\cdot\mathbf{R}} \times \gamma_{\alpha,N,L,M}^{\mathbf{q}}(\mathbf{r}_2) d\mathbf{r}_2 d\mathbf{r}_1. \quad (\text{C.28})$$

The integrations in the variables \mathbf{r}_1 and \mathbf{r}_2 can be separated, giving:

$$v_{i,\mathcal{L}}(\mathbf{q}) = \frac{1}{\Omega} \sum_{\mathbf{q}'} \sum_{\mathbf{G}'} \frac{4\pi}{|\mathbf{q}' + \mathbf{G}'|^2} \sum_{\mathbf{R}} e^{-i(\mathbf{q}-\mathbf{q}')\cdot\mathbf{R}} \mathcal{W}_{\mathbf{G}'}^{*i} \mathcal{W}_{\mathbf{G}'}^{\mathcal{L}}, \quad (\text{C.29})$$

where we made use of the condition $e^{-i\mathbf{G}'\cdot\mathbf{R}} = 1$. Through a series of deduction procedure, this equation can be simplified into:

$$v_{i,\mathcal{L}}(\mathbf{q}) = \frac{(4\pi)^2}{\sqrt{\Omega}} \sum_{\mathbf{G}'} \frac{1}{|\mathbf{q} + \mathbf{G}'|^2} S_{\mathbf{G}',i}^* Y_{L,M}(T_{\alpha}^{-1}(\widehat{\mathbf{G}' + \mathbf{q}})) \langle j_L^{|\mathbf{G}'+\mathbf{q}|} \rangle_{\alpha,L,M}, \quad (\text{C.30})$$

where

$$\langle j_{\lambda}^{|\mathbf{G}+\mathbf{q}|} \rangle_{\alpha,N,L} \equiv \int_0^{R_{\text{MT}}^{\alpha}} j_{\lambda}(|\mathbf{G} + \mathbf{q}| r^{\alpha}) v_{\alpha,N,L}(r^{\alpha}) (r^{\alpha})^2 dr^{\alpha}, \quad (\text{C.31})$$

and $\tilde{S}_{\mathbf{G},i}$ is defined in Eq. 5.14.

C.4 The Singularity at the Γ Point

The divergence of the Coulomb matrix $v_{i,j}(\mathbf{q})$ as $\mathbf{q} \rightarrow 0$ can be easily seen by taking a plane wave expansion:

$$v_{\mathbf{G},\mathbf{G}'}(\mathbf{q}) = \frac{4\pi}{|\mathbf{q} + \mathbf{G}|^2} \delta_{\mathbf{G},\mathbf{G}'}. \quad (\text{C.32})$$

Evidently, $v_{0,0} \rightarrow \infty$ as $\mathbf{q} \rightarrow 0$ since the limit corresponds to the potential generated by a constant, finite charge density, infinitely extended in space.

The advantage of the plane wave expansion is that one can clearly separate the divergent terms by writing:

$$v_{\mathbf{G},\mathbf{G}'}(\mathbf{q} \rightarrow 0) = \lim_{\mathbf{q} \rightarrow 0} \left(\frac{1}{|\mathbf{q}|^2} \right) v_{\mathbf{G},\mathbf{G}'}^s + \tilde{v}_{\mathbf{G},\mathbf{G}'}, \quad (\text{C.33})$$

with

$$\begin{aligned} v_{\mathbf{G},\mathbf{G}'}^s &= 4\pi \delta_{\mathbf{G},\mathbf{G}'} \delta_{\mathbf{G},0} \\ \tilde{v}_{\mathbf{G},\mathbf{G}'} &= \frac{4\pi}{|\mathbf{G}|^2} \delta_{\mathbf{G},\mathbf{G}'} (1 - \delta_{\mathbf{G},0}). \end{aligned} \quad (\text{C.34})$$

The same separation can be done when expanding the Coulomb matrix in the mixed basis, and write:

$$v_{i,j}(\mathbf{q} \rightarrow 0) = \lim_{\mathbf{q} \rightarrow 0} \left(\frac{1}{|\mathbf{q}|^2} \right) v_{i,j}^s + \tilde{v}_{i,j}, \quad (\text{C.35})$$

the singular term can easily be obtained from Eq. C.34 transforming to the mixed basis using Eq. B.1

$$v_{i,j}^s = 4\pi \mathcal{W}_0^i(0) [\mathcal{W}_0^j(0)]^*. \quad (\text{C.36})$$

We still need to calculate $\tilde{v}_{i,j}$. In case B (C.2) and C (C.3), this is trivial. we just need to remove the contribution from $\mathbf{G} = 0$ in the Fourier transformation of the Coulomb interaction from real space to reciprocal space. In Case A (C.1), the divergent component from $\mathbf{q} = 0$ only contributes when $L = L' = 0$. Thus, we make plane wave expansion for these terms and take out the contribution from $\mathbf{G} = 0$.

Appendix D

The Matrix Element $M_{n,m}^i(\mathbf{k}, \mathbf{q})$

The matrix elements are defined by:

$$M_{n,m}^i(\mathbf{k}, \mathbf{q}) \equiv \int_{\Omega} [\tilde{\chi}_i^{\mathbf{q}}(\mathbf{r})\varphi_{m,\mathbf{k}-\mathbf{q}}(\mathbf{r})]^* \varphi_{n,\mathbf{k}}(\mathbf{r}) d\mathbf{r}. \quad (\text{D.1})$$

Taking into account the expression for the eigenvectors $\varphi_{n,\mathbf{k}}(\mathbf{r})$, that is:

$$\varphi_{n,\mathbf{k}}(\mathbf{r}) = \sum_{\mathbf{G}} Z_{\mathbf{k}+\mathbf{G}}^n \phi_{\mathbf{G}}^{\mathbf{k}}(\mathbf{r}), \quad (\text{D.2})$$

Eq. D.1 is converted to:

$$M_{n,m}^i(\mathbf{k}, \mathbf{q}) \equiv \sum_{\mathbf{G}, \mathbf{G}'} Z_{\mathbf{k}+\mathbf{G}}^n [Z_{\mathbf{k}-\mathbf{q}+\mathbf{G}'}^m]^* \int_{\Omega} [\tilde{\chi}_i^{\mathbf{q}}(\mathbf{r})\phi_{\mathbf{G}'}^{\mathbf{k}-\mathbf{q}}(\mathbf{r})]^* \phi_{\mathbf{G}}^{\mathbf{k}}(\mathbf{r}) d\mathbf{r}. \quad (\text{D.3})$$

To shorten the notation we will use:

$$\langle \tilde{\chi}_i^{\mathbf{q}} \phi_{\mathbf{K}'}^{\mathbf{k}-\mathbf{q}} | \phi_{\mathbf{G}}^{\mathbf{k}} \rangle \equiv \int_{\Omega} [\tilde{\chi}_i^{\mathbf{q}}(\mathbf{r})\phi_{\mathbf{G}'}^{\mathbf{k}-\mathbf{q}}(\mathbf{r})]^* \phi_{\mathbf{G}}^{\mathbf{k}}(\mathbf{r}) d\mathbf{r}. \quad (\text{D.4})$$

Since our basis functions describe separately the two regions of space, the calculation of the brackets depends on whether i corresponds to a function in the muffin-tin sphere or an Interstitial Plane Wave.

D.1 $\tilde{\chi}_i^{\mathbf{q}}(\mathbf{r})$ Belongs to the Muffin-Tin Region

In the muffin-tin sphere, the expansion of the wave function in the (L)APW+lo basis can be reformulated as:

$$\begin{aligned} \varphi_{n,\mathbf{k}}(\mathbf{r}) = & \frac{1}{\sqrt{N_c}} \sum_{l,m} [\mathcal{A}_{n,l,m}^{\alpha}(\mathbf{k})u_{\alpha,l}(r^{\alpha}, E_l) + \mathcal{B}_{n,l,m}^{\alpha}(\mathbf{k})\dot{u}_{\alpha,l}(r^{\alpha}, E_l) \\ & + \mathcal{C}_{n,l,m}^{\alpha}(\mathbf{k})u_{\alpha,l}(r^{\alpha}, E_{l_2})] Y_{l,m}(\hat{r}^{\alpha}), \end{aligned} \quad (\text{D.5})$$

where,

$$\mathcal{A}_{n,l,m}^{\alpha}(\mathbf{k}) \equiv \sum_{\mathbf{G}} Z_{\mathbf{k}+\mathbf{G}}^n A_{l,m}^{\alpha}(\mathbf{k} + \mathbf{G}) \quad (\text{D.6a})$$

$$\mathcal{B}_{n,l,m}^{\alpha}(\mathbf{k}) \equiv \sum_{\mathbf{G}} Z_{\mathbf{k}+\mathbf{G}}^n B_{l,m}^{\alpha}(\mathbf{k} + \mathbf{G}) \quad (\text{D.6b})$$

$$\mathcal{C}_{n,l,m}^{\alpha}(\mathbf{k}) \equiv \sum_{\mathbf{G}} Z_{\mathbf{k}+\mathbf{G}}^n C_{l,m}^{\alpha}(\mathbf{k} + \mathbf{G}). \quad (\text{D.6c})$$

Inserting Eqs. D.5, and J.7 into D.1 we get:

$$M_{n,m}^i(\mathbf{k}, \mathbf{q}) = \frac{e^{-i\mathbf{q}\cdot\mathbf{r}_{\alpha}}}{\sqrt{N_c^3}} \sum_{\lambda,\mu;\lambda',\mu'} \left[\mathcal{G}_{L,\lambda;M,\mu}^{\lambda',\mu'} \right]^* \left[\mathcal{A}_{m,\lambda,\mu}^{\alpha*}(\mathbf{k} - \mathbf{q}) \mathcal{A}_{n,\lambda',\mu'}^{\alpha}(\mathbf{k}) \langle NL\lambda|\lambda' \rangle_{\alpha} + \right. \\ \left. \mathcal{B}_{m,\lambda,\mu}^{\alpha*}(\mathbf{k} - \mathbf{q}) \mathcal{A}_{n,\lambda',\mu'}^{\alpha}(\mathbf{k}) \langle NL\dot{\lambda}|\lambda' \rangle_{\alpha} + \right. \\ \left. \mathcal{A}_{m,\lambda,\mu}^{\alpha*}(\mathbf{k} - \mathbf{q}) \mathcal{B}_{n,\lambda',\mu'}^{\alpha}(\mathbf{k}) \langle NL\lambda|\dot{\lambda}' \rangle_{\alpha} + \right. \\ \left. \mathcal{B}_{m,\lambda,\mu}^{\alpha*}(\mathbf{k} - \mathbf{q}) \mathcal{A}_{n,\lambda',\mu'}^{\alpha}(\mathbf{k}) \langle NL\dot{\lambda}|\dot{\lambda}' \rangle_{\alpha} + \dots \right]. \quad (\text{D.7})$$

D.2 $\tilde{\chi}_i^{\mathbf{q}}(\mathbf{r})$ Belongs to the Interstitial Region

In this case, using the definition within one unit cell:

$$\tilde{\chi}_i^{\mathbf{q}}(\mathbf{r}) \equiv \sum_{i'} \chi_{i'}^{\mathbf{q}}(\mathbf{r}) S_{i',i}^{-1} = \sum_{\mathbf{G}} P_{\mathbf{G}}^{\mathbf{q}}(\mathbf{r}) S_{\mathbf{G},i}^{-1}, \quad (\text{D.8})$$

and

$$\phi_{\mathbf{G}}^{\mathbf{k}}(\mathbf{r}) \equiv P_{\mathbf{G}}^{\mathbf{k}}(\mathbf{r}) \equiv \frac{1}{\sqrt{\Omega}} e^{i(\mathbf{k}+\mathbf{G})\cdot\mathbf{r}}, \quad (\text{D.9})$$

inserting Eqs. D.8 and D.9 into Eq. D.4 we have:

$$\left\langle \tilde{\chi}_i^{\mathbf{q}} \phi_{\mathbf{K}'}^{(\mathbf{k}-\mathbf{q})} | \phi_{\mathbf{K}}^{\mathbf{k}} \right\rangle = \frac{1}{\Omega^{\frac{3}{2}}} \sum_{\mathbf{G}_1} [S_{\mathbf{G}_1,i}^{-1}]^* \int_{I_{\Omega}} e^{-i(\mathbf{q}+\mathbf{G}_1)\cdot\mathbf{r}} e^{-i(\mathbf{k}-\mathbf{q}+\mathbf{K}')\cdot\mathbf{r}} e^{i(\mathbf{k}+\mathbf{K})\cdot\mathbf{r}} d\mathbf{r} \\ = \frac{1}{\Omega^{\frac{3}{2}}} \sum_{\mathbf{G}_1} [S_{\mathbf{G}_1,i}^{-1}]^* \int_{I_{\Omega}} e^{i(\mathbf{K}-\mathbf{G}_1-\mathbf{K}')\cdot\mathbf{r}} d\mathbf{r}. \quad (\text{D.10})$$

Making use of Eq. A.7, we get:

$$\left\langle \tilde{\chi}_i^{\mathbf{q}} \phi_{\mathbf{K}'}^{(\mathbf{k}-\mathbf{q})} | \phi_{\mathbf{K}}^{\mathbf{k}} \right\rangle = \frac{1}{\Omega^{\frac{3}{2}}} \sum_{\mathbf{G}_1} \mathcal{I}_{\mathbf{K}-\mathbf{G}_1-\mathbf{K}'} [S_{\mathbf{G}_1,i}^{-1}]^*. \quad (\text{D.11})$$

Appendix E

The Brillouin-Zone Integration

In Sec. 5.4, we introduced the ideas of the \mathbf{q} -dependent linear tetrahedron method we developed for calculating the polarization matrix. Compared with the one introduced by Rath and Freeman in Ref. [104], we included the frequency dependence and the variation of the operator to be integrated within each tetrahedron. To restrict the size of that chapter, we skipped the implementation details. These details will be the content of this appendix. For a clear illustration, we begin with the formula of the traditional linear tetrahedron method and the idea of isoparametric transformation. Then we extend these ideas to the \mathbf{q} -dependent case and illustrate the different configurations of the possible integration region. The frequency dependence is discussed in the end.

E.1 The Linear Tetrahedron Method

The task of this Brillouin-zone integration is to calculate the average expectation value of an operator satisfying the form:

$$\langle X \rangle = \frac{1}{V_G} \sum_n \int_{V_G} X_n(\mathbf{k}) f(\epsilon_n(\mathbf{k})) d\mathbf{k}, \quad (\text{E.1})$$

where

$$X_n(\mathbf{k}) = \langle \varphi_n(\mathbf{k}) | X | \varphi_n(\mathbf{k}) \rangle. \quad (\text{E.2})$$

This $X_n(\mathbf{k})$ is the expectation value of this operator on the state (n, \mathbf{k}) . V_G is the volume of the reciprocal unit cell. $f(\epsilon)$ is the Fermi function. An exact evaluation of Eq. E.1 requires calculating the expectation value of this operator over all its occupied states, including infinite number of \mathbf{k} points in the Brillouin-zone. In practice, this average expectation value is determined from a set of sample points in the Brillouin-zone, each has a certain weight addressing the integration of Eq. E.1 over the region around it.

In the tetrahedron method, this is obtained by dividing the Brillouin-zone into a set of tetrahedra using a grid (as shown in Fig. E.1 for the two-dimensional case). The values of $X_n(\mathbf{k})$ are calculated on the discrete set of vectors \mathbf{k}_i at the vertices of all these tetrahedra, namely the grid points. A function $\bar{X}_n(\mathbf{k})$ obtained by linearly interpolating the function $X_n(\mathbf{k})$ within the tetrahedra using its expectation values on the vertices can be written as a superposition of functions $w_i(\mathbf{k})$, such that

$$\bar{X}_n(\mathbf{k}) = \sum_i X_n(\mathbf{k}_i)w_i(\mathbf{k}), \quad (\text{E.3})$$

where $w_i(\mathbf{k}_j) = \delta_{ij}$ and it is linear within the corresponding tetrahedron and zero outside of it. Now replacing $X_n(\mathbf{k})$ in Eq. E.1 by its linear approximation, one has:

$$\begin{aligned} \langle X \rangle &\cong \frac{1}{V_G} \sum_n \int_{V_G} \bar{X}_n(\mathbf{k})f(\epsilon_n(\mathbf{k}))d\mathbf{k} \\ &= \frac{1}{V_G} \sum_n \int_{V_G} \sum_i X_n(\mathbf{k}_i)w_i(\mathbf{k})f(\epsilon_n(\mathbf{k}))d\mathbf{k} \\ &= \sum_n \sum_i X_n(\mathbf{k}_i) \frac{1}{V_G} \int_{V_G} w_i(\mathbf{k})f(\epsilon_n(\mathbf{k}))d\mathbf{k}. \end{aligned}$$

Defining:

$$w_{n,i} = \frac{1}{V_G} \int_{V_G} w_i(\mathbf{k})f(\epsilon_n(\mathbf{k}))d\mathbf{k}, \quad (\text{E.4})$$

one can write the average expectation value of X in Eq. E.1 as a weighted sum over the discrete set of \mathbf{k} points:

$$\langle X \rangle = \sum_{i,n} X_n(\mathbf{k}_i)w_{n,i}. \quad (\text{E.5})$$

Since $w_i(\mathbf{k})$ is zero for all $\{\mathbf{k}_j\}$ except \mathbf{k}_i , we can rewrite the weights as:

$$w_{n,i} = \frac{1}{V_G} \sum_{T_i} \iiint_{V_T} w_i(\mathbf{k})f(\epsilon_n(\mathbf{k}))d^3k = \sum_{T_i} w_{n,i}^{1T}, \quad (\text{E.6})$$

where T_i means that the sum runs only over those tetrahedra containing \mathbf{k}_i as one of its vertices. And one has defined $w_{n,i}^{1T} = \frac{1}{V_G} \iiint_{V_T} w_i(\mathbf{k})f(\epsilon_n(\mathbf{k}))d^3k$.

With this, it is clear that the integration in Eq. E.1 can be approximated by a sum of the form in Eq. E.5 where $w_{n,i}$ can be calculated by summing its contribution from each tetrahedron containing this \mathbf{k}_i as a vertex. The next job is to define the function $w_i(\mathbf{k})$ in order to calculate these $w_{n,i}$, for this, one needs the isoparametric transformation to be introduced in the next chapter.

E.1.1 The Isoparametric Transformation

In Eq. E.3, the function behaviour is approximated inside each tetrahedron by a linear interpolation between the function values at the vertices. Let \mathcal{F} be such a function, and x , y and z be the coordinates, then:

$$\mathcal{F} = A \cdot x + B \cdot y + C \cdot z + D, \quad (\text{E.7})$$

where the constants A , B , C and D are to be determined. Substituting $x = x_i$, $y = y_i$ and $z = z_i$ where $i = 0, 1, 2, 3$ label the vertices, the values of \mathcal{F}_i at the vertices (which are known) can be written as:

$$\mathcal{F}_i = A \cdot x_i + B \cdot y_i + C \cdot z_i + D. \quad (\text{E.8})$$

Clearly, Eq. E.8 for $i = 0$ can be used to eliminate the constant D . Then we have

$$\mathcal{F} - \mathcal{F}_0 = A \cdot (x - x_0) + B \cdot (y - y_0) + C \cdot (z - z_0). \quad (\text{E.9})$$

The constants A , B and C are determined by solving the system of equations:

$$\begin{aligned} \mathcal{F}_1 - \mathcal{F}_0 &= A \cdot (x_1 - x_0) + B \cdot (y_1 - y_0) + C \cdot (z_1 - z_0) \\ \mathcal{F}_2 - \mathcal{F}_0 &= A \cdot (x_2 - x_0) + B \cdot (y_2 - y_0) + C \cdot (z_2 - z_0) \\ \mathcal{F}_3 - \mathcal{F}_0 &= A \cdot (x_3 - x_0) + B \cdot (y_3 - y_0) + C \cdot (z_3 - z_0), \end{aligned} \quad (\text{E.10})$$

with solution:

$$\begin{pmatrix} A \\ B \\ C \end{pmatrix} = \begin{pmatrix} x_1 - x_0 & y_1 - y_0 & z_1 - z_0 \\ x_2 - x_0 & y_2 - y_0 & z_2 - z_0 \\ x_3 - x_0 & y_3 - y_0 & z_3 - z_0 \end{pmatrix}^{-1} \begin{pmatrix} \mathcal{F}_1 - \mathcal{F}_0 \\ \mathcal{F}_2 - \mathcal{F}_0 \\ \mathcal{F}_3 - \mathcal{F}_0 \end{pmatrix}. \quad (\text{E.11})$$

If one defines a coordinate (ξ, η, ζ) inside this tetrahedron, with each vertex 0, 1, 2, 3 having coordinates $(0,0,0)$, $(1,0,0)$, $(0,1,0)$, $(0,0,1)$ respectively, the function \mathcal{F} can be linearly interpolated as:

$$\mathcal{F} - \mathcal{F}_0 = \xi(\mathcal{F}_1 - \mathcal{F}_0) + \eta(\mathcal{F}_2 - \mathcal{F}_0) + \zeta(\mathcal{F}_3 - \mathcal{F}_0). \quad (\text{E.12})$$

Putting Eq. E.10 into the above equation, we have:

$$\begin{aligned} \mathcal{F} - \mathcal{F}_0 &= (\xi \quad \eta \quad \zeta) \begin{pmatrix} \mathcal{F}_1 - \mathcal{F}_0 \\ \mathcal{F}_2 - \mathcal{F}_0 \\ \mathcal{F}_3 - \mathcal{F}_0 \end{pmatrix} \\ &= (\xi \quad \eta \quad \zeta) \begin{pmatrix} x_1 - x_0 & y_1 - y_0 & z_1 - z_0 \\ x_2 - x_0 & y_2 - y_0 & z_2 - z_0 \\ x_3 - x_0 & y_3 - y_0 & z_3 - z_0 \end{pmatrix} \begin{pmatrix} A \\ B \\ C \end{pmatrix}. \end{aligned} \quad (\text{E.13})$$

On the other hand, Eq. E.9 can be written as:

$$\mathcal{F} - \mathcal{F}_0 = \begin{pmatrix} x - x_0 & y - y_0 & z - z_0 \end{pmatrix} \begin{pmatrix} A \\ B \\ C \end{pmatrix}. \quad (\text{E.14})$$

Comparing Eq. E.14 with Eq. E.13, we have:

$$\begin{aligned} x - x_0 &= \xi(x_1 - x_0) + \eta(x_2 - x_0) + \zeta(x_3 - x_0) \\ y - y_0 &= \xi(y_1 - y_0) + \eta(y_2 - y_0) + \zeta(y_3 - y_0) \\ z - z_0 &= \xi(z_1 - z_0) + \eta(z_2 - z_0) + \zeta(z_3 - z_0) \end{aligned} \quad (\text{E.15})$$

Combining Eq. E.15 with Eq. E.12, we see that the *same* expression holds for the function \mathcal{F} as well as for the coordinates x , y , and z . This coordinate transition from outside the tetrahedron to inside the tetrahedron is called as an isoparametric transformation. The functions $w_i(\mathbf{k})$ used in Eq. E.3 can be simply written as:

$$\begin{aligned} w_0(\xi, \eta, \zeta) &= 1 - \xi - \eta - \zeta \\ w_1(\xi, \eta, \zeta) &= \xi \\ w_2(\xi, \eta, \zeta) &= \eta \\ w_3(\xi, \eta, \zeta) &= \zeta, \end{aligned} \quad (\text{E.16})$$

in terms of this internal coordinates. The energy eigenvalue of the state (n, \mathbf{k}) with the coordinate (ξ, η, ζ) inside this tetrahedron is linearly interpolated as:

$$\epsilon_n(\xi, \eta, \zeta) = (\epsilon_{n,1} - \epsilon_{n,0})\xi + (\epsilon_{n,2} - \epsilon_{n,0})\eta + (\epsilon_{n,3} - \epsilon_{n,0})\zeta + \epsilon_{n,0}, \quad (\text{E.17})$$

where $\epsilon_{n,i}$ is the energy eigenvalue on the vertex i .

E.1.2 Integrals in One Tetrahedron

The integral of any function \mathcal{F} inside one tetrahedron, after applying the isoparametric transformation, is given by:

$$\begin{aligned} \iiint_{V_T} \mathcal{F}(x, y, z) f(\epsilon_n(x, y, z)) dx dy dz &= \int_0^1 \int_0^{1-\zeta} \int_0^{1-\zeta-\eta} [\xi(\mathcal{F}_1 - \mathcal{F}_0) + \eta(\mathcal{F}_2 - \mathcal{F}_0) + \\ &\quad \zeta(\mathcal{F}_3 - \mathcal{F}_0) + \mathcal{F}_0] \left| \frac{\partial(xyz)}{\partial(\xi\eta\zeta)} \right| f(\epsilon_n(\xi, \eta, \zeta)) d\xi d\eta d\zeta, \end{aligned} \quad (\text{E.18})$$

where V_T is the volume of the tetrahedron and $|\frac{\partial(xyz)}{\partial(\xi\eta\zeta)}|$ is the Jacobian determinant given by:

$$\left| \frac{\partial(xyz)}{\partial(\xi\eta\zeta)} \right| = \begin{vmatrix} \frac{\partial x}{\partial \xi} & \frac{\partial x}{\partial \eta} & \frac{\partial x}{\partial \zeta} \\ \frac{\partial y}{\partial \xi} & \frac{\partial y}{\partial \eta} & \frac{\partial y}{\partial \zeta} \\ \frac{\partial z}{\partial \xi} & \frac{\partial z}{\partial \eta} & \frac{\partial z}{\partial \zeta} \end{vmatrix} = \begin{vmatrix} x_1 - x_0 & y_1 - y_0 & z_1 - z_0 \\ x_2 - x_0 & y_2 - y_0 & z_2 - z_0 \\ x_3 - x_0 & y_3 - y_0 & z_3 - z_0 \end{vmatrix}. \quad (\text{E.19})$$

This is just the volume of a parallelepiped whose sides are given by those of the tetrahedron, clearly:

$$\left| \frac{\partial(xyz)}{\partial(\xi\eta\zeta)} \right| = 6V_T. \quad (\text{E.20})$$

Then Eq. E.18 is just:

$$\begin{aligned} & \iiint_{V_T} \mathcal{F}(x, y, z) dx dy dz \\ &= 6V_T \int_0^1 \int_0^{1-\zeta} \int_0^{1-\zeta-\eta} [\xi(\mathcal{F}_1 - \mathcal{F}_0) + \eta(\mathcal{F}_2 - \mathcal{F}_0) + \zeta(\mathcal{F}_3 - \mathcal{F}_0) + \mathcal{F}_0] \\ & \quad f(\epsilon_n(\xi, \eta, \zeta)) d\xi d\eta d\zeta. \end{aligned} \quad (\text{E.21})$$

E.1.3 The Integration Weights

Let's take one of the tetrahedra, its four vertices are denoted as 0, 1, 2, and 3. Using the $w_i(\mathbf{k})$ and $\epsilon_n(\mathbf{k})$ defined in Eq. E.16 and Eq. E.17, one can calculate the integration weights on these vertices. If the four energies are below the Fermi energy, the occupation is identically one and we have:

$$\begin{aligned} w_{n,i}^{1T} &= \frac{6V_T}{V_G} \int_0^1 \int_0^{1-\zeta} \int_0^{1-\zeta-\eta} \zeta d\xi d\eta d\zeta = \frac{6V_T}{V_G} \int_0^1 \int_0^{1-\zeta} \zeta(1-\zeta-\eta) d\eta d\zeta \\ &= \frac{6V_T}{V_G} \int_0^1 \frac{1}{2} \zeta(1-\zeta)^2 d\zeta = \frac{3V_T}{V_G} \left(\frac{1}{2} - \frac{2}{3} + \frac{1}{4} \right) = \frac{V_T}{4V_G}. \end{aligned} \quad (\text{E.22})$$

Let's now take the case where only $\epsilon_{n,0} < \epsilon_F$ and, for the sake of simplicity $\epsilon_{n,3} > \epsilon_{n,2} > \epsilon_{n,1} > \epsilon_{n,0}$, then the integration limits are changed, and one gets:

$$\begin{aligned} w_{n,3}^{1T} &= \frac{6V_T}{V_G} \int_0^{\frac{\epsilon_F - \epsilon_{n,0}}{\epsilon_{n,3} - \epsilon_{n,0}}} \int_0^{\frac{\epsilon_F - \epsilon_{n,0} - \zeta(\epsilon_{n,3} - \epsilon_{n,0})}{\epsilon_{n,2} - \epsilon_{n,0}}} \int_0^{\frac{\epsilon_F - \epsilon_{n,0} - \zeta(\epsilon_{n,3} - \epsilon_{n,0}) - \eta(\epsilon_{n,2} - \epsilon_{n,0})}{\epsilon_{n,1} - \epsilon_{n,0}}} \zeta d\xi d\eta d\zeta \\ &= \frac{V_T}{4V_G} \frac{(\epsilon_F - \epsilon_{n,0})^4}{(\epsilon_{n,1} - \epsilon_{n,0})(\epsilon_{n,2} - \epsilon_{n,0})(\epsilon_{n,3} - \epsilon_{n,0})^2}. \end{aligned} \quad (\text{E.23})$$

A similar calculation for the rest of the vertices leads to:

$$\begin{aligned}
 w_{n,2}^{1T} &= \frac{V_T}{4V_G} \frac{(\epsilon_F - \epsilon_{n,0})^4}{(\epsilon_{n,1} - \epsilon_{n,0})(\epsilon_{n,2} - \epsilon_{n,0})^2(\epsilon_{n,3} - \epsilon_{n,0})} \\
 w_{n,1}^{1T} &= \frac{V_T}{4V_G} \frac{(\epsilon_F - \epsilon_{n,0})^4}{(\epsilon_{n,1} - \epsilon_{n,0})^2(\epsilon_{n,2} - \epsilon_{n,0})(\epsilon_{n,3} - \epsilon_{n,0})} \\
 w_{n,0}^{1T} &= \frac{V_T}{V_G} \frac{(\epsilon_F - \epsilon_{n,0})^3}{(\epsilon_{n,1} - \epsilon_{n,0})(\epsilon_{n,2} - \epsilon_{n,0})(\epsilon_{n,3} - \epsilon_{n,0})} - w_{n,1}^{1T} - w_{n,2}^{1T} - w_{n,3}^{1T}.
 \end{aligned} \tag{E.24}$$

The last line in Eq. E.24 can be calculated using $w_0(\mathbf{k}) = 1 - \xi - \eta - \zeta = w_t - w_1(\mathbf{k}) - w_2(\mathbf{k}) - w_3(\mathbf{k})$, where w_t means the total weight over this tetrahedron. Expressions for the remaining cases can be found in Ref. [105]. Since these vertices are also sample points in the grid mesh, the integration weight on each grid points can be calculated from Eq. E.6.

E.2 Tetrahedron Method for \mathbf{q} -dependent Brillouin-zone Integration

If one wants to calculate the mean value of a \mathbf{q} -dependent operator, the situation becomes more complicated. In this section, we discuss the case when the expectation value of this operator satisfies:

$$\langle X(\mathbf{q}) \rangle = \frac{1}{V_G} \sum_{n,n'} \int_{V_G} X_{nn'}(\mathbf{k}, \mathbf{q}) f[\epsilon_n(\mathbf{k})] (1 - f[\epsilon_{n'}(\mathbf{k} - \mathbf{q})]) d^3k, \tag{E.25}$$

where

$$X_{n,n'}(\mathbf{k}, \mathbf{q}) = \langle \varphi_n(\mathbf{k}) | X(\mathbf{q}) | \varphi_{n'}(\mathbf{k} - \mathbf{q}) \rangle. \tag{E.26}$$

To evaluate this operator, one needs to know $X_{nn'}(\mathbf{k}, \mathbf{q})$ on each \mathbf{k} point in the Brillouin-zone in principle. In practice, again, this is obtained by calculating the expectation value of this operator on a set of sample points weighted by a certain factor. In addition to $\epsilon_n(\mathbf{k}_i)$ and $\varphi_n(\mathbf{k}_i)$ on the set of sample points $\{\mathbf{k}_i\}$, one also needs to know $\epsilon_{n'}(\mathbf{k}_i - \mathbf{q})$ and $\varphi_{n'}(\mathbf{k}_i - \mathbf{q})$ on another set of sample points $\{\mathbf{k}_i - \mathbf{q}\}$.

In our implementation, we make an even division of the Brillouin-zone along each axis. Then, we take the \mathbf{q} vector from this mesh. With this treatment, the meshes of \mathbf{k}_i and $\mathbf{k}_i - \mathbf{q}$ overlap totally with each other. We just need to know the eigen wave functions and the energy eigenvalues in one mesh. A two-dimensional sketch for the \mathbf{k} -mesh is shown in Fig. E.1.

Using this grid, the Brillouin-zone is divided into a set of tetrahedra. The expectation values of the function $X_{n,n'}(\mathbf{k}, \mathbf{q})$ are calculated on the vertices of these tetrahedra, namely, the grid points, giving $X_{n,n'}(\mathbf{k}_i, \mathbf{q})$.

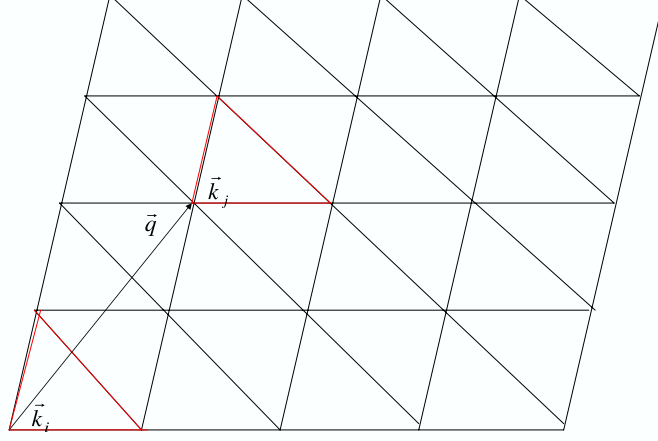


Figure E.1: The two-dimensional sketch of the BZ in the tetrahedron method, in this case, the space is divided into a list of triangles. One triangle is related to another by a vector \mathbf{q} .

Following the same procedure as the above section, we interpolate the function $X_{n,n'}(\mathbf{k}, \mathbf{q})$ linearly within each tetrahedron using:

$$\bar{X}_{n,n'}(\mathbf{k}, \mathbf{q}) = \sum_i X_{n,n'}(\mathbf{k}_i, \mathbf{q}) w_i(\mathbf{k}, \mathbf{q}), \quad (\text{E.27})$$

where $w_i(\mathbf{k}_j, \mathbf{q}) = \delta_{i,j}$ and it is a linear function. Since the integration is over the vector \mathbf{k} and this $w_i(\mathbf{k}_j, \mathbf{q})$ is only a function of the coordinates of \mathbf{k} for a fixed \mathbf{q} , it is easy to see that we can get rid of the \mathbf{q} dependence. Eq. E.27 becomes:

$$\bar{X}_{n,n'}(\mathbf{k}, \mathbf{q}) = \sum_i X_{n,n'}(\mathbf{k}_i, \mathbf{q}) w_i(\mathbf{k}). \quad (\text{E.28})$$

For the expectation value, we get:

$$\langle X(\mathbf{q}) \rangle = \sum_{i,n,n'} X_{n,n'}(\mathbf{k}_i, \mathbf{q}) w_{n,n',i}(\mathbf{q}), \quad (\text{E.29})$$

with

$$w_{n,n',i}(\mathbf{q}) = \frac{1}{V_G} \int_{V_G} w_i(\mathbf{k}) f[\epsilon_n(\mathbf{k})] (1 - f[\epsilon_{n'}(\mathbf{k} - \mathbf{q})]) d^3k. \quad (\text{E.30})$$

To calculate the weights, following the steps as in the previous section, we obtain:

$$w_{n,n',i}(\mathbf{q}) = \sum_{T_i} w_{n,n',i}^{1T}(\mathbf{q}), \quad (\text{E.31})$$

where

$$w_{n,n',i}^{1T}(\mathbf{q}) = \frac{1}{V_G} \iiint_{V_T} w_i(\mathbf{k}) f[\epsilon_n(\mathbf{k})] (1 - f[\epsilon_{n'}(\mathbf{k} - \mathbf{q})]) d^3k. \quad (\text{E.32})$$

T_i runs over all the tetrahedra in which the sample point \mathbf{k}_i serves as a vertex.

E.2.1 Isoparametric Transformation

Now, we perform the isoparametric transformation to calculate the integration of Eq. E.32 in one tetrahedron. If we denote the vertices of this tetrahedron as 0, 1, 2, 3 respectively, we have:

$$\begin{aligned} w_0(\mathbf{k}) &= w_0(\xi, \eta, \zeta) = 1 - \xi - \eta - \zeta \\ w_1(\mathbf{k}) &= w_1(\xi, \eta, \zeta) = \xi \\ w_2(\mathbf{k}) &= w_2(\xi, \eta, \zeta) = \eta \\ w_3(\mathbf{k}) &= w_3(\xi, \eta, \zeta) = \zeta \\ \epsilon_n(\mathbf{k}) &= \epsilon_n(\xi, \eta, \zeta) = \xi(\epsilon_{n,1} - \epsilon_{n,0}) + \eta(\epsilon_{n,2} - \epsilon_{n,0}) + \zeta(\epsilon_{n,3} - \epsilon_{n,0}) + \epsilon_{n,0} \\ \epsilon_{n'}(\mathbf{k} - \mathbf{q}) &= \epsilon_{n'}(\xi, \eta, \zeta) = \xi(\epsilon_{n',1} - \epsilon_{n',0}) + \eta(\epsilon_{n',2} - \epsilon_{n',0}) + \zeta(\epsilon_{n',3} - \epsilon_{n',0}) + \epsilon_{n',0}, \end{aligned} \quad (\text{E.33})$$

where we have used the shorthand notation $\epsilon_{n,i}$ and $\epsilon_{n',i}$ to represent the energy eigenvalues of the state (n, \mathbf{k}) and $(n', \mathbf{k} - \mathbf{q})$ on the vertices of this tetrahedron.

Then, the general formula for the contribution of one tetrahedron to the weight is:

$$\begin{aligned} w_{n,n',i}^{1T}(\mathbf{q}) &= \\ & \frac{6V_T}{V_G} \int_0^1 \int_0^{1-\zeta} \int_0^{1-\zeta-\eta} w_i(\xi, \eta, \zeta) \Theta[\epsilon_F - \xi(\epsilon_{n,1} - \epsilon_{n,0}) - \eta(\epsilon_{n,2} - \epsilon_{n,0}) - \zeta(\epsilon_{n,3} - \epsilon_{n,0}) - \epsilon_{n,0}] \\ & \times \Theta[\xi(\epsilon_{n',1} - \epsilon_{n',0}) + \eta(\epsilon_{n',2} - \epsilon_{n',0}) + \zeta(\epsilon_{n',3} - \epsilon_{n',0}) + \epsilon_{n',0} - \epsilon_F] d\xi d\eta d\zeta, \end{aligned} \quad (\text{E.34})$$

where Θ is the step function to address the Fermi function in Eq. E.32.

E.2.2 The Integration Region

From Eq. E.34, we see that the Θ functions determine the integration region within this tetrahedron. For insulators and semiconductors, this region is either the full tetrahedron or zero. For metals, the situation becomes more complicated. If not all the $\epsilon_{n,i}$ s are smaller or bigger than ϵ_F , the Fermi surface represented by the first Θ function in Eq. E.34 will intersect with this tetrahedron, leading to only part of it satisfying the condition the first Θ function equals one. If not all the $\epsilon_{n',i}$ are smaller

or bigger than ϵ_F , the Fermi surface represented by the second Θ function in Eq. E.34 will intersect with this tetrahedron, leading to only part of it satisfying the condition the second Θ function equals one. If neither of these cases happen, the integration region is either the full tetrahedron or zero. Otherwise, the integration region is determined by the intersection of these Fermi surfaces with this tetrahedron (Fig. 5.6 shows one example when both of them intersect with this tetrahedron).

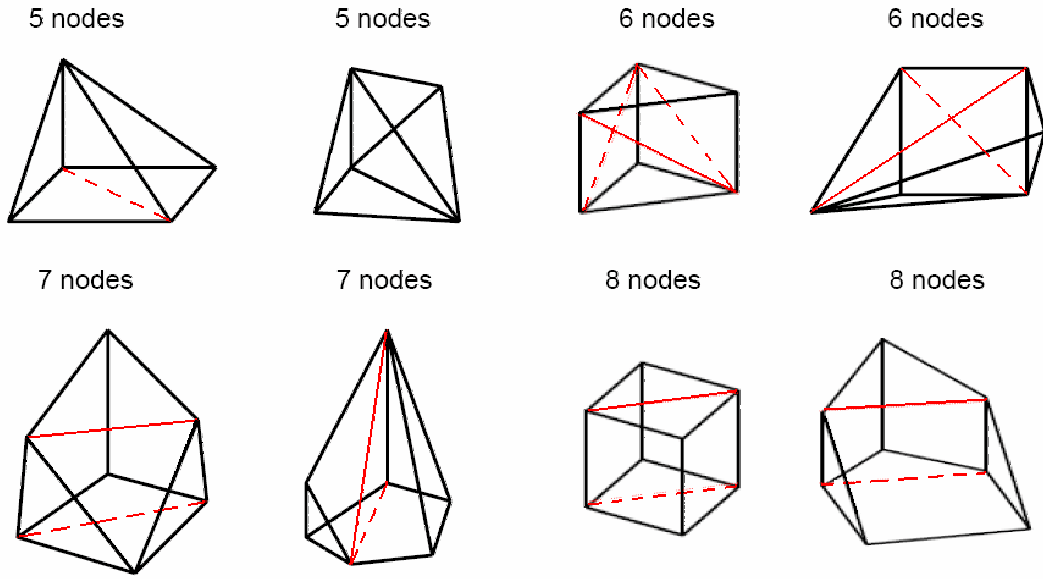


Figure E.2: The configurations for the region to be integrated. How these regions are decomposed into the principle units of the small tetrahedra is shown by the red lines in the graph.

There are in total 9 different configurations for this region. They are shown in Fig. E.2 except the simplest case of a tetrahedron. All of them can be subdivided into smaller tetrahedron. Then, we perform one further isoparametric transformation inside each of these small tetrahedron. The weight on each of its vertices is:

$$w_0 = \frac{6V_T}{V_G} \frac{V_{ST}}{V_T} \int_0^1 \int_0^{1-z} \int_0^{1-y-z} (1-x-y-z) dx dy dz = \frac{V_{ST}}{4V_G} \quad (\text{E.35})$$

$$w_1 = w_2 = w_3 = w_0,$$

where V_{ST} is the volume of the small tetrahedron, and $w_i (i = 0, 3)$ represents the weight on each vertex. We further distribute these weights linearly into the vertices of the big tetrahedron. Assuming the coordinates of one vertex of this small

tetrahedron is (ξ_1, η_1, ζ_1) in the big tetrahedron before the second parametric transformation, the integration weight on this point will be distributed with the ration $1 - \xi_1 - \eta_1 - \zeta_1$, ξ_1 , η_1 , and ζ_1 to the vertices 0, 1, 2, 3 of the big tetrahedron.

E.2.3 Polarizability

As already mentioned in Sec. 5.4, for the polarizability we can not assume both the energies and the integrand to be simultaneously linear in the coordinates of the tetrahedron. In this case, we have to include the energy-dependent factor of Eq. 5.22 into the analytical integration. In Sec. 5.6, we have discussed the frequency integrations in the *GW* calculations, where we pointed out that we calculate all the frequency dependent properties on the imaginary frequency axis. The polarizability is such a property. In this section, we will discuss the integration weight of the polarizability on both the real and imaginary frequency axis. The latter is the one used in the *GW* calculation. The former can be used to calculate the macroscopic dielectric constant.

E.2.3.1 Polarisability on the Real Frequency Axis

On the real frequency axis, the polarization matrix is:

$$P_{i,j}(\mathbf{q}, \omega) = \frac{N_c}{\hbar} \sum_{\mathbf{k}}^{BZ} \sum_n^{\text{occ}} \sum_{n'}^{\text{unocc}} M_{n,n'}^i(\mathbf{k}, \mathbf{q}) [M_{n,n'}^i(\mathbf{k}, \mathbf{q})]^* \left\{ \frac{1}{\omega - \epsilon_{n',\mathbf{k}-\mathbf{q}} + \epsilon_{n,\mathbf{k}} + i\eta} - \frac{1}{\omega - \epsilon_{n,\mathbf{k}} + \epsilon_{n',\mathbf{k}-\mathbf{q}} - i\eta} \right\}. \quad (\text{E.36})$$

We define the weight as:

$$w_{n,n',i}(\mathbf{q}, \omega) = \sum_{T_i} w_{n,n',i}^{1T}(\mathbf{q}, \omega), \quad (\text{E.37})$$

where

$$w_{n,n',i}^{1T}(\mathbf{q}, \omega) = \frac{1}{V_G} \int \int \int_{V_T} w_i(\mathbf{k}) f[\epsilon_n(\mathbf{k})] (1 - f[\epsilon_{n'}(\mathbf{k} - \mathbf{q})]) \times \left\{ \frac{1}{\omega - \epsilon_{n'}(\mathbf{k} - \mathbf{q}) + \epsilon_n(\mathbf{k}) + i\eta} - \frac{1}{\omega - \epsilon_n(\mathbf{k}) + \epsilon_{n'}(\mathbf{k} - \mathbf{q}) - i\eta} \right\} d^3\mathbf{k}. \quad (\text{E.38})$$

Following the procedures in Sec. E.2.2, the weight on each vertex of the small

tetrahedron is calculated by:

$$\begin{aligned}
 w_0 &= \frac{6V_{\text{ST}}}{V_{\text{G}}} \int_0^1 \int_0^{1-z} \int_0^{1-y-z} \frac{2(1-x-y-z)}{\omega^2 - (x\Delta_{1,0} + y\Delta_{2,0} + z\Delta_{3,0} + \Delta_0)^2} dx dy dz \\
 w_1 &= \frac{6V_{\text{ST}}}{V_{\text{G}}} \int_0^1 \int_0^{1-z} \int_0^{1-y-z} \frac{2x}{\omega^2 - (x\Delta_{1,0} + y\Delta_{2,0} + z\Delta_{3,0} + \Delta_0)^2} dx dy dz \\
 w_2 &= \frac{6V_{\text{ST}}}{V_{\text{G}}} \int_0^1 \int_0^{1-z} \int_0^{1-y-z} \frac{2y}{\omega^2 - (x\Delta_{1,0} + y\Delta_{2,0} + z\Delta_{3,0} + \Delta_0)^2} dx dy dz \\
 w_3 &= \frac{6V_{\text{ST}}}{V_{\text{G}}} \int_0^1 \int_0^{1-z} \int_0^{1-y-z} \frac{2z}{\omega^2 - (x\Delta_{1,0} + y\Delta_{2,0} + z\Delta_{3,0} + \Delta_0)^2} dx dy dz.
 \end{aligned} \tag{E.39}$$

Here, $\Delta_i = \epsilon_{n',i} - \epsilon_{n,i}$ and $\Delta_{i,j} = \Delta_i - \Delta_j$.

The first equation in Eqs. E.39 is more complicated to be solved analytically compared with the other three due to the presence of three variables in the numerator. So, we solve the other three respectively and then calculate the total integration weight over this tetrahedron with:

$$w_t = \frac{6V_{\text{ST}}}{V_{\text{G}}} \int_0^1 \int_0^{1-z} \int_0^{1-y-z} \frac{2}{\omega^2 - (x\Delta_{1,0} + y\Delta_{2,0} + z\Delta_{3,0} + \Delta_0)^2} dx dy dz. \tag{E.40}$$

The corresponding w_0 is then calculated from $w_0 = w_t - w_1 - w_2 - w_3$.

Even with this treatment, these analytical integration is very complicated to be solved. We use Mathematica to treat it. There exists a general solution. To restrict the size of this appendix, we just list that of w_t here which is the simplest case due to the absence of variables in the numerator in Eq. E.39:

$$\begin{aligned}
 f(\omega) &= (\omega - \Delta_3)^3 \Delta_{1,0}^2 \Delta_{2,0} \Delta_{2,1}^2 \ln[|\omega - \Delta_3|] - (\omega - \Delta_2)^3 \Delta_{1,0}^2 \Delta_{3,0} \Delta_{3,1}^2 \ln[|\omega - \Delta_2|] \\
 f(\omega) &= f(\omega) + [\Delta_{1,0} \Delta_{2,1} (\omega - \Delta_3) - (\omega - \Delta_0) \Delta_{2,1} \Delta_{3,1} + (\omega - \Delta_2) \Delta_{1,0} \Delta_{3,1}] \times \\
 &\quad \Delta_{2,0} \Delta_{3,0} \Delta_{3,2} (\omega - \Delta_1)^2 \ln[|\omega - \Delta_1|] \\
 f(\omega) &= f(\omega) + (\omega - \Delta_0)^3 \Delta_{2,1}^2 \Delta_{3,2} \Delta_{3,1}^2 \ln[|\omega - \Delta_0|] - (\omega - \Delta_1)^2 \Delta_{1,0} \Delta_{2,0} \times \\
 &\quad \Delta_{2,1} \Delta_{3,0} \Delta_{3,1} \Delta_{3,2} \\
 f(\omega) &= \frac{f(\omega)}{6\Delta_{1,0}^2 \Delta_{2,0} \Delta_{2,1}^2 \Delta_{3,0} \Delta_{3,1}^2 \Delta_{3,2}} \\
 w_t &= \frac{6V_{\text{ST}}}{V_{\text{G}}} [f(\omega) + f(-\omega)]
 \end{aligned} \tag{E.41}$$

(this equations is written following the programming rules cause it is too long). In this equation, it is required that $\omega \neq \Delta_i$ and $\Delta_{i,j} \neq 0$. $\Delta_{i,j} \neq 0$ is required because of this analytical solution. $\omega \neq \Delta_i$ is required because the denominators in Eq. E.39 and Eq. E.40 can not be zero. When these conditions are not fulfilled, we use Mathematica to get the analytical solution of that specific case respectively.

E.2.3.2 Polarisability on the Imaginary Frequency Axis

The polarization matrix of our calculation on the imaginary frequency axis is:

$$P_{i,j}(\mathbf{q}, \omega) = \frac{N_c}{\hbar} \sum_{\mathbf{k}}^{BZ} \sum_n^{\text{occ}} \sum_{n'}^{\text{unocc}} M_{n,n'}^i(\mathbf{k}, \mathbf{q}) [M_{n,n'}^i(\mathbf{k}, \mathbf{q})]^* \frac{-2(\epsilon_{n',\mathbf{k}-\mathbf{q}} - \epsilon_{n,\mathbf{k}})}{\omega^2 + (\epsilon_{n',\mathbf{k}-\mathbf{q}} - \epsilon_{n,\mathbf{k}})^2}. \quad (\text{E.42})$$

In this case, the procedure is essentially the same as above, except for the fact that the weight on the vertices of each small tetrahedron is calculated with:

$$\begin{aligned} w_0 &= \frac{6V_{\text{ST}}}{V_G} \int_0^1 \int_0^{1-z} \int_0^{1-y-z} \frac{2(1-x-y-z)}{\omega^2 + (x\Delta_{1,0} + y\Delta_{2,0} + z\Delta_{3,0} + \Delta_0)^2} dx dy dz \\ w_1 &= \frac{6V_{\text{ST}}}{V_G} \int_0^1 \int_0^{1-z} \int_0^{1-y-z} \frac{2x}{\omega^2 + (x\Delta_{1,0} + y\Delta_{2,0} + z\Delta_{3,0} + \Delta_0)^2} dx dy dz \\ w_2 &= \frac{6V_{\text{ST}}}{V_G} \int_0^1 \int_0^{1-z} \int_0^{1-y-z} \frac{2y}{\omega^2 + (x\Delta_{1,0} + y\Delta_{2,0} + z\Delta_{3,0} + \Delta_0)^2} dx dy dz \\ w_3 &= \frac{6V_{\text{ST}}}{V_G} \int_0^1 \int_0^{1-z} \int_0^{1-y-z} \frac{2z}{\omega^2 + (x\Delta_{1,0} + y\Delta_{2,0} + z\Delta_{3,0} + \Delta_0)^2} dx dy dz. \end{aligned} \quad (\text{E.43})$$

Again, we introduce w_t as:

$$w_t = \frac{6V_{\text{ST}}}{V_G} \int_0^1 \int_0^{1-z} \int_0^{1-y-z} \frac{2}{\omega^2 + (x\Delta_{1,0} + y\Delta_{2,0} + z\Delta_{3,0} + \Delta_0)^2} dx dy dz, \quad (\text{E.44})$$

to avoid solving the first equation of Eqs. E.43 directly. Its general solution is:

$$\begin{aligned}
 f(\omega) &= 2(\omega - \Delta_0^2)\Delta_{0,1}\Delta_{0,2}\Delta_{0,3}\Delta_{1,2}\Delta_{1,3}\Delta_{2,3} \\
 f(\omega) &= f(\omega) + 2\omega[3\Delta_0^4 - \omega^2(\Delta_1\Delta_2 + \Delta_2\Delta_3 + \Delta_3\Delta_1) \\
 &\quad - 3\Delta_0^2(\omega^2 + \Delta_2\Delta_3 + \Delta_1\Delta_2 + \Delta_1\Delta_3) \\
 &\quad + 2\Delta_0(\omega^2\Delta_2 + \omega^2\Delta_3 + \Delta_1\omega^2 + 3\Delta_1\Delta_2\Delta_3)]\Delta_{1,2}\Delta_{1,3}\Delta_{2,3}\text{ArcTan}[\Delta_0/\omega] \\
 f(\omega) &= f(\omega) + 2\omega(\omega^2 - 3\Delta_1^2)\Delta_{0,2}^2\Delta_{0,3}^2\Delta_{2,3}\text{ArcTan}[\Delta_1/\omega] \\
 f(\omega) &= f(\omega) - 2\omega(\omega^2 - 3\Delta_2^2)\Delta_{0,1}^2\Delta_{0,3}^2\Delta_{1,3}\text{ArcTan}[\Delta_2/\omega] \\
 f(\omega) &= f(\omega) + 2\omega(\omega^2 - 3\Delta_3^2)\Delta_{0,1}^2\Delta_{0,2}^2\Delta_{1,2}\text{ArcTan}[\Delta_3/\omega] \\
 f(\omega) &= f(\omega) + [\Delta_0^4(\Delta_1 + \Delta_2 + \Delta_3) - 3\omega^2\Delta_1\Delta_2\Delta_3 \\
 &\quad - 2\Delta_0^3(3\omega^2 + \Delta_2\Delta_3 + \Delta_1\Delta_2 + \Delta_1\Delta_3) \\
 &\quad + 3\Delta_0^2(\omega^2\Delta_1 + \omega^2\Delta_2 + \omega^2\Delta_3 + \Delta_1\Delta_2\Delta_3)]\Delta_{1,2}\Delta_{1,3}\Delta_{2,3}\ln[\omega^2 + \Delta_0^2] \\
 f(\omega) &= f(\omega) + \Delta_1(3\omega^2 - \Delta_1^2)\Delta_{0,2}^2\Delta_{0,3}^2\Delta_{2,3}\ln[\omega^2 + \Delta_1^2] \\
 f(\omega) &= f(\omega) + \Delta_2(\Delta_2^2 - 3\omega^2)\Delta_{0,1}^2\Delta_{0,3}^2\Delta_{1,3}\ln[\omega^2 + \Delta_2^2] \\
 f(\omega) &= f(\omega) - \Delta_3(\Delta_3^2 - 3\omega^2)\Delta_{0,1}^2\Delta_{0,2}^2\Delta_{1,2}\ln[\omega^2 + \Delta_3^2] \\
 w_t &= \frac{6V_{\text{ST}}}{V_{\text{G}}} \frac{f(\omega)}{6\Delta_{0,1}^2\Delta_{0,2}^2\Delta_{0,3}^2\Delta_{1,2}\Delta_{1,3}\Delta_{2,3}}.
 \end{aligned} \tag{E.45}$$

Again, in this equation, it is required that $\Delta_{i,j} \neq 0$. When this condition is not fulfilled, same as the above section, we use Mathematica to get the analytical solution of that case again specifically.

Appendix F

The Dielectric Matrix at the Γ Point

On the frequency axis, the *dielectric matrix* $\varepsilon(\mathbf{q}, \omega)$ can be calculated via:

$$\boxed{\varepsilon(\mathbf{q}, \omega) = 1 - \mathbf{v}(\mathbf{q})\mathbf{P}(\mathbf{q}, \omega)}. \quad (\text{F.1})$$

It is well-known that it diverges for $\mathbf{q} = 0$. To solve this problem one can make use of the symmetrized dielectric matrix.

F.1 The Symmetrized Dielectric Matrix

The symmetrized dielectric matrix is defined as:

$$\tilde{\varepsilon}_{i,j}(\mathbf{q}, \omega) = \sum_{l,m} v_{i,l}^{-\frac{1}{2}}(\mathbf{q}) \varepsilon_{l,m}(\mathbf{q}, \omega) v_{m,j}^{\frac{1}{2}}(\mathbf{q}). \quad (\text{F.2})$$

It has no divergences, and is hermitian. It has also been shown that $\tilde{\varepsilon}(\mathbf{q}, \omega)$ and $\varepsilon(\mathbf{q}, \omega)$ have the same eigenvalues (See Ref. [151]). It can be easily shown, from Eq. F.2 that:

$$\tilde{\varepsilon}_{i,j}^{-1}(\mathbf{q}, \omega) = \sum_{l,m} v_{i,l}^{-\frac{1}{2}}(\mathbf{q}) \varepsilon_{l,m}^{-1}(\mathbf{q}, \omega) v_{m,j}^{\frac{1}{2}}(\mathbf{q}). \quad (\text{F.3})$$

Inserting Eq. F.1 into F.2 we have:

$$\boxed{\tilde{\varepsilon}_{i,j}(\mathbf{q}, \omega) = 1 - \sum_{l,m} v_{i,l}^{\frac{1}{2}}(\mathbf{q}) P_{l,m}(\mathbf{q}, \omega) v_{m,j}^{\frac{1}{2}}(\mathbf{q})}. \quad (\text{F.4})$$

In the next section we calculate the symmetrized dielectric matrix at the Γ point, and show that it does not diverge.

F.2 Plane wave expansion of the symmetrized dielectric matrix at the Γ point

The advantage of the plane wave expansion is that the bare Coulomb potential is diagonal, simplifying the algebra. Expanded in plane waves, the expression for the matrix elements of the symmetrized dielectric function is:

$$\tilde{\epsilon}_{\mathbf{G},\mathbf{G}'}(\mathbf{q}, \omega) = \delta_{\mathbf{G},\mathbf{G}'} - \frac{4\pi}{|\mathbf{q} + \mathbf{G}||\mathbf{q} + \mathbf{G}'|} P_{\mathbf{G},\mathbf{G}'}(\mathbf{q}, \omega), \quad (\text{F.5})$$

where $P_{\mathbf{G},\mathbf{G}'}(\mathbf{q}, \omega)$ is given by:

$$P_{\mathbf{G},\mathbf{G}'}(\mathbf{q}, \omega) = N_c \sum_{\mathbf{k}} \sum_{n,n'}^{BZ} M_{n,n'}^{\mathbf{G}}(\mathbf{k}, \mathbf{q}) \left[M_{n,n'}^{\mathbf{G}'}(\mathbf{k}, \mathbf{q}) \right]^* f_0(\epsilon_{n,\mathbf{k}})(1 - f_0(\epsilon_{n',\mathbf{k}-\mathbf{q}})) \times \left\{ \frac{1}{\omega - \epsilon_{n',\mathbf{k}-\mathbf{q}} + \epsilon_{n,\mathbf{k}} + i\eta} - \frac{1}{\omega - \epsilon_{n,\mathbf{k}} + \epsilon_{n',\mathbf{k}-\mathbf{q}} - i\eta} \right\}, \quad (\text{F.6})$$

and

$$M_{n,n'}^{\mathbf{G}}(\mathbf{k}, \mathbf{q}) = \langle \varphi_{n',\mathbf{k}-\mathbf{q}} | e^{-i(\mathbf{q}+\mathbf{G})\cdot\mathbf{r}} | \varphi_{n,\mathbf{k}} \rangle. \quad (\text{F.7})$$

We can see that the possible divergences are located in $\tilde{\epsilon}_{0,0}$, usually called the head, and $\tilde{\epsilon}_{0,\mathbf{G}'}$ and $\tilde{\epsilon}_{\mathbf{G},0}$, usually called the wing.

Expressions for the limit $|\mathbf{q}| \rightarrow 0$ can be obtained by using the $\mathbf{k} \cdot \mathbf{p}$ perturbation theory. Taking into account the Bloch character of the eigenfunctions and according to the results of the $\mathbf{k} \cdot \mathbf{p}$ perturbation theory [152] one can write:

$$\varphi_{n,\mathbf{k}+\mathbf{q}}(\mathbf{r}) = \varphi_{n,\mathbf{k}}(\mathbf{r}) + \sum_{n' \neq n} \frac{\mathbf{p}_{n',n,\mathbf{k}} \cdot \mathbf{q}}{\epsilon_{n,\mathbf{k}} - \epsilon_{n',\mathbf{k}}} \varphi_{n',\mathbf{k}}(\mathbf{r}) \quad (\text{F.8a})$$

$$\epsilon_{n,\mathbf{k}+\mathbf{q}} = \epsilon_{n,\mathbf{k}} + \mathbf{p}_{n,n,\mathbf{k}} \cdot \mathbf{q}. \quad (\text{F.8b})$$

The matrix elements $M_{n,n'}^{\mathbf{G}}(\mathbf{k}, \mathbf{q})$ for $\mathbf{G} = 0$ can be written as:

$$M_{n,n'}^0(\mathbf{k}, \mathbf{q}) = \frac{1}{\Omega} \int_{\Omega} \varphi_{n',\mathbf{k}-\mathbf{q}}^*(\mathbf{r}) \varphi_{n,\mathbf{k}}(\mathbf{r}) d^3r. \quad (\text{F.9})$$

Applying Eq. F.8a we have:

$$M_{n,n'}^0(\mathbf{k}, \mathbf{q}) = \frac{1}{\Omega} \int_{\Omega} \varphi_{n',\mathbf{k}}^*(\mathbf{r}) \varphi_{n,\mathbf{k}}(\mathbf{r}) d^3r - \sum_{n'' \neq n'} \frac{\mathbf{p}_{n'',n',\mathbf{k}} \cdot \mathbf{q}}{\epsilon_{n',\mathbf{k}} - \epsilon_{n'',\mathbf{k}}} \frac{1}{\Omega} \int_{\Omega} \varphi_{n'',\mathbf{k}}^*(\mathbf{r}) \varphi_{n,\mathbf{k}}(\mathbf{r}) d^3r, \quad (\text{F.10})$$

taking into account the orthogonality of the eigenfunctions:

$$M_{n,n'}^0(\mathbf{k}, \mathbf{q} \rightarrow 0) = \delta_{n,n'} - (1 - \delta_{n,n'}) \frac{\mathbf{p}_{n,n',\mathbf{k}} \cdot \mathbf{q}}{\epsilon_{n',\mathbf{k}} - \epsilon_{n,\mathbf{k}}}. \quad (\text{F.11})$$

F.2.1 The Head

Inserting Eq. F.11 into F.6 we have:

$$\begin{aligned}
P_{0,0}(\mathbf{q} \rightarrow 0, \omega) = \lim_{\mathbf{q} \rightarrow 0} N_c \sum_{\mathbf{k}} \sum_{n, n'}^{BZ} \left[\delta_{n, n'} + (1 - \delta_{n, n'}) \left(\frac{\mathbf{p}_{n, n', \mathbf{k}} \cdot \mathbf{q}}{\epsilon_{n', \mathbf{k}} - \epsilon'_{n', \mathbf{k}}} \right)^2 \right] \times \\
f_0(\epsilon_{n, \mathbf{k}})(1 - f_0(\epsilon_{n', \mathbf{k} - \mathbf{q}})) \times \\
\left\{ \frac{1}{\omega - \epsilon_{n', \mathbf{k} - \mathbf{q}} + \epsilon_{n, \mathbf{k}} + i\eta} - \frac{1}{\omega - \epsilon_{n, \mathbf{k}} + \epsilon_{n', \mathbf{k} - \mathbf{q}} - i\eta} \right\}.
\end{aligned} \tag{F.12}$$

Separating the intraband and interband contributions, we get:

$$\begin{aligned}
P_{0,0}(\mathbf{q} \rightarrow 0, \omega) = \lim_{\mathbf{q} \rightarrow 0} N_c \sum_{\mathbf{k}} \sum_n^{BZ} f_0(\epsilon_{n, \mathbf{k}})(1 - f_0(\epsilon_{n, \mathbf{k} - \mathbf{q}})) \times \\
\left\{ \frac{1}{\omega - \epsilon_{n, \mathbf{k} - \mathbf{q}} + \epsilon_{n, \mathbf{k}} + i\eta} - \frac{1}{\omega - \epsilon_{n, \mathbf{k}} + \epsilon_{n, \mathbf{k} - \mathbf{q}} - i\eta} \right\} + \\
\sum_{n' \neq n} \left(\frac{\mathbf{p}_{n, n', \mathbf{k}} \cdot \mathbf{q}}{\epsilon_{n', \mathbf{k}} - \epsilon_{n, \mathbf{k}}} \right)^2 f_0(\epsilon_{n, \mathbf{k}})(1 - f_0(\epsilon_{n', \mathbf{k} - \mathbf{q}})) \times \\
\left\{ \frac{1}{\omega - \epsilon_{n', \mathbf{k} - \mathbf{q}} + \epsilon_{n, \mathbf{k}} + i\eta} - \frac{1}{\omega - \epsilon_{n, \mathbf{k}} + \epsilon_{n', \mathbf{k} - \mathbf{q}} - i\eta} \right\}.
\end{aligned} \tag{F.13}$$

The interband part, second term, is proportional to q^2 . For the intraband term we can replace $\epsilon_{n, \mathbf{k} - \mathbf{q}}$ using Eq. F.8b and take the Taylor series up to second order in $\Delta = \mathbf{p}_{n, n, \mathbf{k}} \cdot \mathbf{q}$:

$$\begin{aligned}
\frac{f(\epsilon_{n, \mathbf{k}})(1 - f(\epsilon_{n, \mathbf{k}} + \Delta))}{\omega - \Delta + i\eta} - \frac{f(\epsilon_{n, \mathbf{k}})(1 - f(\epsilon_{n, \mathbf{k}} + \Delta))}{\omega + \Delta - i\eta} = \\
f(\epsilon_{n, \mathbf{k}}) \left[\left(\frac{1}{\omega - i\eta} - \frac{1}{\omega + i\eta} \right) \left(\frac{\partial f(\epsilon)}{\partial \epsilon} \right)_{\epsilon_{n, \mathbf{k}}} \Delta \right. \\
+ \left(\frac{1}{(\omega - i\eta)^2} + \frac{1}{(\omega + i\eta)^2} \right) \left(\frac{\partial f(\epsilon)}{\partial \epsilon} \right)_{\epsilon_{n, \mathbf{k}}} \Delta^2 \\
\left. + \frac{1}{2} \left(\frac{1}{\omega - i\eta} - \frac{1}{\omega + i\eta} \right) \left(\frac{\partial^2 f(\epsilon)}{\partial \epsilon^2} \right)_{\epsilon_{n, \mathbf{k}}} \Delta^2 \right].
\end{aligned} \tag{F.14}$$

Since η is arbitrarily small we can discard the first and third terms, obtaining:

$$\frac{f(\epsilon_{n,\mathbf{k}})(1 - f(\epsilon_{n,\mathbf{k}} + \Delta))}{\omega - \Delta + i\eta} - \frac{f(\epsilon_{n,\mathbf{k}})(1 - f(\epsilon_{n,\mathbf{k}} + \Delta))}{\omega + \Delta - i\eta} = \left(\frac{1}{(\omega - i\eta)^2} + \frac{1}{(\omega + i\eta)^2} \right) \left(\frac{\partial f(\epsilon)}{\partial \epsilon} \right)_{\epsilon_{n,\mathbf{k}}} \Delta^2. \quad (\text{F.15})$$

Inserting the result of Eq. F.15 into F.13 we have:

$$P_{0,0}(\mathbf{q} \rightarrow 0, \omega) = \lim_{\mathbf{q} \rightarrow 0} N_c \sum_{\mathbf{k}} \sum_n^{BZ} \left(\frac{1}{(\omega - i\eta)^2} + \frac{1}{(\omega + i\eta)^2} \right) \left(\frac{\partial f(\epsilon)}{\partial \epsilon} \right)_{\epsilon_{n,\mathbf{k}}} \times \left(\mathbf{p}_{n,n,\mathbf{k}} \cdot \mathbf{q} \right)^2 + \sum_{n' \neq n} \left(\frac{\mathbf{p}_{n',n',\mathbf{k}} \cdot \mathbf{q}}{\epsilon_{n',\mathbf{k}} - \epsilon_{n,\mathbf{k}}} \right)^2 f_0(\epsilon_{n,\mathbf{k}})(1 - f_0(\epsilon_{n',\mathbf{k}-\mathbf{q}})) \times \left\{ \frac{1}{\omega - \epsilon_{n',\mathbf{k}-\mathbf{q}} + \epsilon_{n,\mathbf{k}} + i\eta} - \frac{1}{\omega - \epsilon_{n,\mathbf{k}} + \epsilon_{n',\mathbf{k}-\mathbf{q}} - i\eta} \right\}. \quad (\text{F.16})$$

Finally, replacing $P_{0,0}$ in Eq. F.5 by Eq. F.16, we have:

$$\begin{aligned} \varepsilon_{0,0}(\mathbf{q} \rightarrow 0, \omega) = & 1 - 4\pi N_c \sum_{\mathbf{k}} \left[\left(\frac{1}{(\omega - i\eta)^2} + \frac{1}{(\omega + i\eta)^2} \right) \sum_n \left(-\frac{\partial f}{\partial \epsilon} \right)_{\epsilon_{n,\mathbf{k}}} \lim_{\mathbf{q} \rightarrow 0} \left(\frac{\mathbf{p}_{n,n,\mathbf{k}} \cdot \mathbf{q}}{|\mathbf{q}|} \right)^2 + \right. \\ & \left. \sum_{nn'} \frac{\lim_{\mathbf{q} \rightarrow 0} \left(\frac{\mathbf{p}_{n',n',\mathbf{k}} \cdot \mathbf{q}}{|\mathbf{q}|} \right)^2}{(\epsilon_{n',\mathbf{k}} - \epsilon_{n,\mathbf{k}})^2} f_0(\epsilon_{n,\mathbf{k}})(1 - f_0(\epsilon_{n',\mathbf{k}})) \times \right. \\ & \left. \left\{ \frac{1}{\omega - \epsilon_{n',\mathbf{k}} + \epsilon_{n,\mathbf{k}} + i\eta} - \frac{1}{\omega - \epsilon_{n,\mathbf{k}} + \epsilon_{n',\mathbf{k}} - i\eta} \right\} \right] \end{aligned} \quad (\text{F.17})$$

F.2.2 The Wings

We follow similar steps for the wings, using Eq. F.11, the polarization is:

$$P_{0,\mathbf{G}'}(\mathbf{q} \rightarrow 0, \omega) = \lim_{\mathbf{q} \rightarrow 0} N_c \sum_{\mathbf{k}} \sum_{n,n'}^{BZ} \left(\delta_{n,n'} - (1 - \delta_{n,n'}) \frac{\mathbf{p}_{n',n',\mathbf{k}} \cdot \mathbf{q}}{\epsilon_{n',\mathbf{k}} - \epsilon_{n,\mathbf{k}}} \right) \left[M_{n,n'}^{\mathbf{G}'}(\mathbf{k}, 0) \right]^* \times f_0(\epsilon_{n,\mathbf{k}})(1 - f_0(\epsilon_{n',\mathbf{k}-\mathbf{q}})) \left\{ \frac{1}{\omega - \epsilon_{n',\mathbf{k}-\mathbf{q}} + \epsilon_{n,\mathbf{k}} + i\eta} - \frac{1}{\omega - \epsilon_{n,\mathbf{k}} + \epsilon_{n',\mathbf{k}-\mathbf{q}} - i\eta} \right\}. \quad (\text{F.18})$$

Again we can separate the intra- and interband terms:

$$\begin{aligned}
P_{0,\mathbf{G}'}(\mathbf{q} \rightarrow 0, \omega) = & \lim_{\mathbf{q} \rightarrow 0} N_c \sum_{\mathbf{k}} \left[\sum_n \left[M_{n,n}^{\mathbf{G}'}(\mathbf{k}, 0) \right]^* f_0(\epsilon_{n,\mathbf{k}})(1 - f_0(\epsilon_{n,\mathbf{k}-\mathbf{q}})) \times \right. \\
& \left. \left\{ \frac{1}{\omega - \epsilon_{n,\mathbf{k}-\mathbf{q}} + \epsilon_{n,\mathbf{k}} + i\eta} - \frac{1}{\omega - \epsilon_{n,\mathbf{k}} + \epsilon_{n,\mathbf{k}-\mathbf{q}} - i\eta} \right\} - \right. \\
& \sum_{n' \neq n} \frac{\mathbf{p}_{n,n',\mathbf{k}} \cdot \mathbf{q}}{\epsilon_{n',\mathbf{k}} - \epsilon_{n,\mathbf{k}}} \left[M_{n,n'}^{\mathbf{G}'}(\mathbf{k}, \mathbf{q}) \right]^* f_0(\epsilon_{n,\mathbf{k}})(1 - f_0(\epsilon_{n',\mathbf{k}-\mathbf{q}})) \times \\
& \left. \left. \left\{ \frac{1}{\omega - \epsilon_{n',\mathbf{k}-\mathbf{q}} + \epsilon_{n,\mathbf{k}} + i\eta} - \frac{1}{\omega - \epsilon_{n,\mathbf{k}} + \epsilon_{n',\mathbf{k}-\mathbf{q}} - i\eta} \right\} \right]. \right. \tag{F.19}
\end{aligned}$$

From Eq. F.15 we know that the intraband term is proportional to q^2 . Compared with the interband term, this is one order of magnitude smaller. Thus we discard it. We have:

$$\begin{aligned}
P_{0,\mathbf{G}'}(\mathbf{q} \rightarrow 0, \omega) = & - \lim_{\mathbf{q} \rightarrow 0} N_c \sum_{\mathbf{k}} \left[\sum_n \sum_{n' \neq n} \frac{\mathbf{p}_{n,n',\mathbf{k}} \cdot \mathbf{q}}{\epsilon_{n',\mathbf{k}} - \epsilon_{n,\mathbf{k}}} \left[M_{n,n'}^{\mathbf{G}'}(\mathbf{k}, \mathbf{q}) \right]^* f_0(\epsilon_{n,\mathbf{k}}) \times \right. \\
& \left. (1 - f_0(\epsilon_{n',\mathbf{k}-\mathbf{q}})) \left\{ \frac{1}{\omega - \epsilon_{n',\mathbf{k}-\mathbf{q}} + \epsilon_{n,\mathbf{k}} + i\eta} - \frac{1}{\omega - \epsilon_{n,\mathbf{k}} + \epsilon_{n',\mathbf{k}-\mathbf{q}} - i\eta} \right\} \right]. \tag{F.20}
\end{aligned}$$

Inserting Eq. F.20 into F.5 we obtain, for the wing:

$$\boxed{
\begin{aligned}
\varepsilon_{0,\mathbf{G}'}(\mathbf{q} \rightarrow 0, \omega) = & \frac{4\pi N_c}{|\mathbf{G}'|} \sum_{\mathbf{k}} \left[\sum_n \sum_{n' \neq n} \frac{\lim_{\mathbf{q} \rightarrow 0} \left(\frac{\mathbf{p}_{n,n',\mathbf{k}} \cdot \mathbf{q}}{|\mathbf{q}|} \right)}{(\epsilon_{n',\mathbf{k}} - \epsilon_{n,\mathbf{k}})} \left[M_{n,n'}^{\mathbf{G}'}(\mathbf{k}, 0) \right]^* f_0(\epsilon_{n,\mathbf{k}}) \times \right. \\
& \left. (1 - f_0(\epsilon_{n',\mathbf{k}})) \left\{ \frac{1}{\omega - \epsilon_{n',\mathbf{k}} + \epsilon_{n,\mathbf{k}} + i\eta} - \frac{1}{\omega - \epsilon_{n,\mathbf{k}} + \epsilon_{n',\mathbf{k}} - i\eta} \right\} \right]. \tag{F.21}
\end{aligned}$$

The matrix elements $\varepsilon_{\mathbf{G},0}(\mathbf{q} \rightarrow 0, \omega)$ are obtained by hermiticity.

F.3 Mixed basis expansion of the symmetrized dielectric matrix at the Γ point

The use of the symmetrized dielectric matrix expanded in other basis set than plane waves presents several difficulties:

- The divergences for $|\mathbf{q}| \rightarrow 0$ are not located in particular matrix elements of the bare Coulomb potential, the same is, as a consequence, true for the dielectric matrix.
- The bare Coulomb potential is no longer diagonal.

From the second item, we can see that already the calculation of the matrix elements $v_{i,j}^{\frac{1}{2}}$ is no longer simple. The simplest option for the expansion of the symmetrized dielectric matrix in our mixed basis is to perform the calculation in a plane wave basis and then make the corresponding matrix multiplications to change the basis.

It is then straightforward to show that:

$$\tilde{\varepsilon}_{i,j}(\mathbf{q}, \omega) = \sum_{\mathbf{G}, \mathbf{G}'} \mathcal{W}_{\mathbf{G}}^i(\mathbf{q}) \tilde{\varepsilon}_{\mathbf{G}, \mathbf{G}'}(\mathbf{q}, \omega) \mathcal{W}_{\mathbf{G}'}^{j*}(\mathbf{q}) \quad (\text{F.22a})$$

$$v_{i,j}^{\frac{1}{2}}(\mathbf{q}) = 2\sqrt{\pi} \sum_{\mathbf{G}} \frac{\mathcal{W}_{\mathbf{G}}^i(\mathbf{q}) \mathcal{W}_{\mathbf{G}}^{j*}(\mathbf{q})}{|\mathbf{q} + \mathbf{G}|}, \quad (\text{F.22b})$$

where the matrix elements $\mathcal{W}_{\mathbf{G}}^i(\mathbf{q})$ are defined in Appendix B.1.

The number of PW's needed for expanding the polarization becomes prohibitively large due to the fast oscillations of the LAPW eigenvalues in the region close to the ions. To avoid this, in this section we develop a method to calculate the long range term of the symmetrized dielectric matrix avoiding the expansion of the polarization in plane waves.

To begin with, let's rewrite Eq. F.22a in the following way:

$$\begin{aligned} \tilde{\varepsilon}_{i,j}(\mathbf{q}, \omega) &= \sum_{\mathbf{G}, \mathbf{G}'} \mathcal{W}_{\mathbf{G}}^i(\mathbf{q}) \tilde{\varepsilon}_{\mathbf{G}, \mathbf{G}'}(\mathbf{q}, \omega) \mathcal{W}_{\mathbf{G}'}^{j*}(\mathbf{q}) \\ &= \mathcal{W}_0^i(\mathbf{q}) \tilde{\varepsilon}_{0,0}(\mathbf{q}, \omega) \mathcal{W}_0^{j*}(\mathbf{q}) + \\ &\quad \sum_{\mathbf{G} \neq 0} \{ \mathcal{W}_{\mathbf{G}}^i(\mathbf{q}) \tilde{\varepsilon}_{\mathbf{G},0}(\mathbf{q}, \omega) \mathcal{W}_0^{j*}(\mathbf{q}) + \mathcal{W}_0^i(\mathbf{q}) \tilde{\varepsilon}_{0,\mathbf{G}}(\mathbf{q}, \omega) \mathcal{W}_{\mathbf{G}}^{j*}(\mathbf{q}) \} + \\ &\quad \sum_{\mathbf{G}, \mathbf{G}' \neq 0} \mathcal{W}_{\mathbf{G}}^i(\mathbf{q}) \tilde{\varepsilon}_{\mathbf{G}, \mathbf{G}'}(\mathbf{q}, \omega) \mathcal{W}_{\mathbf{G}'}^{j*}(\mathbf{q}) \\ &= \tilde{\varepsilon}_{i,j}^H(\mathbf{q}, \omega) + \tilde{\varepsilon}_{i,j}^W(\mathbf{q}, \omega) + \tilde{\varepsilon}_{i,j}^B(\mathbf{q}, \omega), \end{aligned} \quad (\text{F.23})$$

thus defining:

$$\tilde{\varepsilon}_{i,j}^H(\mathbf{q}, \omega) = \mathcal{W}_0^i(\mathbf{q}) \tilde{\varepsilon}_{0,0}(\mathbf{q}, \omega) \mathcal{W}_0^{j*}(\mathbf{q}) \quad (\text{F.24a})$$

$$\tilde{\varepsilon}_{i,j}^W(\mathbf{q}, \omega) = \sum_{\mathbf{G} \neq 0} \{ \mathcal{W}_{\mathbf{G}}^i(\mathbf{q}) \tilde{\varepsilon}_{\mathbf{G},0}(\mathbf{q}, \omega) \mathcal{W}_0^{j*}(\mathbf{q}) + \mathcal{W}_0^i(\mathbf{q}) \tilde{\varepsilon}_{0,\mathbf{G}}(\mathbf{q}, \omega) \mathcal{W}_{\mathbf{G}}^{j*}(\mathbf{q}) \} \quad (\text{F.24b})$$

$$\tilde{\varepsilon}_{i,j}^B(\mathbf{q}, \omega) = \sum_{\mathbf{G}, \mathbf{G}' \neq 0} \mathcal{W}_{\mathbf{G}}^i(\mathbf{q}) \tilde{\varepsilon}_{\mathbf{G}, \mathbf{G}'}(\mathbf{q}, \omega) \mathcal{W}_{\mathbf{G}'}^{j*}(\mathbf{q}). \quad (\text{F.24c})$$

The head term (Eq. F.24a) is easy to calculate, since there are no sums on \mathbf{G} . For the second term of the wings (F.24b), using Eq. F.21 we have:

$$\begin{aligned} & \sum_{\mathbf{G} \neq 0} \mathcal{W}_0^i(\mathbf{q}) \tilde{\varepsilon}_{0,\mathbf{G}}(\mathbf{q}, \omega) \mathcal{W}_{\mathbf{G}}^{j*}(\mathbf{q}) = \\ & 4\pi N_c \mathcal{W}_0^i(\mathbf{q}) \sum_{\mathbf{k}} \left[\sum_n \sum_{n' \neq n} \lim_{\mathbf{q} \rightarrow 0} \left(\frac{\mathbf{p}_{n,n',\mathbf{k}} \cdot \mathbf{q}}{|\mathbf{q}|} \right) \frac{f_0(\epsilon_{n,\mathbf{k}})(1 - f_0(\epsilon_{n',\mathbf{k}})) \times}{(\epsilon_{n',\mathbf{k}} - \epsilon_{n,\mathbf{k}})} \right. \\ & \left. \left\{ \frac{1}{\omega - \epsilon_{n',\mathbf{k}} + \epsilon_{n,\mathbf{k}} + i\eta} - \frac{1}{\omega - \epsilon_{n,\mathbf{k}} + \epsilon_{n',\mathbf{k}} - i\eta} \right\} \sum_{\mathbf{G} \neq 0} \frac{[M_{n,n'}^{\mathbf{G}}(\mathbf{k}, 0)]^*}{|\mathbf{G}|} \mathcal{W}_{\mathbf{G}}^{j*}(\mathbf{q}) \right]. \end{aligned} \quad (\text{F.25})$$

Assuming that the mixed basis is complete and using the orthogonality of the plane waves we have:

$$\sum_i \mathcal{W}_{\mathbf{G}}^i \mathcal{W}_{\mathbf{G}'}^{i*} = \delta_{\mathbf{G}-\mathbf{G}'}. \quad (\text{F.26})$$

We can write:

$$\begin{aligned} \sum_{\mathbf{G} \neq 0} \frac{[M_{n,n'}^{\mathbf{G}}(\mathbf{k}, 0)]^*}{|\mathbf{G}|} \mathcal{W}_{\mathbf{G}}^{j*}(\mathbf{q}) &= \sum_{\mathbf{G}, \mathbf{G}' \neq 0} [M_{n,n'}^{\mathbf{G}}(\mathbf{k}, 0)]^* \frac{\delta_{\mathbf{G}-\mathbf{G}'}}{|\mathbf{G}'|} \mathcal{W}_{\mathbf{G}'}^{j*}(\mathbf{q}) \\ &= \sum_{\mathbf{G}, \mathbf{G}' \neq 0} [M_{n,n'}^{\mathbf{G}}(\mathbf{k}, 0)]^* \sum_p \mathcal{W}_{\mathbf{G}}^{p*} \mathcal{W}_{\mathbf{G}'}^p \frac{1}{|\mathbf{G}'|} \mathcal{W}_{\mathbf{G}'}^{j*}(\mathbf{q}) \\ &= \sum_p \sum_{\mathbf{G}} [M_{n,n'}^{\mathbf{G}}(\mathbf{k}, 0)]^* \mathcal{W}_{\mathbf{G}}^{p*} \sum_{\mathbf{G}' \neq 0} \mathcal{W}_{\mathbf{G}'}^p \frac{1}{|\mathbf{G}'|} \mathcal{W}_{\mathbf{G}'}^{j*}(\mathbf{q}). \end{aligned} \quad (\text{F.27})$$

Using the completeness of the PW's and Eq. F.22b we have:

$$\sum_{\mathbf{G} \neq 0} \frac{[M_{n,n'}^{\mathbf{G}}(\mathbf{k}, 0)]^*}{|\mathbf{G}|} \mathcal{W}_{\mathbf{G}}^{j*}(\mathbf{q}) = \frac{1}{\sqrt{4\pi}} \sum_p [M_{n,n'}^p(\mathbf{k}, 0)]^* \tilde{v}_{p,j}^{\frac{1}{2}}(\mathbf{q}), \quad (\text{F.28})$$

where $\tilde{v}_{p,j}^{\frac{1}{2}}(\mathbf{q})$ is the non-divergent part of $v_{p,j}^{\frac{1}{2}}(\mathbf{q})$. Inserting Eq. F.28 into Eq. F.25 we obtain:

$$\begin{aligned} & \sum_{\mathbf{G} \neq 0} \mathcal{W}_0^i(\mathbf{q}) \tilde{\varepsilon}_{0,\mathbf{G}}(\mathbf{q}, \omega) \mathcal{W}_{\mathbf{G}}^{j*}(\mathbf{q}) = \\ & \sqrt{4\pi} N_c \mathcal{W}_0^i(\mathbf{q}) \sum_p \sum_{\mathbf{k}} \left[\sum_n \sum_{n' \neq n} \lim_{\mathbf{q} \rightarrow 0} \left(\frac{\mathbf{p}_{n,n',\mathbf{k}} \cdot \mathbf{q}}{|\mathbf{q}|} \right) \frac{f_0(\epsilon_{n,\mathbf{k}})(1 - f_0(\epsilon_{n',\mathbf{k}})) \times}{(\epsilon_{n',\mathbf{k}} - \epsilon_{n,\mathbf{k}})} \right. \\ & \left. \left\{ \frac{1}{\omega - \epsilon_{n',\mathbf{k}} + \epsilon_{n,\mathbf{k}} + i\eta} - \frac{1}{\omega - \epsilon_{n,\mathbf{k}} + \epsilon_{n',\mathbf{k}} - i\eta} \right\} [M_{n,n'}^p(\mathbf{k}, 0)]^* \right] \tilde{v}_{p,j}^{\frac{1}{2}}(0). \end{aligned} \quad (\text{F.29})$$

The same procedure can be applied to the first term in Eq. F.24b and to Eq. F.24c, Eq. F.24 becomes:

$$\tilde{\varepsilon}_{i,j}^H(0, \omega) = \mathcal{W}_0^i(0) \tilde{\varepsilon}_{0,0}(0, \omega) \mathcal{W}_0^{j*}(\mathbf{q}) \quad (\text{F.30a})$$

$$\begin{aligned} \tilde{\varepsilon}_{i,j}^W(0, \omega) = & \sqrt{4\pi} N_c \sum_p \sum_{\mathbf{k}} \left[\sum_n \sum_{n' \neq n} \lim_{\mathbf{q} \rightarrow 0} \left(\frac{\mathbf{p}_{n,n',\mathbf{k}} \cdot \mathbf{q}}{|\mathbf{q}|} \right) \frac{1}{(\epsilon_{n',\mathbf{k}} - \epsilon_{n,\mathbf{k}})} \times \right. \\ & f_0(\epsilon_{n,\mathbf{k}})(1 - f_0(\epsilon_{n',\mathbf{k}})) \times \\ & \left. \left\{ \frac{1}{\omega - \epsilon_{n',\mathbf{k}} + \epsilon_{n,\mathbf{k}} + i\eta} - \frac{1}{\omega - \epsilon_{n,\mathbf{k}} + \epsilon_{n',\mathbf{k}} - i\eta} \right\} \times \right. \\ & \left. \left(\mathcal{W}_0^i(0) [M_{n,n'}^p(\mathbf{k}, 0)]^* \tilde{v}_{p,j}^{\frac{1}{2}}(0) + \right. \right. \\ & \left. \left. \tilde{v}_{i,p}^{\frac{1}{2}}(0) M_{n,n'}^p(\mathbf{k}, 0) \mathcal{W}_0^{j*}(0) \right) \right] \end{aligned} \quad (\text{F.30b})$$

$$\begin{aligned} \tilde{\varepsilon}_{i,j}^B(0, \omega) = & N_c \sum_{pq} \tilde{v}_{i,p}^{\frac{1}{2}}(0) \sum_{\mathbf{k}} \left[\sum_n \sum_{n' \neq n} f_0(\epsilon_{n,\mathbf{k}})(1 - f_0(\epsilon_{n',\mathbf{k}})) \times \right. \\ & \left. \left\{ \frac{1}{\omega - \epsilon_{n',\mathbf{k}} + \epsilon_{n,\mathbf{k}} + i\eta} - \frac{1}{\omega - \epsilon_{n,\mathbf{k}} + \epsilon_{n',\mathbf{k}} - i\eta} \right\} \times \right. \\ & \left. M_{n,n'}^p(\mathbf{k}, 0) [M_{n,n'}^q(\mathbf{k}, 0)]^* \right] \tilde{v}_{q,j}^{\frac{1}{2}}(0) \end{aligned} \quad (\text{F.30c})$$

For calculating $\mathbf{p}_{n,n',\mathbf{k}} \cdot \mathbf{q}$, we follow Ref. [153].

Appendix G

The Dynamically Screened Potential

G.1 General Expression

From the definition given in Eq. 5.4 we have:

$$W_0(\mathbf{r}_1, \mathbf{r}_2; \omega) = \int \varepsilon^{-1}(\mathbf{r}_1, \mathbf{r}_3; \omega) v(\mathbf{r}_3, \mathbf{r}_2) d\mathbf{r}_3. \quad (\text{G.1})$$

From Eq. I.10 the matrix form can be written as:

$$W_{i,j}(\mathbf{q}, \omega) = \sum_l \varepsilon_{i,l}^{-1}(\mathbf{q}, \omega) v_{l,j}(\mathbf{q}). \quad (\text{G.2})$$

Using Eq. F.3 the screened potential is then rewritten as:

$$\begin{aligned} W_{i,j}(\mathbf{q}, \omega) &= \sum_m \varepsilon_{i,m}^{-1}(\mathbf{q}, \omega) v_{m,j}(\mathbf{q}) \\ &= \sum_{lm} v_{i,l}^{\frac{1}{2}}(\mathbf{q}) \tilde{\varepsilon}_{l,m}^{-1}(\mathbf{q}, \omega) v_{m,j}^{\frac{1}{2}}(\mathbf{q}). \end{aligned} \quad (\text{G.3})$$

And we can, as already mentioned in Sec. 5.3, separate it into an exchange and a correlation term, where:

$$\begin{aligned} W_{i,j}^x(\mathbf{q}) &= v_{i,j}(\mathbf{q}) \\ W_{i,j}^c(\mathbf{q}, \omega) &= W_{i,j}(\mathbf{q}, \omega) - v_{i,j}(\mathbf{q}) = \sum_{l,m} v_{i,l}^{\frac{1}{2}}(\mathbf{q}) [\tilde{\varepsilon}_{l,m}^{-1}(\mathbf{q}, \omega) - \delta_{l,m}] v_{m,j}^{\frac{1}{2}}(\mathbf{q}). \end{aligned} \quad (\text{G.4})$$

G.2 The Singularity of the Screened Coulomb Potential

As we have seen in Appendix F.1 the symmetrized dielectric function has no divergencies, but we are still left with the singularity of v , and hence of W , at the Γ point.

As mentioned in Appendix C.4 (Eqs. C.33 to C.36), for the bare Coulomb matrix we can write:

$$v_{i,j}^{\frac{1}{2}}(\mathbf{q} \rightarrow 0) = \frac{v_{i,j}^{s\frac{1}{2}}}{|\mathbf{q}|} + \tilde{v}_{i,j}^{\frac{1}{2}}(\mathbf{q}). \quad (\text{G.5})$$

Inserting it into Eq. G.3 we get:

$$\begin{aligned} W_{i,j}^c(\mathbf{q}, \omega) &= \sum_{l,m} v_{i,l}^{\frac{1}{2}}(\mathbf{q}) [\tilde{\epsilon}_{l,m}^{-1}(\mathbf{q}, \omega) - \delta_{l,m}] v_{m,j}^{\frac{1}{2}}(\mathbf{q}) \\ &= \frac{1}{|\mathbf{q}|^2} \sum_{l,m} v_{i,l}^{s\frac{1}{2}}(\mathbf{q}) [\tilde{\epsilon}_{l,m}^{-1}(\mathbf{q}, \omega) - \delta_{l,m}] v_{m,j}^{s\frac{1}{2}}(\mathbf{q}) + \\ &\quad \frac{1}{|\mathbf{q}|} \left\{ \sum_{l,m} v_{i,l}^{s\frac{1}{2}}(\mathbf{q}) [\tilde{\epsilon}_{l,m}^{-1}(\mathbf{q}, \omega) - \delta_{l,m}] \tilde{v}_{m,j}^{\frac{1}{2}}(\mathbf{q}) + \right. \\ &\quad \left. \tilde{v}_{i,l}^{\frac{1}{2}}(\mathbf{q}) [\tilde{\epsilon}_{l,m}^{-1}(\mathbf{q}, \omega) - \delta_{l,m}] v_{m,j}^{s\frac{1}{2}}(\mathbf{q}) \right\} + \\ &\quad \sum_{l,m} \tilde{v}_{i,l}^{\frac{1}{2}}(\mathbf{q}) [\tilde{\epsilon}_{l,m}^{-1}(\mathbf{q}, \omega) - \delta_{l,m}] \tilde{v}_{m,j}^{\frac{1}{2}}(\mathbf{q}). \end{aligned} \quad (\text{G.6})$$

Defining:

$$\begin{aligned} W_{i,j}^{cs2}(\mathbf{q}, \omega) &= \sum_{l,m} v_{i,l}^{s\frac{1}{2}}(\mathbf{q}) [\tilde{\epsilon}_{l,m}^{-1}(\mathbf{q}, \omega) - \delta_{l,m}] v_{m,j}^{s\frac{1}{2}}(\mathbf{q}) \\ W_{i,j}^{cs1}(\mathbf{q}, \omega) &= \sum_{l,m} v_{i,l}^{s\frac{1}{2}}(\mathbf{q}) [\tilde{\epsilon}_{l,m}^{-1}(\mathbf{q}, \omega) - \delta_{l,m}] \tilde{v}_{m,j}^{\frac{1}{2}}(\mathbf{q}) + \\ &\quad \tilde{v}_{i,l}^{\frac{1}{2}}(\mathbf{q}) [\tilde{\epsilon}_{l,m}^{-1}(\mathbf{q}, \omega) - \delta_{l,m}] v_{m,j}^{s\frac{1}{2}}(\mathbf{q}) \\ \tilde{W}_{i,j}^c(\mathbf{q}, \omega) &= \sum_{l,m} \tilde{v}_{i,l}^{\frac{1}{2}}(\mathbf{q}) [\tilde{\epsilon}_{l,m}^{-1}(\mathbf{q}, \omega) - \delta_{l,m}] \tilde{v}_{m,j}^{\frac{1}{2}}(\mathbf{q}) \end{aligned}$$

we can write

$$W_{i,j}^c(\mathbf{q}, \omega) = \frac{1}{|\mathbf{q}|^2} W_{i,j}^{cs2}(\mathbf{q}, \omega) + \frac{1}{|\mathbf{q}|} W_{i,j}^{cs1}(\mathbf{q}, \omega) + \tilde{W}_{i,j}^c(\mathbf{q}, \omega). \quad (\text{G.8})$$

This screened Coulomb interaction only include the correlation term. It still diverges. We need to integrate \mathbf{q} over the Brillouin-zone. This integration is discussed in Sec. 5.5.

Appendix H

The Frequency Integration

In this section we show how to perform the integration on the frequency axis in Eq. 5.39.

This integration is peaked around $\omega' = \omega$ when $\epsilon_{n\mathbf{k}+\mathbf{q}}$ is small. To handle this problem one can add and subtract the term

$$\frac{1}{\pi} \int_0^\infty \frac{(\epsilon_{n',\mathbf{k}+\mathbf{q}} - i\omega) W_{i,j}^c(\mathbf{q}, i\omega)}{(i\omega - \epsilon_{n',\mathbf{k}+\mathbf{q}})^2 + \omega'^2} d\omega' = \frac{1}{2} \text{sgn}(\epsilon_{n',\mathbf{k}+\mathbf{q}}) W_{i,j}^c(\mathbf{q}, i\omega). \quad (\text{H.1})$$

Then we have:

$$\mathbb{I} = \frac{1}{\pi} \int_0^\infty \frac{(\epsilon_{n',\mathbf{k}+\mathbf{q}} - i\omega) [W_{i,j}^c(\mathbf{q}, i\omega') - W_{i,j}^c(\mathbf{q}, i\omega)]}{(i\omega - \epsilon_{n',\mathbf{k}+\mathbf{q}})^2 + \omega'^2} d\omega' + \frac{1}{2} \text{sgn}(\epsilon_{n',\mathbf{k}+\mathbf{q}}) W_{i,j}^c(\mathbf{q}, i\omega). \quad (\text{H.2})$$

The integrand is now smooth and a Gaussian quadrature may be used.

To solve the semiinfinite integral of Eq. H.2 which has the form:

$$\mathbb{I} = \int_0^\infty f(\omega) d\omega, \quad (\text{H.3})$$

we split it into (following Ref. [107])

$$\mathbb{I} = \mathbb{I}_1 + \mathbb{I}_2 \quad (\text{H.4a})$$

$$\mathbb{I}_1 = \int_0^{\omega_0} f(\omega) d\omega \quad (\text{H.4b})$$

$$\mathbb{I}_2 = \int_{\omega_0}^\infty f(\omega) d\omega. \quad (\text{H.4c})$$

For \mathbb{I}_1 we make the change of variables $u = 2\omega/\omega_0 - 1$ and thus $d\omega = \frac{\omega_0}{2} du$. Then we have:

$$\mathbb{I}_1 = \int_0^{\omega_0} f(\omega) d\omega = \frac{\omega_0}{2} \int_{-1}^1 f[(u+1)\omega_0/2] du, \quad (\text{H.5})$$

which can be solved by standard Gauss-Legendre quadrature. For \mathbb{I}_2 we make the change of variables $u = 2\omega_0/\omega - 1$ and thus $d\omega = -\frac{2\omega_0}{(u+1)^2}du$. Then we have:

$$\mathbb{I}_2 = \int_{\omega_0}^{\infty} f(\omega)d\omega = 2\omega_0 \int_{-1}^1 f\left[\frac{2\omega_0}{u+1}\right](u+1)^{-2}du, \quad (\text{H.6})$$

which can also be solved by standard Gauss-Legendre quadrature.

Appendix I

Expansion of a Non-local Function

We need to calculate a non-local function $f(\mathbf{r}_1, \mathbf{r}_2, \tau)$ (τ can be a time as well as a frequency coordinate) with a lattice translation symmetry \mathbf{R} (*i. e.* v , W , P , ε , etc.):

$$f(\mathbf{r}_1 + \mathbf{R}, \mathbf{r}_2 + \mathbf{R}, \tau) = f(\mathbf{r}_1, \mathbf{r}_2, \tau). \quad (\text{I.1})$$

To calculate a function of this type, we use the expansion in a complete set of Bloch functions $\{\chi_i^{\mathbf{q}}(\mathbf{r})\}$ in the following way:

$$\begin{cases} f(\mathbf{r}_1, \mathbf{r}_2, \tau) = \sum_{\mathbf{q}} \sum_{\mathbf{q}'} \sum_{i,j}^{BZ} \chi_i^{\mathbf{q}}(\mathbf{r}_1) f_{i,j}(\mathbf{q}, \mathbf{q}', \tau) (\chi_j^{\mathbf{q}'}(\mathbf{r}_2))^* \\ f_{i,j}(\mathbf{q}, \mathbf{q}', \tau) = \int_V \int_V (\chi_i^{\mathbf{q}}(\mathbf{r}_1))^* f(\mathbf{r}_1, \mathbf{r}_2, \tau) \chi_j^{\mathbf{q}'}(\mathbf{r}_2) d\mathbf{r}_2 d\mathbf{r}_1. \end{cases} \quad (\text{I.2})$$

Since $\chi_i^{\mathbf{q}}(\mathbf{r}_1)$ is a Bloch function ($\chi_i^{\mathbf{q}}(\mathbf{r} - \mathbf{R}) = e^{-i\mathbf{q}\cdot\mathbf{R}} \chi_i^{\mathbf{q}}(\mathbf{r})$) normalized to unity in the crystal with volume V , the matrix element $f_{i,j}(\mathbf{q}, \mathbf{q}', \tau)$ can be evaluated as

follows:

$$\begin{aligned}
f_{i,j}(\mathbf{q}, \mathbf{q}', \tau) &= \int_V \int_V (\chi_i^{\mathbf{q}}(\mathbf{r}_1))^* f(\mathbf{r}_1, \mathbf{r}_2, \tau) \chi_j^{\mathbf{q}'}(\mathbf{r}_2) d\mathbf{r}_2 d\mathbf{r}_1 \\
&= \sum_{\mathbf{R}, \mathbf{R}'} \int_{\Omega} \int_{\Omega} (\chi_i^{\mathbf{q}}(\mathbf{r}_1 - \mathbf{R}))^* f(\mathbf{r}_1 - \mathbf{R}, \mathbf{r}_2 - \mathbf{R} - \mathbf{R}', \tau) \times \\
&\quad \chi_j^{\mathbf{q}'}(\mathbf{r}_2 - \mathbf{R} - \mathbf{R}') d\mathbf{r}_2 d\mathbf{r}_1 \\
&= \sum_{\mathbf{R}} \int_{\Omega} \sum_{\mathbf{R}'} \int_{\Omega} e^{i\mathbf{q}\cdot\mathbf{R}} (\chi_i^{\mathbf{q}}(\mathbf{r}_1))^* f(\mathbf{r}_1, \mathbf{r}_2 - \mathbf{R}', \tau) e^{-i\mathbf{q}'\cdot\mathbf{R}} e^{-i\mathbf{q}'\cdot\mathbf{R}'} \times \\
&\quad \chi_j^{\mathbf{q}'}(\mathbf{r}_2) d\mathbf{r}_2 d\mathbf{r}_1 \\
&= \sum_{\mathbf{R}} e^{i(\mathbf{q}-\mathbf{q}')\cdot\mathbf{R}} \int_{\Omega} \sum_{\mathbf{R}'} \int_{\Omega} (\chi_i^{\mathbf{q}}(\mathbf{r}_1))^* f(\mathbf{r}_1, \mathbf{r}_2 - \mathbf{R}', \tau) e^{-i\mathbf{q}'\cdot\mathbf{R}'} \chi_j^{\mathbf{q}'}(\mathbf{r}_2) d\mathbf{r}_2 d\mathbf{r}_1 \\
&= N_c \delta_{\mathbf{q}, \mathbf{q}'} \int_{\Omega} \int_{\Omega} (\chi_i^{\mathbf{q}}(\mathbf{r}_1))^* \sum_{\mathbf{R}'} f(\mathbf{r}_1, \mathbf{r}_2 - \mathbf{R}', \tau) e^{-i\mathbf{q}'\cdot\mathbf{R}'} \chi_j^{\mathbf{q}}(\mathbf{r}_2) d\mathbf{r}_2 d\mathbf{r}_1,
\end{aligned} \tag{I.3}$$

where we have made use of this relation for the Bravais lattice:

$$\sum_{\mathbf{R}} e^{-i(\mathbf{q}-\mathbf{q}')\cdot\mathbf{R}} = N_c \delta_{\mathbf{q}, \mathbf{q}'}. \tag{I.4}$$

N_c is the number of cells in the crystal.

With these treatments, the expansion of Eq. I.2 is written as

$$\left\{ \begin{aligned} f(\mathbf{r}_1, \mathbf{r}_2, \tau) &= \sum_{\mathbf{q}} \sum_{i,j}^{BZ} \chi_i^{\mathbf{q}}(\mathbf{r}_1) f_{i,j}(\mathbf{q}, \tau) (\chi_j^{\mathbf{q}}(\mathbf{r}_2))^* \\ f_{i,j}(\mathbf{q}, \tau) &= \int_V \int_V (\chi_i^{\mathbf{q}}(\mathbf{r}_1))^* f(\mathbf{r}_1, \mathbf{r}_2, \tau) \chi_j^{\mathbf{q}}(\mathbf{r}_2) d\mathbf{r}_2 d\mathbf{r}_1 \end{aligned} \right\}, \tag{I.5}$$

where the integration must be done on the whole volume of the crystal, or:

$$\left\{ \begin{aligned} f(\mathbf{r}_1, \mathbf{r}_2, \tau) &= \sum_{\mathbf{q}} \sum_{i,j}^{BZ} \chi_i^{\mathbf{q}}(\mathbf{r}_1) f_{i,j}(\mathbf{q}, \tau) (\chi_j^{\mathbf{q}}(\mathbf{r}_2))^* \\ f_{i,j}(\mathbf{q}, \tau) &= N_c \int_{\Omega} \int_{\Omega} (\chi_i^{\mathbf{q}}(\mathbf{r}_1))^* \sum_{\mathbf{R}} f(\mathbf{r}_1, \mathbf{r}_2 - \mathbf{R}, \tau) e^{-i\mathbf{q}\cdot\mathbf{R}} \chi_j^{\mathbf{q}}(\mathbf{r}_2) d\mathbf{r}_2 d\mathbf{r}_1 \end{aligned} \right\}, \tag{I.6}$$

where the integration must be performed only on the Wigner-Zeits cell.

If we have a product of operators, say:

$$h(\mathbf{r}_1, \mathbf{r}_2, \tau) = \int_V f(\mathbf{r}_1, \mathbf{r}_3, \tau) g(\mathbf{r}_3, \mathbf{r}_2, \tau) d\mathbf{r}_3, \tag{I.7}$$

then, according to Eq. I.5 the expansion of h in the set of functions $\{\chi_i^{\mathbf{q}}(\mathbf{r})\}$ is:

$$\begin{aligned} h_{i,j}(\mathbf{q}, \tau) &= \int_V \int_V [\chi_i^{\mathbf{q}}(\mathbf{r}_1)]^* h(\mathbf{r}_1, \mathbf{r}_2, \tau) \chi_j^{\mathbf{q}}(\mathbf{r}_2) d\mathbf{r}_2 d\mathbf{r}_1 \\ &= \int_V \int_V [\chi_i^{\mathbf{q}}(\mathbf{r}_1)]^* \left(\int_V f(\mathbf{r}_1, \mathbf{r}_3, \tau) g(\mathbf{r}_3, \mathbf{r}_2, \tau) d\mathbf{r}_3 \right) \chi_j^{\mathbf{q}}(\mathbf{r}_2) d\mathbf{r}_2 d\mathbf{r}_1 \end{aligned} \quad (\text{I.8})$$

We can now use the second line of equation I.5 for f and g and the orthogonality of the basis to get:

$$\begin{aligned} h_{i,j}(\mathbf{q}, \tau) &= \int_V \int_V [\chi_i^{\mathbf{q}}(\mathbf{r}_1)]^* \left(\int_V f(\mathbf{r}_1, \mathbf{r}_3, \tau) g(\mathbf{r}_3, \mathbf{r}_2, \tau) d\mathbf{r}_3 \right) \chi_j^{\mathbf{q}}(\mathbf{r}_2) d\mathbf{r}_2 d\mathbf{r}_1 \\ &= \int_V \int_V [\chi_i^{\mathbf{q}}(\mathbf{r}_1)]^* \left(\int_V \sum_{\mathbf{q}_1}^{BZ} \sum_{l,m} \chi_l^{\mathbf{q}_1}(\mathbf{r}_1) f_{l,m}(\mathbf{q}_1, \tau) [\chi_m^{\mathbf{q}_1}(\mathbf{r}_3)]^* \times \right. \\ &\quad \left. \sum_{\mathbf{q}_2}^{BZ} \sum_{n,p} \chi_n^{\mathbf{q}_2}(\mathbf{r}_3) g_{n,p}(\mathbf{q}_2, \tau) [\chi_p^{\mathbf{q}_2}(\mathbf{r}_2)]^* d\mathbf{r}_3 \right) \chi_j^{\mathbf{q}}(\mathbf{r}_2) d\mathbf{r}_2 d\mathbf{r}_1 \\ &= \sum_{\mathbf{q}_1}^{BZ} \sum_{\mathbf{q}_2}^{BZ} \sum_{l,m} \sum_{n,p} \left(\int_V [\chi_i^{\mathbf{q}}(\mathbf{r}_1)]^* \chi_l^{\mathbf{q}_1}(\mathbf{r}_1) d\mathbf{r}_1 \right) f_{l,m}(\mathbf{q}_1, \tau) \times \\ &\quad \left(\int_V [\chi_m^{\mathbf{q}_1}(\mathbf{r}_3)]^* \chi_n^{\mathbf{q}_2}(\mathbf{r}_3) d\mathbf{r}_3 \right) g_{n,p}(\mathbf{q}_2, \tau) \times \\ &\quad \left(\int_V [\chi_p^{\mathbf{q}_2}(\mathbf{r}_2)]^* \chi_j^{\mathbf{q}}(\mathbf{r}_2) d\mathbf{r}_2 \right) \\ &= \sum_{\mathbf{q}_1}^{BZ} \sum_{\mathbf{q}_2}^{BZ} \sum_{l,m} \sum_{n,p} \delta(\mathbf{q}, \mathbf{q}_1) \delta_{i,l} f_{l,m}(\mathbf{q}_1, \tau) \delta(\mathbf{q}_1, \mathbf{q}_2) \delta_{m,n} g_{n,p}(\mathbf{q}_2, \tau) \delta(\mathbf{q}_2, \mathbf{q}) \delta_{pj}, \end{aligned} \quad (\text{I.9})$$

then we arrive at the expected expression:

$$\boxed{h_{i,j}(\mathbf{q}, \tau) = \sum_l f_{i,l}(\mathbf{q}, \tau) g_{l,j}(\mathbf{q}, \tau)}. \quad (\text{I.10})$$

Appendix J

Useful Mathematical Relations

In this chapter we give a digest of useful mathematical formulae that are used throughout the text.

J.1 Spherical Harmonics

- Definition: In the Condon Shortley convention the spherical harmonics are defined as,

$$Y_{l,m}(\theta, \phi) \equiv (-1)^m \sqrt{\frac{2l+1}{4\pi} \frac{(l-m)!}{(l+m)!}} P_l^m(\cos \theta) e^{im\phi}, \quad (\text{J.1})$$

where $P_l^m(x)$ is the corresponding Legendre-polynomial (See Ref. [154]).

- Recurrence relations:

$$Y_{0,0}(\theta, \phi) = \sqrt{\frac{1}{4\pi}} \quad (\text{J.2a})$$

$$Y_{1,0}(\theta, \phi) = \sqrt{\frac{3}{4\pi}} \cos(\theta) \quad (\text{J.2b})$$

$$Y_{1,1}(\theta, \phi) = -\sqrt{\frac{3}{8\pi}} \sin(\theta) e^{i\phi} \quad (\text{J.2c})$$

$$Y_{1,-1}(\theta, \phi) = -Y_{1,1}(\theta, \phi) \quad (\text{J.2d})$$

$$Y_{l,l}(\theta, \phi) = -\sqrt{\frac{2l+1}{2l}} \sin(\theta) e^{i\phi} Y_{l-1,l-1} \quad (\text{J.2e})$$

$$Y_{l,m}(\theta, \phi) = \sqrt{\frac{(2l-1)(2l+1)}{(l-m)(l+m)}} \cos(\theta) Y_{l-1,m}(\theta, \phi) - \sqrt{\frac{(l-1+m)(l-1-m)(2l+1)}{(2l-3)(l-m)(l+m)}} Y_{l-2,m}(\theta, \phi) \quad (\text{J.2f})$$

- Conjugation:

$$Y_{l,-m}(\theta, \phi) = (-1)^m Y_{l,m}^*(\theta, \phi) \quad (\text{J.3})$$

- Inversion:

$$Y_{l,m}(\hat{r}) = (-1)^l Y_{l,m}(-\hat{r}) \quad (\text{J.4})$$

- Other relations:

$$e^{i\phi} \sin \theta Y_{l,m}(\theta, \phi) = F^{(1)} Y_{l+1,m+1}(\theta, \phi) + F^{(2)} Y_{l-1,m+1}(\theta, \phi) \quad (\text{J.5a})$$

$$e^{-i\phi} \sin \theta Y_{l,m}(\theta, \phi) = F^{(3)} Y_{l+1,m-1}(\theta, \phi) + F^{(4)} Y_{l-1,m-1}(\theta, \phi) \quad (\text{J.5b})$$

$$\cos \theta Y_{l,m}(\theta, \phi) = F^{(5)} Y_{l+1,m}(\theta, \phi) + F^{(6)} Y_{l-1,m}(\theta, \phi) \quad (\text{J.5c})$$

$$e^{i\phi} \left(\cos \theta \frac{\partial}{\partial \theta} + \frac{i}{\sin \theta} \frac{\partial}{\partial \theta} \right) Y_{l,m}(\theta, \phi) = -l F^{(1)} Y_{l+1,m+1}(\theta, \phi) + (l+1) F^{(2)} Y_{l-1,m+1}(\theta, \phi) \quad (\text{J.5d})$$

$$e^{-i\phi} \left(\cos \theta \frac{\partial}{\partial \theta} - \frac{i}{\sin \theta} \frac{\partial}{\partial \theta} \right) Y_{l,m}(\theta, \phi) = -l F^{(3)} Y_{l+1,m-1}(\theta, \phi) + (l+1) F^{(4)} Y_{l-1,m-1}(\theta, \phi) \quad (\text{J.5e})$$

$$-\sin \theta \frac{\partial}{\partial \theta} Y_{l,m}(\theta, \phi) = -l F^{(5)} Y_{l+1,m}(\theta, \phi) + (l+1) F^{(6)} Y_{l-1,m}(\theta, \phi) \quad (\text{J.5f})$$

where:

$$F_{l,m}^{(1)} = -\sqrt{\frac{(l+m+1)(l+m+2)}{2l+1)(2l+3)}} \quad (\text{J.6a})$$

$$F_{l,m}^{(2)} = \sqrt{\frac{(l-m)(l-m-1)}{2l-1)(2l+1)}} \quad (\text{J.6b})$$

$$F_{l,m}^{(3)} = \sqrt{\frac{(l-m+1)(l-m+2)}{2l+1)(2l+3)}} \quad (\text{J.6c})$$

$$F_{l,m}^{(4)} = -\sqrt{\frac{(l+m)(l+m-1)}{2l-1)(2l+1)}} \quad (\text{J.6d})$$

$$F_{l,m}^{(5)} = \sqrt{\frac{(l-m+1)(l+m+1)}{2l+1)(2l+3)}} \quad (\text{J.6e})$$

$$F_{l,m}^{(6)} = \sqrt{\frac{(l-m)(l+m)}{2l-1)(2l+1)}} \quad (\text{J.6f})$$

- Gaunt coefficients:

$$\mathcal{G}_{l,l';m,m'}^{LM} = \int Y_{L,M}^*(\hat{r}) Y_{l,m}(\hat{r}) Y_{l',m'}(\hat{r}) d\hat{r} \quad (\text{J.7})$$

J.2 Plane Waves

- Rayleigh expansion:

$$\begin{aligned}
 e^{i\mathbf{g}\cdot\mathbf{r}} &= 4\pi \sum_{\lambda=0}^{\infty} \sum_{\mu=-\lambda}^{+\lambda} i^{\lambda} j_{\lambda}(gr) Y_{\lambda,\mu}^*(T^{-1}\hat{\mathbf{g}}) Y_{\lambda,\mu}(T^{-1}\hat{\mathbf{r}}) \\
 &= 4\pi \sum_{\lambda=0}^{\infty} \sum_{\mu=-\lambda}^{+\lambda} i^{\lambda} j_{\lambda}(gr) Y_{\lambda,\mu}(T^{-1}\hat{\mathbf{g}}) Y_{\lambda,\mu}^*(T^{-1}\hat{\mathbf{r}})
 \end{aligned} \tag{J.8}$$

J.3 Fourier Transform

- Definition: We use the following convention for the time-frequency Fourier Transform:

$$\begin{aligned}
 F(\omega) &= \int_{-\infty}^{\infty} F(t) e^{i\omega t} dt \\
 F(t) &= \frac{1}{2\pi} \int_{-\infty}^{\infty} F(\omega) e^{-i\omega t} d\omega.
 \end{aligned} \tag{J.9}$$

- Imaginary axes: The Fourier transform between imaginary axes work like its counterpart on the real axes, except that additional factors of $\pm i$ have to be included:

$$\begin{aligned}
 F(i\omega) &= -i \int_{-\infty}^{\infty} F(i\tau) e^{-i\omega\tau} d\tau \\
 F(i\tau) &= \frac{i}{2\pi} \int_{-\infty}^{\infty} F(i\omega) e^{i\omega\tau} d\omega.
 \end{aligned} \tag{J.10}$$

J.4 Spherical Coordinates

- Derivatives:

$$\begin{aligned}
 \partial x \pm i\partial y &= \sin\theta e^{\pm i\phi} \frac{\partial}{\partial r} + \frac{e^{\pm i\phi}}{r} \left(\cos\theta \frac{\partial}{\partial\theta} \pm \frac{i}{\sin\theta} \frac{\partial}{\partial\phi} \right) \\
 \partial z &= \cos\theta \frac{\partial}{\partial r} - \frac{1}{r} \sin\theta \frac{\partial}{\partial\theta}
 \end{aligned} \tag{J.11}$$

J.5 The Step(Heaviside) Function

Definition:

$$\Theta(\mathbf{r}) = \begin{cases} 1 & \mathbf{r} \in \text{interstitial} \\ 0 & \mathbf{r} \notin \text{interstitial} \end{cases} \quad (\text{J.12})$$

Since the step function $\Theta(\mathbf{r})$ has the periodicity of the lattice we may expand it in a Fourier series as:

$$\Theta(\mathbf{r}) = \sum_{\mathbf{G}} \tilde{\Theta}_{\mathbf{G}} e^{i\mathbf{G}\cdot\mathbf{r}}, \quad (\text{J.13})$$

where $\tilde{\Theta}_{\mathbf{G}}$ can be calculated analytically, giving:

$$\tilde{\Theta}_{\mathbf{G}} = \begin{cases} 1 - \sum_a \frac{4\pi r_a^3}{3\Omega} & \mathbf{G} = 0 \\ -\frac{4\pi}{\Omega G} \sum_a j_1(Gr_a) r_a^2 e^{i\mathbf{G}\cdot\mathbf{r}_a} & \mathbf{G} \neq 0 \end{cases}. \quad (\text{J.14})$$

Bibliography

- [1] R. M. Martin, *Electronic Structure, Basic Theory and Practical Methods* (Univ. Princeton, Cambridge, 2004).
- [2] G. Onida, L. Reining, and A. Rubio, *Rev. Mod. Phys.* **74**, 601 (2002).
- [3] P. Hohenberg and W. Kohn, *Phys. Rev.* **136**, B864 (1964).
- [4] W. Kohn and L. J. Sham, *Phys. Rev.* **140**, A1133 (1965).
- [5] V. L. Moruzzi, J. F. Janak, and A. R. Williams, *Calculated Electronic Properties of Metals* (Pergamon Pr., Oxford, 1978).
- [6] G. D. Mahan, *Many-Particle Physics* (Plenum Press, New York, 1990).
- [7] R. P. Feynman, *Phys. Rev.* **76**, 769 (1949).
- [8] L. Hedin, *Phys. Rev.* **139**, A796 (1965).
- [9] M. S. Hybertsen and S. G. Louie, *Phys. Rev. Lett.* **55**, 1418 (1985).
- [10] M. S. Hybertsen and S. G. Louie, *Phys. Rev. B* **34**, 5390 (1986).
- [11] X. J. Zhu and S. G. Louie, *Phys. Rev. B* **43**, 14142 (1991).
- [12] E. L. Shirley, Z. J. Zhu, and S. G. Louie, *Phys. Rev. B* **56**, 6648 (1997).
- [13] T. Kotani and M. van Schilfgaarde, *Solid State Commun.* **121**, 461 (2002).
- [14] W. Ku and A. G. Eguiluz, *Phys. Rev. Lett.* **89**, 126401 (2002).
- [15] K. Delaney, P. Garcia-Gonzalez, A. Rubio, P. Rinke, and R. W. Godby, *Phys. Rev. Lett.* **93**, 249701 (2004).
- [16] W. Ku and A. G. Eguiluz, *Phys. Rev. Lett.* **93**, 249702 (2004).
- [17] F. Jensen, *Introduction to Computational Chemistry* (John Wiley and sons, 1999).
- [18] D. R. Hartree, *Proc. Cambridge Phil. Soc.* **24**, 89 (1928).

-
- [19] V. Fock, Z. Physik **61**, 126 (1930).
- [20] J. A. Pople and P. K. Nesbet, J. Chem. Phys. **22**, 571 (1954).
- [21] A. Szabo and N. S. Ostlund, *Modern Quantum Chemistry: Introduction to Advanced Electronic Structure Theory* (Dover Pub. Inc., New York, 1996).
- [22] C. Møller and M. S. Plesset, Phys. Rev. **46**, 618 (1934).
- [23] F. Coester, Nucl. Phys. **7**, 421 (1958).
- [24] F. Coester and H. Kummel, *ibid* **17**, 477 (1960).
- [25] L. H. Thomas, Proc. Cambridge Phil. Soc. **23**, 542 (1927).
- [26] E. Fermi, Rend. Accad. Naz. Lincei **6**, 602 (1927).
- [27] E. Fermi, Z. Physik **48**, 73 (1928).
- [28] P. A. M. Dirac, Proc. Cambridge Phil. Soc. **26**, 361 (1930).
- [29] U. von Barth and L. Hedin, J. Phys.: Cond. Mat. **5**, 1629 (1972).
- [30] O. Gunnarsson, B. I. Lundqvist, and J. W. Wilkins, Phys. Rev. B **10**, 1319 (1974).
- [31] R. O. Jones and O. Gunnarsson, Rev. Mod. Phys. **61**, 689 (1989).
- [32] M. Levy, Proc. Nat. Acad. Sci. (USA) **76**, 6062 (1979).
- [33] M. Levy, Phys. Rev. A **26**, 1200 (1982).
- [34] A. Shimony and H. Feshbach, *Physics as Natural Philosophy* (p. 111, MIT Press, Cambridge, 1982).
- [35] E. H. Lieb, Int. J. Quant. Chem. **24**, 243 (1983).
- [36] R. M. Dreizler and J. da Providencia, *Density Functional Methods in Physics* (p. 31, Plenum, New York, 1985).
- [37] R. M. Dreizler and E. K. U. Gross, *Density Functional Theory* (Springer-Verlag, Berlin, Heidelberg, 1990).
- [38] A. K. Rajagopal and J. Callaway, Phys. Rev. B **7**, 1912 (1973).
- [39] L. N. Oliveira, E. K. U. Gross, and W. Kohn, Phys. Rev. Lett. **60**, 2430 (1988).
- [40] S. Kurth, M. Marques, M. Lüders, and E. K. U. Gross, Phys. Rev. Lett. **83**, 2628 (1999).

- [41] J. P. Perdew and K. Schmidt, *Density Functional Theory and Its Applications to Materials* (edited by V. Van Doren *et al.*, American Institute of Physics, New York, 2001).
- [42] D. M. Ceperley and B. J. Alder, *Phys. Rev. Lett.* **45**, 566 (1980).
- [43] J. P. Perdew and A. Zunger, *Phys. Rev. B* **23**, 5048 (1981).
- [44] J. P. Perdew and Y. Wang, *Phys. Rev. B* **33**, 8800 (1986).
- [45] J. P. Perdew and Y. Wang, *Phys. Rev. B* **40**, 3399 (1989).
- [46] J. P. Perdew, K. Burke, and M. Ernzerhof, *Phys. Rev. Lett.* **77**, 3865 (1996).
- [47] J. P. Perdew, K. Burke, and Y. Wang, *Phys. Rev. B* **54**, 16533 (1996).
- [48] W. Kohn, A. D. Becke, and R. G. Parr, *J. Chem. Phys.* **100**, 12974 (1996).
- [49] A. D. Becke, *J. Chem. Phys.* **102**, 8554 (1997).
- [50] J. P. Perdew, A. Ruzsinszky, J. M. Tao, V. N. Staroverov, G. E. Scuseria, and G. I. Csonka, *J. Chem. Phys.* **123**, 062201 (pages 9) (2005).
- [51] J. C. Slater and K. H. Johnson, *Phys. Rev. B* **5844** (1972).
- [52] J. F. Janak, *Phys. Rev. B* **18**, 7165 (1978).
- [53] C. O. Almbladh and U. von Barth, *Phys. Rev. B* **31**, 3231 (1985).
- [54] S. Lizzit, A. Baraldi, A. Groso, K. Reuter, M. V. Ganduglia-Pirovano, C. Stampfl, M. Scheffler, M. Stichler, C. Keller, W. Wurth, *et al.*, *Phys. Rev. B* **63**, 205419 (2001).
- [55] J. P. Perdew, D. C. Langreth, and V. Sahni, *Phys. Rev. Lett.* **38**, 1030 (1977).
- [56] A. Görling and M. Levy, *Phys. Rev. A* **50**, 196 (1994).
- [57] A. Görling, *Phys. Rev. B* **53**, 7024 (1996).
- [58] S. Sharma, J. K. Dewhurst, and C. Ambrosch-Draxl, *Phys. Rev. Lett.* **95**, 136402 (2005).
- [59] M. Städele, J. A. Majewski, P. Vogl, and A. Görling, *Phys. Rev. Lett.* **79**, 2089 (1997).
- [60] T. Kotani, *Phys. Rev. Lett.* **74**, 2989 (1995).
- [61] J. P. Perdew and M. Levy, *Phys. Rev. Lett.* **51**, 1884 (1983).

- [62] L. J. Sham and M. Schlüter, Phys. Rev. Lett. **51**, 1888 (1983).
- [63] L. J. Sham and M. Schlüter, Phys. Rev. B **32**, 3883 (1985).
- [64] M. Grüning, A. Marini, and A. Rubio, J. Chem. Phys. **124**, 154108 (2006).
- [65] D. J. Singh, *Planewaves, Pseudopotential and the LAPW method* (Kluwer Aca. Pub., Norwell, Massachusetts, 1994).
- [66] D. R. Hamann, M. Schlüter, and C. Chiang, Phys. Rev. Lett. **43**, 1494 (1979).
- [67] G. B. Bachelet, D. R. Hamann, and M. Schlüter, Phys. Rev. B **26**, 4199 (1982).
- [68] D. Vanderbilt, Phys. Rev. B **41**, 7892 (1990).
- [69] K. Laasonen, A. Pasquarello, R. Car, C. Lee, and D. Vanderbilt, Phys. Rev. B **47**, 10142 (1993).
- [70] D. R. Hamann, Phys. Rev. B **40**, 2980 (1989).
- [71] N. Troullier and J. L. Martins, Phys. Rev. B **43**, 1993 (1991).
- [72] L. Kleinman and D. M. Bylander, Phys. Rev. Lett. **48**, 1425 (1982).
- [73] U. von Barth and C. D. Gelatt, Phys. Rev. B **21**, 2222 (1980).
- [74] S. G. Louie, S. Froyen, and M. L. Cohen, Phys. Rev. B **26**, 1738 (1982).
- [75] P. Puschnig and C. Ambrosch-Draxl, Phys. Rev. B **66**, 165105 (2002).
- [76] J. C. Slater, Phys. Rev. **51**, 846 (1937).
- [77] P. de Ciccio, Phys. Rev. **153**, 931 (1967).
- [78] N. Elyashar and D. D. Koelling, Phys. Rev. B **13**, 5362 (1976).
- [79] O. K. Andersen, Phys. Rev. B **12**, 3060 (1975).
- [80] E. Sjöstedt, L. Nordström, and D. J. Singh, Solid State Commun. **114**, 15 (2000).
- [81] G. K. H. Madsen, P. Blaha, K. Schwarz, E. Sjöstedt, and L. Nordström, Phys. Rev. B **64**, 195134 (2001).
- [82] D. Singh, Phys. Rev. B **43**, 6388 (1991).
- [83] M. E. Rose, *Elementary Theory of Angular Momentum* (John Wiley and sons, 1957).
- [84] M. Kara and K. Kurki-Suonio, Acta Crystallografica A **37**, 201 (1981).
- [85] M. R. A. Shegelski, Am. J. Phys. **72**, 676 (2004).

- [86] A. L. Fetter and J. D. Walecka, *Quantum Theory of Many-Particle Systems* (McGraw-Hill, 1971).
- [87] L. Hedin and S. Lundqvist, *Solid State Phys.: Advances in Research and Applications* **23**, 1 (1969).
- [88] F. Aryasetiawan and O. Gunnarsson, *Rep. Prog. Phys.* **61**, 237 (1998).
- [89] J. Schwinger, *Proc. Natl. Acad. Sci. U. S.* **37**, 452 (1951).
- [90] G. Pratt, *Phys. Rev.* **118**, 462 (1960).
- [91] G. Pratt, *Rev. Mod. Phys.* **35**, 502 (1963).
- [92] L. Hedin, *Bull. Am. Phys. Soc.* **8**, 535 (1963).
- [93] E. K. U. Gross, R. Runge, and O. Heinonen, *Many-Particle Theory* (Adam Hilger, 1991).
- [94] J. E. Northrup, M. S. Hybertsen, and S. G. Louie, *Phys. Rev. Lett.* **59**, 819 (1987).
- [95] C. Petrillo and F. Sacchetti, *Phys. Rev. B* **38**, 3834 (1988).
- [96] O. Zakharov, A. Rubio, X. Blase, M. L. Cohen, and S. G. Louie, *Phys. Rev. B* **50**, 10780 (1994).
- [97] P. Blaha, K. Schwarz, G. K. H. Madsen, D. Kvasnicka, and J. Luitz, *WIEN2k, An Augmented Plane Wave Plus Local Orbitals Program for Calculating Crystal Properties* (Tchn. Universität Wien, Austria, 2002), ISBN 3-9501031-1-2.
- [98] A. Baldereschi, *Phys. Rev. B* **7**, 5212 (1973).
- [99] D. J. Chadi and M. L. Cohen, *Phys. Rev. B* **7**, 692 (1973).
- [100] D. J. Chadi and M. L. Cohen, *Phys. Rev. B* **8**, 5747 (1973).
- [101] H. J. Monkhorst and J. D. Pack, *Phys. Rev. B* **13**, 5188 (1976).
- [102] O. Jepsen and O. K. Andersen, *Solid State Comm.* **9**, 1763 (1971).
- [103] G. Lehmann, P. Rennert, M. Taut, and H. Wonn, *Phys. Status Solidi* **37**, K27 (1970).
- [104] J. Rath and A. J. Freeman, *Phys. Rev. B* **11**, 2109 (1975).
- [105] P. E. Blöchl, O. Jepsen, and O. K. Andersen, *Phys. Rev. B* **49**, 16223 (1994).
- [106] S. Massidda, M. Posternak, and A. Baldereschi, *Phys. Rev. B* **48**, 5058 (1993).

- [107] R. W. Godby, M. Schlüter, and L. J. Sham, Phys. Rev. B **37**, 10159 (1988).
- [108] T. Matsubara, Prog. Theor. Phys. **14**, 351 (1955).
- [109] M. M. Rieger, L. Steinbeck, I. D. White, H. N. Rojas, and R. W. Godby, Comput. Phys. Commun. **117**, 211 (1999).
- [110] M. L. Tiago, S. Ismail-Beigi, and S. G. Louie, Phys. Rev. B **69**, 125212 (2004).
- [111] C. Friedrich, A. Schindlmayr, S. Blügel, and T. Kotani, Phys. Rev. B **74**, 045104 (2006).
- [112] A. Fleszar and W. Hanke, Phys. Rev. B **56**, 10228 (1997).
- [113] F. Gygi and A. Baldereschi, Phys. Rev. Lett. **62**, 2160 (1989).
- [114] R. W. Godby, M. Schlüter, and L. J. Sham, Phys. Rev. B **36**, 6497 (1987).
- [115] M. van Schilfgaarde, T. Kotani, and S. V. Faleev, Phys. Rev. B **74**, 245125 (2006).
- [116] J. Q. Wang, Z. Q. Gu, and M. F. Li, Phys. Rev. B **44**, 8707 (1991).
- [117] E. L. Shirley and R. M. Martin, Phys. Rev. B **47**, 15404 (1993).
- [118] URL <http://www.sxlib.de>.
- [119] L. Steinbeck, A. Rubio, L. Reining, M. Torrent, I. D. White, and R. W. Godby, Comput. Phys. Commun. **125**, 105 (2000).
- [120] M. Fuchs and M. Scheffler, Comput. Phys. Commun. **119**, 67 (1999).
- [121] F. Bechstedt, K. Seino, P. H. Hahn, and W. G. Schmidt, Phys. Rev. B **72**, 245114 (2005).
- [122] M. Piacentini, D. W. Lynch, and C. G. Olson, Phys. Rev. B **13**, 5530 (1976).
- [123] M. van Schilfgaarde, T. Kotani, and S. Faleev, Phys. Rev. Lett. **96**, 226402 (2006).
- [124] M. P. Surh, S. G. Louie, and M. L. Cohen, Phys. Rev. B **43**, 9126 (1991).
- [125] E. L. Shirley, Phys. Rev. B **58**, 9579 (1998).
- [126] O. Madelung, W. von der Osten, and U. Rössler, *Intrinsic Properties of Group IV Elements and III-V, II-VI and I-VII Compounds, Vol. 22A of Landolt-Börnstein: Numerical Data and Functional Relationships in Science and Technology - New Series; Group III* (Springer Verlag, New York,, 1987).
- [127] M. Miyata, K. Moriki, O. Mishima, M. Fujisawa, and T. Hattori, Phys. Rev. B **40**, 12028 (1989).

- [128] R. T. Poole, J. G. Jenkin, J. Liesegang, and R. C. G. Leckey, *Phys. Rev. B* **11**, 5179 (1975).
- [129] D. E. Aspnes, *Phys. Rev. B* **14**, 5331 (1976).
- [130] D. Straub, L. Ley, and F. J. Himpsel, *Phys. Rev. Lett.* **54**, 142 (1985).
- [131] T. C. Chiang, J. A. Knapp, M. Aono, and D. E. Eastman, *Phys. Rev. B* **21**, 3513 (1980).
- [132] D. Straub, M. Skibowski, and F. J. Himpsel, *Phys. Rev. B* **32**, 5237 (1985).
- [133] M. Rohlfing, P. Krüger, and J. Pollmann, *Phys. Rev. Lett.* **75**, 3489 (1995).
- [134] T. Böttcher, S. Figge, S. Einfeldt, R. Chierchia, R. Kröger, C. Petter, C. Zellweger, H.-J. Bühlmann, M. Dießelberg, D. Rudloff, et al., *physica status solidi (c)* **0**, 1846 (2003).
- [135] M. Jain, ed., *II-VI Semiconductor Compounds* (World Scientific Publishing, Singapore, 1993).
- [136] S. H. Wei and A. Zunger, *Phys. Rev. B* **37**, 8958 (1988).
- [137] P. Schröer, P. Krüger, and J. Pollmann, *Phys. Rev. B* **47**, 6971 (1993).
- [138] V. Fiorentini, M. Methfessel, and M. Scheffler, *Phys. Rev. B* **47**, 13353 (1993).
- [139] M. Rohlfing, P. Krüger, and J. Pollmann, *Phys. Rev. B* **57**, 6485 (1998).
- [140] W. D. Luo, S. Ismail-Beigi, M. L. Cohen, and S. G. Louie, *Phys. Rev. B* **66**, 195215 (2002).
- [141] T. Miyake, P. H. Zhang, M. L. Cohen, and S. G. Louie, *Phys. Rev. B* **74**, 245213 (2006).
- [142] P. Rinke, A. Qteish, J. Neugebauer, C. Freysoldt, and M. Scheffler, *New J. Phys.* **7**, 126 (2005).
- [143] A. Fleszar and W. Hanke, *Phys. Rev. B* **71**, 045207 (2005).
- [144] K. H. Hellwege and O. Madelung, *Landolt-Börnstein: Numerical Data and Functional Relationship in Science and Technology, New Series, Group III, Vols. 17a and 22a* (Springer, New York, 1982).
- [145] G. Ramirez-Flores, H. Navarro-Contreras, A. Lastras-Martinez, P. C. Powell, and J. E. Greene, *Phys. Rev. B* **50**, 8433 (1994).
- [146] W. R. L. Lambrecht, B. Segall, S. Strite, G. Martin, A. Agarwal, H. Morkoc, and A. Rockett, *Phys. Rev. B* **50**, 14155 (1994).

-
- [147] L. Zhou, T. A. Callcott, J. J. Jia, D. L. Ederer, and R. Perera, *Phys. Rev. B* **55**, 5051 (1997).
- [148] K. O. Magnusson, G. Neuhold, K. Horn, and D. A. Evans, *Phys. Rev. B* **57**, 8945 (1998).
- [149] M. E. Rose, *J. Math. and Phys.* **37**, 215 (1958).
- [150] B. R. A. Nijboer and F. W. de Wette, *Physica* **23**, 309 (1957).
- [151] A. Baldereschi and E. Tosatti, *Solid State Commun.* **29**, 131 (1979).
- [152] J. G. Broerman, *J. Phys. Chem. Solids* **29**, 1147 (1968).
- [153] C. Ambrosch-Draxl and J. O. Sofo, *Comput. Phys. Commun.* **175**, 1 (2006).
- [154] M. Abramowitz and I. A. Stegun, *Handbook of Mathematical Functions* (Dover Pub. Inc., New York, 1972).

Acknowledgements

In the first place I would like to thank Prof. Dr. Matthias Scheffler for kindly offering me the opportunity to study in his wonderful group, and being extremely patient, helpful throughout my Ph.D. Discussions with him and listening to his lectures are always pleasant experiences which improve my understanding about electronic structures in such a way that I like it even more.

For this ongoing project of the all-electron G_0W_0 code, the topic of my thesis, I sincerely thank Dr. Ricardo I. Gomez-Abal, the architect of it, for his detailed and patient direct supervision and instruction. The help from him and his family makes life much easier in Berlin. Without this help and supervision, this thesis can never be finished.

In addition, I thank Prof. Dr. Claudia Ambrosch-Draxl from the University of Leoben, for the helpful discussions about the LAPW method. Many thanks also go to Dr. Hong Jiang, for his work on improving the code's efficiency and extremely helpful discussions when I wrote this thesis. Together with him, Dr. Xinguo Ren also made many helpful suggestions.

I sincerely thank my colleagues Dr. Patrick Rinke, Dr. Christoph Freysoldt, Dr. Philipp Eggert, Dr. Volker Blum and his family for their generous help in the last four years. Together with them, I also want to thank Yongsheng Zhang, Haiping Lin, Dr. Martin Friak, Dr. Ville Havu, Dr. Paula Havu, Dr. Johan Carlsson, Dr. Imad Belabbas, Sergio Durdagi, Jie Cao, Dr. Karsten Reuter, Dr. Li Sheng, Dr. Jutta Rogal, Dr. Qiangmiao Hu, Erik McNellis, Dr. Angelos Michaelides, Xiaoliang Hu, Dr. Liumin Liu, Ding Pan, Dr. Javier Carrasco, Bo Li, Biswajit Santra, Dr. Hua Wu, Dr. Wei Guo, Dr. Huiqiu Deng, Volker Hargis, and Dr. Dengke Yu.

I am deeply grateful to all the love and constant encouragement given by my wife, who brought me a lovely daughter during this Ph.D. I am grateful to my parents-in-law, who helped us to take care of our baby so that I can finish the work in time. Many thanks to my sister and her family for their constant support!

The deepest in my heart, I send this thesis as a present to my late parents, to whom I own every everything!

Lebenslauf

Personal Data

- Name: Xinzheng Li
- Date of Birth: July 04th, 1978
- Place of Birth: Juoyang, China
- Family Status: Married

Education

- 1984-1990: Preliminary School, Luoyang, China
- 1990-1996: Middle School, Luoyang, China
- 1996-2000: Bachelor in the Physics Department of Wuhan University, Wuhan, China
- 2000-2003: Master in the Semiconductor Institute of Chinese Academy of Science, Beijing, China
- 12/2003-07/2008: Doctor in the Fritz-Haber-Institut der Max-Planck-Gesellschaft

Publication

- i. Ricardo Gómez-Abal, Xinzheng Li, Matthias Scheffler, and Claudia Ambrosch-Draxl, *Influence of Core-Valence Interaction and Pseudoization on the Electron Self-Energy*, accepted by Phys. Rev. Lett.